Progress in Materials Science 155 (2026) 101492

Contents lists available at ScienceDirect

Progress in Materials Science

journal homepage: www.elsevier.com/locate/pmatsci

Critical current density in advanced superconductors☆

H.S. Ruiz [a,*], J. Hänisch [b], M. Polichetti [c,d], A. Galluzzi [c,d], L. Gozzelino [e,f], D. Torsello [e,f], S. Milošević-Govedarović [g], J. Grbović-Novaković [g], O.V. Dobrovolskiy [h], W. Lang [i], G. Grimaldi [d], A. Crisan [j], P. Badica [j], A.M. Ionescu [j], P. Cayado [k,l], R. Willa [m,n], B. Barbiellini [o,p], S. Eley [q,r], A. Badía–Majós [s]

[a] School of Engineering and Space Park Leicester, University of Leicester, University Rd, Leicester LE1 7RH, United Kingdom
[b] Karlsruhe Institute of Technology, Institute for Technical Physics, Hermann-von-Helmholtz-Platz 1, Eggenstein-Leopoldshafen 76344, Germany
[c] Department of Physics "E.R. Caianiello", University of Salerno, via Giovanni Paolo II, 132, Fisciano (SA) 84084, Italy
[d] Consiglio Nazionale delle Ricerche, CNR-SPIN, c/o Università di Salerno- via Giovanni Paolo II, 132, Fisciano (SA) 84084, Italy
[e] Department of Applied Science and Technology, Politecnico di Torino, Corso Duca degli Abruzzi, 24, Torino 10129, Italy
[f] Istituto Nazionale di Fisica Nucleare, Sezione di Torino, Via P. Giuria, 1, Torino 10125, Italy
[g] University of Belgrade, Vinča Institute of Nuclear Sciences, National Institute of Republic of Serbia, Centre of Excellence for Hydrogen and Renewable Energy - CONVINCE, Mike Petrovića Alasa 12-14, Belgrade 11000, Serbia
[h] Cryogenic Quantum Electronics, EMG and LENA, Technische Universität Braunschweig, Hans-Sommer-Str. 66, Braunschweig 38106, Germany
[i] Faculty of Physics, University of Vienna, Boltzmanngasse 5, Vienna 1090, Austria
[j] National Institute of Materials Physics, 405A Atomistilor Str., Magurele 077125, Romania
[k] University of Geneva, Department of Quantum Matter Physics (DQMP), Quai Ernest-Ansermet 24, Geneva 1211, Switzerland
[l] Departamento de Física, Universidad de Oviedo, Campus Llamaquique, C/ Calvo Sotelo s/n, Oviedo 33007, Spain
[m] Institute for Theoretical Condensed Matter Physics, Karlsruhe Institute of Technology, Wolfgang-Gaede Strasse 1, Karlsruhe D-76131, Germany
[n] Institute of Systems Engineering, School of Engineering, HES-SO Valais-Wallis, rue de l'Industrie 23, Sion CH-1950, Switzerland
[o] Department of Physics, School of Engineering Science, LUT University, Yliopistonkatu 34, Lappeenranta FI-53850, Finland
[p] Quantum Materials and Sensing Institute, Department of Physics, Northeastern University, 147 S Bedford St, Burlington MA 01803, USA
[q] Department of Physics, Colorado School of Mines, Golden Colorado 80401, USA
[r] Department of Electrical & Computer Engineering, University of Washington, Seattle WA 98195-2500, USA
[s] Departamento de Física de la Materia Condensada and Instituto de Nanociencia y Materiales de Aragón (INMA), Universidad de Zaragoza–CSIC, C/ María de Luna 3, Zaragoza E-50018, Spain

ARTICLE INFO

Keywords:
Superconductivity
Superconducting materials
Critical current density
Vortices
High temperature superconductors
Flux flow instabilities
Flux creep

ABSTRACT

This review paper delves into the concept of critical current density (J_c) in high-temperature superconductors (HTS) across macroscopic, mesoscopic, and microscopic perspectives. Through this exploration, a comprehensive range of connections is unveiled aiming to foster advancements in the physics, materials science, and the engineering of applied superconductors. Beginning with the macroscopic interpretation of J_c as a central material law, the review traces its development from C.P. Bean's foundational work to modern extensions. Mesoscopic challenges in understanding vortex dynamics and their coherence with thermodynamic anisotropy

☆ This review is result of the European Cooperation in Science and Technology (COST) action CA19108 entitled, High-Temperature Superconductivity for Accelerating the Energy Transition. https://www.cost.eu/actions/CA19108/.

* Corresponding author.
E-mail addresses: dr.harold.ruiz@leicester.ac.uk (H.S. Ruiz), jens.haenisch@kit.edu (J. Hänisch), mpolichetti@unisa.it (M. Polichetti), agalluzzi@unisa.it (A. Galluzzi), laura.gozzelino@polito.it (L. Gozzelino), daniele.torsello@polito.it (D. Torsello), sanjam@vinca.rs (S. Milošević-Govedarović), jasnag@vinca.rs (J. Grbović-Novaković), oleksandr.dobrovolskiy@tu-braunschweig.de (O.V. Dobrovolskiy), wolfgang.lang@univie.ac.at (W. Lang), gaia.grimaldi@spin.cnr.it (G. Grimaldi), acrisan652@gmail.com (A. Crisan), badica2003@yahoo.com (P. Badica), alina.ionescu@infim.ro (A.M. Ionescu), pablo.cayado@unige.ch (P. Cayado), roland.willa@hevs.ch (R. Willa), bernardo.barbiellini@lut.fi (B. Barbiellini), serename@uw.edu (S. Eley), anabadia@unizar.es (A. Badía–Majós).

https://doi.org/10.1016/j.pmatsci.2025.101492
Received 20 May 2024; Received in revised form 2 October 2024; Accepted 12 April 2025
Available online 26 May 2025

Flux pinning
Vortex–defect interactions

regimes are addressed, underscoring the importance of understanding the limitations and corrections implicit in the macroscopic measurement of J_c, linked with mesoscopic phenomena such as irradiation effects, defect manipulation, and vortex interactions. The transition to supercritical current densities is also discussed, detailing the superconductor behavior beyond critical thresholds with a focus on flux-flow instability regimes relevant to fault current limiters and fusion energy magnets. Enhancing J_c through tailored material microstructures, engineered pinning centers, grain boundary manipulation, and controlled doping is explored, along with radiation techniques and their impact on large-scale energy systems. Emphasizing the critical role of J_c, this review focuses on its physical optimization and engineering manipulation, highlighting its significance across diverse sectors.

Contents

Nomenclature

Below, we give a list of acronyms and symbols used for the physical quantities and characteristic material parameters. We recall that along this review physical units are expressed in the M. K. S. system. We have used upper-case for the electromagnetic fields $\mathbf{B}(\mathbf{r}), \mathbf{J}(\mathbf{r}), \mathbf{E}(\mathbf{r})$, that are coarse-grained averages at the macroscopic level.

Acronyms

1D	One dimensional system
2D	Two dimensional system
2G	Second generation
3D	Three dimensional system
AC	Alternating current
APC	Artificial Pinning Center
Ba122	$BaFe_2As_2$
Bi2212	$Bi_2Sr_2CaCu_2O_{8+x}$
Bi2223	$Bi_2Sr_2Ca_2Cu_3O_{10+x}$
BSCCO	$Bi_2Sr_2Ca_{n-1}Cu_nO_{2n+4+x}$
BZO	$BaZrO_3$
CC	Coated conductor
Co-Ba122	$Ba(Fe_{1-x}Co_x)_2As2$
cp	Collective pinning
CS	Critical State
CSD	Chemical solution deposition
DC	Direct current
DCS	Double Critical State
DFT	Density Functional Theory
DT	Deuterium–Tritium
DyBCO	$DyBa_2Cu_3O_y$
FFI	Flux flow instability
FLL	Flux line lattice
GB	Grain boundary
GdBCO	$GdBa_2Cu_3O_y$
GGA	Generalized gradient approximation
GL	Ginzburg–Landau
HBCO	$HgBa_2CuO_{4+\delta}$
Hg1212	$HgBa_2CaCu_2O_{6+\delta}$
HTS	High temperature superconductor

IBAD	Ion beam-assisted deposition
IBS	Iron (Fe)-based superconductors
ISD	Inclined substrate deposition
K-Ba122	$Ba_{1-x}K_xFe_2As_2$
LAADF	Low-angle annular dark-field scanning electron microscopy
LH2	Liquid Hydrogen
LHe	Liquid Helium
LN2	Liquid Nitrogen
LO	Larkin and Ovchinnikov
LSCO	$La_{2-x}Sr_xCuO_4$
LTS	Low temperature superconductor
MD	Molecular dynamics
MOCVD	Metal–Organic chemical vapor deposition
MOD	Metal–Organic Decomposition
MOI	Magneto-optical imaging
NPs	Embedded nanoparticles
P-Ba122	$BaFe_2(As_{1-x}P_x)_2$
PLD	Pulsed laser deposition
QCP	Quantum critical point
RABiTS	Rolling assisted biaxially textured substrate
REBCO	(Rare earth)$Ba_2Cu_3O_{7-x}$
SCAN	Strongly-Constrained and Appropriately-Normed
SCDFT	Superconducting density functional theory
SFs	Stacking Faults
SMP	Second magnetization peak
sp	strong pins
SPS	Spark plasma sintering
STM	Scanning tunneling microscopy
TBCCO	$Tl_2Ba_2Ca_{n-1}Cu_nO_{2n+4+x}$
TDGL	Time dependent Ginzburg–Landau
TEM	Transmission electron microscopy
Tl1212	$TlBa_2CaCu_2O_{7-\delta}$
Tl1223	$TlBa_2Ca_2Cu_3O_9$
Tl2212	$Tl_2Ba_2CaCu_2O_8$
Tl2223	$Tl_2Ba_2Ca_2Cu_3O_{10}$
VP	Vodolazov and Peeters
wcp	Weak collective pinning
YBCO	$YBa_2Cu_xO_{7-x}$

Vectorial (bold) and other physical quantities

$\mathcal{F}$	Ginzburg–Landau's free energy
$\mathbf{A}$	Magnetic vector potential
$\mathbf{B}$	Magnetic field (macroscopic)
$\mathbf{b}$	Magnetic field (mesoscopic)
$\mathbf{E}$	Electric field
$\mathbf{F}$	Mechanical force (macroscopic)
$\mathbf{f}$	Mechanical force (mesoscopic)
$\mathbf{f}_p$	Individual pinning force per unit volume
$\mathbf{F}_P$	Macroscopic average of the individual vortex pinning force density
$\mathbf{H}_a$	Applied magnetic field strength
$\mathbf{J}$	Current density (macroscopic)
$\mathbf{J}_\parallel$	Component of $\mathbf{J}$ parallel to $\mathbf{B}$

$\mathbf{J}_{\perp}$	Component of **J** perpendicular to **B**
$\mathbf{K}$	Surface current density/Sheet current
a_0	Intervortex separation
E_0	Threshold electric field
Gi	Ginzburg(–Levanyuk) number
H_{c1}	Lower critical field
H_{c2}	Upper critical field
H_c	Thermodynamic critical field
H_{sp}	Second magnetization peak field
h	Reduced magnetic field H/H_{irr}
h_0	Reduced magnetic field of maximum pinning force density
I	Current
I_c	Critical current
J_c	Critical current density
J_c^{sf}	J_c measured at self-field conditions
J_{dp}	Ginzburg–Landau depairing critical current density
k_B	Boltzmann constant
m_{ab}	Charge carriers' mass in the ab-plane
m_c	Charge carriers' mass on the c-axis
n	Power law index in empirical $E-J$ relationships
V	Voltage
V_{sc}	Volume of the superconductor
$\mathbf{J}_c$	Critical current density (macroscopic)
$\mathbf{K}_c$	Critical surface/sheet current density
H_p	Full penetration field (critical state)
M_V	Volume magnetization
T_c	Critical Temperature
t	Time
t_c	Reduced or normalized temperature T/T_c
$(\hat{\boldsymbol{\imath}}, \hat{\boldsymbol{\jmath}}, \hat{\boldsymbol{k}})$	Unit vectors for the Cartesian coordinates (x, y, z), respectively.
e	Electron's charge
h	Planck constant
m	Sample's magnetic moment
$\mathcal{P}$	Dissipation function (power per unit volume)
Q	Heat generated per unit volume
T	Temperature

Greek Symbols

γ	Anisotropy constant (unless otherwise stated)
γ^{-2}	Electronic mass anisotropy ratio, m_{ab}/m_c
$\mathbf{\Gamma}$	Current density's vector potential
Γ_c	Critical boundary of Δ_c
Δ	Superconducting energy gap
Δ_c	Yield region for the current density
ϵ_0	Vacuum's electrical permittivity
ϵ	Anisotropy ratio, $\epsilon = \gamma^{-1}$
ε_F	Fermi energy
ε_0	Vortex line energy
η	Vortex viscosity or vortex drag coefficient
Θ	Heaviside step function
θ	Angle between magnetic field and crystallographic c-axis
κ	Ginzburg–Landau's parameter

λ	London's penetration depth
μ_0	Vacuum's magnetic permeability
μ_n'	AC permeability (in-phase)
μ_n''	AC permeability (out-of-phase)
ν	Frequency
ξ	Coherence length
ξ_c	Coherence length along the c-axis
ξ_{ab}	Coherence length in the ab-planes
ρ	Resistivity
ρ_s	Superfluid density
$\boldsymbol{\tau}$	Torque
$\boldsymbol{\Phi}_0$	Flux quantum
χ	Magnetic anisotropy bandwidth
Ψ	Superconducting order parameter

1. Introduction

Governments around the world have shown varying levels of interest and support for superconductivity due to its potential technological, scientific, and economic benefits [1,2] and continue to consider this as a strategically important area of research and development. Advancements in superconducting technologies can enhance a country's competitiveness in various industries and contribute to technological leadership [3–9]. Although the industrialization processes that lead to the mass production of superconducting materials have currently reached a highly promising level [1], there is still sizeable room for optimization. Advancements are commonly linked with their progress in two separate physical parameters: the critical current density of the superconductor, J_c, and its critical temperature, T_c, both demarking the transitioning between the nearly zero electrical resistivity seen in superconductors and their dissipative behavior. One challenge lies in the fact that, to present, the most promising materials for large-scale applications categorized as *High-Temperature Superconductors* (HTS) still necessitate cryogenic environments due to their relatively low critical temperature (T_c) of typically less than 100 K.

We adopt here the notion of HTS as any type-II superconducting compound with a critical temperature well over 20 K. In fact, the concept starts from the ground-breaking discovery of superconductivity in copper oxides [10], which marked a turning point after decades of slow progress with the record value of $T_c = 23$ K for the *low-temperature superconductors* (LTS) [11]. Thus, the HTS era considers the rise of multiple families of cuprates with rapid increase in the T_c values (in particular for the celebrated REBCO [12] and BSCCO families [13], with T_c above 80 K), as well as other materials among which MgB_2 ($T_c \simeq 39$ K) [14] and Fe-based compounds (with T_c above or quite above 20 K) [15] appear as promising options regarding applications. Altogether, they constitute the object of study of this work, i.e. the development of advanced superconductors. As will be detailed later, this temperature threshold, which well begins with the boiling temperature of liquid hydrogen, LH2, at atmospheric pressure (20.28 K) is indeed surpassed to several degrees by such superconducting materials. As a matter of fact, this limitation of cryogenic temperatures hardly impedes their applicability in real-world systems [1–8,16–21]. Today's cryogenic industry is sufficiently mature to support superconductivity applications at temperatures as low as the liquefaction temperature of nitrogen (< 77.35 K), hydrogen (< 20.15 K), or even helium (< 4.15 K), as strictly required for some applications with LTS, with compact designs that, although specialized and application-tailored, are also efficient and cost-effective [22–25]. Nonetheless, irrespective of the cryogenic hurdles, and even in the event of discovering a 'room-temperature' superconductor, the trajectory of their real-world application and market integration is likely to be predominantly shaped by the advancement of a single key parameter, i.e., its J_c. This is because this crucial parameter delineates the threshold for a superconductor's current-carrying capacity and, consequently, its potential to carry high currents [1,6,7] and associated to this, to generate or sustain powerful magnetic fields [26–28] unparalleled by any other material.

Remarkably, the concept of critical current density is ubiquitous in research areas spanning from fundamental microscopic condensed matter studies to applied electrical engineering, with material science and chemistry in between. In fact, if one scrutinizes the physical mechanisms that eventually lead to acceptable engineering parameters, one necessarily ends up with the mesoscopic vortex physics and eventually with the microscopic superconducting coupling mechanisms [29–31]. This complexity manifests itself specially in HTS materials, for which reason three decades of intensive research have led to much progress but still leave a somehow blurry scenario. In this sense, advances in fundamental investigations (e.g. large-scale numerical simulations of the vortex physics [32]) that allow designing material structures "à la carte", the application of new strategies in the material processing based on the advance of nanotechnologies [33], and ever more sophisticated simulation and design methods in engineering [34,35], all related to the J_c problem, are coming to light.

In this work we aim to offer an exhaustive up-to-date review and analysis of the principal theoretical and experimental determinants that might contribute to a more precise delineation and current understanding of J_c, encompassing synergistic insights by experts from the macroscopic to the microscopic world in advanced superconductors with practical applications at high temperatures, such as cuprates [10,36,37], Fe-based superconductors [38–40], and MgB_2 [14,41,42]. Our exposition will adopt a

top-down strategy, starting by a review of the phenomenological macroscopic models that encompass the concept of critical current density, offering an intuitive and practical knowledge though still not detailed about the background *atomic-level* interactions. Progressively, this will guide our tour through the mesoscopic and eventually microscopic levels needed for mastering advanced superconductors.

As will be shown, at the macroscopic level, physical modeling of superconducting materials may be done on the basis of mathematical statements for quantities that do not need to be resolved below the length of millimeters (or more). Thus, electromagnetic fields are evaluated in terms of the Maxwell equations and material laws that are well-defined as averages in volume elements of such dimensions. Certainly, meaningful material laws and their connection to some specific superconducting sample may only be understood correctly if one considers the physics at the nanometer scale because this is the range that dominates the interactions of vortices [29,30], which are the basic element in practical superconductors at high magnetic fields. In fact, within the macroscopic domain, two length scales are typically ignored: firstly, the microscopic distance characterizing the formation of superconductivity at the microscale, and secondly, the average size and spacing between flux quanta at the mesoscale, whose interconnections and existing interpretations will be revised across the following chapters, forming thence a broader and sounder definition of the *a priori* phenomenological parameter J_c for advanced superconductors.

Thus, in Section 2 our analysis commences with an emphasis on averaged properties, specifically directing attention toward the gradient of magnetic flux within the pinning landscape (Section 2.1), giving onset to the quasi-steady form of the Maxwell equations, which will allow understanding the penetration and expulsion of magnetic flux in type-II superconductors without major mathematical complications (Section 2.2). Thence, the main physical quantities that in the macroscopic scale are customarily used for the characterization of applied superconductors, such as their magnetization and energy losses, will be analyzed within this context (Section 2.2.1). This will be presented by adopting a mean-field description of the fundamental phenomena related to the interactions of the flux line lattice (Section 2.2.2), with a contribution related to the displacement of vortices out of equilibrium in the underlying crystal structure. Subsequently, we will establish the mathematical framework governing the evolution of the macroscopic group of vortices using an isothermal approach (Section 2.2.3). As a natural consequence, this will lead us towards the related material laws in applied superconductivity with a J_c definition meaningful at a phenomenological level (Section 2.2.4), providing a powerful tool at the engineering design level as well as a solid physical framework.

Then, from the practical point of view (Section 3), and assuming a low level of dissipation, we discuss some of the criteria that allow for a straightforward comparison between different samples and characterization techniques with the established definition of J_c and its related $\mathbf{E}-\mathbf{J}$ law of the macroscopic world. In this sense, we show here how the determination or definition of J_c by experimental methods is not univocal (Section 3.1); rather, it intricately hinges on a predefined set of experimental conditions and ad-hoc criteria commonly defined for electrical transport measurements (Section 3.1.1), magnetic inductive measurements (Section 3.1.2), or data derived from magneto-optical imaging (Section 3.1.3). This allows understanding better the scope and implications of the different constituent macroscopic models of J_c, such as the simplified Critical State or Bean's model (Section 3.2.1), the more general and physically sound Double Critical State models (Section 3.2.2), and possibly the most practical use of the $\mathbf{E}-\mathbf{J}$ power law models for engineering purposes (Section 3.2.3), including also the dependence of J_c and the flux pinning regime with temperature, magnetic field, and the orientation of this field with regard to the symmetry axes of the superconducting crystal (Section 3.3). In this sense, different models of the $J_c(T,B,\theta)$ function are revised (Section 3.3.1), including the intriguing occurrence of the so-called second magnetization phenomena (Section 3.3.2) that is thought to give hints on the underlying physics of the flux-line lattice and its interaction with the pinning landscape. Therefore we will be establishing connections between the phenomenological models above described with the more sophisticated quasi-mesoscopic (Section 3.3.3), statistical (Section 3.3.4), and semi-empirical models (Section 3.3.5) capable to estimate the Ginzburg–Landau depairing critical current density for the whole range of temperatures applicable to advanced type-II superconductors, as a mesoscopic measure of J_c.

Thus, upon attaining a mesoscopic comprehension of the macroscopic current density within a superconductor, where this density is envisaged as a distribution of finite currents capable of generating self and mutual magnetic induction, the consequential outcome involves the emergence of substantial Lorentz-type forces among associated vortices. This, in turn, can propel the vortices to elevated velocities, opening the door to a diverse spectrum of non-equilibrium phenomena, collectively referred to as flux-flow instability regimes, broadly discussed in Section 4. This includes investigations of superconducting fluctuations at high current density and strong electric fields (Section 4.1), as well as non-equilibrium effects at large transport currents and magnetic fields near or below T_c (Section 4.2), where a connection with the microscopic world is given through the localization and velocities of the superconducting quasiparticles near or within the vortex core. This means in the region where the time derivative of the superconducting order parameter $\partial|\psi|/\partial t$ of the moving vortex is finite, which can vary depending on the vortex–defect interactions occurring in practical superconductors.

Therefore, in order to understand the possible causes for the enhancement (or diminishing) of J_c, in Section 5 we engage in an in-depth dialogue that delves into the intricate interplay between the quantum pinning and creep mechanisms (Section 5.1), establishing how the collective pinning theory, strong pinning theory, and the thermally-activated hopping of vortices, all can significantly impact our comprehension of the J_c concept. Additionally, we investigate the pronounced effects stemming from correlated disorder in contrast to random disorder, offering a comprehensive microscopic understanding of the complex vortex–defect and vortex–vortex interactions that underlie the J_c behavior of advanced superconductors. Then, as aiming for quantitative accuracy in the presence of mixed pinning landscapes usually requires resorting to numerical methods, in Section 5.2 we present state-of-the-art methods on the simulation of vortex–defect interactions, starting from First-principles computations including the microscopical spectrum provided by DFT models and the Bogoliubov–de Gennes equations (Section 5.2.1), for then reconnecting with the more mesoscopic approaches via time-dependent Ginzburg–Landau (TDGL) simulations (Section 5.2.2), and molecular dynamics (MD) simulations (Section 5.2.3).

Table 1
Range of application of the quasi-steady macroscopic modeling of J_c.

Property	Typical Range
Temperature	$T < 0.8\,T_c$
Applied magnetic field	$H_{c1} \ll H \ll H_{c2}$
Sample dimensions	$L >$ μm (λ), (ξ is implicit)
Frequency	$\nu < 1$ kHz

Clearly, HTS materials, which enable energy-efficient and high-power-density electricity delivery, are challenging to produce, particularly due to their brittle nature and complex structural characteristics. Hence, either guided by mesoscopic or microscopic theoretical models, numerical simulations, or experimental approaches, our final chapter is devoted to exploring both the most advanced techniques for engineering the flux pinning properties in these materials and the primary methods for fabricating superconducting tapes and wires. These techniques are essential for the practical advancement of HTS materials, as they rely on developing innovative strategies for increasing or maximizing the macroscopic J_c in these structures.

Thus, in Section 6 we begin by outlining the historical and technological milestones achieved in the development of HTS wires and tapes, providing a chronological journey through the evolution of different HTS materials such as Bi-based superconductors (BSCCO), which were among the first HTS materials to be commercially available (Section 6.1.1), toward the REBCO families, which represent a significant leap in high-field applications of HTS (Section 6.1.2), and the relatively newer but promising MgB_2 and Fe-based superconductors (Section 6.1.3). We will cover the fabrication methods, key achievements, and challenges faced in producing these HTS compounds, and how these materials have set the foundation for subsequent advancements in HTS technology. Thence, in Section 6.2 we explore advanced strategies that have emerged to optimize J_c in HTS materials, addressing inherent challenges such as controlling defect structures, improving grain connectivity, and enhancing flux pinning. Simultaneously, we analyze how these strategies are applied across the different HTS materials and their impact on improving performance. This pursuit entails exploring techniques where the charge carrier doping plays a crucial role in tuning the superconducting properties of HTS materials. Therefore, in Section 6.3 we focus on how precise control of doping levels can alter the carrier concentration, modify the superconducting gap, and ultimately enhance the J_c values, highlighting the effects of hole and electron doping, and how these modifications lead to improved pinning landscapes and superfluid densities.

Finally, we explore the various engineering techniques developed to minimize the detrimental effects of grain boundaries, due to the coherence lengths being of the order of a few nanometers in these HTS materials (Section 6.4). Approaches such as introducing buffer layers, using textured substrates, and employing chemical modifications are discussed, with an emphasis on how they facilitate the growth of well-aligned grains and improve J_c. Likewise, we present a detailed analysis of the introduction of artificial pinning centers through material doping (Section 6.5), as a powerful method for enhancing J_c in HTS materials. Similarly, as the manipulation of defects by using irradiation techniques (Section 6.6) can play a vital role in determining the J_c properties, especially in superconductors used in high-radiation environments like fusion reactors, the final pages of this review will be devoted to explore the types of defect structures induced by radiation and their influence on the vortex pinning landscape (Section 6.6.1); and to how different types of radiation like photons, electrons, and neutrons (Section 6.6.2) or protons and heavier ions (Section 6.6.3) produce varying defect morphologies. The latter will be revised in great detail due to their uttermost importance in the energy sector, because, on the one hand, the pinning properties of advanced superconductors can often be improved by suitably choosing the type and energy of the striking particles while controlling the density of defects by tuning the irradiation fluence; and on the other hand, because the radiation hardness of J_c in HTS materials (Section 6.6.4) is critical for the successful development of the fusion energy sector.

We conclude this review paper by providing a summarized account of our findings and likewise, offering insights into possible future enhancements of the critical current density in practical superconductors across Section 7.

2. Understanding J_c from the macroscopic world

Generally speaking, the *macroscopic critical current* problem in type-II superconductors consists of determining the *coarse grained* electromagnetic quantities **E**, **B**, **J** for a given configuration of superconductors and electromagnetic excitation. In practice, one must solve the problem defined by exposing the superconductors either to an external magnetic field created by, e.g., a solenoid, a permanent magnet, or other superconductors, or by injecting a transport current to them through some external power source. Stand to reason averaging means in particular that, in terms of the microscopic to mesoscopic field **b**, one has $\mathbf{B}(\mathbf{r}) \equiv \langle \mathbf{b} \rangle$ over the elements represented by **r**, withholding volumes that smooth out fluctuations related to microscopic or mesoscopic interactions, but still allowing for space and time dependence $(\mathbf{r}, t)$ in the *macroscopic world*. Precisely, two length scales are supposed to be negligible in our case: the microscopic distance characterizing the formation of superconductivity (microscale) and the typical size and separation between flux quanta (mesoscale).

As remarked by B. D. Josephson [43], in quasi-steady conditions, if one starts with **B** defined in such a manner, the problem may be stated consistently in terms of the Maxwell equations for the fields **E** and **J**, and this applies to both type-I and type-II superconductors (our focus in this review being the latter), i.e., with,

$$\nabla \times \mathbf{B} = \mu_0 \mathbf{J} \qquad \text{(Ampere's law)},$$

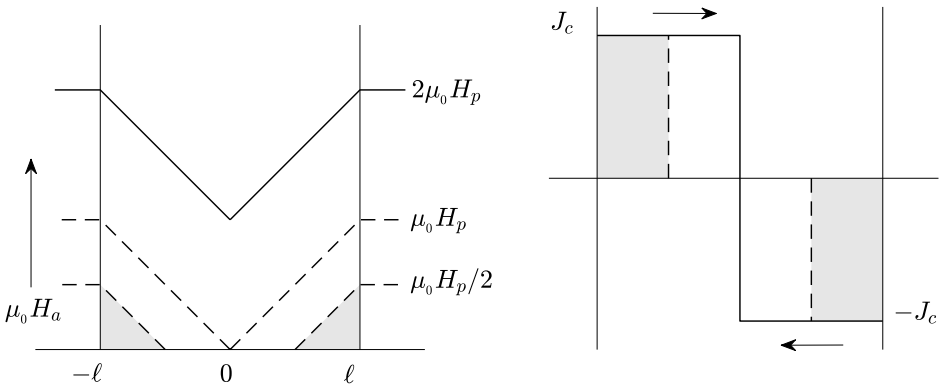

Fig. 1. Initial magnetization profiles for a superconducting slab in the critical state. Left: magnetic field penetration profiles. Right: evolution of the superconducting current density. H_p is the so-called full penetration field.
Source: Adapted with permission from [48]

$$\begin{aligned} &\nabla \times \mathbf{E} = -\frac{\partial \mathbf{B}}{\partial t} \qquad \text{(Faraday's law)}, \\ &\nabla \cdot \mathbf{B} = 0 \qquad \text{(Solenoidality of } \mathbf{B}\text{)}. \end{aligned} \tag{1}$$

In particular, this makes sense for samples and experimental resolutions with dimensions well beyond micrometers, as shown in Table 1.

As will be further developed, the response of the superconductor to the applied excitation is customarily modeled by adding a phenomenological material law [30], which typically takes the form,

$$\mathbf{E} = \mathbf{E}(\mathbf{J}, \mathbf{B}). \tag{2}$$

In essence, the selection of the material law must be such that the physics of vortices in type-II superconductors is captured [44–47]. In many cases, such dependence acquires a particularly simple form, allowing us to include the material properties by means of a single parameter, the sample's *critical current density* J_c. In brief, J_c is defined as the maximum value of J allowed within the superconducting state, which will suffice for building up macroscopic models and analyzing experiments for simplified configurations. In fact, in the following subsections, we will show how a solid theoretical background can support such a concept, allowing for its generalization by defining $\mathbf{E}$ in terms of J_c as follows,

$$\mathbf{E} = \mathbf{E}(\mathbf{J}/|J_c|). \tag{3}$$

As J_c is in general anisotropic and inhomogeneous as well as dependent on temperature, field magnitude, and direction via dynamic creep effects, it can be expressed as a time-dependent vector $\mathbf{J}_c(\mathbf{B}, T, t)$ to account for the different components of the critical current density either regarding the crystallographic axes of the superconducting compound, or the direction of the applied magnetic field (or transport current) from which the time-dependence comes from. Furthermore, the experimental value of J_c may depend strongly on its measurement method, as it will be shown in Section 3.

Also, it is worth to recall that in the macroscopic description one implicitly assumes $\mathbf{B} = \mu_0 \mathbf{H}$, an approximation that is valid for technological (strong pinning) type-II superconductors, as they are of interest at high fields. This is equivalent to say, that in practical superconductors the equilibrium magnetization may be neglected and magnetostatics is well stated in terms of the global irreversible current flow, i.e., the current that circulates within the superconductor to create a counteracting magnetic field, preventing the penetration of the external magnetic field without any resistance or energy loss. Therefore, the detailed structure concerning the Meissner currents and the individual vortices can be neglected, and one just focuses on averaged properties as the gradient of magnetic flux in the pinning landscape, that enters the theory through the specific $\mathbf{E}(\mathbf{J}/J_c)$ material law.

Consequently, we present below a hierarchical overview of the models developed over the years to address the previously described phenomenological approach. These empirical models, with background physics influenced by the complex microscopic interactions within superconducting materials (discussed in detail in later sections), have undergone extensions and upgrades to enhance their predictive power for increasingly sophisticated experimental setups and material optimization protocols. They form the foundation for our *top-down* approach to the critical-current issue in superconducting materials and provide the essential background for final engineering modeling.

2.1. The most elementary approach

The Critical State (CS) model, in its most simplified (and celebrated) version, predicts the magnetization process of superconductors even without explicit mention of the electric field. This model, also known as Bean's model in recognition to Charles Palmer Bean [49,50], establishes without mathematical complication a thumb rule, which results sufficient to describe the penetration

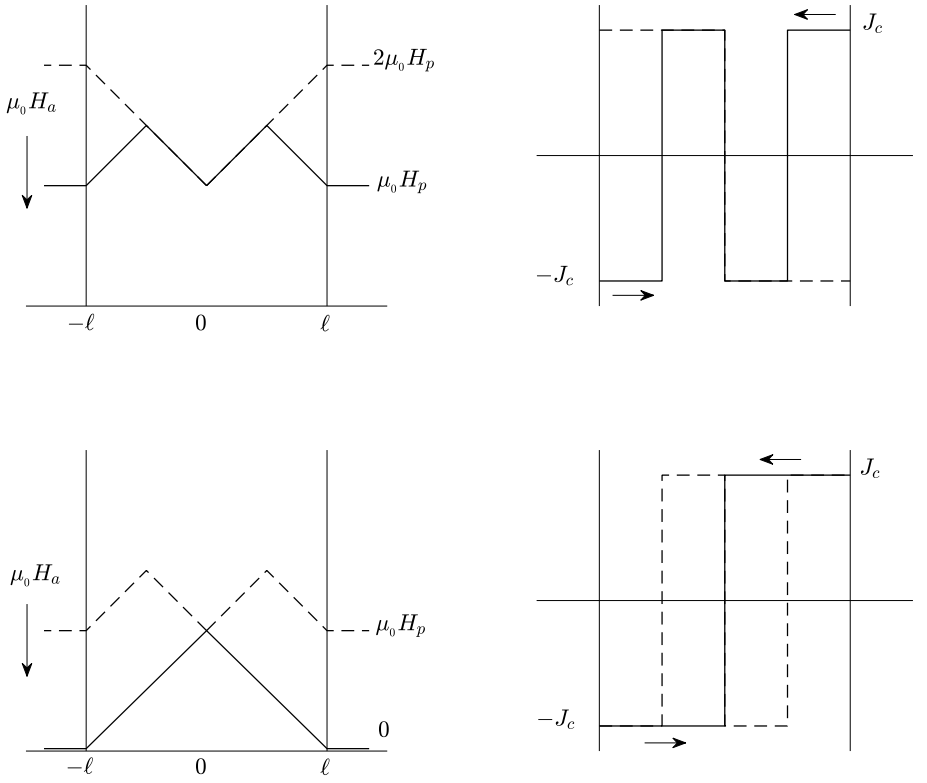

Fig. 2. Same as Fig. 1 but for the applied magnetic field cycling back.
Source: Adapted with permission from [48]

and expulsion of magnetic flux in type-II superconductors. This will be shown below from simplified symmetries that can be well understood in one dimensional (1D) approaches, to more complex scenarios that demand a three dimensional (3D) analysis of the vortex dynamics.

2.1.1. One-dimensional statement

To start with, in 1D problems, i.e., infinite slabs or cylinders under longitudinal magnetic field, for which the magnetic field has a single component, say $\mathbf{B} = B\hat{\mathbf{k}}$, it is postulated that, wherever penetrated by flux, the sample holds a *steepest metastable gradient of B* (basically J_c) supported by *material* internal forces, that builds up to counterbalance magnetic flux variations. In equivalent physical terms, this corresponds to the behavior of a perfect conductor with limited current density. For instance, for an infinite slab occupying the region $-\ell < x < \ell$, this is formulated via the critical-state equation for the single component of the current density ($\mathbf{J} = J\hat{\jmath}$ in this geometry), through $J = \pm J_c$ or 0.

As said, J_c is a phenomenological parameter related to the equilibrium between magnetic and internal forces in the superconductor [30]. Then, the field penetration profile can be derived by inserting this *ansatz* into Ampère's law, which in the slab geometry reads

$$\frac{dB}{dx} = \pm\mu_0 J_c(B) \quad \text{or} \quad 0\,, \tag{4}$$

supplemented with the appropriate boundary conditions, i.e., $B(x = \pm\ell) = \mu_0 H_a$, where H_a is the applied magnetic field.

As one may see in Fig. 1, for the case of constant J_c, the simplicity of Eq. (4) allows obtaining the response of the sample straightforwardly. Nevertheless, even for this simplified geometry, an additional physical ingredient must be considered if field reversal is assumed (Fig. 2), where negative increments of magnetic field correspond to counter-circulating currents. One may recall that, indeed, this rule entails the implicit application of Faraday's law and the tendency to perfect conductivity. Thus, the reaction of the material opposes the external excitation.

A further implicit assumption behind Bean's model relates to time dependencies and ultimately to the omission of the current–voltage relation (Eq. (3)). In fact, as one may deduce from Fig. 3, the implicit *instantaneous response* hypothesis that one uses on making the 1D plots of the successive field and current density profiles corresponds to the limiting vertical $E(J)$ relation, where diffusion processes related to finite resistivity are neglected as compared to the quasi-instantaneous propagation of supercurrents. In other words, the CS model may be understood in terms of some physical interaction characterized by a threshold current density J_c, separating a dissipationless regime ($J < J_c$) and a high dissipation regime ($J > J_c$). Therefore, the evolution of the fields from

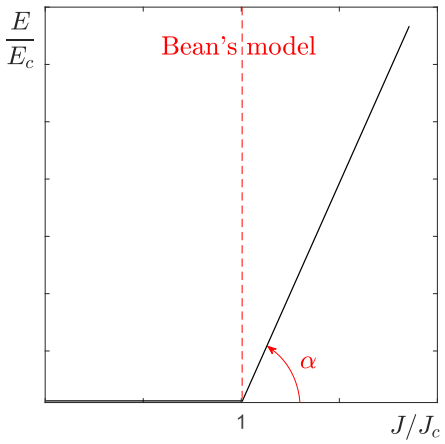

Fig. 3. Model approximation of the process describing flux penetration in a type-II superconductor (1D model). An electric field is induced if magnetic flux changes, and a transient overcritical current appears.
Source: Adapted with permission from [48]

one equilibrium state to another is induced by the external sources and regulated by such $\mathbf{E}(\mathbf{J})$ relation and Faraday's law. In brief, the underlying physical mechanisms are (i) the competition between magnetic and internal pinning forces (as formulated by the equilibrium condition [43], $\mathbf{J}\times\mathbf{B}+\mathbf{F}_{\mathrm{P}}=0$, see below, Eq. (12)), and (ii) the dissipation law (related to the value of α in Fig. 3) that characterizes the flux avalanche processes when pinning is overcome.

2.1.2. Two-dimensional approaches

There have been a number of smart approximations upgrading Bean's model for incorporating the CS concept in practical configurations with the least mathematical complication. Such approximations have enabled an accurate prediction of magnetization and AC losses in many superconducting systems, simultaneously leading to adequate physical explanations for challenging experimental effects such as the flux-shaking in thin films [51,52] or the magnetic moment decay of superconducting arrangements in crossed magnetic fields [53,54]. An excellent review of the advances related to the concept of critical state in planar samples may be found in Ref. [55].

Of particular relevance is the consideration of thin samples under a perpendicular (or inclined) magnetic field. Seminal contributions by Mikheenko [56] and Brandt and Indenbom [57] are to be mentioned, later followed by many others both in analytical as well as numerical calculations (see, e.g., [55,58] and references therein). As noticed in those papers, the problem may be well approximated through simplified statements in terms of the so-called *sheet current* density, that averages $\mathbf{J}$ over the thickness of the sample (lying on the $XY-$plane),

$$\mathbf{K}(x,y)\equiv\int_{-d}^{d}\mathbf{J}(x,y,z)dz\,. \tag{5}$$

Thus, for the case of long, thin strips along the Y-axis one has $\mathbf{K}=K(x)\hat{\boldsymbol{\jmath}}$, and for thin disks one has $\mathbf{K}=K_{\varphi}(\rho)\hat{\boldsymbol{\varphi}}$. The statement leaves a 1D problem in both cases, but with boundary conditions more involved than in the longitudinal geometry due to the demagnetization effects.

For illustration, we include Fig. 4, which displays the sheet current density and accompanying profiles of magnetic field evaluated with the expressions given in Ref. [57]. Several facts are to be recalled: (i) the *artificial* divergences of the magnetic field at the sample edges, and (ii) the *subcritical* regions for $K_y(x)$. The relation of such features to the model assumptions is illustrated in Fig. 5. There, considering the thin disk geometry, we display the behavior of the average quantity $K_{\varphi}(r)$ together with the more realistic 2D behavior of the current density $J_{\varphi}(r,z)$, also known as penetration profile, for a sample with small though finite thickness. One may notice that, in fact, the *subcritical* sheet current $K<K_{\mathrm{c}}$ corresponds to the partial penetration of the field.

2.1.3. The three-dimensional scenario

Upgrading the CS modeling to 3D geometry has been a long-awaited achievement, hindered by both technical and fundamental issues. Not only does one have to deal with non-trivial mathematical statements of the Maxwell equations, but also to ensure a physically sound formulation. Thus, considering that vortices are in general three-dimensional objects experiencing complex interactions in space, macroscopic modeling must include more physics than the competition between pinning and *Lorentz-like* forces over one-dimensional long filaments, and their eventual avalanche processes. In particular, flux-cutting, bending, and recombination events must be considered as related to the appearance of macroscopic electric fields [59]. With this in mind, analytical [60] and numerical [61] modeling based on vortex physics has to be mentioned, accompanied by a number of approximations [34,62–72] that rely on different expressions for the $\mathbf{E}(\mathbf{J})$ law based on phenomenological considerations.

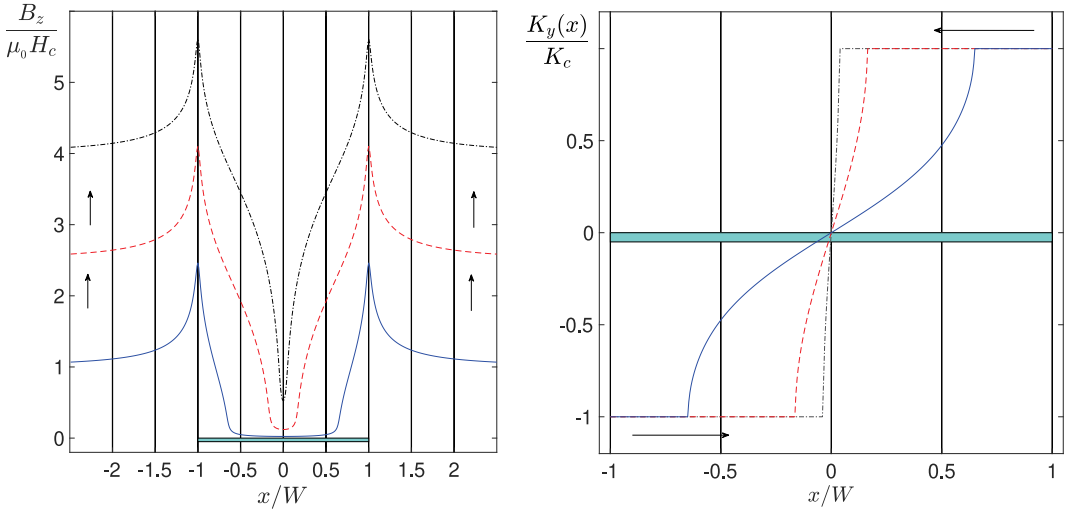

Fig. 4. Left: Magnetic flux distribution at a distance $h = 0.02d$ above the long superconducting strip of width $2W$ and thickness $2d \ll 2W$ under increasing applied perpendicular magnetic field (asymptotic value for large x). Units are normalized as in Ref. [57] ($K_c \equiv 2dJ_c$). To the right, we plot the profiles of the induced current density penetrating the sample for each value of the magnetic field.
Source: Adapted with permission from [48].

As a remarkable result of 3D modeling, the authors of Ref. [66] validated the extensively used 2D approximations in rectangular samples of small thicknesses. By contrast to the quasi-1D situation in Fig. 5, where circular trajectories may be assumed, the actual current density streamlines in prismatic samples are unknown *a priori* and must be obtained as a part of the problem's solution. Assuming an isotropic model (non-linear $\mathbf{E}(\mathbf{J})$ law with $\mathbf{E}\|\mathbf{J}$), it was shown that the predicted and measured 2D trajectories [55] in rectangular platelets could be obtained by averaging the full 3D solution $\mathbf{J}(x, y, z)$ (Fig. 6 schematically displays this situation). As remarked in that article, quasi-2D models may supply reasonable predictions of global quantities as the full magnetic moment, or the AC losses in relatively thick samples such as bulks or stacks made of superconducting tapes [67]. Thus, although there may be rather inaccurate predictions of local quantities related to geometry end effects which might affect properties such as the value of the local magnetic field on the sample's surface, the impact of these discrepancies might not be so relevant for the practical use of superconducting tapes. This reminding that the thickness of the superconducting layer is of about just 1 μm, embedded more or less at the middle of a relatively large arrangement of thin films and coating layers that form the actual superconducting tape of approximately 100 μm thickness.

Thus, in the context of experimental conditions where flux pinning and cutting events may exert a significant influence on the spatial distribution of current density within a superconducting tape, the attainment of a sufficiently high-resolution framework encompassing both temporal and spatial domains becomes pivotal. This resolution is essential for facilitating the observation of how the superconducting current density evolves across the tape's cross-section in response to external electromagnetic excitations, such as transport currents or applied magnetic fields. In this sense, 3D modeling techniques have already demonstrated their efficacy in capturing not only the fundamental physical phenomena predicted by Bean's model, as discussed earlier in this chapter, but also the empirically observed hysteresis losses within intricate cable designs characterized by three-dimensional complexities, such as tape twisting and pitch winding [71–74].

2.2. Physical background

This section deals with the physical grounds that support the different $\mathbf{E}(\mathbf{J})$ material laws that have been used for decades for the simulation and analysis of the electromagnetic properties of type-II superconductors. As said, combined with the quasi-steady form of the Maxwell equations, they will provide a model for the macroscopic electromagnetics of superconductors.

2.2.1. Macroscopic observables

Let us start by introducing the main physical quantities that in the macroscopic scale (Table 1) are customarily used for the characterization of superconductors, hence those that are intrinsically related to our understanding of J_c.

As it is obvious from Figs. 1 and 2, $\mathbf{B}(\mathbf{r})$ and $\mathbf{J}(\mathbf{r})$ are *native* quantities in the CS theory. In fact, they are not independent but connected through Ampère's law. Straightforwardly, they may be used for macroscopic studies of magnetic flux penetration by comparing to experimental results. Thus, local profiles of $\mathbf{B}$ have been obtained by different techniques (micro Hall probe [75–77] or Magneto Optical Imaging, MOI [78–80]) and used to derive the underlying current density profile by inversion procedures. Two additional observable quantities have been of much importance in developing macroscopic superconducting electromagnetics, named the superconductor magnetization and the superconductor's energy losses.

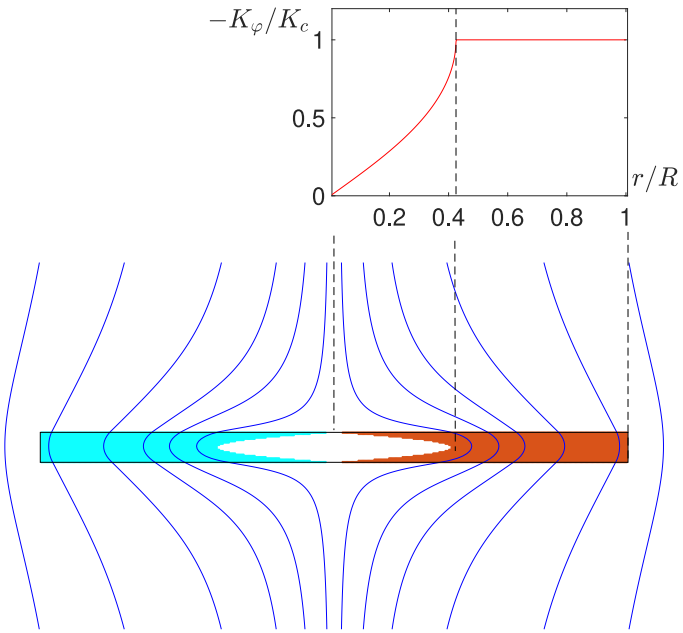

Fig. 5. Comparison of Mikheenko's formula for the sheet current and the exact penetration profile of the current density in a thin cylinder of aspect ratio 0.05. *Source:* Adapted with permission from [48]

On the one hand, we have the so-called volume magnetization $\mathbf{M}_\mathrm{V}$ involving the flux penetration profile through the relation

$$\mathbf{M}_\mathrm{V} = \frac{\langle \mathbf{B} \rangle}{\mu_0} - \mathbf{H}_\mathrm{a}\,, \tag{6}$$

where $\langle \mathbf{B} \rangle$ is the average of the macroscopic flux density within the sample (often also called magnetic field), and $\mathbf{H}_\mathrm{a}$ the applied magnetic field. This expression (particularized for each geometry) has been customarily used to establish the value of J_c, its field or temperature dependence, anisotropy, etc., typically by studying hysteresis cycles $\mathbf{M}_\mathrm{V}(\mathbf{H}_\mathrm{a})$, where several expressions of this sort may be found in Ref. [44].

Outstandingly, as recalled in [81], the importance of finite-size effects is to be considered. In particular, one must consider that the local magnetic field within the sample will not generally coincide with the experimental quantity $\mathbf{H}_\mathrm{a}$. In that work, it was shown that using the well-known expression for analyzing experimental data of cylindrical samples

$$J_\mathrm{c}(\mu_0 H_\mathrm{a}) = \frac{3\,\Delta M_\mathrm{V}(\mu_0 H_\mathrm{a})}{2R}\,, \tag{7}$$

is more and more representative of the internal behavior $J_\mathrm{c}(B)$ as the sample becomes thinner and thinner. This is enabled by the presence of demagnetizing effects that contribute to producing a more uniform field within the sample (as foreseen in Fig. 5).

In some problems (2D or 3D in nature), the theoretical predictions of $\mathbf{M}_\mathrm{V}$ are done in terms of the current density itself through the sample's magnetic moment

$$\mathbf{m} = \frac{1}{2}\int d^3\mathbf{r}\,[\mathbf{r}\times\mathbf{J}]\,. \tag{8}$$

Then, $\mathbf{J}$ is more conveniently expressed either in terms of the stream function $\mathbf{K} = -\hat{\boldsymbol{z}}\times\boldsymbol{\nabla} g$ or the related vector potential $\mathbf{J} = \nabla\times\boldsymbol{\Gamma}$ respectively (see [58,66] as examples).

On the other hand, the analysis of energy losses is certainly a primordial aspect that may be done in terms of either the straightforward and general definition

$$L = \int dt \int d^3\mathbf{r}\,[\mathbf{E}(\mathbf{J})\cdot\mathbf{J}]\,, \tag{9}$$

customarily applied to *per cycle* in AC operation of the excitation source (either magnetic field or transport current), or equivalently through the area of the related hysteresis loop in magnetization experiments [82]

$$L = \oint \mathbf{B}(\mathbf{H}_\mathrm{a})\cdot d\mathbf{H}_\mathrm{a}\,. \tag{10}$$

Finally, focusing on applications, another macroscopic quantity that deserves much attention and which is traditionally analyzed in terms of the CS theory, is the interaction force between a superconductor and a permanent magnet. Again, one may issue

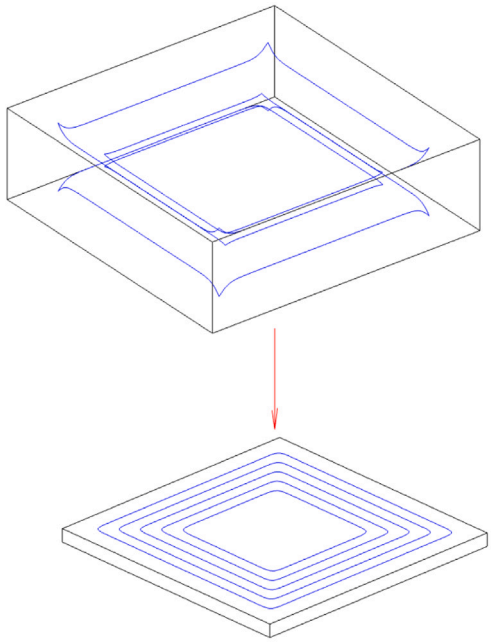

Fig. 6. Comparison of the streamlines for the average sheet current (lower) and the exact 3D trajectories as obtained from numerical calculations (upper) in a rectangular prism under a vertical magnetic field (schematic).
Source: Inspired by [66]

predictions on the complex behavior of such systems by deriving the superconducting currents $\mathbf{J}(\mathbf{r})$ through the CS theory [83][84] and then applying

$$\mathbf{F} = -\boldsymbol{\nabla} \int d^3\mathbf{r}\, [\mathbf{A}_{\mathrm{PM}} \cdot \mathbf{J}]\,, \tag{11}$$

with $\mathbf{A}_{\mathrm{PM}}$ the magnet's vector potential.

2.2.2. Vortex physics fingerprints in the macroscopic world

Let us briefly review the physical scenario that supports the usage of Eq. (1) and Eq. (2) for establishing a common methodology in the electromagnetic and thermodynamic modeling of applied superconductors.

Fundamentally, large-scale applications concern type-II superconductors operating at magnetic fields characterized by the presence of a huge number of vortices, but still far from the upper critical field [45–47]. Thus, phenomena such as the condensation to the superconducting state, the kinetic energy of supercurrents, the formation of individual vortices, or the transition to the normal state, which are all contained up to some extent within the mesoscopic formulation of the Ginzburg–Landau theory [85], may be simply skipped either for being negligible in our range or, for being implicitly incorporated in the material law $\mathbf{E}(\mathbf{J})$. Hence, for macroscopic purposes, we can adopt a mean-field description of the fundamental phenomena related to the interactions of the flux line lattice (FLL) that produce macroscopic observables, which will be object of this study in Section 4 and Section 5. In particular, the description of metastable states of equilibrium for systems with many vortices may be achieved by using an expression for the free energy $\mathcal{F}$, that includes a magnetostatic term proportional to $|\mathbf{B}|^2$, together with a contribution related to the *displacement* of vortices out of equilibrium in the underlying crystal structure.

As shown in [43], the minimization of $\mathcal{F}$ leads to the condition

$$\mathbf{J} \times \mathbf{B} + \mathbf{F}_{\mathrm{P}} = 0\,, \tag{12}$$

with $\mathbf{F}_{\mathrm{P}}$ a macroscopic average of the individual vortex pinning force density. However, Eq. (12) alone does not always provide a criterion to obtain a unique solution for the penetration profile. In fact, multiple (history-dependent) metastable states are compatible with the balance between magnetostatic and pinning forces, as one may easily check for the 1D situation sketched in Fig. 1 and Fig. 2 (mind, for instance, the admissible penetration profiles corresponding to the applied field $H_{\mathrm{a}} = \mu_0 H_{\mathrm{p}}$). In fact, the situation in real 3D problems may be much more complex. For this reason, the minimal physical modeling must adopt an advanced statement as described in the following subsections.

Thus, in order to predict the actual configuration of the system, one must have a model of the specific dynamics induced by a certain excitation process. In physical terms, the material pinning force acts in a similar fashion as the static friction force in mechanics. It provides a threshold for the eventual equilibrium that is reached subsequent to some process determined by kinetic

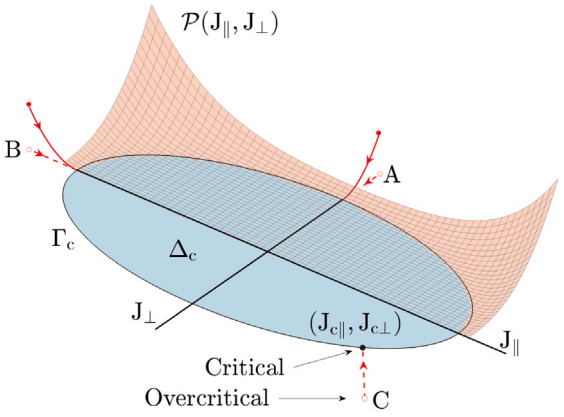

Fig. 7. Yield region for the current density in a type-II superconductor illustrated for the elliptical instance, i.e.: dissipationless transport occurs for **J** within the elliptical domain Δ_c. The relation between the actual geometry of Δ_c and the physical background is discussed in Section 3. This construction generalizes Fig. 3 via $\mathbf{E} = -\boldsymbol{\nabla}_J \mathcal{P}$. The points A, B, C indicate possible overcritical initial conditions for **J** and subsequent spontaneous evolution (relaxation) toward an equilibrium point $(J_{c\parallel}, J_{c\perp})$ on the critical density contour Γ_c.
Source: Adapted with permission from [88]

friction. At the mesoscopic level, this is posed in terms of the time-dependent Ginzburg–Landau theory [86,87]. Tracing back again to the 1D model, recall that the actual dynamics and arising metastable states will be given by the criticality condition (J_c) and the dissipation law in between equilibrium states (determined by the resistivity coefficient α in Fig. 3). Thus, along the lines established in [43] and in view of the underlying vortex physics, below we are ready to introduce the minimal framework that allows generalizing these ideas to 3D situations.

2.2.3. *The quasi-steady thermodynamic isothermal approach*

As said, the superconducting electrodynamics will be determined by specifying the mechanism that describes the formation of metastable states for a given intermediate dissipative regime. The elementary event that one has to treat statistically is the unpinning of the vortex and the subsequent dissipative motion until a new equilibrium position is found [44–47]. In our case, since the number of vortices involved in macroscopic experimental conditions is so huge ($\sim B/\Phi_0$ piercing the unit area), the formal justification of the macroscopic models may be done through the introduction of thermodynamic concepts applied to the ensemble. Here, we will provide the mathematical framework for processes that rule the evolution of the vortex lattice configuration and, as a consequence, their macroscopic manifestation. With this at hand, one may build a wide class of models that may be applied at the phenomenological level. In this sense, as recalled in [88], a rather general theory of superconducting electromagnetics may be issued if one introduces a first-order (linear) approximation of the irreversible driving forces at the macroscopic level.

To start with, we must recall that for linear (*ohmic*) conductors, the steady current density distribution $\mathbf{J}(\mathbf{r})$ may be obtained by minimizing the total rate of dissipation of energy $\dot{Q} = \int d^3\mathbf{r}\ \dot{Q} = \int d^3\mathbf{r}\ [\mathbf{E}(\mathbf{J}) \cdot \mathbf{J}]$ [89]. In isothermal conditions (that may be assumed if one ensures a good thermal coupling to the coolant), this implies the *minimum rate of entropy production*, which is a rather general principle that rules the steady states in non-equilibrium thermodynamics [90]. Obviously, proper heat release is fundamental in applied superconductivity and modeling in terms of electrical and thermal conductivity is indeed a topic of intense research. However, for our purposes (i.e.: understanding the concept of critical current density), even though a T-dependent critical current density is considered, perfect heat transport is assumed and instantaneous heat removal allows for constant T. Thus, considering that the microscopic mechanism regulating the steady states is the same that leads to equilibrium in the absence of external driving forces, one may assume that, to leading order, the dissipation of energy per unit volume admits the following expression

$$\dot{Q} = \sum_{i,j} J_i R^{ij} J_j \,, \tag{13}$$

with R^{ij} being the components of the positive definite resistivity tensor (linear terms must be zero so as to reach equilibrium in the absence of driving forces).

Apparently, one may understand the steady state as a balance between the action of the electric field and the *thermal* driving force that is encoded by some dissipation function. Notice that, if one defines the dissipation function by $2\mathcal{P} \equiv \dot{Q}$, this gives

$$\mathbf{E}_{\mathrm{thermal}} = -\mathbf{E} = -\boldsymbol{\nabla}_J \mathcal{P} = -\boldsymbol{\nabla}_J \left(\frac{1}{2} \sum_{i,j} J_i R^{ij} J_j \right) . \tag{14}$$

Therefore, conduction in ohmic matter may be described in terms of a quadratic dissipation function whose J-gradient corresponds to the driving force (electric field). These concepts may be exported to type-II superconductors just by properly defining $\mathcal{P}(\mathbf{J})$ in view of the underlying physics, i.e., dissipation related to depinning and drift of vortices [88].

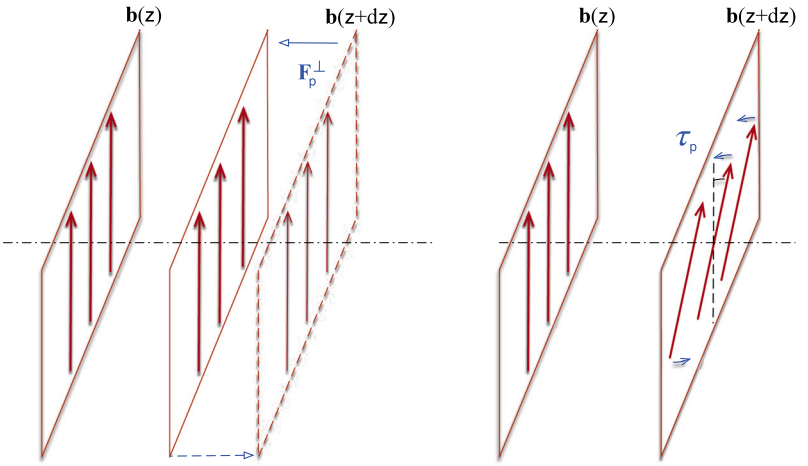

Fig. 8. Sketch of virtual perturbations of the flux line lattice relative to the configuration of equilibrium. Left: compression of flux lines (related to $J_\perp$). Right: rotation (related to $J_\parallel$).
Source: Adapted with permission from [92]

In a pictorial representation of the main facts, Fig. 7, we can notice that as the vortex physics is involved, the relevant axes for the dissipative function are not the cartesian axes, but those defined intrinsically by the directions parallel and perpendicular to the local magnetic field (on occasion, crystal anisotropies will have to be included). Therefore, as sketched in Fig. 8, in a first approximation, the perturbations of the flux line lattice may be classified in compressions and rotations, which are related to the components of the current density either perpendicular or parallel to the magnetic field by straightforward application of Ampère's law in the local axes [59]. In fact, related to the concept of pinning forces and the balance between them and the applied magnetic pressure, notice that for the simplest case $\mathbf{B} = B(z)(\cos\varphi(z), \sin\varphi(z), 0)$ depicted in Fig. 8, one gets $\mu_0 J_\parallel = -B\,\partial_z\varphi$ and $\mu_0 J_\perp = -\partial_z B$, with the equilibrium states defining a full region in the $J_\parallel J_\perp$-plane (Δ_c in the plot), where no flux creep and flux flow events exist for $\mathbf{J} \in \Delta_c$. Its boundary generalizes the condition in Eq. (12), that relates to $J_{c\perp}$. Thus, electric fields in the transition from the overcritical regime toward equilibrium occur perpendicular to the boundary Γ_c ($\mathbf{E} = -\boldsymbol{\nabla}_J \mathcal{P}$), i.e.: if the action driving the system dissipative ceases, it will go back to equilibrium along the shortest path.

We stress that Fig. 7 conceptualizes the basic physics involved in the *critical-current problem* of practical superconductors. Three dynamical relaxation processes are illustrated. Thus, driven by some external agent, the superconductor is pushed to some overcritical point (A, B, or C) and then allowed to relax to a new configuration: generic point $(J_{c\parallel}, J_{c\perp})$ in the yield region boundary Γ_c. Notice that A represents the most usual situation in which parallel vortices evolve toward a new configuration compressed by the action of external field and perpendicular currents. On the other hand, the actual dissipation function indicated by the $\mathcal{P}$ surface, and that encodes the related $\mathbf{E}(\mathbf{J})$ dependence, will depend both on material and on the experimental conditions, i.e.: level of current, applied magnetic field and temperature. Then, either experimental data (see Section 3) or fundamental studies are needed to guide in the selection of a meaningful representation. For instance, at low temperatures and with $\mathbf{J}$ exceeding the critical value moderately, the actual functional dependence is not critical, and piece-wise parabolic or power-law functions work well [88]. For extreme conditions, i.e.: high values of J, H or T, one must consider instabilities that require specific formulation (Section 4). On the other hand, the particular Γ_c boundary delimiting the non-dissipative regime (static vortices with maximum compression or torsion profiles) must also be determined for a given material and conditions. In this regard, of special mention is the work on YBCO thin films at Ref. [91], where by taking advantage of a well-controlled sample's geometry, the authors concluded that for this material the elliptical yield region is a rather accurate description from the macroscopical point of view. In general, dedicated experiments and fundamental studies of the vortex–defect interactions (as introduced in Section 5) have to be used in order to determine the full picture for a given material.

2.2.4. Underlying electrodynamics

Having established the overall framework that allows for a definition of the material law in applied superconductivity, one may straightforwardly pose the problem of their electrodynamics at the macroscopic level. For low frequencies (see Table 1), one may solve the differential Maxwell equations together with the $\mathbf{E}(\mathbf{J})$ relationship (see Eq. (1) to Eq. (3)), taking into account the boundary conditions and/or physical constraints, if any, which are commonly imposed by the excitation process and the geometry of the system. Here, we recall a variational interpretation more convenient for 2D and 3D statements, and also advantageous when non-trivial *dissipation functions* $\mathcal{P}$ are to be used. Remarkably, within this formalism, the main *ansatz* of Bean's model (infinite slope in Fig. 7) can be straightforwardly included, which allows a better disclosing of the underlying physics.

As shown in [88,92], upon discretizing in time and changing variables, the differential statement in Eq. (1)) is equivalent to the step-by-step minimization of the functional in Eq. (15), defined over the volume of the superconductor, which can be solved with

the help of minimization packages as the ones included in the optimization toolbox solver by Matlab, or by free-license specialized solvers for large-scale nonlinear optimization problems such as Lancelot [93].

$$\mathcal{L}[\mathbf{J}_{\iota+1}] = \int_{V_{sc}} d^3\mathbf{r} \int_{V_{sc}} d^3\mathbf{r}\,' \left[\frac{\mathbf{J}_{\iota+1}(\mathbf{r}) \cdot \mathbf{J}_{\iota+1}(\mathbf{r}\,')}{\|\mathbf{r}-\mathbf{r}\,'\|} - 2\frac{\mathbf{J}_{\iota}(\mathbf{r}) \cdot \mathbf{J}_{\iota+1}(\mathbf{r}\,')}{\|\mathbf{r}-\mathbf{r}\,'\|} \right] + \frac{8\pi}{\mu_0} \int_{V_{sc}} d^3\mathbf{r} \left(\mathbf{A}_{e,\iota+1} - \mathbf{A}_{e,\iota}\right) \cdot \mathbf{J}_{\iota+1} + \frac{4\pi\Delta t}{\mu_0} \int_{V_{sc}} d^3\mathbf{r}\, \mathcal{P}(J_{\parallel,\iota+1}, J_{\perp,\iota+1}), \tag{15}$$

In Eq. (15), the index 'ι' indicates the value of the quantity for the time layer t_ι, Δt is the time interval ($\Delta t \equiv t_{\iota+1} - t_\iota$) and $\mathbf{A}_e$ stands for the vector potential related to the external sources. Formally, the problem of functional analysis to be solved is: find the vector field $\mathbf{J}_{\iota+1}$ (the current density distribution) that minimizes $\mathcal{L}_\iota$ subject to the constraints and boundary conditions (in particular, the values at previous time step $\mathbf{J}_\iota$). From the physical point of view, the above variational principle implies the balance between reversible (magnetostatic) energy variation and irreversible dissipation (heat), compatible with the external drive forces. Also, sufficiently low frequencies of the excitation are assumed so as to avoid energy storage in accumulated charges (Table 1).

This formulation is rather flexible for exploring different $\mathbf{E}(\mathbf{J})$ laws. In particular, the pure CS model, as exposed by Bean [50] may be interpreted as a limiting situation (visualized as $\alpha \to \pi/2$ in Fig. 3) that would imply an arbitrarily large term of dissipation for $J > J_c$. As a matter of fact, one straightforwardly obtains the flux penetration profiles just by minimizing $\mathcal{L}[\mathbf{J}_{\iota+1}]$ with the last term replaced by the condition $J \le J_c$. Consequently, in multidimensional problems, this condition becomes $\mathbf{J}_{\iota+1} \in \Delta_c$ as shown in Fig. 7. Then, the ingredient remaining is precisely the $\mathbf{E}(\mathbf{J})$ law to be considered for describing the superconducting state and its relation with real-world measurements as it will be described in the following section.

3. J_c from real-life scenarios

The macroscopic concept of critical current density J_c results from the physics of vortices, with Eq. (12) providing the basic interpretation in terms of the equilibrium between magnetic pressure and the pinning forces. Thus, J_c and its dependence on H_a, T, and field/sample orientation will be influenced by the properties of the flux line lattice, as well as by the underlying microstructure of the superconducting sample. Complex situations may arise when both factors need to be combined, which is why this section begins by addressing the experimental issues related to the measurement of J_c, followed by a discussion of state-of-the-art flux pinning models.

3.1. Experimental considerations

Although the model approximation in Fig. 3 provides a sound theoretical concept for the critical current density, in practice, such behavior is seldom found for several reasons. On the one hand, unless for low temperatures, thermal activation phenomena will induce detectable non-zero voltages even for the smallest currents. On the other hand, associated with the existence of inhomogeneities in the sample, a distribution of local values $J_c(x, y, z)$ will give place to smoother $\mathbf{E}(\mathbf{J})$ curves. These facts motivate the discussion on whether to use a modified CS model or straightforwardly some heuristic approximation as the power-law model. Thus, experimentally, J_c may be less well defined, especially for bulk samples at finite temperatures.

Together with other issues related to the experimental techniques themselves, the topic on how to determine the critical current density has deserved prominent attention over the years. Readers are directed to instructive textbooks for comprehensive coverage of the subject [44,94,95]. Now, from the practical point of view, it may be argued that the discussion on the determination of the actual value for J_c loses importance in favor of some phenomenological approximation as the so-called power-law model. This is because what most actual applications require is just a low level of dissipation, i.e., sufficiently small $V \cdot I$. In fact, the engineering parameter of interest is indeed $I_c = \langle J_c \rangle \cdot A$ and therefore, some tolerance on the local values for $J_c(x, y, z)$ may be assumed. Nevertheless, for envisaging applications it is necessary to establish some criterion that allows for comparison between different characterization techniques and samples. Thus, aiming at the most detailed characterization of the material, experimental setups usually include the possibility of regulating temperature and magnetic field (intensity and orientation). These possibilities are implicit in the discussion below, which briefly centers on determining J_c under the most popular experimental methods, emphasizing their advantages and shortcomings.

3.1.1. Electrical transport measurements

The most straightforward experiment for determining the critical current density consists of ramping the applied current along a superconducting wire or microbridge, while recording the voltage in a 4-probe configuration. I_c is defined by the condition that the voltage reaches some conventional threshold for the electric field at self-field conditions, E_0, typically 1 μV/cm. Isothermal conditions are to be ensured, which requires a good thermal contact to dissipate the generated heat, as well as good electrical contacts in the current pads to avoid excessive contact resistance and, hence, sample heating. In addition, in the case of superconducting ceramics like the cuprates, unbalanced contact resistances may introduce thermal gradients that alter the process by inducing spurious vortex drift.

This electrical method is better suited to characterize strong-pinning samples at high magnetic fields, yet sufficiently far away from the so-called irreversibility line, that establishes the boundary for lossless current flow in the presence of thermal fluctuations [96]. Then (i) one obtains a rather steep $V(I)$ curve, which makes the voltage criterion less critical, and (ii) diminishes the influence of the self-field created by the measuring current. When such conditions cannot be met, one may take advantage of

the diverse power law approaches of the form $E(I) \propto E_c(I/I_c)^n$, as the ones introduced in Refs. [97–99]. In this sense, there are two correction methods for artificially high I_c values near the irreversibility line due to low n values [99]: (i) Using a constant-resistivity criterion ρ_c instead of E_c (or E_0), and (ii) The offset method, i.e., introducing a factor correcting I_c determined by a constant E_c with a factor $1\text{-}n^{-1}$ for compensating thermally activated flux flow near B_{irr}, or alternatively correcting I_c by an instrumental offset E_0 and a linear term with slope k accommodating incomplete current transfer, such that $E(I) = E_0 + kI + E_c(I/I_c)^n$. Whilst the former method is suited for limited critical current ranges and may underestimate J_c occasionally, the latter forces J_c to zero for fields and temperatures where the $V(I)$ curve is ohmic at the chosen E_c. However, as suggested by Alexey Pan et al. [98], one may straightforwardly analyze the data by a flux creep model that incorporates the electric field criterion E_c. This has the additional advantage that one may compare different experimental methods through the evaluation of the equivalent electric field threshold for each case. Furthermore, if one records the magnetic field on top of the sample (through Hall microprobes, for instance), a robust voltage-criterion-independent method can be introduced [97], where a well-defined transition of the curve $B_z(I)$ to a linear regime characterizes the beginning of uniform current flow $I = I_c$, and thus $J_c = I_c/A$.

Finally, unlike granular fiber-textured wires like NbTi [100,101], Nb_3Sn [101,102], Bi2212 [103,104], MgB_2 [105–107], or 122-type IBS[1] [108,109], REBCO coated conductors exhibit a very large field-angular variation of J_c. This occurs when a magnetic field is applied parallel or perpendicular to the *ab*-planes of the REBCO crystal structure, which in a grained-average approach is deposited to be aligned with the plane of the wider surface of the REBCO CC. In fact, for fields close to the *ab*-planes ($\theta = 90°$), the characteristic I_c of a REBCO CC at LHe temperatures (<4.2 K) can reach up to several kilo-amperes, making the usual transport current method of I_c measurements extremely difficult to use [110].

3.1.2. Magnetic inductive measurements

Several experimental techniques based on the detection of the sample's magnetic moment and/or its variation have been used routinely for determining J_c, including DC and AC magnetization measurements.

On the one hand, DC magnetization measurements under applied field can provide the value of J_c with relative ease. Typically, one records the hysteresis cycle and determines the critical current density by using an expression like the one introduced with Eq. (7). The advantage of this method is that, by averaging the increasing and decreasing branches of the magnetization cycle, one 'compensates' the possible influence of reversible magnetization (sometimes unnecessary for being very small). However, an important shortcoming is that, unless for the case of long cylinders, demagnetizing effects may strongly change the field within the sample (especially for low values of the applied field $\mu_0 H_a$), and the plot $J_c(\mu_0 H_a)$ is not representative of the actual $J_c(B)$ behavior, which is the wanted (shape independent) result. Nevertheless, as said, a possible detour for this problem was suggested in [81], just by considering the opposite limit. Therein, it was shown that in appropriate units, the plot of $\Delta M(\mu_0 H_a)$ converges to $J_c(B)$ as the sample gets thinner and thinner, because the full penetration field is reached for smaller and smaller values of H_a where the self field is less and less important.

On the other hand, about the AC magnetization measurements, the superposition of an AC ripple $h_0 \cos(\omega t)$ onto the DC magnetic field can be used in a variety of forms to characterize J_c too [111]. For instance, by means of lock-in amplifier techniques [112], phase-sensitive and frequency-dependent detection methods can provide a number of advantages such as noise cancellation, high sensitivity, and the possibility of analyzing in-phase and out-of-phase components as well as the harmonic response [113]. The detection of harmonics in the signal, as already suggested by Bean [50] is a sensitive, noise-protected technique that straightforwardly gives the critical current density. In particular, one may show that for a slab of thickness d in parallel field configuration, the out-of-phase component of the third harmonic of the magnetic permeability fulfills the relation $\mu_3'' = 2\mu_0 h_0/(15\pi J_c d)$. Also, if one measures the out-of-phase component of the first harmonic, J_c may be determined, because this quantity reaches a maximum for the field

$$h_m = \frac{4J_c d}{3}\,. \tag{16}$$

Similarly, there is the so-called *Campbell's method* [114], which allows extracting the field penetration profile by measuring the in-phase signal when an AC field of small amplitude is added to the DC profile. Then, $B(x)$ is obtained from the recorded signal, and by taking its derivative one has $J_c(x)$. The sensitivity of the method has not only allowed obtaining the value J_c that corresponds to some average "barrier height" for the vortices in their potential wells but, additionally, several authors have been able to record the oscillations of vortices, centered at the minimum of the potential well, thus giving a picture of the wells close to their minima. However, a shortcoming of this method is that it may not be applied to thin samples (as compared to the characteristic distance $\lambda_{Campbell} = h_0/J_c$), because the critical state is not established in such conditions and one may only detect the oscillations of vortices.

Consequently, although for given values of the applied DC field and temperature, $J_c(B,T)$ may be obtained by using the DC or the AC techniques described above, it is worth noticing that the main shortcoming of the AC methods is their limitation in frequency. Typically, it is recognized that one should use $\nu < 1$ kHz but, as noticed by many authors, the best strategy is to double-check that the results do not change with frequency for the range of interest.

Finally, conceptually different from the above, a number of less widespread methods for obtaining J_c have appeared. One may mention those related to the detection of forces (or torques) between superconductors and external magnetic fields. In particular, the measurement of cantilever deflections due to the torque $\boldsymbol{\tau} = \mathbf{M}_V \times \mathbf{B}$ exerted on an attached superconducting sample (of magnetization $\mathbf{M}_V$) directly gives the critical current density. The torque being proportional to M_V, one may apply the methods in Section 2.2.2 on

[1] Iron (Fe) Based Superconductor, in literature also often called FBS.

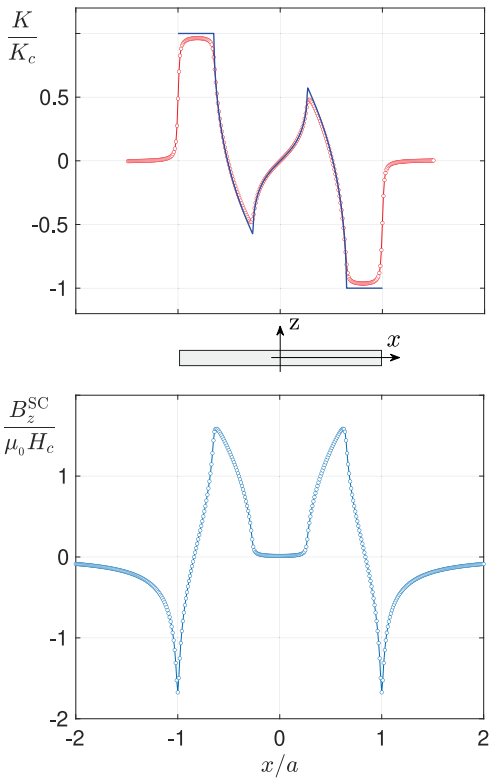

Fig. 9. Top pane: the sheet current density profile along the superconducting tape for synthetic data (continuous line), together with the recovered curve by means of (Eq. (17))(symbols). Bottom pane: calculated profile of perpendicular magnetic flux on top of the tape. Forward calculations were done following Ref. [57]. B_z^{SC} stands for the flux created by the superconductor, i.e., recorded minus applied. We have used the definitions $K_c = 2dJ_c$ and $H_c = K_c/\pi$.
Source: Adapted with permission from [48].

DC and AC magnetization measurements and derive I_c [115]. This is a highly sensitive technique, mostly adapted to small samples, but which results of utter importance for the measurement of the $J_c(B,\theta,T)$ characteristics of REBCO CCs at LHe temperatures [110], as at these conditions access to strong magnetic fields in resistive measurements is limited.

3.1.3. MOI measurements and other methods

The magneto-optical imaging (MOI) of superconductors is already an established technique that provides, straightforwardly, information about the component of the magnetic field (say B_z) normal to the surface of flat samples [80,116–118]. Outstandingly, for such a geometry, one may invert the on-surface $B_z(x,y)$ data and recover the local sheet current density $\mathbf{K}(x,y)$ on the sample by a direct method, free from any fit parameter. Nevertheless, we recall that for the general case, a possibly non-affordable amount of experimental data, including the field components B_x, B_y, and B_z around the sample, would be needed. In mathematical terms, the inversion of Biot–Savart's law is an ill-posed problem. As a simple example of such difficulties, just consider a long cylinder that carries a full current I along the length. By measuring the magnetic flux around it, one may not resolve the actual distribution of $J_z(r)$ within, but only its integral. However, MOI techniques have provided a clear demonstration that Bean's model gives a remarkably accurate description of many experimental observations.

Let us provide an illustration of the actual procedure in thin samples. As discussed in [78–80,118], for the usual case of long flat samples, a relatively simple scheme allows deriving the current density profiles by applying an inversion matrix $\mathcal{R}$ on the B_z data. Thus, assuming a long beam along the y-axis of width $2a$ along x and, of negligible thickness $2d$ along z, one has

$$K_y(x_i) = \sum_{i,j} \mathcal{R}_{ij} B_z(x_j)\,. \tag{17}$$

Here, it has been assumed that the magnetic field data have been recorded along the x-axis in a discrete set of points x_j, and at a given (small) height above the superconductor, from which one obtains the sheet current along the width ($-a < x_i < a$). The process is illustrated in Fig. 9. In this example, the superconducting tape was subjected to an external magnetic field that was initially ramped to a partial penetration regime and then reversed. Notice that $\mathcal{R}_{ij}$ is a purely geometrical matrix that one may calculate in advance, as shown in Ref. [78], and is nothing but the implementation of Biot–Savart's law. Thus, by applying Eq. (17) one gets a picture of the $K_y(x)$ profile, which, in particular, gives the value of the critical current density: $J_c = K_c/2d$. We emphasize that the information provided is both local and quantitative upon calibration of the MOI instrument. Remarkably, a spatial resolution in the submicron scale has been achieved, even allowing for the observation of individual vortices.

However, as one may notice in Fig. 9, which has been built with synthetic data, the reconstruction of the current density profile is influenced by technical issues concerning the signal processing methods. In particular, the cutoff of high-frequency components of the signal is advisable in order to avoid overshooting related to sharp peaks in the signal [78]. As seen, this leads to some smoothing of the reconstructed profile. A number of additional considerations related to the anisotropic nature of J_c, its field dependence, the influence of defect structures, the effect of finite thickness of the samples, and other features concerning the analysis of MOI data may be found in Ref. [80]. Moreover, by contrast to the above "clean" synthetic data, a practical but vital issue has to be mentioned as real-life experiments are affected by noise. This noise can substantially increase the difficulty of the inversion process, for which reason significant efforts for producing robust reconstruction algorithms from magnetic field measurements have been recently introduced in the literature [119–121].

3.2. Constituent macroscopic models

The simplest pinning models consider situations in which the pinning interaction may be described as an isotropic force that does not induce preferential orientations of the vortices,[2] simply acting as the macroscopic mechanism that freezes their positions. This entails considering that energy dissipation occurs only if external perturbations induce either compression or rotation of flux lines. However, depending on the orientation of the force perturbing the pinned layout of flux lines, cumbersome two-dimensional and three-dimensional approaches might be needed if a sound physical understanding of the macroscopic origin of J_c is sought (Section 2.1); otherwise J_c will have to be accepted as a somehow averaged quantity that comes from the experimental considerations described in Section 3.1. Nonetheless, a good number of properties of type-II superconductors in the range of applications may be well described by simplified models that, to some degree, are able to capture the macroscopically observable physical properties. Some of the most celebrated are recalled below.

3.2.1. Pure CS also known as Bean's model

Undoubtedly, as said in Section 2, the big success of Bean's model may be ascribed to its elegance achieving a minimized mathematical effort for analyzing/predicting experimental results in a complex system, viz.: the type-II superconductor with vortex pinning effects. However, one should be aware of its limitations, some of which have already been discussed in Section 2.1.

Thus, keeping up within the 1D approximation, valid for slabs and long cylinders in parallel fields, a major concern is the assumption of a constant J_c. Even in the already simplified framework of Eq. (12) that overrides the detailed behavior of the FLL, a field independent J_c may be hardly accepted, as it may be deduced from the condition $\mathbf{J}_c \times \mathbf{B} + \mathbf{F}_P = 0$. At most, one could assume $\mathbf{F}_P$ to be constant (e.g., for very strong pinning and magnetic fields well below H_{c2}) and then $J_c \propto 1/B$. Thus, only under restricted conditions, where internal variations of B are not relevant, one could expect to have reasonable predictions within the pure critical state.

Therefore, in the light of Eq. (7), it is only for the infrequent situation of having a square hysteresis cycle that Bean's model makes full sense. Remarkably, as it is well known, such an expression is still very useful for obtaining the actual $J_c(B)$ dependence from experimental measurements, although one has to ensure that the B profile within the sample is nearly uniform if not fully. This implies discarding the data in the low field range, so as to warrant full penetration of the magnetic field. In this regard, a smart experimental design that leads to this situation in a good range of fields is to use flat samples in a perpendicular field configuration, as shown in [81]. Otherwise, if the direction of the applied magnetic field changes, such that the perpendicularity condition between the perturbation field and the induced current density cannot be ensured any longer, more sophisticated models need to be invoked, such as the ones shown below.

3.2.2. Double critical state models

Another limitation of Bean's model in its original form relates to the dimensionality of the experimental situation, where effectively, only for the mentioned 1D problems, one has $\mathbf{E} \parallel \mathbf{J}$, with both quantities being orthogonal to $\mathbf{B}$. Just recall that pinning forces appear to compensate $\mathbf{J} \times \mathbf{B}$ and that when the threshold is *exceeded*, one has $\mathbf{E}$ along $\mathbf{B} \times (\mathbf{J} \times \mathbf{B})$ as one may show by starting with Faraday's law. In such case, a macroscopic material law of the kind $\mathbf{E} \propto E_0(J/J_c)^n(\mathbf{J}/J)$ makes sense, as long as the (positive) exponent n is sufficiently large to resemble the flux pinning mechanism attained by the CS model (recall Fig. 3). However, related to a series of experiments with samples under rotating magnetic fields, initially developed along the early 80's [122], interest arose concerning the appearance of components of $\mathbf{E}$ and $\mathbf{J}$ along the direction of $\mathbf{B}$. In particular, the focus was on the search for a meaningful relationship $\mathbf{E}(\mathbf{J})$ similar to the above described, which eventually led to the so-called Double Critical State (DCS) model [59] that provides the basic framework for the related phenomenology.

Briefly, the DCS theory assumes that two critical parameters exist, $J_{c\parallel}$ and $J_{c\perp}$. They are the thresholds for the components of $\mathbf{J}$ either parallel or perpendicular to the local magnetic field. $J_{c\perp}$ accounts for the flux depinning threshold whilst $J_{c\parallel}$ relates to the maximum gradient of the angle between adjacent vortices (see Fig. 8). Thus, the material law (which generalizes the Bean's model $\mathbf{J} = J_c\hat{\mathbf{E}}$) is then written as

$$\begin{cases} \mathbf{J}_\parallel = J_{c\parallel}\hat{\mathbf{E}}_\parallel & \text{if} \quad E_\parallel \neq 0 \\ \mathbf{J}_\perp = J_{c\perp}\hat{\mathbf{E}}_\perp & \text{if} \quad E_\perp \neq 0\,. \end{cases} \tag{18}$$

[2] Here, the term isotropic applies to the properties of the pinning force $\mathbf{F}_P$ in Eq. (12). Then, if the orientation of either $\mathbf{J}$ or $\mathbf{B}$ relative to the crystal axes does not matter, $\mathbf{F}_P$ just opposes to $\mathbf{J} \times \mathbf{B}$.

The actual implementation of these equations, together with Ampère's and Faraday's laws, may be found in several publications, starting with the seminal work by Clem and Perez-Gonzalez [59], which was later extended by Badía-Majós, López and Ruiz [123] when including more realistic situations on which the magnetic anisotropy bandwidth, $\chi \equiv J_{c\parallel}/J_{c\perp}$, is not constant. This is indeed the case observed in epitaxially grown YBCO thin films [91] where the geometry of the yield region for the current density, Δ_c, is precisely elliptical as shown in Fig. 7. Remarkably, the experimental design introduced in [91] demonstrated beyond any doubt the existence of the flux cutting (or alike) mechanism, showing that macroscopically the vortex physics governed by the concept of critical current density is in fact smoothed, and possibly favors the use of elliptical models. However, it remains unknown if the magnetic (vortex deformation) anisotropy of other REBCO materials, or in general other superconductors, can be described by the same DCS Δ_c function.

Noticeably, from the technical point of view, the DCS model may be pictured as well by Fig. 7 if Δ_c is being transformed into a rectangle. This means assuming that $J_{c\parallel}$ and $J_{c\perp}$ remain constant in time, while the induced components of current density, $J_\perp$ and $J_\parallel$, respectively, vary with the changing applied magnetic field or transport current. In fact, as argued by Ruiz and Badía-Majós in [124], one may still keep the fundamental significance of this theory but reduce its mathematical difficulties by using a 'smooth' model that rounds the corners of the rectangular yield region of the DCS model by means of the family of superelliptic functions that defines the critical boundary Γ_c (see Section 2.2.3),

$$\left(\frac{J_\parallel}{J_{c\parallel}}\right)^{2m} + \left(\frac{J_\perp}{J_{c\perp}}\right)^{2m} = 1\,. \tag{19}$$

From Eq. (19) it becomes evident that rectangular shapes for Δ_c can be obtained for the limit $m \to \infty$ and arbitrary anisotropy bandwidth χ. More importantly, the elegance of this equation is in its unified mathematical description for all possible scenarios within the DCS theory, including extreme cases such as the pure CS where flux pinning and flux cutting events are indistinguishable (isotropic), i.e., with $\chi = 1$ and $m = 1$, passing through the more realistic elliptic models with arbitrary but material-dependent χ and $m = 1$, and slight deformations of it ($m > 1$), until the infinite magnetic anisotropy bandwidth or so-called T-state model ($\chi \to \infty$) where $J_\parallel$ is unbounded.

Thus, if, for the sake of simplicity, we introduce the dissipation function (recalling the concept behind Eq. (14)),

$$\mathcal{P}_{PL}(\mathbf{J}) = F_0 \left[\left(\frac{J_\parallel}{J_{c\parallel}}\right)^2 + \left(\frac{J_\perp}{J_{c\perp}}\right)^2\right]^m , \tag{20}$$

and then, by taking derivatives as dictated by $\mathbf{E} = -\nabla_{\mathbf{J}}\mathcal{P}$ (reminding Eq. (14) and Fig. 7), but now along the principal directions, the $\mathbf{E}(\mathbf{J})$ law in the elliptical approach can be naturally defined by

$$\mathbf{e}(\mathbf{j}) = \left(j^2 + \gamma\, j_\parallel^2\right)^{m-1} \left(\mathbf{j} + \gamma\, \mathbf{j}_\parallel\right) . \tag{21}$$

Notice that dimensionless units have been introduced for convenience through the definitions

$$\begin{aligned} &\gamma \equiv \chi^{-2} - 1\,, \\ &\mathbf{j} \equiv \mathbf{J}/J_{c\perp}\ ;\ \mathbf{j}_\parallel = j_\parallel \hat{\mathbf{h}}\,, \\ &\mathbf{e} \equiv \mathbf{E}/(2mF_0/J_{c\perp})\,, \end{aligned} \tag{22}$$

where F_0 is an empirical parameter, either constant or not, which in principle could be extracted from experimental considerations (see Section 3.1), i.e., similarly to how the threshold value for the electric field E_0 is chosen.

Making use of the anisotropy constant γ, one can notice that the isotropic law, i.e., $\mathbf{e}(\mathbf{j}) = j^{2m-1}\,\hat{\boldsymbol{j}}$ is obtained in the limit $\gamma \to 0$, as expected. Then, in those problems for which the parallel current flow may be neglected ($j_\parallel/j_\perp \to 0$) one also recovers the formula $\mathbf{e}(\mathbf{j}) = j^{2m-1}\,\hat{\boldsymbol{j}}$. This corresponds to the very usual situation for which $\mathbf{J} \perp \mathbf{B}$ is verified (as in flat samples under perpendicular field $\mathbf{H}_a$).

Finally, concerning the origin of the limitations for the parallel and perpendicular components of the critical current density, as extensively compiled in [47], the main facts can be summarized as follows: Contrary to the case of $J_{c\perp}$, which is rather well understood as the balance between *Lorentz-like* and material pinning forces, no consensus exists yet about the real nature of the critical value $J_{c\parallel}$. In fact, the main topic about the parallel critical current threshold is whether the underlying physical mechanism is flux cutting or not. It is however rather clear that $J_{c\parallel}$ is noticeably influenced by the pinning landscape and that this could explain the much lower values in observations than expected according to the cutting mechanism [91].

It is important to stress that the anisotropy discussed in this section relates to the physics of vortex deformations (compression or rotations) in isotropic media. Additional factors introduced by crystal anisotropy (smartly circumvented in the experiment of Ref. [91]) will be treated below.

3.2.3. Simplified $E - J$ power law models

It is well known that the knowledge of the exact $\mathbf{E}(\mathbf{J})$ curves for particular superconducting structures (e.g., thin films, CCs, or bulks) is paramount for achieving reliable FEM simulations [125]. However, if simplified models are to be used, their actual physical meaning may be accepted only under certain cautions.

Let us start by somehow neglecting or ignoring the distinction between the flux-pinning limitation, i.e.: $J_{c\perp}$, and the flux-cutting mechanism (behind the $J_{c\parallel}$ limitation), mostly because this phenomenon may occur only in experimental conditions where the local components of the magnetic field are not always perpendicular to the direction of the induced currents. In such case, the critical

current density is simply averaged by an empirical and somehow limited definition to the macroscopic domain of the $\mathbf{E}(\mathbf{J})$ material law through an isotropic *ansatz* (i.e.: Δ_c is a circle in Section 2). In this sense, many experimental results have been successfully explained by a combination of the above ideas and a heuristic expression for the material law in the form,

$$\mathbf{E}(\mathbf{J}) = E_0 \left(\frac{J}{J_c} \right)^n \frac{\mathbf{J}}{J} . \tag{23}$$

This is the so-called $\mathbf{E}-\mathbf{J}$ *power-law* dependence that, without losing any generality when introducing the J_c dependence with $\mathbf{B}$ and T, is to be analyzed below.

On the one hand, notice that according to Eq. (23), for moderate or high values of the exponent n, one has negligibly small electric fields for current densities below J_c, while a sudden increase occurs when the threshold is passed.[3] Moreover, the 'pure' CS can be recovered for $n \gg 1$ where one gets $\mathbf{J} = J_c \hat{\mathbf{E}}$ if $E \neq 0$ (Fig. 3). Worth to say that this model assumes, in principle, that the electric field is parallel to $\mathbf{J}$, corresponding then to the isotropic limit hypothesis in the DCS theory. Nevertheless, material anisotropy may be incorporated by introducing dimensionless angular dependent prefactors for the magnetic field, $\epsilon(\theta)\mathbf{B}$, as it will be shown in Section 3.3. On the other hand, in order to see how the power-law modeling finds a connection to the underlying physical mechanisms, let us recall that in the absence of thermal agitation or other statistical effects one has the high-exponent limit, which practically meets the conditions of the critical state regime, i.e., sudden transitions of the FLL, avalanching from one configuration to another when the flux pinning threshold is exceeded. Then, electric fields appear abruptly when this occurs. Yet, either related to finite temperatures, gradients, or to inhomogeneous pinning interactions [126,127], a smoothing effect takes place and one can also use a power law dependence, now with a reduced value of n [29].

The validity of the simplified $\mathbf{E}-\mathbf{J}$ power-law formula over a noticeable range of electric field was justified in [128] based on the concept of partial flux flow in the presence of thermal agitation. However, for a pure power-law $E(J)$ in the proximity or over the transition thresholds, H_{c2} and T_c, the J_c would strictly be zero. In fact, within the glass–liquid transition scenario or the percolation model of Yamafuji and Kiss [129], a pure power law is only expected at the transition temperature, where below the transition the scaling curves show negative curvature in double-logarithmic presentation and hence finite J_c values. Nonetheless, for considering overcritical regimes, which means near the critical parameters for transitioning to the normal state, the $E(J)$ curves may well be approximated by the so-called percolation model,

$$\mathbf{E}(\mathbf{J}) = E_{c0} \left(\frac{J - J_{c,\min}}{J_c - J_{c,\min}} \right)^n \frac{\mathbf{J}}{J} , \tag{24}$$

where $J_{c,\min}$ is the minimum value of the critical current density that allows the depinning of flux bundles that induces the flux flow resistivity in this model. However, it must be noted that J_c in the above function is not always the same one determined by the electric field criterion in electrical transport measurements, i.e., $E_{c0} \neq E_0$. This is because Eq. (24) is mainly designed for taking into account the nonlinearity of the flux creep and flux flow behaviors, for which the minimum value of pinning potential is now the one that allows determining the maximum creep electric field, i.e., the field level at which flux creep crosses over to flux flow [130]. Therefore, overcritical regimes can also be accounted for through an $\mathbf{E}-\mathbf{J}$ power-law, with the difference that rather than considering three 'free' parameters as in Eq. (23), i.e., E_0, J_c, and n, it demands for the introduction of at least a new parameter that might account for the flux creep, such as $J_{c,\min}$. Thus, if for practical applications, the physics of interest remains well below the non-dissipative regime, then $J_{c,\min}$ can be approached to zero such that a field excitation could lead to a nearly instantaneous creep within a quasi-steady transition between successive flux pinning events, as it is the case of the conventional $\mathbf{E}-\mathbf{J}$ power-law at Eq. (23) and the well-supported CS models. Likewise, it is possible to retain the original E_0 and J_c values of the simplified $\mathbf{E}-\mathbf{J}$ power-law formula, but this would demand the introduction of an exponential model with two new free parameters, η and β, as has been recently shown in [131].

Finally, if the n value in Eq. (23) is treated as the local logarithmic gradient of $E(J)$, it results related to the flux creep rate S at the chosen electrical field criterion E_c via $S = (n-1)^{-1}$ [132,133]. In fact, in practical cases, n is an empirical parameter that may be experimentally determined for the material of interest under specific conditions. This is the reason why often a power-law dependence between J_c and n or (n-1) is found without distinction [106,134,135]. Consequently, this definition is somehow general for the exponent n allows evaluating the creep rate at elevated driving forces [136] as well as discerning pinning at strongly correlated structures (e.g., intrinsic *ab*-planar pinning or well-aligned nanocolumns) from random, uncorrelated pinning with different causes for creep (see e.g., [135,137,138]), a matter that will be discussed in future sections, prior to addressing the most important physical dependencies of J_c under the flux pinning regime.

3.3. T, B, θ dependence

As explained in the previous section, the variety of choices for the $\mathbf{E}-\mathbf{J}$ law is certainly diverse. Even from purely macroscopic physical principles, different options have become available depending on the interest or actual regime on which the superconductor needs to be assessed [139]. Also, although all these models are indeed connected under the same principles of Bean's model, what has led to the CS, DCS, and the simplified $\mathbf{E}-\mathbf{J}$ power-law models to show good qualitative and quantitative resemblance with many experimental observations, it is known that the used J_c parameter may strongly depend not only on the temperature but also

[3] Yet one has to keep in mind, the so-determined value of J_c is different from the onset of dissipation in real conductors [97].

on the magnitude and orientation of the local magnetic field. This is especially true in the case of superconducting thin films and, more generally, for commercially available CCs, also known as the second generation of high-temperature superconductors (2G-HTS), which exhibit a wide range of magneto-angular anisotropies [110,140,141]. In this sense, despite the fundamental physical principles of the constituent macroscopic models discussed does not change, for attaining a complete macroscopic description of the critical current density in applied superconductors, it is necessary to revise below the origins and meanings of the derived J_c functions with magnetic crystallographic anisotropy.

3.3.1. Kim's model and other phenomenological extensions

Probably the most celebrated contribution concerning the B-dependence of J_c is the seminal work by Kim, Hempstead and Strnad [142], nowadays simply referred to as Kim's model. Arguing in terms of a power series expansion and based on experimental results for Nb tubes, these authors proposed a phenomenological expression of the kind

$$J_c(\mathbf{B}) = J_{c0}\left(1+\frac{|\mathbf{B}|}{B_0}\right)^{-1}, \tag{25}$$

that incorporates the constants B_0 and J_{c0}, two phenomenological material parameters, with J_{c0} commonly assumed to be the self-field critical current density from electrical transport measurements, and B_0 a control parameter that depends on the sample's geometry (e.g., if it is a SC bulk or a SC thin film). The exponent -1 has been generalized already in 1990 to a free fit parameter $-\beta$ by Xu et al. [143] since it is more appropriate for HTS cuprates, see Section 3.3.5.

From the theoretical point of view, based on fundamental simulations for interacting vortices in a pinning landscape, the authors of Ref. [144] obtained a linear fit to the predicted B-dependence of $1/J_c$. For this, they just assumed parabolic potentials for the vortex–vortex and vortex–pin interactions, which gives elegant support for the CS theory and Kim's model. On the other hand, being this a phenomenological *ansatz*, Eq. (25) has still been a very useful tool in many investigations, allowing to adjustment of many observations with two sole additional parameters.

Nonetheless, for the majority of known coated conductors or 2G-HTS wires, the superconducting film exhibits a marked magneto-angular anisotropy. This implies that the component of the critical current along the *ab*-planes of the REBCO compound, J_c^{ab}, differs from the critical current that could be developed along the *c*-axis, J_c^c. However, they mutually contribute to increasing the overall critical current density of the SC sample, as the actual J_c is, in general, larger than its components for fields aligned in the *c*-direction or along the *ab*-planes. Thus, if the external magnetic field is applied parallel to the wider surface of the CC, i.e., parallel to the *ab*-plane of the REBCO layer, and perpendicular to the direction of the applied transport current (maximum Lorenz force configuration), there will be an additional component of current flowing along the *c*-axis, which allows for the increment of the total critical current density either by the possible appearance of superconducting currents (cooper pairs) along the *c*-axis or due to the occurrence of flux cutting.

Consequently, a number of modifications of Eq. (25) have appeared over the years, so as to describe better the behavior of a given material [110,140,141,145,146]. The main features to be mentioned are: on the one hand, the discrimination of the parallel and perpendicular components of the applied magnetic field in Eq. (25), but considering a different weighting between both, i.e., with $|\mathbf{B}|$ replaced by $\sqrt{k|B_\parallel|^2+|B_\perp|^2}$ in the J_c dependence [139,145,147]. On the other hand, probably in a more general way, the inclusion of local angular dependencies for anisotropic samples as the one proposed in [141], where the field prefactor

$$\epsilon(\theta) = \sqrt{\gamma^{-2}\sin^2(\theta)+\cos^2(\theta)} \tag{26}$$

is introduced. As will be seen below, this allows for a straightforward connection between the phenomenological models with quasi-mesoscopic and statistical models, where $\gamma^{-2} = m_{ab}/m_c$ is defined as the mass anisotropy ratio of the SC compound, and θ is the angle between the applied field and the crystallographic *c*-axis.

3.3.2. The second magnetization peak phenomenon

At this point, note that the above models consider only the possibility of having a monotonic decreasing $J_c(B)$ dependence, regardless of whether the magneto-angular dependence of CCs [141] has been considered or not. From the experimental point of view, and to the best of our knowledge, the critical current density extracted from transport measurements always agrees with this behavior. However, certain experimental measurements have shown that this is not always true [148–162], as the J_c(B) function can show a non-monotonic behavior with the presence of an absolute maximum at zero field, and a second relative maximum at a higher field characteristic of the SC sample. In fact, when J_c is obtained from magnetic inductive techniques (Section 3.1.2), the measured magnetic hysteresis loops $m(H)$ always show the presence of a peak around $H = 0$ T [163], generally called *Central peak*, and occasionally an additional peak at higher fields, generally defined as the *Second Magnetization Peak* (SMP). An example of the central peak can be seen in the inset of (a) Fig. 10(a), where the precise position of this peak depends on the sample's geometry and granularity, as well as on the field orientation [164]. However, many practical superconductors such as BSCCO show the occurrence of an SMP (Fig. 10(b)), revealing the non-monotonic decrease of the critical current density, i.e., breaking the standard B dependence of J_c. Consequently, this phenomenon is thought to give hints on the underlying physics of the Flux Line Lattice (FLL) and its interaction with the pinning landscape, as it can be located at different field values depending on temperature, material, sample geometry, and the physics associated with the birth of the phenomenon.

Since the discovery of the SMP, many researchers have tried to explain its origin by considering the vortex–vortex and the vortex–pinning center interactions, proposing different explanations and theoretical models [153–156] depending on the crystal structure

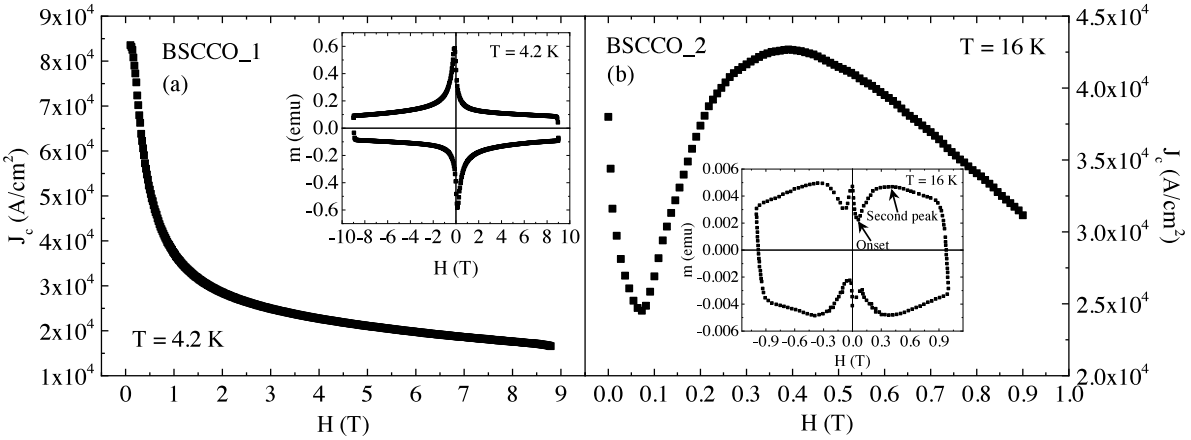

Fig. 10. $J_c(H)$ curves (main panels) extracted from the magnetic hysteresis loops (insets) for two BSCCO samples. (a) Shows the common monotonous decrease of J_c with field for a sample measured at 4.2 K. (b) Shows the occurrence of the SMP for an equivalent sample measured at 16 K.

and defect typologies present in the sample. Moreover, the SMP phenomenon has been found in different kinds of samples such as single crystals, thin films, or bulks, and for different field orientations [148,157–159]. Thence, the SMP phenomenon is particularly interesting not only from a theoretical point of view, but also due to its potential usefulness, as it might allow superconductors to sustain higher critical current densities at higher magnetic fields for practical purposes. For these reasons, since the 90s, the SMP phenomenon has been deeply investigated especially in the well-known families of superconducting cuprates [151–153] and more recently in the different families of iron-based superconductors [149,160–162], which were discovered in 2006 [38].

It is important to highlight that sometimes the papers facing the SMP phenomenon focus their analysis on different points of the $m(H)$ curve, such as the onset and the second peak (see Fig. 10(b)). Therefore, it can happen that the same phenomenon could be attributed to different mechanisms. Nevertheless, as recently reported by Polichetti et al. [165], the SMP can be framed in a general scenario of a vortex lattice crossover from a configuration with less efficient pinning to another one with higher pinning efficiency, although several causes can in general contribute to the birth of this phenomenon. However, it is worth underlining that the SMP phenomenon cannot be enclosed in a fixed range of temperatures and magnetic fields. In fact, it is well visible from the vortex phase diagrams reported, e.g., in Refs. [166–168], how different materials show different SMP characteristic values. This makes it even harder to get to a common understanding of the SMP phenomenon and therefore we will summarize below the main SMP observations in diverse HTS materials, which have been organized, just for clarity, in copper-oxides with and without calcium, and other HTS compounds.

SMP in HTS with CuO_2 planes. Among the cuprates, the most studied are probably the family of $YBa_2Cu_xO_y$ compounds, particularly $YBa_2Cu_3O_{7-\delta}$ (YBCO) samples where the SMP phenomenon can be seen in either single crystals, bulks (e.g. melt-textured samples), or straightforwardly on the 2G-HTS tapes available in the commercial market. In this context, it is pertinent to highlight several seminal works that have significantly contributed to the field, with their origins dating back to the early 1990s. Among these contributions, one of the key studies is the work of Daeumling et al. [159] in 1990, where the oxygenation conditions of three YBCO crystals were varied, finding that a decrease in δ tends to eliminate the anomalous double-peaked magnetization curve. In this context, Zhukov et al. [169] studied YBCO single crystals for $0 \leq \delta \leq 0.55$ connecting the observed increase of the current to synchronization effects of the increased disorder in the vortex lattice, as the distribution of the oxygen deficiency can induce stronger pinning as reported in [170]. Likewise, in 1993 Cohen et al. [171] revealed that the SMP phenomenon in YBCO samples was possibly facilitated by microstructural regions that, once they become normal with increasing field, act as additional pinning centers. On the other hand, in 1994, Küpfer et al. [157] analyzed not only YBCO single crystals but also known melt-textured samples [172], aiming to find a correlation between the relaxation in the magnetization and the SMP phenomenon, concluding that indeed the SMP phenomenon is not based on magnetic relaxation processes but related to the pinning mechanisms of the sample.

Building upon the above findings, Reissner and Lorenz [173] observed the existence of two different types of pinning centers in a YBCO melt-textured sample: one dominating in the low-field regime and associated with its 3D behavior, and the other type of pinning centers dominating at higher fields and temperatures, exhibiting a 2D pinning behavior. In this context, the authors suggested that the transition between 3D and 2D behaviors in vortex dynamics is responsible for the observed SMP phenomenon in their samples. Another recurrent cause associated with the SMP phenomenon is the crossover from pinning characterized by elastic deformations to pinning characterized by plastic deformations. For example, in the seminal works of Küpfer et al. [174], Abulafia et al. [153], and Miu et al. [175], the crossover in flux dynamics from elastic to plastic creep is shown to be the possible cause for the SMP phenomenon in their YBCO samples.

Similarly, Giller et al. [176] have ascribed the origin of the SMP phenomenon for YBCO single crystals to a crossover between the flux pinning and the flux creep mechanism, which is also supported by the works of Pissas et al. [177] whose experimental studies, at low and high temperatures, conclude that the SMP might indeed be caused by a disorder-induced transition (or crossover) from

a relatively ordered vortex lattice to a highly disordered vortex solid. Nevertheless, in 2018, Ionescu et al. [148] studied a twinned optimally doped YBCO crystal, stating that the SMP phenomenon is not due to a crossover between single-vortex to collective pinning but rather triggered by an increase of the characteristic pinning energy between the onset and the SMP. Still, what remains evident is that a more quantitative and sound theory of the SMP phenomena is to be achieved even with these highly explored materials.

Likewise, for the case of bulks, a particular explanation of the SMP phenomenon for undoped and Ag-doped YBCO samples has been given by Lotnyk et al. [158], where the origin of the SMP phenomenon arises from the competition between surface barriers and bulk pinning at intermediate temperatures $0.4 \leq t_c = T/T_c \leq 0.8$. Thus, doping can also be a tool to induce the SMP phenomenon in high-T_c superconductors. In this framework, Gokhfeld et al. [178], Antal et al. [179], and Vojtkova et al. [180] have reported more recently that doping with Nd, Li, Sm and Yb, respectively, can induce the SMP phenomenon in YBCO bulk samples due to the improvement of the pinning properties.

Finally, concerning the YBCO thin films employed as precursors for the production of 2G-HTS tapes, it is worth noting that the oxygen concentration, traditionally viewed as the primary parameter influencing the presence of the SMP, may not necessarily be the most optimal avenue for controlling its occurrence. Instead, a more appealing approach involves the incorporation of microstructural elements that, without altering the underlying crystallographic structure of the superconducting layer, offers the advantage of preserving the quality of the deposition buffer [30]. In this sense, at the beginning of 2019, Marchiori and Bending [181] analyzed the flux penetration profile of a 2G-YBCO tape doped with Dy_2O_3 nanoparticles, noticing that the presence of the SMP in the magnetization loop was due to an increase of J_c near the edge of the sample, linked to vortex pinning matching effects. Similarly, Galstyan et al. [182] studied the correlation features between J_c and the microstructural characteristics of Zr-added $RE Ba_2Cu_3O_{7-x}$ (RE rare-earth element) coated conductors, observing that the SMP phenomenon is not an inherent property of the REBCO matrix but due to matching field effects correlated with the distribution of $BaZrO_3$ (BZO) nanocolumns inside the sample.

Another popular member of the REBCO family of cuprates mostly studied in the 90's is $DyBa_2Cu_3O_y$ (DyBCO), which not only showed the SMP phenomenon but was at the time of major interest due to the apparent possibility to enhance J_c by changing its sintering temperatures. Thus, in 1994, Koblischka et al. [183] studied the SMP in a DyBCO single crystal, finding that the SMP phenomenon was due to a reorientation of the vortex lattice after reaching the full penetration field. Then, when analyzing the relaxation effects of twin-free DyBCO single crystals in 1995, van Dalen et al. [184] attributed the birth of the SMP phenomenon to a dynamic contribution of single-vortex pinning. This conclusion arose from the fact that the calculated critical current density $J_c(B,T)$, which by definition is independent of relaxation effects, results to be in good agreement with the predictions of simplified mesoscopic models where the crossover from single–vortex pinning to pinning of flux bundles does not occur, at least in the case of van Dalen's samples. Nevertheless, in 1997, Jirsa et al. [185,186] showed that in several DyBCO single crystals with the SMP phenomenon seen at a wide range of temperatures $(3-70\ \mathrm{K})$ and fields $(0-7\ \mathrm{T})$, the SMP can be the result of two different pinning contributions, one active at low fields and the other one at high fields, but in some occasions may result from the interplay of two different pinning regimes, leaving the problem still open for further research.

Analogously, an interesting cuprate with $T_c > 90$ K is $HgBa_2CuO_{4+\delta}$ (HBCO), which presents a single CuO_2 layer per unit cell and can be produced with high phase purity. In this regard, already in 1998 Pissas et al. [187] studied the SMP phenomenon for HBCO and Pb-doped HBCO single crystals, finding that the temperature-dependent SMP field, $H_{sp}(T)$, separates two distinct solid phases. In particular, for $H < H_{sp}$ the sample is in a weakly disordered quasi-lattice phase (Bragg glass) while for $H > H_{sp}$ it is in a highly disordered entangled state. Later it was confirmed that the SMP is related to an elastic to plastic pinning crossover if analyzed by the behavior of the activation energy as a function of the magnetic field [188]. Similarly, Stamopoulos and Pissas [166] proved that the SMP phenomenon in HBCO single crystals with different amounts of disorder (e.g., in two platelet crystals having $T_c = 89.9$ K and 94.8 K) reveals that the Bragg glass state below H_{sp} is replaced by plastic deformation of the vortex matter when the magnetic field exceeds the second peak field. Related to that, interesting results have been found very recently by Eley et al. [189] when analyzing an HBCO single crystal, showing that at sufficiently low temperatures ($t_c < 0.2$) the SMP coincides with the elastic to plastic crossover, but for $t_c > 0.2$ it is caused by a structural transition of the vortex lattice.

A high-T_c superconductor that is particularly interesting for energy harvesting applications at low temperatures [190,191] is $La_{2-x}Sr_xCuO_4$ (LSCO). Kodama et al. [152] studied in 1997 the SMP phenomenon manifested by a LSCO single crystal, finding that the SMP can be associated with the maximum flux pinning energy U_0 in the framework of the Anderson-Kim model [192] (see Section 5.1.3), and in particular to a crossover from collective creep to a catastrophic flux creep controlled by the glassy exponent μ inherent to the collective creep model [193]. More recently (2018), by studying underdoped ($x = 0.12$) and overdoped ($x = 0.2$) LSCO single crystals, with critical temperatures ranging from $\sim$ 27.5 K to $\sim$ 30.5 K, Ionescu et al. [148] found that the SMP phenomenon in LSCO is triggered by a disorder of the quasi-ordered vortex solid at low magnetic fields induced by random pinning. However, although for LSCO single crystals the SMP at various temperatures and field regions can be well described within the existing theoretical models, the temperature-dependent behavior of the SMP onset field for Sm-doped LSCO samples, such as $SmLa_{0.8}Sr_{0.2}CuO_{4-\delta}$ [194], appear to defy any model known.

SMP in HTS with $CaCuO_2$ planes. In 1993, the pioneering studies of Tamegai et al. [195] and Yang et al. [151] associated the SMP in $Bi_2Sr_2CaCu_2O_{8+x}$ (Bi2212) single crystals to a dimensional crossover in the pinning mechanism from 3D pinning at low fields to a 2D pinning at high fields, through a competing correlation between the magnetic hysteresis measurements obtained by Hall probe magnetometry and defect structures studied by transmission electron microscopy. This explanation is somehow supported by the magneto-optical measurements of high temporal resolution reported by Kalisky et al. [196]. They attributed the particular shape of the SMP phenomenon to long-living transient disordered states induced by edge contamination for inductions in the vicinity of the order–disorder vortex phase transition, showing that the thermodynamics evolution of SMP is governed by the relaxation times of the metastable disordered vortex states. Another interesting explanation of the SMP phenomenon in BSCCO single crystals by Khaykovich

et al. in 1996 [197] postulated that the birth of the SMP phenomenon is triggered by an underlying thermodynamic phase transition of the flux-line lattice. Following this *ansatz*, the work of Miu et al. [175,198] concluded later that the SMP phenomenon in Bi2212 and in YBCO single crystals is due to a crossover from elastic to plastic vortex creep, based on a careful analysis of the vortex activation energy and the critical current density of their samples. Similarly, in the early 2000s, Sun et al. [199,200] investigated the SMP in Pb-doped BSCCO single crystals, finding that the onset of the SMP phenomenon is caused by a disorder-induced vortex structure transition from an ordered vortex quasi-lattice (or Bragg glass) to a vortex glass state, at least in the case of partially Pb-substituted samples. However, in the case of heavily Pb-doped samples, the SMP phenomenon may be of dynamic origin and related to the underlying change of the vortex structure together with the competition between collective and plastic flux creep, just as in the case of BSCCO single crystals.

Finally, we conclude this section with some remarks for the case of Tl-based cuprates (TBCCO), as among all the HTS materials with potential for applications at LN2 conditions (77 K), the TBCCO family shows one of the highest T_c ($\approx$ 125 K for Tl2223). However, the study of Tl-based superconductors has been strongly limited by the inherent difficulties in their growth, which implies to deal also with the high toxicity of the thallium oxides. Nevertheless, when studied after diverse irradiation treatments, quite interesting observations related to J_c and the SMP could be mentioned. In this sense, the seminal works of Brandstätter et al. [201] for neutron-irradiated crystals of Tl1223 and Tl2223 and with similar purpose by Singh et al. [202] on ion-irradiated Tl2223 samples can be taken as an example. In the case of neutron-irradiated samples where the fast neutrons produce 'defect cascades', which consist of highly disordered or even amorphous material in the irreversible range (see Section 6.6 for further info), the $J_c(B,T)$ values obtained from the $M(H)$ hysteresis loops revealed that even though the pinning behavior at low temperatures (< 20 K) is nearly unchanged, for higher temperatures J_c is strongly enhanced by the radiation-induced defects. This is remarkable in superconductors such as Tl2223, where the distance between the copper oxide planes is much larger than in other REBCO materials, as J_c has been seen to increase by a factor of 52 at 40 K and under a 1 T field [201]. However, as the SMP phenomenon occurs in both regimes, hinting at the existence of at least two concomitant pinning mechanisms, one being dominant at low temperatures and the other being present over the entire temperature range but becoming dominant at high temperatures, it has not been possible yet to get a consensus on the actual physical mechanism that leads the occurrence of the SMP. Similarly, in 2011, the effect of Ag^{15+} and Li^{3+} ion irradiation on the SMP and hysteresis behavior of Tl2223 single crystals was studied, from which Singh et al. [202] reported the disappearance of the SMP for high ion fluence, while annealing the samples after irradiation partially recovered it. Therefore, it is speculated that if the SMP and, consequently, the hysteresis loop of cuprate superconductors is affected by the defects formed by the effects of radiation, this 'experimental tool' can give further insight into the possible origin and maybe control of the $J_c(B,T)$ of practical superconductors.

SMP in MgB_2 and IBS compounds

Despite being less common in superconducting materials with low critical temperatures, the second magnetization peak (SMP) phenomenon – also referred to as the fishtail effect – is frequently observed in intermetallic compounds like MgB_2 [203,204]. It typically manifests as a hump in the $J_c(B)$ curve, well below the upper critical fields $H_{c2}(T)$ [205]. More pronounced fishtails have also been found in neutron-irradiated MgB_2 crystals, particularly at low neutron fluences, that extend typically across a large portion of the superconducting phase diagram at higher doses [206]. Even in cases of moderate neutron fluences and moderate levels of carbon substitution, the phenomenon has been reported for MgB_2 single crystals [204]. Notably, the SMP is clearly visible in samples that are both neutron-irradiated and carbon-doped but not in unirradiated C-doped samples. In fact, Zehetmayer et al. [203] demonstrated how neutron irradiation allows for controlled variation of defect density, thereby tuning the birth and development of the SMP. They attributed the appearance of the SMP to an order–disorder transition between a flux lattice dominated by elastic energy and a state dominated by interactions between flux lines and defects. An intriguing SMP has also been reported in an ultra-thin MgB_2 film, with a thickness of 10 nm, deposited using a hybrid physical–chemical vapor deposition technique. This is attributed to the presence of defects, likely at grain-boundary sites, which act as vortex pinning centers. In addition, small peaks commonly known as the 'Peak Effect' occur near $H_{c2}(T)$, and have been already attributed to the occurrence of thermomagnetic instabilities [207]. Yet, the origin of the SMP remains under debate. Still, it is widely accepted that the presence and number of defects which act as flux-pinning centers that become active at high fields play a crucial role in this phenomenon, which is consistent with the effect of local damages observed in neutron-irradiated MgB_2 single crystals [208]. Interestingly, in polycrystalline samples containing embedded carbon nanotubes, analytical fits to magnetization data suggest that the same flux-pinning mechanisms responsible for the SMP in MgB_2 are also at play in YBCO single crystals [209], likely due to lattice defects associated with carbon substitution.

On the other hand, in the case of iron-based superconductors (IBS), the occurrence of the SMP is not a universal phenomenon across the various pnictide families [210]. For instance, a pronounced SMP is generally observed in both hole- and electron-doped Ba-122 compounds, which has been attributed to different mechanisms [211,212]. However, the appearance of the SMP is sensitive to the compositional elements within the 122 IBS family (AFe$_2$As$_2$, A = Ba, Sr, Ca, etc.). For example, in Co-doped Ca-122 compounds, the SMP does not occur [213], while it is generally present in Pt$_n$As$_8$-containing systems [214]. The SMP is also observed in the 1111 (LnFeAsO, Ln = La, Nd, Ce, Sm, etc.) IBS family and has been attributed to an increase in the effectiveness of pinning centers [215]. Similarly, the SMP has also been observed in the 1144 (RAFe$_4$As$_4$, R = Ca, Eu; A = K, Rb) family due to the existence of surface as well as point core pinning of the vortices in the low field regime [216], and in the 11 (FeSe) IBS families due to the vortex–vortex and vortex–defect interactions [217]. Nonetheless, in the 111 family (AFeAs, A = Li, Na, etc.), such as LiFeAs, the SMP is only observed when the magnetic field is applied parallel to the crystallographic *ab*-plane, suggesting that the SMP's origin may be linked to a vortex lattice phase transition [218] in line with what is seen in Ba-122 single crystals [211]. Notably, the SMP disappears in *c*-axis grain-textured Ba-122 polycrystals [219]. More recently, the SMP has been reported in the triclinic iron-pnictide superconductor $(Ca_{0.85}\ La_{0.15})_{10}(Pt_3\ As_8)(Fe_2\ As_2)_5$ [220], with a superconducting transition temperature $T_c \sim 31$ K. This behavior can be explained

by the collective creep theory (discussed in Section 5), involving an elastic-to-plastic vortex creep crossover when the magnetic field is applied parallel to the crystallographic c-axis. However, the SMP for $H \| ab$ seems to be of a different nature, potentially involving a vortex phase transition characteristic of an entangled pinned vortex-liquid. In contrast, simpler 11 IBS crystals like $FeSe_{0.5}Te_{0.5}$ have been found to exhibit a more universal behavior. The SMP onset is triggered by a weak-to-strong pinning crossover occurring in the field region preceding the elastic-to-plastic transition, which corresponds to the maximum in J_c. Remarkably, this crossover appears to be independent of the specific type of pinning centers involved [165].

3.3.3. Blatter's Quasi-mesoscopic models

Due to the rich microstructures (pinning landscapes) and the softness of the vortex matter in HTS cuprates, the J_c anisotropy results to be a very complex subject and, therefore, usually handled only from the macroscopic perspective. However, despite the phenomenological models may allow for an accurate description of many phenomena [71,139], the magneto-anisotropy of J_c can also be approached from a quasi-mesoscopic point of view, with the main features of these models being summarized by the so-called *scaling approach or Blatter's model*, and the consideration of the defects dependence and correlated disorder.

On the one hand, let us remind the work of Blatter, Geshkenbein, and Larkin, who in 1992 developed a method for mapping results obtained for isotropic superconductors onto the anisotropic case [29,221]. That means, instead of solving basic equations for anisotropic superconductors directly, which can be rather complex and tedious, the problem is scaled to the isotropic case, solved, and scaled back. Worth mentioning is that this work builds upon older publications by Kogan and Clem [222] as well as Hao and Clem [223]. The main, general scaling between a quantity Q in the anisotropic case and its equivalent $\tilde{Q}$ in the isotropic case, in which mass anisotropy γ^{-2} and angle θ between uniaxial direction (c-axis for cuprates) and magnetic field[4] are eliminated, is

$$Q\left(\theta, H, T, \xi, \lambda, \epsilon, \gamma'\right) = s_Q \tilde{Q}\left(\epsilon_\theta, H, T/\epsilon, \xi, \lambda, \gamma'/\epsilon\right) . \tag{27}$$

In this expression, ξ and λ are the (in-plane) values for the coherence length and penetration depth of the SC, and γ' is the degree of disorder. Also, the factor s_Q depends on the quantity Q, and what we have called the field prefactor ϵ_θ at Eq. (26) results from no other than the elliptic term of the anisotropic Ginzburg–Landau theory. Thus, shortly after, Kumar et al. [224] and Xu et al. [225,226] showed that indeed the magneto-anisotropy of J_c can be scaled in this way, with $s_{J_c} = 1$, i.e., $J_c(H,\theta) \equiv \tilde{J}_c(\epsilon_\theta H)$. This is surprising at first since J_c is not a thermodynamic quantity within the developed formalism of the scaling model. This implies that these scaling results can be debated regarding their physical background or lack thereof (see e.g., [227]). Nevertheless, one has to keep in mind that pinning, being a force, is an interaction, and both the more or less intrinsic elastic properties of the individual flux lines (or the flux line ensembles as a whole, i.e., the vortex matter) and the extrinsic properties related to the pinning landscape determine the pinning force densities.

Application to anisotropic HTS. Notice that if the anisotropic superconductor is relatively clean microstructurally, i.e., without large densities of extended defects of diameter $> \xi$, or even correlated structures (columnar or planar defects, inter-plane distances $> \xi_c$), the pinning will be predominantly determined by the intrinsic properties of the flux lines, yet be extrinsic of nature since it needs small and random pinning centers (e.g., atomic disorder, small precipitates). In such a case, it is feasible that J_c will scale with the mass anisotropy, as the coherence length along a specific direction x, either along the ab-planes or the c-axis for cuprates, is defined as $\xi_x = \sqrt{-\hbar^2/2m_x^*\alpha}$, with α being a constant with respect to the space variable x, $h = 2\pi\hbar$ is the Planck's constant, and m_x^* is the mass of the superconducting charge-carriers of electric charge $e^* = 2e$ related to Cooper pairs that exist along x. This has been nicely illustrated by Civale et al. [228], see Fig. 11, who showed how to use Blatter scaling to discern regions of random pinning (where the scaling works) from correlated pinning for fields near c-axis (e.g., dislocations and twin boundaries) and for fields near the ab-planes (stacking faults, intrinsic ab-planar pinning).

Blatter's scaling method has been used extensively for a wide variety of samples with artificial pinning centers. Especially for nanocomposite films with perovskite nanoparticles, it has been found that Blatter scaling works in a wide range of medium angles if an 'effective anisotropy' γ_{eff} is introduced. This anisotropy parameter is a field-independent measure of the nanoparticles' ability to reduce the J_c anisotropy (see, e.g., [229]). However, it seems to depend on microstructure, the reason why this scaling method is already used outside the actual applicability range of the theoretical framework. For instance, whereas the H_{c2} anisotropy in nanocomposite films grown by Pulsed Laser Deposition (PLD) is reduced due to dirty-limit scattering [230], which can partially explain the reduced scaling parameter, it is more or less unchanged in films grown by Chemical Solution Deposition (CSD) with large amounts of nanoscale strain-induced pair suppression [231]. In both cases, the anisotropy of the irreversibility field can be described with the scaling parameter γ_{eff} in the relevant angular range, where scaling of J_c is possible.

Application to highly anisotropic HTS. For highly anisotropic superconductors, such as BSCCO, a further extension of the Blatter scaling method has been found by replacing the 3D H_{c2} anisotropy as a scaling function with the Tinkham formula of $H_{c2}(\theta)$ for thin films [232]. Nonetheless, although this leads to a slightly more complicated scaling function for fields not too close to the ab-planes, the 2D scaling remains a good approximation. In this sense, a similar reduction of the anisotropy parameter as often seen in REBCO nanocomposite films related to the pinning landscape ($\gamma_{\text{eff}} = 7$ vs $\gamma \approx 50$) has been found in BSCCO tapes [233]. Also for several classes of IBS compounds, this scaling method has been employed, mostly in order to estimate the electronic anisotropy for microstructurally clean films. However, due to the multiband superconductivity in these materials, the scaling parameter γ

[4] Often, the anisotropy is defined as $\gamma = 1/\epsilon$, and sometimes the angle θ is measured between the applied magnetic field and the ab-plane. The formula for ϵ_θ and other scaling functions have to be adjusted accordingly.

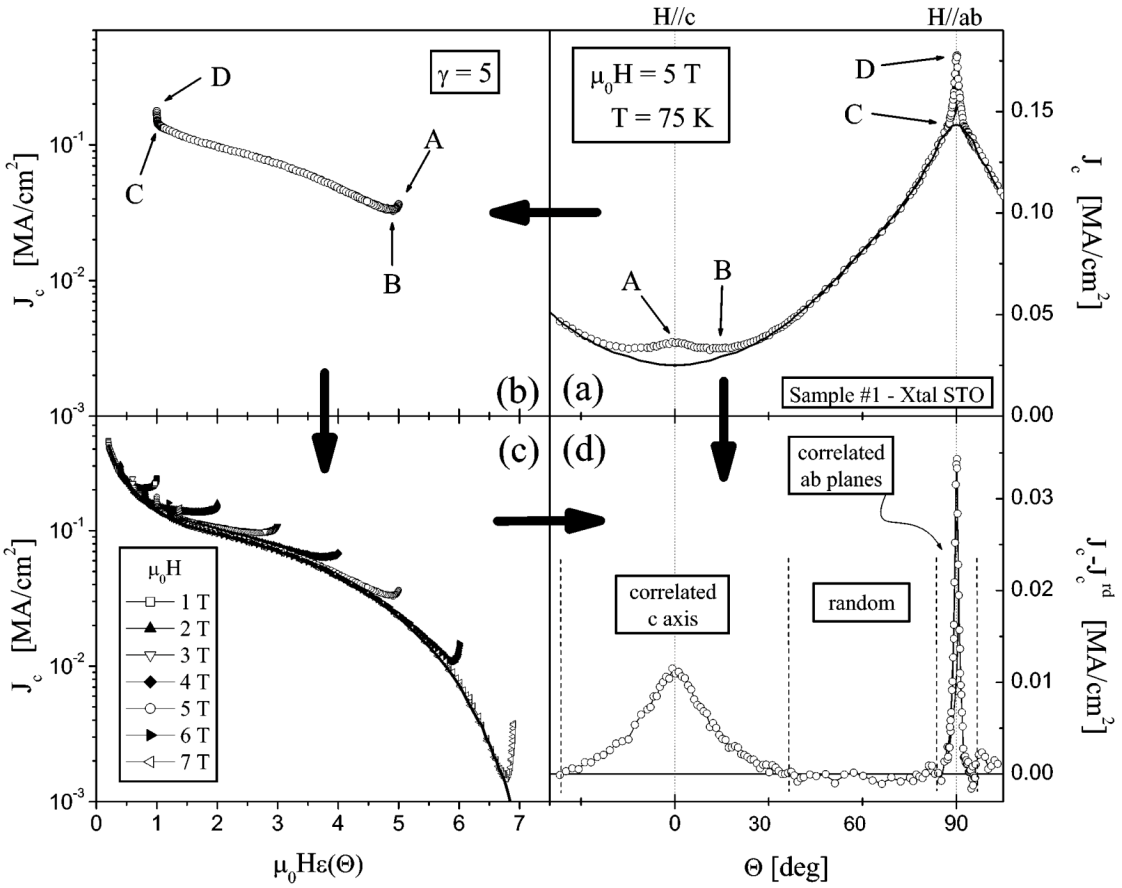

Fig. 11. Anisotropic scaling approach diagram. (a) $J_c(\theta)$ for a YBCO film on single-crystalline STO at $\mu_0 H = 5$ T. The solid line represents J_c^{rd}, as obtained from the anisotropic scaling approach. (b) $J_c(\theta)$ as function of $\tilde{H} = \epsilon_\theta H$ for the same data in Fig. 11(a). A, B, C and D indicates $J_c(\theta)$ for $\theta = 0$, 15°, 85° and 90° respectively. (c) $J_c(\theta)$ as function of $\tilde{H}$ for different fields. The solid line, J_c^{rd}, is obtained in the region where the measurements collapse. (d) Angular dependence of $J_c - J_c^{rd}$ for $\mu_0 H = 5$ T.
Source: Adapted with permission from [228]

is generally temperature dependent [234,235], and sometimes (especially for quasi-2D materials) follows the anisotropy of the penetration depth rather than H_{c2} [137].

Two further extensions of the scaling method may be mentioned here, the first one developed by Matsui et al. [236], who used Blatter's approach for scaling the pinning force density F_p rather than J_c, and in this way explaining the so-called 'dimpling effect', i.e., the disappearance of a *c*-axis peak for higher applied fields. On the other hand, Mishev et al. [237] scaled not only B with ϵ_θ but also J_c by ϵ_θ^{-1} to account for the interaction of the anisotropic vortex cores with extended isotropic defects.

Thus, the advantages of the Blatter scaling method are the connection to a microscopic intrinsic explanation and the low number of fitting/scaling parameters, but its disadvantage is that it often works without proper microscopic backing, which may lead to erroneous interpretations. It is worth mentioning that it is in general not possible to *fit* $J_c(\theta)$ by means of Eq. (26) (just to *scale* it), see, e.g., [238], and in doing so, the fit would always be a mere phenomenological model.

Inclusion of small or extended defects. On the other hand, another point to consider when discussing the mesoscopic scaling approach is that it only considers defects somewhat smaller than the coherence length, i.e., somehow assuming an isotropic atomic disorder. Defects that are slightly larger than the coherence length in at least one direction are called extended defects. They can be (more or less) isotropic in shape and orientation (often modeled as ellipsoids) or have large aspect ratios and be well aligned. The former case is treated below. In the range of single-vortex pinning, i.e., if the vortex–vortex interactions are negligible compared to the interaction between vortex and pinning center, isotropic (i.e., round) extended defects lead to isotropic pinning and hence J_c, since the anisotropies of coherence volume and interaction distance cancel out [47]. However, this is not the case for increased magnetic fields in the regions of collective pinning, which is easily seen by the anisotropy of the irreversibility field. In these regions, isotropic extended defects will also lead to anisotropic pinning. This can manifest in reduced effective anisotropies as described above, but also in shoulders of $J_c(\theta)$ near the *ab*-peak, especially for sparse large isotropic precipitates, or even a pronounced *c*-axis peak. The latter has been shown theoretically by van der Beek et al. [239] for uniaxially anisotropic superconductors by extending the above-mentioned scaling rules to different anisotropies in ξ and λ, as it is typical for multiband superconductors.

Thus, depending on the size (and shape) of the precipitates, minima or maxima of J_c near $B \parallel c$ are found. An interesting side result of this analysis is that the J_c anisotropy ratio of currents flowing perpendicular and parallel to the c-axis, while the magnetic field is applied perpendicular to the c-axis in both cases, yields directly the anisotropy of the coherence length and even its possible field dependence. This theory has been extended later to different field regimes (small bundles, large bundles) by Li et al. [240].

Correlated disorder. Finally, regarding correlated disorder, i.e., highly parallel 1-dimensional or 2-dimensional pinning structures such as: (*i*) nanocolumnar precipitates, dislocations, twin boundaries, anti-phase boundaries parallel to the c-axis, (*ii*) stacking faults, i.e., extra or missing CuO planes, or the layered crystal structure itself with parallel ab-planes (intrinsic pinning), and (*iii*) irradiation tracks in any direction; the pinning properties of these defects with significant peaks for fields parallel to them have been described also by Blatter et al. [29]. These defects lead in general to strong matching effects for field strengths roughly matching the mean defect density, which can be observed by changes in the exponent n of the $V(I)$ curves (i.e., at the $\mathbf{E}-\mathbf{J}$ power law) due to changes in the creep behavior (see e.g., [135,241,242]). Thus, for highly anisotropic superconductors with strong intrinsic ab-planar pinning, such as BSCCO, $\gamma \gg 1$ and the sinusoidal term in ϵ_θ (Eq. (26)) can be disregarded. This leads to the older stair-case model of Tachiki and Takahashi [243] of strongly pinned components parallel to ab, and the relevant weakly pinned components parallel to c, i.e., a cosine dependence of J_c with field angle.

In conclusion, even though these models are based on scaling rules and microscopic considerations, they are not easily applicable to real J_c anisotropy curves in a wide range of angles. This is simply due to the manifold of different defects in real samples (e.g., coated conductors [33]) and their synergistic effects so that the contribution of a particular defect species is often not easily recognized. Therefore, statistical and phenomenological models have been developed to describe the $J_c(B,\theta)$ anisotropy, as they will be presented below.

3.3.4. The maximum entropy or statistical models

Although the fundamental understanding of J_c can be based on microscopic and mesoscopic considerations as described by the previous models, it is also possible to start from the macroscopic observations of J_c's anisotropy, and treat it as an outcome of the behavior of a large ensemble of vortices. This has been developed by N.J. Long in the so-called Maximum Entropy model, also known as the Vortex Path model [244,245], where instead of asking 'Which force is needed to move a vortex?,' the proposed question is 'What is the probability for a vortex to be pinned?' Within this approach, the vortices can be modeled as elastic strings threading through the superconductor in global alignment with the macroscopic field direction. Thus, they will preferentially align themselves with pre-existing non-superconducting regions (e.g., material defects) so as to lower the total free energy of the system, while keeping aligned with the field in the average. This preferential alignment with a non-superconducting region is what is termed 'pinning' within this model. Thus, lacking a reliable methodology to sum the effects of all the defects distributed throughout a material for finding the flux pinning force per unit volume, by adopting a maximum entropy approach, Long managed to model J_c while avoiding the need to construct a model of $\mathbf{F}_p$ [246].

In the most simple scenario, Long found that for systems of orthogonal 1D pinning centers where each pinned vortex i must be stationary over the total pinned lengths y_i and z_i, with the macroscopic angle at which the vortex is pinned satisfying $z_i/y_i = \cot(\theta_i)$, it is possible to consider its mean value $\langle z/y\rangle = \langle\cot(\bar{\theta})\rangle$ as the most relevant constraint rather than the summation of pinned vortex segments. Thus, in combination with certain constraints (e.g., $J_c(\bar{\theta})$ periodic in 2π), two maximum entropy functions were introduced, one for a Gaussian distribution of pinning lengths:

$$J_c(\bar{\theta}) = \frac{J_0}{\sqrt{2\pi}\sigma\sin^2(\bar{\theta})}\exp\left(-\frac{1}{2\sigma^2\tan^2(\bar{\theta})}\right), \tag{28}$$

and another for a Lorentzian distribution,

$$J_c(\bar{\theta}) = \frac{1}{\pi}\frac{J_0\gamma}{\cos^2(\bar{\theta})+\gamma^2\sin^2(\bar{\theta})}. \tag{29}$$

In this approach, the prefactor J_0 and the width parameters σ and γ yield all information about the microstructure of the material.

On the one hand, it is to be noticed that Eq. (29) is an elliptic function that resembles the scaling function of Blatter's model. On the other hand, if there are no constraints, Eq. (29) leads to a uniform distribution $J_c(\theta) = J_0/\pi$ for isotropic materials ($\gamma = 1$), providing a straightforward solution for LTS rounded wires where such an angular dependence is a trivial result. For interpretation of the results, one has to keep in mind that in general all pinning center species contribute to all pinning contributions to different amounts. Furthermore, in most cases, there is indeed a contribution of constant J_c, the isotropic pinning contribution. This should not be mixed up with the isotropic pinning centers of the Blatter scaling approach (random pinning), which give an anisotropic pinning contribution due to the mass anisotropy ratio.

Remarkably, for REBCO materials, such as YBCO, Knibbe et al. [247] have shown that the full J_c anisotropy curve can indeed be described by the summation of the above functions, namely one per distinct pinning center species in the pinning landscape with angular offsets for the respective J_c maximum position. Thus, the isotropic pinning contribution of the Maximum Entropy model $J_c(\theta) = J_0/\pi$ can have different reasons, e.g., the superposition of similar angular functions with π shift due to small and extended isotropic defects. Similarly, Wimbush and Long [245] pointed out that the possibility of scaling J_c in samples with extended defects with an effective anisotropy γ_{eff} can be related to a Lorentzian distribution and may therefore be a stretch of the theory. Nevertheless, it is often used because its γ_{eff} yields a field-independent anisotropy parameter in contrast to the parameters of the Maximum Entropy model, let alone the ratio $J_c(B\|ab)/J_c(B\|c)$, which even diverges for $B \sim B_{\mathrm{irr}}^{\|c}$.

Finally, it should be noted that the same considerations made about the maximum entropy model can also be applied to the temperature and field dependencies of J_c as shown in [246]. Therefore, in recent years several groups have successfully used

the Maximum Entropy model on different cuprate nanocomposite films, either deposited on single crystals [248,249] or technical substrates [250,251], to explain non-intuitive experimental observations such as peaks in the critical current at angles which are intermediate between the known correlated defect directions. Nevertheless, although these statistical models can describe the J_c anisotropy of complex superconductors very well and in the full angular range, occasionally, their aggregated cost is the need to deal with a relatively large number of fitting parameters to model the behavior of the ensemble of vortices.

3.3.5. Semi-empirical $J_c(B,\theta)$ models

For simulations and magnet design with CCs, often good fitting functions for the J_c anisotropy exist, preferably derived with a few open parameters yet with sufficient accuracy to describe the local or global behavior of the superconducting tapes in the field-temperature-orientation environment of the intended application. Often, these models combine an elliptical angular dependence (inspired by the Anisotropic Ginzburg–Landau scaling) with a semi-empirical field dependence. The latter can be seen as a modified Anderson-Kim function for REBCO thin films, i.e., a power law with an off-set field and exponent not necessarily equal to −1 (see Eq. (25)), which leads to [252–255]

$$J_c(B,\theta) = J_{c0}\left[1+\epsilon_\theta\left(\frac{B}{B_0}\right)\right]^{-\beta}. \tag{30}$$

This function, which has been initially adapted by Leys et al. [255] for the sole case of SuNAM tapes [256] to

$$J_c(B,\theta) = J_{c0}\left[1+\epsilon_\theta^{\alpha}\left(\frac{B}{B_0}\right)^{\beta}\right]^{-1}, \tag{31}$$

has been generalized by Zhang et al. [141] to incorporate a wide range of 2G-HTS tapes manufactured by different companies. This is a semi-empirical but general model for the CC, in the sense that the authors have built a minimization algorithm capable to find the lowest level of 'free' parameters in a univocal function modeling the magneto-angular anisotropy of multiple 2G-HTS tapes. Thus, up to date [140,141], it has been found that the same function,

$$J_c(B,\theta) = J_{c0}\left[1+\epsilon_\theta\left(\frac{B}{B_0}\right)^{\alpha}\right]^{-\beta}, \tag{32}$$

is capable of modeling 2G-HTS tapes as diverse as the ones fabricated by SuNAM [256], SuperPower Inc., [257], American Superconductor [258], Shanghai Superconductor Technology [259], and SuperOx [260].

Thus, in contrast with the original phenomenological model of Kim for isotropic LTS, i.e., with the mass anisotropy $\gamma^{-2}=1$ (see Eq. (25) and Eq. (26)), relatively smooth single-peaked anisotropy curves seem to require at least one additional fitting parameter, referred here as the field exponent α. Likewise, it should be stressed that the anisotropy ratio γ is usually larger than the intrinsic anisotropy considered in Blatter's scaling model, as this only considers random pinning, whilst in the phenomenological approaches the correlated pinning (usually parallel to *ab*) is taken into the fits.

A similar but slightly more complex generalization was introduced by Hu et al. for rather complex and asymmetric anisotropies with several pinning components [261]:

$$J_c(B,\theta) = J_{c0}\left[1+\sqrt{v^2\cos^2\theta+u^2\sin^2\theta}\left(\frac{B}{B_0}\right)\right]^{-\beta}, \tag{33}$$

where u and v are both trigonometric, polynomial, and/or exponential functions of B and θ.

On the other hand, similar to the Gaussian distribution of pinning lengths derived from the Maximum Entropy model, for a restricted angular range, exponential functions on field and/or angle have been proposed either based on the percolation model [262],

$$J_c(B,\theta) = J_{c0}\left\{\delta+\exp\left[-\epsilon_\theta^{\alpha}\left(\frac{B}{B_0}\right)\right]\right\}^{-1}, \tag{34}$$

or based on the magnetization modeling of LTS wires [255],

$$J_c(B,\theta) = J_{c0}\exp\left[\lambda-\epsilon_\theta^{\alpha}\left(\frac{B}{B_0}\right)^{\beta}\right], \tag{35}$$

where J_{c0}, B_0, and δ (or λ) are physical fit parameters extracted from electrical transport measurements, and α and β are two mathematical fit parameters.

Likewise, to some extent related to the Lorentzian form of the Maximum Entropy model, a relatively often-used phenomenological model for cuprates was introduced by Hilton et al. [253]. The relevance of this model is that instead of adding mathematical fitting parameters for single-peak anisotropy cases, this model incorporates simple threshold values for the individual components of J_c when **B** is parallel or perpendicular to the *c*-axis, such that the anisotropy parameter ϵ_θ is governed by the relation

$$\frac{J_c(B,\theta)-J_{c0}(B\parallel c)}{J_{c0}(B\parallel ab)-J_{c0}(B\parallel c)} = \left[\frac{\epsilon_\theta^{-1}-1}{\gamma-1}\right], \tag{36}$$

with γ being called the peak sharpness parameter, not to be confused with the mass anisotropy ratio in Eq. (26), as this is indeed just a physical fit parameter. Then, fitting multiple peaks requires Eq. (36) to become a term in a scaled summation, with each peak represented by a term, and each term angularly shifted to its corresponding field angle.

3.3.6. Temperature dependent models

The temperature dependence of the critical current density, $J_c(T)$, at a certain field strength and direction (B,θ), can be used to clarify which kind and mechanism of pinning (or more general J_c limitation) is prevalent. Theoretically, the phenomenological theory of Ginzburg and Landau [263] could be used to determine the critical current and critical fields for any type II superconductor at temperatures relatively close to T_c, as long as the dimensions of the samples are smaller than the coherence length, ξ, so that changes in the energy gap within the reciprocal space may be neglected. However, for the majority of HTS materials (cuprates), not only Δ has been found to be a function of the angular components of the electronic states ($\mathbf{k}$) in the reciprocal space [264–266], but also their coherence length (typically of the order of a few nanometers), is too small to allow a direct measurement of J_c that could be free of macroscopic effects such as those related to artificial pinning elements not bonded to the electronic coupling mechanism. Nonetheless, if the path on which the current flows across a superconducting sample, let us say a superconducting bridge of width d and thickness h, is such that their dimensions are comparable with the London's penetration depth, λ, it would be expected that a DC current will distribute homogeneously once the transport current reaches J_c. In this sense, at this scale of measuring, our previously developed macroscopic definitions for J_c in Section 2, where the flux pinning theory was inherently ascribed to its magneto-angular dependence $J_c(B,\theta)$, becomes a most fundamental definition for the critical current, commonly called the depairing current, J_{dp}, from which the actual dependence of J_c on temperature can be analyzed.

Thus, self-field transport measurements on nanobridges with widths smaller than the penetration depth [267], have often been used to estimate the Ginzburg–Landau depairing critical current density,

$$J_{dp}(T) = \Phi_0/3\sqrt{3}\pi\mu_0\lambda^2(T)\xi(T) \tag{37}$$

under the consideration that vortices are not able to enter such small structures of a superconductor. In fact, by inserting the usual temperature dependence of the Ginzburg–Landau parameters, $\lambda(t) \propto \lambda(0)/\left(1-t_c^4\right)^{1/2}$, and $\xi(t_c) \propto \xi(0)/\left(1-t_c\right)^{1/2}$, it was already known by the seminal work of Bardeen [268], that Eq. (37) could be written as a function of the normalized temperature $t_c = T/T_c$ as,

$$J_c(T) = J_{dp}(0)\left(1-t_c^2\right)^{3/2} \tag{38}$$

for the whole temperature range. Nonetheless, good care must be taken in such measurements to avoid any spurious magnetic fields (vortices) and heating effects, especially at low temperatures, as low-temperature deviations from the GL dependence are known to lead to critical currents with temperature dependence of the form,

$$J_c(T) = J_{dp}(0)\left(1-t_c^2\right)^{3/2}\left(1+t_c^2\right)^{1/2}, \tag{39}$$

as introduced by Kupriyanov and Lukichev [269], which near T_c can be reduced to,

$$J_c(T) = 4J_{dp}(0)\left(1-t_c\right)^{3/2}, \tag{40}$$

where the prefactor 4 is sometimes omitted to form the widely adopted phenomenological formula

$$J_c(T) = J_c(0)\left(1-t_c\right)^{n} \tag{41}$$

with n ranging from $n = 1$ to 5/2 [96,270]. This relation seems to hold also for magnetization-derived zero-field $J_c(T)$ data, i.e. calculated from the remanent state. Albrecht et al. found indeed two distinct $J_c(T)$ dependencies according to Eq. (41) for YBCO films with different degrees of disorder. Near T_c, the dependence is linear ($n = 1$), whereas at low temperatures, n is around 1.5. This was explained by J_c depending on the depth of the pinning potential U_0 at high temperatures but rather on the shape of the pinning potential at low temperatures for sufficiently small fields [271].

In contrast, Talantsev et al. [272] recently pointed out that the transport self-field J_c of microbridges in thin-film samples with a thickness of the order of λ is determined by the lower critical field via $J_c^{sf} = H_{c1}/\lambda$, which is a further development of general ideas proposed by Silsbee [273,274] and the London brothers [275]. This resulted in what is possibly a universal expression valid for all superconducting metals, oxides, cuprates, pnictides, borocarbides and heavy Fermions:

$$J_c^{sf}(T) = \frac{\Phi_0}{4\pi\mu_0\lambda^3(T)}\left(\ln\kappa(T) + 0.5\right). \tag{42}$$

This result, in its simplest form, is independent of geometry and pinning properties, and it also depends only on fundamental properties of the superconductor, such as the GL parameter, $\kappa(T) = \lambda(T)/\xi(T)$, yet its nature is completely empirical and in this sense differs from the depairing J_c above discussed. However, this model has been extended by taking into account geometric effects and anisotropy [272,276] as well as different order parameter symmetries [277].

The role of vortex pinning.

Whether Eq. (42) should be considered as a lower bound for J_c, and the extent to which strong single-vortex pinning contributes once vortices form in the sample, remains a topic of debate and ongoing investigation.

On the other hand, for finite yet sufficiently small applied magnetic fields, fulfilling the condition $B_{appl} \lesssim B_{c2}(T \approx T_c)$, the temperature dependence of J_c can be used to distinguish between the vortex pinning resulting from lattice defects of spatial variations in the mean free path of charge carriers, δl, or from variations in the GL coefficient associated with fluctuations of the critical temperature, δT_c. Thus, from the collective pinning theory, it has been shown [278] that these temperature dependencies are generally described by the relationships,

$$J_c(t) = J_c(0)\left(1-t_c^2\right)^{5/2}\left(1+t_c^2\right)^{-1/2}, \tag{43}$$

for δl pinning, and

$$J_c(t_c) = J_c(0)\left(1-t_c^2\right)^{7/6}\left(1+t_c^2\right)^{5/6} \tag{44}$$

for δT_c pinning, where for low-temperature superconductors, it generally results easier to distinguish experimentally whether the dominant pinning mechanism is δl or δT_c [29].

However, for high-temperature superconductors or, in general, superconductors with large fluctuation ranges, the distinction between the δl and δT_c pinning is probably not as well-founded since any defect lowering the mean free path l can be pair-breaking and hence decreasing T_c. Conversely, regions of lower T_c may influence λ and ξ. Furthermore, creep-corrected J_c data should be actually used for reliable analyses [279]. Nevertheless, it is applied occasionally without losing too much of generality. Especially, Griessen et al. [278] have shown that in stoichiometric YBCO samples, δl pinning is dominant. However, also δT_c pinning could be shown for (Pr-doped) YBCO samples if the measured current density is enhanced by the substitution of Y with Pr [280].

For higher applied magnetic fields and for temperatures sufficiently far away from the irreversibility line, the temperature dependence of J_c is used to distinguish between weak and strong pinning. In weak collective pinning,[5] the interaction of a vortex with a multitude of pinning centers is necessary to have a net pinning effect, whereas in principle one strong pinning center is sufficient to immobilize the vortex up to a certain driving force. In these cases, the temperature dependencies are commonly defined by:

$$J_c^{wk}(t) = J_c^{wk}(0)\exp\left[-\left(\frac{T}{T_0^{wk}}\right)\right] \tag{45}$$

for weak pinning materials [29], and

$$J_c^{str}(t) = J_c^{str}(0)\exp\left[-3\left(\frac{T}{T_0^{str}}\right)^2\right] \tag{46}$$

for strong pinning [281], with $k_B T_0^{wk}$ and $k_B T_0^{str}$ are certain field-dependent energy scales for the weak and strong pinning mechanisms, respectively. Whilst Eq. (45) is based on the collective pinning theory [221], Eq. (46) is based on the theory of Bose glass due to correlated [281] or splayed [282] columnar defects, as found for irradiated BSCCO films [283,284] in the middle 1990s. In following years, it was transferred with somewhat less theoretical backup to interfaces [285], i.e., more or less correlated planar disorder, and finally to any strong-pinning disorder such as oxide [286,287] and perovskite [288] nanoparticles. In this context, the combination of Eq. (45) and Eq. (46) is used to classify and compare samples in regards to their respective weak and strong pinning contributions, where usually the energy scales and prefactors are not analyzed in detail [287,289][288].

Thus, despite the cause for the temperature dependence of J_c is still subject to debate, and the fact that it seems to generally depend on the GL parameter for diverse materials, one can conclude that if phenomenological functions for fitting the $J_c(T)$ data are needed, it is possible to use the function:

$$J_c(T) = J_0\left(1-t_c^2\right)^{\alpha}\left(1+t_c^2\right)^{\beta}, \tag{47}$$

for the whole temperature range, which near T_c and for low magnetic fields can be simply written as

$$J_c(T) = J_0\left(1-t_c\right)^{\alpha}, \tag{48}$$

or for higher fields and sufficiently low temperatures by,

$$J_c(T) = J_0\exp\left[\left(1-t_c\right)^{\alpha}\right], \tag{49}$$

with α and β being exponents tailored to the experimental observations.

4. J_c and the flux-flow instability regimes

While much attention has been paid to the low-temperature part of the superconducting transition at intense currents, especially in regards to the critical current as a measure of the onset of dissipation, the transition into the normal state has been commonly considered only for low current densities. However, for applications of HTS, such as fault current limiters that drive the material into the normal state, detailed knowledge of the upper part of the superconducting transition at high power dissipation would be helpful. Similarly, applications where high transport currents and intense magnetic fields are required, such as the magnets demanded by the fusion energy sector, require further knowledge on the onset of dissipation and the vortex dynamics at high velocities, where the understanding of non-equilibrium regimes near J_c is of practical interest [29,31,290].

In fact, if, as discussed in Section 2, the macroscopic elements of current density within a superconductor can be treated as a distribution of finite currents whose self and mutual magnetic induction is capable of creating a large Lorentz-type force between the associated vortices, then such force can accelerate the vortices to high velocities, making this scenario accessible to a rich palette of non-equilibrium phenomena [290]. These phenomena include flux-flow instabilities [291–302], crystallization of the vortex lattice [303], the formation of hot domains, and thermal runaway effects [304], of which the flux-flow instability (FFI)

[5] This does not exclude single vortex pinning at low fields.

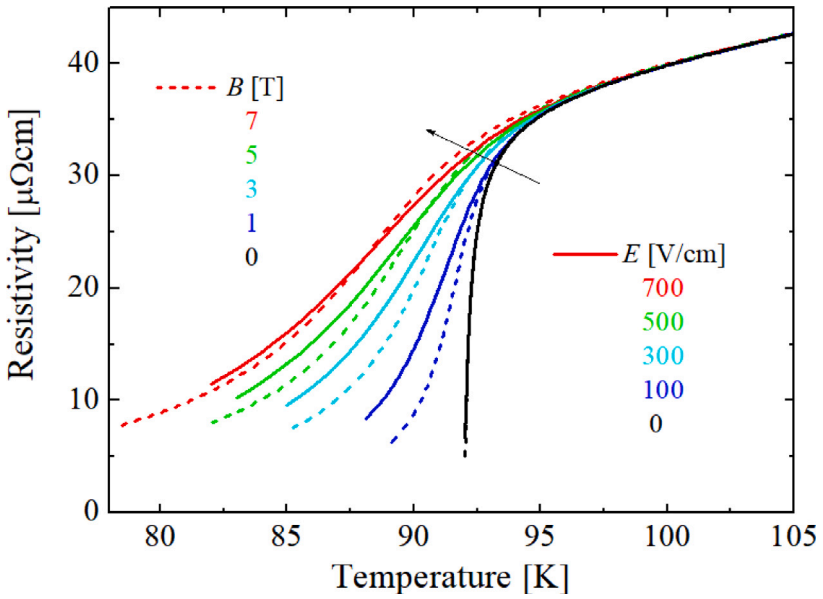

Fig. 12. Calculation of the superconducting transition of YBCO in zero magnetic field at different electric fields (lines). For comparison, the transition in a magnetic field but in the limit of vanishing electric fields, calculated according to [308], is shown (dotted lines).
Source: Adapted with permission from [309]

phenomenon is the one that probably offers a better insight into the intrinsic nature of J_c. This is particularly true when the superconductor is subjected to transport current densities near the self-field critical current density J_c^{sf}, and either under strong electrical fields or magnetic fields, as discussed below. As it will be discussed, the consideration of these phenomena will require to go microscopic in the models, at least to some minimum extent.

4.1. Fluctuations at high current density and strong electric fields

Let us start with a brief review of the theoretical predictions in this situation. As is well known, a pronounced rounding characterizes the transition to the normal state of HTS cuprates due to the emergence of superconducting fluctuations [305,306]. The layered crystal structures and the small Ginzburg–Landau coherence lengths in-plane, ξ_{ab}, and out-of-plane, ξ_c, with the resulting tiny coherence volume lead to tremendous superconducting order-parameter fluctuations that can extend far beyond T_c [307]. On the other hand, related to the low carrier mobility in HTS materials, the normal state behaves ohmic even in intense electric fields. In contrast, the lifetime of superconducting fluctuations is gradually reduced at higher electric fields. Thus, in order to understand the upper part of the superconducting transition, one must evaluate the non-ohmic behavior of superconducting fluctuations.

The theoretical investigations of superconducting fluctuations began with the work of Aslamazov and Larkin [310], who calculated the fluctuation-induced electrical conductivity in the vicinity of the transition temperature, a measure also known as paraconductivity or excess conductivity, for isotropic materials in the absence of a magnetic field in the limiting case of vanishing electric fields. An essential extension of this theory, relevant to HTS materials, is the Lawrence–Doniach model [311] of two-dimensional layered superconductors. However, these theories are valid only at some 'distance' from T_c since they do not consider the fluctuations' interactions. Analytically, this means that the Gaussian approximation of the time-dependent Ginzburg–Landau (TDGL) theory is used, i.e., the quartic term in the free energy is neglected [312]. Then, in order to estimate the fluctuations in the critical region very close to T_c, the Hartree approximation for a self-consistent treatment of the quartic term in the GL free-energy expansion has been applied [308], and the Landau quantization in a magnetic field has been considered [313,314]. Only with such extensions can the contributions of superconducting fluctuations to the electric transport indeed be calculated. In fact, these theories allow a satisfactory phenomenological description of the smooth transition from the fluctuation region above T_c, to the vortex liquid regime in magnetic fields below T_c.

Most work on superconducting fluctuations, both theoretical and experimental, has been done in the linear response approximation of weak electric fields that do not perturb the fluctuation spectrum. By contrast, the paired charge carriers created where a thermodynamic fluctuation occurs are rapidly accelerated in high electric fields. Consequently, they leave this area before decaying thermodynamically, thus reducing the lifetime of the fluctuations. In experiments, this effect manifests itself in a nonlinear current–voltage characteristic of the normal-state resistivity near the superconducting transition, which has been studied theoretically for conventional superconductors [315,316], and likewise confirmed experimentally [317,318]. In fact, the theory has been extended to arbitrary electric fields in layered superconductors in zero [319] and in finite applied magnetic fields [320], and generalized to the case of arbitrary dimensions in the Gaussian approximation of the TDGL theory [321]. Moreover, as the inclusion of the

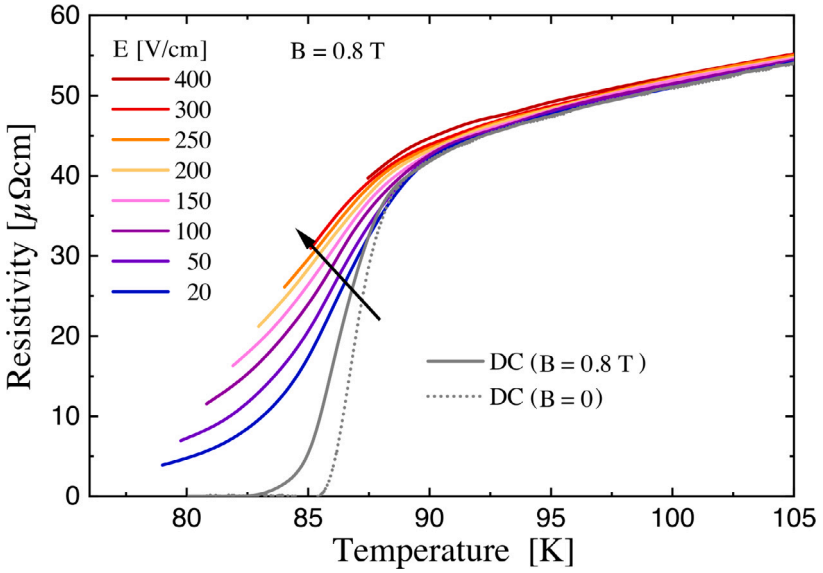

Fig. 13. Resistivity of a YBCO film at increasing electric fields (indicated by the arrow) in a magnetic field of 0.8 T oriented perpendicular to the surface. The resistivity measured at a low DC current is also shown for $B = 0.8$ T (solid gray line) and at $B = 0$ T (dotted gray line).
Source: Adapted with permission from [325].

Hartree approximation of the quartic term of the TDGL equation allowed the exploration of the temperature region very close to T_c in isotropic superconductors [322], the situation most relevant to HTS cuprates has been the solution of the TDGL equation in the Lawrence–Doniach model of layered superconductors at arbitrary electric fields, in zero [309] and finite applied magnetic fields [323,324].

The influence of high electric fields on the superconducting transition of HTS materials is illustrated in Fig. 12, where commonly used parameters for the calculations are namely for a YBCO sample with a measured $T_c = 92$ K at zero magnetic and zero electric fields [309]: the interlayer spacing, $s = 1.17$ nm; the in-plane and out-of-plane coherence lengths at zero temperature, $\xi_{ab}(0) = 1.2$ nm and $\xi_c(0) = 0.14$ nm, respectively; and the GL parameter $\kappa = 70$. In this case, as it can be seen, high electric fields led to a substantial increase of resistivity at the superconducting transition due to the suppression of the fluctuation paraconductivity. The effect bears similarities to the broadening of the transition by a magnetic field as it will be seen in the following section. Nonetheless, experimental verification of the theories mentioned above is not an easy task.

High-current suppression of superconducting fluctuations has also been proposed as a possible source of high-frequency radiation generation by exploiting a negative differential resistance regime [326]. Early experiments have at least pointed to nonlinear behavior of the resistance of TBCCO thin films [327], YBCO single crystals [328], and Bi2212 whiskers [329] near the superconducting transition, studied by DC measurements and at moderate current densities. Exploring the transition to the normal state at high electric fields and corresponding high current densities inevitably leads to enormous dissipation. For example, a typical critical current density of $J_c \sim 3$ MA/cm^2 at 77 K in YBCO thin films can lead to a power dissipation of about 500 MW/cm^3 in the normal state at 100 K. Only by using very short current excitation pulses and by establishing a fast phonon escape time from the HTS film to the substrate is it possible to explore the full superconducting transition at intense currents [330–332].

Thus, although the experimental data are collected at constant current densities, it can be converted to curves of constant electric fields as shown in Fig. 13, where a 50 nm-thin YBCO film has been measured with 3.5 μs-long current pulses [325]. Note that this kind of data representation inherently limits the accessible temperature range at high electric fields since they cannot be obtained even at huge current densities when the resistance is small at lower temperatures. Likewise, measurements at zero magnetic field are practically impossible at such high current densities because of their indispensable self-fields. So, a moderate magnetic field $B = 0.8\ T$ has been used. Nonetheless, the significant non-ohmic behavior at a fixed temperature is definitely visible and supports the theoretical predictions, where a qualitatively similar behavior has also been reported for Bi2202 and Bi2212 thin films [331].

Finally, it is worth mentioning that the reductions of superconducting fluctuations by a magnetic and an electric field acting together are not simply additive, which could be an essential point for the simulation of the quenching of superconducting solenoids. Moreover, it should be noted that the theoretical calculations require the electric field as an input parameter. Nevertheless, it can be seen that when an HTS cuprate transits from the superconducting into the normal conducting state due to super-critical currents, the electric field increases rapidly, driving the transition curves to change according to Figs. 12 and 13. This means that the resistance increases even faster than suggested by the thermal models, which are commonly based on the transition curves measured at small electric fields. Quite significantly, at high magnetic fields, the additional influence of a strong electric field becomes much weaker [323].

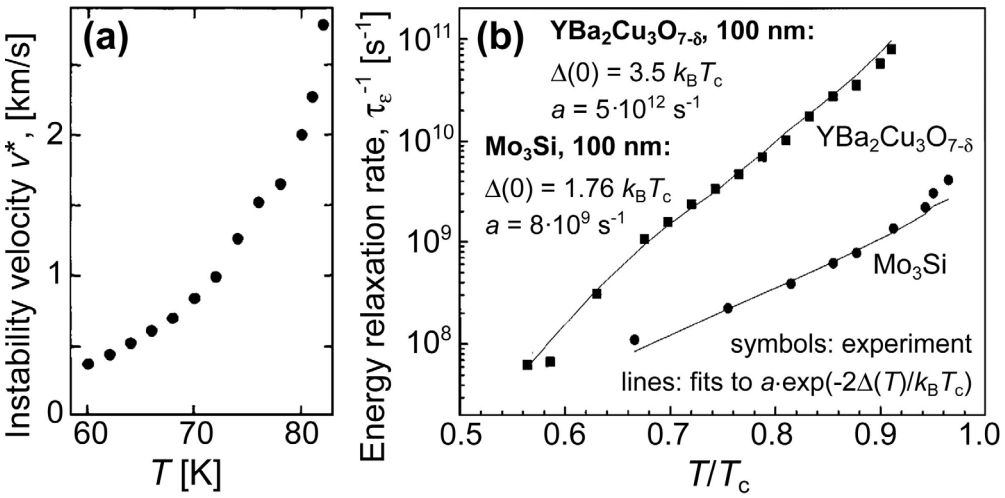

Fig. 14. (a) Instability velocity vs temperature for a c-axis oriented epitaxial $YBa_2Cu_3O_{7-\delta}$ film. (b) Quasiparticle energy relaxation rate τ_ε^{-1} plotted logarithmically versus the normalized temperature $t_c = T/T_c$ for $YBa_2Cu_3O_{7-\delta}$ and a-Mo_3Si films.
Source: Adapted with permission from [295].

4.2. Non-equilibrium effects at large transport currents and magnetic fields

A particularly interesting regime for superconducting applications under external magnetic fields is the regime of large transport currents [333], where flux-flow instabilities leading to discontinuous jumps in the current–voltage characteristics of the HTS material might appear [334]. In this sense, the quench of superconductivity at intense currents has been the subject of extensive studies, from which we could start by mentioning some of the seminal works for epitaxial [293,294,296,335], vicinal [336] and He ion-irradiated [337] YBCO films, as well as on BSCCO [298,338], LSCO [295], $Nd_{2-x}Ce_xCuO_y$ [339–341], MgB_2 films [342], and the more recent studies on YBCO nanowires [343,344] and IBS compounds [345,346].

Starting with the FFI context, i.e., where the energy relaxation rate of quasiparticles (unpaired electrons) plays a central role [347–350], the maximal vortex velocity v^*, also called the *instability velocity*, is the parameter that sets the actual current limit above which the superconductor (or part of it) transits to a highly resistive state. Thus, at the corresponding instability current I^*, the current–voltage characteristic of the HTS materials exhibits a discontinuous jump, which occurs as a consequence of the FFI. However, similar to the attained macroscopic definitions of J_c, or even for the intrinsically related but more fundamental J_{dp}, the v^* and I^* values also depend on external conditions such as temperature and magnetic field. Nonetheless, these are considerably more influenced by the operation regime with which the transport current properties of the HTS are measured (voltage-driven or driven by steady, fast-sweep, pulsed, high-frequency current), and by other extrinsic factors such as the conduit geometry and the thermal contact with the cooling medium, what poses significant difficulties on understanding the actual effect of the FFI on $J_c(B,\theta)$ at high transport currents, and for the whole range of temperatures.

On the one hand, the typical temperature dependence of the instability velocity $v^*(T)$ in HTS films is shown in Fig. 14(a) for YBCO, generally showing a growing tendency as the temperature increases. On the other hand, concerning energy relaxation, it can be mediated by a scattering process with a phonon [351], changing the quasiparticle excitation energy, or by a recombination process halving the number of quasiparticles and transferring the excess quasiparticle energy to an emitted phonon [333]. For instance, in many HTS films the relaxation rate shows an exponential decrease with decreasing temperature, with the relaxation time reaching a value of around 10^{-8} s at $T_c/2$ for YBCO (see Fig. 14(b)) and 10^{-10} s for LSCO [295]. However, when talking about the FFI, one has to distinguish between the high-temperature ($T \approx T_c$) and low-temperature ($T \ll T_c$) regimes, together with the impact of the magneto-angular anisotropy $J_c(B,\theta)$ on such phenomena, as it will be discussed below.

4.2.1. Flux-flow instabilities near T_c

Close to the superconducting transition temperature T_c, the FFI is described within the framework of the Larkin and Ovchinnikov (LO) theory [291,292], whose central point is illustrated in Fig. 15(a). At high vortex velocities, the quasiparticles within the vortex core (whose diameter is $\simeq 2\xi$) are accelerated toward the core boundary, where they undergo Andreev reflections and alternate between electrons and holes. As a result, their energy increases and they eventually escape from the vortex core. The quasiparticle relaxation outside the vortex core causes a retarded recovery of the superconducting order parameter. As a result of the quasiparticle escape, the vortex core shrinks, and the vortex viscosity, also called vortex drag coefficient, $\eta(v) = \eta(0)/[1 + (v/v^*)^2]$ diminishes with the vortex velocity v. The damping force ηv becomes a non-monotonic function of the velocity, with a maximum at a critical (instability) value v^*. Above this critical velocity, ηv decreases, leading to an even further increase of the vortex velocity, causing an instability in the vortex motion.

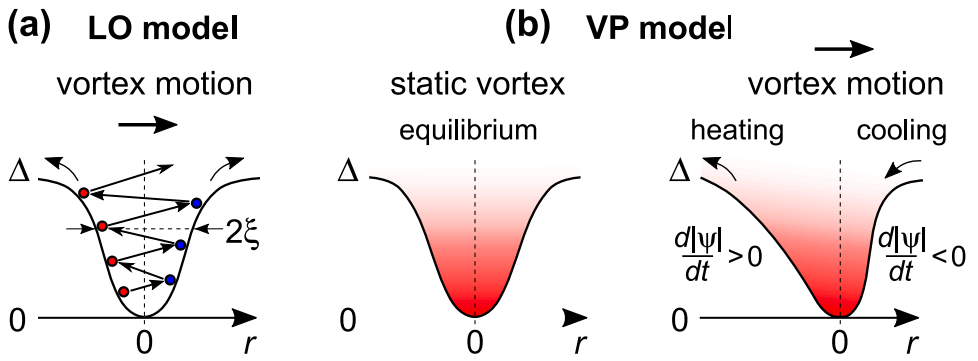

Fig. 15. Schematics of the vortex core shapes in the LO [291] and VP [352] models assuming spatially uniform and nonuniform nonequilibrium quasiparticle distributions, respectively. (a) The electric field generated by fast vortex motion raises the energy of the quasiparticles trapped in the core. During this process, the particle character alternates between electron-like and hole-like due to Andreev reflections. The vortex core shrinks as a consequence of the quasiparticle escape. (b) Deformation of the vortex core due to vortex motion. The color depth indicates the density of the quasiparticles. In case the quasiparticle diffusion length is smaller than ξ, diffusion of the quasiparticles is not strong and locally there is an effective cooling and heating of the quasiparticles.
Source: Adapted with permission from [334].

An alternative view on the moving vortex at high velocities in which it loses the assumed shape of a rigid cylinder was suggested by Vodolazov and Peeters (VP) [352], who argued that quasiparticles are primarily localized in the region where the time derivative of the superconducting order parameter $\partial|\psi|/\partial t$ is finite, i.e. only near the moving vortex core (see Fig. 15(b)). Effectively, this can be viewed as a "cooling" of the quasiparticles in front of the vortex core and "heating" behind it. Since the relaxation time of ψ depends on temperature as $\tau_{|\psi|} \sim 1/(T_c - T)$, the recovery time of the order parameter behind the vortex is long while the time of the order parameter suppression in front of the vortex core is short. Interestingly, this leads to an elongated shape of the vortex core with a point where $|\psi| = 0$ is displaced in the direction of the vortex motion. Thus, going beyond the LO theory, the shape of the core of a fast-moving vortex becomes asymmetric and elongated in the direction opposite to the direction of its motion.

The highest vortex velocities (5 – 20 km/s) were reported for superconductors with fast relaxation of quasiparticles [353–358] and in the regime of vortex channeling (guiding) in vicinal YBCO [336] and nanopatterned Nb [354] films. In the dirty limit, i.e., when the electron mean free path l is smaller than the superconducting coherence length ξ, the energy distribution of the quasiparticles in the vortex core is strongly smeared out due to their high scattering rate. The separation between the quasiparticles' energy levels and between the Fermi energy and the lowest bound state in the vortex core is proportional to ξ^{-2} [333]. With an estimate $\xi \lesssim 10$ nm for disordered low-temperature superconductors [359–361], the core can be treated as an energy continuum of quasiparticles. By contrast, the extremely small $\xi \lesssim 1$ nm in the HTS cuprates makes the electron quantum structure of the vortex core essential. Thus, for its experimental observation, the energy smearing $\delta\varepsilon = \hbar/\tau$ due to the mean electronic scattering time τ must be sufficiently small, $\delta\varepsilon \ll \Delta^2/\varepsilon_F$, corresponding to the ultraclean superconducting limit ($l \gg \xi$). Such a regime has been experimentally realized in Refs. [339–341]. Proceeding from an isolated vortex to the vortex lattice, the discrete energy levels within the vortex core interact between neighboring vortices and broaden into minibands [333]. In this case, vortex motion at high velocities is accompanied by emerging phenomena, such as Bloch oscillations of the quasiparticles, negative differential resistance, and multi-step instabilities [333,339–341].

4.2.2. Flux-flow instabilities at $T \ll T_c$

At temperatures $T \ll T_c$, which are easily accessible for HTS, the FFI phenomenon was considered by Kunchur [301] within a different "hot-electron" framework. In this regime, Δ is not sensitive to small changes in the electron distribution function. Furthermore, at $T \sim 0$, the electron–electron scattering time becomes smaller than the electron–phonon scattering time. Accordingly, the electron distribution function remains thermal-like and the electronic system exhibits a temperature shift with respect to the lattice temperature. In this regime, the main effects are the electronic temperature increase, creation of additional quasiparticles, and the depression of Δ. The vortex expands rather than shrinks, and the viscous drag is reduced because of a softening of gradients of the vortex profile rather than a removal of quasiparticles.

There has also been great interest in physical phenomena that can occur in superconductors with a multicomponent order parameter, which describes superfluid electron condensates originating from different electron bands [362]. The multicomponent nature of the superconducting state is now recognized for several superconducting materials, including MgB_2, IBS compounds, and heavy-fermion compounds, among others, and it creates opportunities for the emergence of various new phenomena, for instance, the so-called fractional vortices [363]. Experimentally, fractional vortices have been observed for MgB_2, FeSe, and highly underdoped $YBa_2Cu_3O_{7-x}$ [364,365]. Fractional vortices from different electron bands bear a reduced flux quantum, attract to each other, and try to merge into the single composite vortex with the whole flux quantum Φ_0. With increase of the transport current density, different scenarios preceding the quench to a highly resistive state can be realized, depending on the pinning strength in the material [366]. Thus, for the case of weak pinning, the composite vortices will likely be first depinned, and then they will dissociate into fast-moving fractional components. By contrast, for the case of strong pinning, the composite vortices can first dissociate into the fractional

components, of which one will be set in motion while the other one will remain pinned. The sequence of these processes determines a very peculiar shape of the current–voltage curve, which can not only exhibit multiple instability-like steps but might even lead to jumps to states of lower resistivity.

Overall, ultra-fast vortex motion tackles fundamental questions regarding the ultimate speed limit for magnetic flux transport via Abrikosov vortices and their stability as topological excitations of the order parameter in superconductors [347,353]. In addition, fast vortex dynamics is essential for the photoresponse of superconductor microstrip single-photon detectors, which enable a vortex-assisted mechanism of single-photon counting [367]. Operated at large bias currents [360,368–370], such microstrips appear as viable candidates for various applications requiring large-area detectors, e.g., free-space quantum cryptography, deep-space optical communication, etc. However, whilst the single-photon counting capability of MgB_2 has been established [371,372], single-photon detectors based on HTS cuprates remain a subject of long-standing discussions with reports of not only dark counts [373] and signatures of single-photon operation [374], but of reasonable skepticism too [375]. Therefore, further studies are required to explore the possibilities of using other HTS materials for single-photon counting in the visible light and infrared range [376].

4.2.3. The (B,θ) anisotropy of the FFI

As discussed in previous sections, the vast majority of HTS materials are well-known to present anisotropy characteristics in their macroscopic properties, such as the magneto angular dependence of the critical current density, $J_c(B,\theta)$, which has been studied in depth in Section 3. Therefore, it is straightforward to ask whether the voltage jumps of the FFI can be affected by these anisotropy factors, too, and therefore to clarify whether the FFI can be used as a tool to probe the anisotropic nature of the superconducting gap in any superconductor.

In this sense, Xiao et al. [299] have already described the anisotropy effects on the FFI parameters of BSCCO films, which show a characteristic 2D behavior. The experimental setup is similar to the one used for determining the semi-empirical $J_c(B,\theta)$ models for 2G-HTS tapes introduced in Section 3.3.5, i.e., with $\theta = 0$ implying that a homogeneous magnetic field B is applied along the same direction (parallel) as the c-axis of the HTS sample. Then, by measuring the corresponding $I-V$ curves for different angles, the authors established that the observed voltage jumps can indeed be interpreted within the standard LO model if extended by the theory of Bezuglyi and Shklovskij [377], which considers the unavoidable heating of quasiparticles due to the finite rate of removing the power dissipated in the sample. Nevertheless, depending on whether the component of the field perpendicular to the CuO_2 planes may form vortices or not [378], different possible scenarios can be analyzed.

On the one hand, following similar principles as the scaling approach of Blatter (Section 3.3.3), the instability current sometimes called the critical current under the FFI framework, I^*, and the maximal vortex velocity, v^*, also known as the critical velocity, both resulted to be functions of the anisotropy parameters (B,θ), such that the entire $I-V$ characteristics in these measurements, $f(B,\theta,T)$, can be obtained from the corresponding curves when the magnetic field is applied parallel to the c-axis ($\theta = 0$), i.e., $f(B_{\parallel},T)$, with $B_{\parallel} = B\cos\theta$ (see Fig. 16). This is assuming that the critical velocity can be extracted from the critical voltage measurements, $V^* = Blv^*$, with l being the length of the microbridge (sample), d its thickness, and w its width.

On the other hand, owing to the 2D anisotropy of BSCCO, the model by Lawrence and Doniach [311] can be applied for $H_{c2}(\theta) \approx H_{c2}(\theta = 0)/\cos\theta$ [45,311], leading to the characteristic magnetic field that separates the regions where the influence of the self-heating is of minor or major importance for the flux-flow instability, B_T, to show the same angular anisotropy, i.e., $B_T(\theta) \approx B_T(\theta = 0)/\cos\theta$. Within this model B_T can be obtained by fitting the experimental data with the magnetic-field dependence of the normalized power density $J^*E^*/J_0E_0 = (1-t)$, with $J^* = I^*/(dw)$ and $E^* = Bv^*$ being the corresponding critical current density and critical electric field under the FFI framework, while t is here a polynomial function that depends on the normalized magnetic field $b = B/B_T$. This function has been analytically derived at a fixed bath temperature by Xiao et al. [299], to obtain $t = [1+b+(b^2+8b+4)^{1/2}]/[3(1+2b)]$, where the dependence with the temperature of the critical current density can be recovered by introducing the normalizing current density J_0 and electric field E_0 as,

$$J_0 = 2.62\sigma_n/e\left(D\tau_{in}\right)^{-1/2} k_B T_c \left(1-t_c\right)^{3/4}, \tag{50}$$

$$E_0 = 1.02 B_T \left(D\tau_{in}\right)^{1/2} \left(1-t_c\right)^{1/4}, \tag{51}$$

where τ_{in} is the inelastic scattering time of quasiparticles and D the quasiparticle diffusion coefficient according to the Larkin and Ovchinnikov theory [379].

Nonetheless, in the previous models, we have somehow considered that the anisotropy of the vortex instability of BSSCO has its main origin within its intrinsic layer material and the 2D geometry of the CuO_2 (ab) planes where the superconducting quasiparticles are formed. However, in the case of magnetized thin films, it is known that a geometry effect could also induce an extrinsic anisotropy. This is because despite knowing that in this material the vortices are only formed along the c-axis component of the field, it is also possible to demagnetize the superconductor by applying a crossed or rotating magnetic field, i.e., a field along the ab-planes, which are in principle transparent to any magnetic field [380]. This demagnetization phenomenon is as a matter of fact a common characteristic between superconducting bulks [51,381,382] and thin films [53,54,69,383,384] for any type-II superconductor, for which reason it has been widely studied within the most elementary approaches of the critical state theory in Section 2 and the constituent macroscopic models presented in Section 3.2. Thus, if the magnetic anisotropy of J^* and E^* as a function of B/B_{c2} were caused by the demagnetization effect, then J^* and E^* should be both scaled by $\cos^2(\theta)$, because B is proportional to $\cos(\theta)$ and B_{c2} to $1/\cos(\theta)$, but that is not the case for E^* in BSSCO as the experimental measurement of V^* in Fig. 16 shows a $\cos(\theta)$ dependence. Nevertheless, at temperatures very close to T_c, i.e., at temperatures where the FFI and pinning mechanism is dominated by thermal

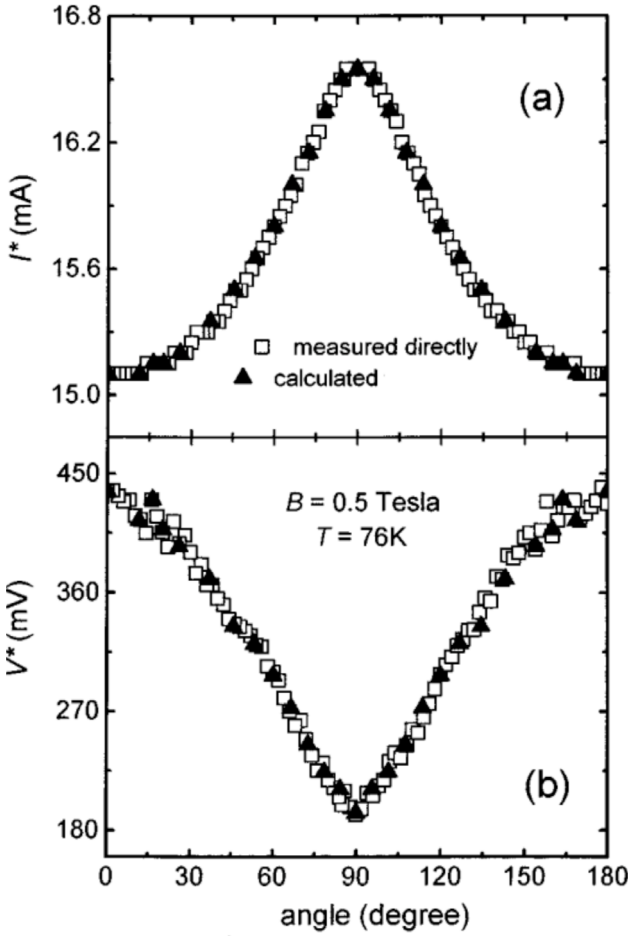

Fig. 16. FFI critical parameters I^* and V^* on a 320 nm thick BSCCO microbridge with T_c = 85.2 K and ρ(100 K) = 506 μΩcm, where both functions can be scaled by $f(B,\theta,T) = f(B_{\|},0,T)$, with the applied field parallel to the c-axis ($\theta = 0$) defined by $B_{\|} = B\cos\theta$.
Source: Adapted with permission from [299].

effects rather than magnetization currents, the J^* of the BSSCO system may undergo a 3D to a 2D anisotropy transition resulting in a simplified $\cos(\theta)$ scaling rule, a phenomenon that has also been observed in pristine and Pr-doped YBCO samples [385].

Having proven that the FFI phenomenon can be used as a means for studying or determining the magneto-angular anisotropy of some of the most conventional superconductors at high transport currents and magnetic fields, the study of IBS compounds has been the focus of most recent efforts for understanding the behavior of the critical current density at high transport currents and magnetic fields, at least within the framework of the FFI theory. In this sense, the FFI mechanism has been extensively investigated in what is probably the most simple and isotropic compound of the family of iron chalcogenides, Fe(Se,Te) [345,386], under magnetic fields of up to 5 T, and with the field angle θ defined as shown in Fig. 17(a). In fact, because the observed current-driven instability in Fe(Se,Te) thin films shows a hybrid behavior between the one expected for LTS materials, such as Nb-Ti, and the one encountered for HTS cuprates, such as BSCCO, understanding this material results of particular importance as it exhibits an unexpected competition between thermal and intrinsic electronic effects.

Thus, for the case of Fe(Se,Te), it has been proven that although the critical voltage $V^*(\theta,H,T)$ can be explained by the standard principles of the anisotropic GL theory [346], as it was indeed the case for BSCCO [299], the same approach does not work for the instability current $I^*(\theta,H,T)$. This can be seen by simple inspection of Fig. 17(b), where clearly the same scaling function could not be used for reproducing the angular dependence of both of the instability curves simultaneously, as was the case on Fig. 16 for BSCCO. Moreover, the critical current $I^*(\theta,H,T)$ that results from the FFI phenomenon in Fe(Se,Te), is almost insensitive to field angle variations (see Fig. 17(c)), contrary to the critical voltage $V^*(\theta,H,T)$ that shows a strong angular dependence similar to the one seen for BSCCO. Probably such main difference can be ascribed to the different pinning acting in Fe(Se,Te) [387], enabling a more isotropic pinning landscape that dominates at lower temperature and high fields, i.e. allowing us to assume $I^* \approx I_c$, so that it can be regarded as a good candidate for high-field applications [388].

Indeed, the observation of the FFI and thus the usability of this method strongly depends on the material properties, but also on other factors such as sample geometry [389,390], pinning effects [346,391–394], and experimental conditions [345,386]

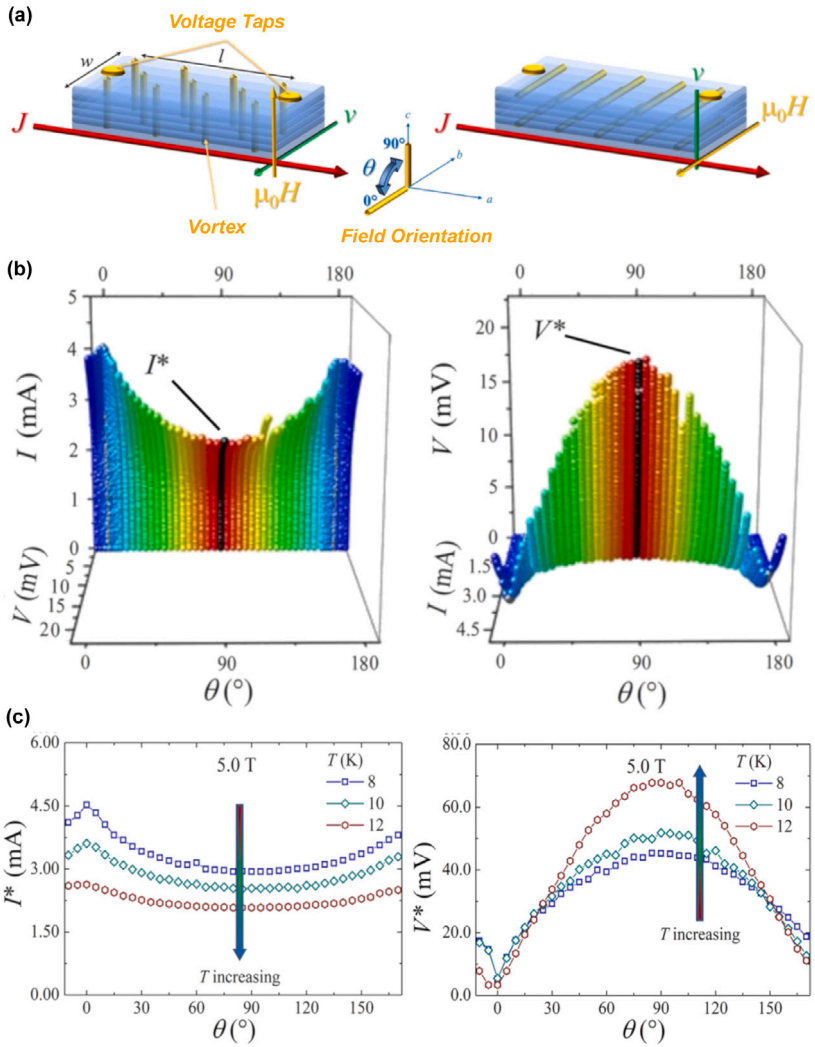

Fig. 17. FFI characteristics measured in (a) Fe(Se,Te) microbridge with the crystallographic orientation of the sample as shown in the top pane, with (b) the obtained $I-V$ curves as a function the field angle θ at $B = 2$ T and $T = 10$ K, and (c) the derived critical voltage V^* and instability current I^* at $B = 5$ T and for three different temperatures.
Source: Adapted with permission from [346].

(e.g. absence of self-heating) that have to be taken into account for further studies. Nonetheless, quench features related to FFI have been identified, and the relation between the instability (quenching) current I^* and the critical current I_c, the latter as defined by constituent macroscopic models (Section 3.2), has been analyzed for both LTS [346,389,391–394] and HTS cuprates [299,395]. For example, we can see how this behavior is rather opposite in the case of HTS and LTS, such as YBCO [396] and Nb [397] in Fig. 18, respectively, as the quenching properties and therefore the FFI of HTS materials is thermally driven, contrary to the LTS materials like Nb, whose FFI is electronically driven. However, as the instability current I^* has a weaker dependence on the applied magnetic field than the critical current I_c, which is an aggregate or 'bulk' value of the peculiar pinning landscape of the superconducting material at lengths much greater than ξ, a constant trend can be found in both cases at high magnetic fields. Therefore, at least for the case of HTS materials assessed at high magnetic fields and high transport currents, it is completely sensible to define the instability current I^* as the actual critical current I_c of the material.

5. J_c and the vortex–defect interactions

As explained, the dissipative motion of vortices often impairs the performance of superconducting materials and their applications. However, in the occurrence of defects in the crystallographic arrangement or microstructure of the material, it is well known that such defects can eventually inflict a force on the vortices that counteracts this motion. In consequence, the deliberate adding of defects can in principle lead to a dramatic boost of the critical current, motivating thence decades of intense efforts to tune the

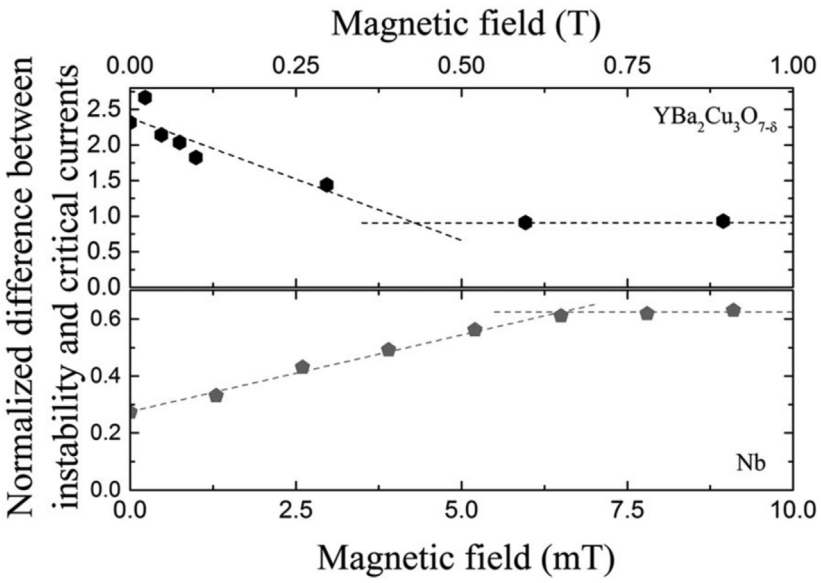

Fig. 18. Difference between the instability current I^* and the macroscopic critical current I_c as a function of the applied field, normalized to the critical current value at zero field and different temperatures. The YBCO data has been extracted from [396] and Nb data from [397]. The dashed lines are guides for the eye. *Source:* Adapted with permission from [398].

material microstructure for maximizing J_c, see Section 6. Therefore, to understand the origin of this enhancement in J_c, here, we detail the underlying mechanisms governing vortex–defect interactions and associated modeling schemes.

On the one hand, despite impressive successes in boosting J_c by tuning the material structure, there is no set prescription to cure the dissipative effects of vortices. Understanding vortex dynamics is complicated by the convoluted interplay among vortex elasticity, vortex–vortex interactions, vortex–defect interactions, and thermal energy. The effectiveness of pinning centers depends on the comparative defect geometry and vortex structure, the latter controlled by material-specific parameters such as the coherence length ξ, penetration depth λ, and the anisotropy constant γ. Consequently, the optimal defect landscape is material dependent. It also depends on temperature and field, as those parameters themselves vary with temperature, and the vortex density is proportional to the magnetic field. Furthermore, the microscopic details governing vortex–defect interactions depend on the type of defects, i.e., on their shape, density, size, and dimensionality. In fact, the defect morphology determines the type of vortex excitation that emerges during the vortex depinning process. Size determines whether an individual defect acting alone can exert sufficient force to pin a vortex – *strong pinning* – or if only their collective action has a measurable effect, as is the case with atomic-scale defects — *weak pinning*.

Thus, in what follows, the reader will encounter a brief but comprehensive discussion on how the collective pinning theory, strong pinning theory, and the thermally-activated hopping of vortices can all influence our understanding of the J_c concept. Then, we will discuss the notable effects of correlated disorder, as opposed to random disorder, to allow us to garner a sufficient microscopic understanding of the vortex–defect and vortex–vortex interactions. Finally, by recognizing that the ultimate goal is a materials-by-design approach, from a practical standpoint, in Section 5.2 we will describe how these fundamental principles are embedded into effective simulations based either on molecular dynamics or the solution of the TDGL equations.

5.1. Pinning and creep mechanisms

Understanding the interplay between material defects and vortex dynamics in HTS materials is crucial for optimizing their performance in engineering applications. However, the reader would have noticed at this point that describing the concerted action of pins on the vortex system relates not only to a complex statistical problem, which can be treated either from purely macroscopic approaches as the ones described in Sections Section 2 & 3, or by mesoscopic approaches as the ones discussed in Section 4, but from the actual quantum nature of the pinning and creep mechanisms. Therefore, in this section we expand the acquired knowledge on flux mobility and pinning properties of HTS materials, discussing the known theories for the formation of vortex phases in the mixed state of type-II superconductors, which are governed by the competition of the elastic energy of the vortices, the pinning interaction energy, and the energy of thermal fluctuations.

5.1.1. Collective pinning theory

In clean superconductors, the pinning action is usually attributed to atomic defects (e.g. oxygen vacancies and interstitials in cuprates) that provide a very weak pinning potential and perturb the superconducting state on length scales much smaller than the superconducting coherence length ξ. Individual defects produce no net force on the vortex system, and it is only their *collective*

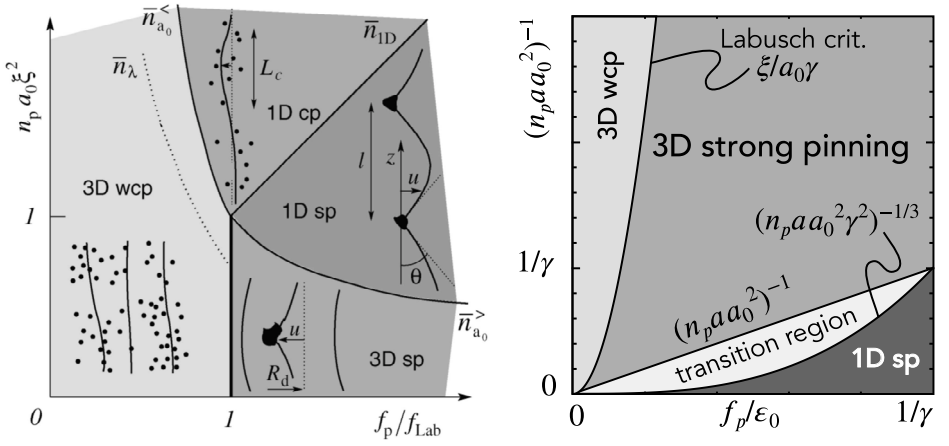

Fig. 19. Phase diagrams of the different pinning regimes as a function of the pinning force, f_p/f_{Lab}, and defect density $n_p a_0 \xi^2$, with *cp* and *wcp* being the collective and weak collective pinning regimes, respectively, and *sp* regimes where strong pinning has been found. Panel (a) focuses on the low defect density regime (reprinted from [400]), while panel (b) includes anisotropic effects (γ) and accounts for defects with a finite diameter a, see Ref. [401].

action that is capable of immobilizing vortices. The theory of weak collective pinning that captures this phenomenology (see Fig. 19), was originally formulated by Larkin and Ovchinnikov [379,399], and later extensively revisited for anisotropic superconductors in the review by Blatter and co-workers [29]. Here, it is worth reminding that the LO theory has also served to describe the FFI phenomena at temperatures close to T_c, as has been shown in Section 4.2.1.

Within this framework the pinning energy within a volume V containing many defects averages to zero, $\langle E_{coll}(V)\rangle = 0$. Only statistical fluctuations around that mean value yield an average pinning energy,

$$\langle E_{coll}(V)^2\rangle^{1/2} \sim [n_p(\xi/a_0)^2 V]^{1/2} f_p \xi\,, \tag{52}$$

with f_p a characteristic individual pinning force and n_p the defect density. The intervortex separation is defined as $a_0 = (\Phi_0/B)^{1/2}$, with $\Phi_0 = h/2e$ the superconducting flux quantum, and B the applied magnetic field.

From this sublinear growth, *rigid* vortices would not lead to a finite critical current, as the Lorentz force grows linearly in V. It is the finite elasticity of the vortex lines that truncates the sublinear growth at a critical (Larkin) volume V_c, within which the vortex system is deformed by ξ. Each volume segment then carries a typical pinning energy $U_c = \langle E_{coll}(V_c)^2\rangle^{1/2}$, from which a characteristic pinning force density $U_c/V_c\xi$ can be deduced. Similarly, the critical current density can be formally evaluated from

$$J_c \sim (U_c/V_c\xi)/B \sim (n_p/V_c)^{1/2}(f_p/\sqrt{BH_{c2}})\,, \tag{53}$$

where $H_{c2} = \Phi_0/2\pi\mu_0\xi^2$ is the upper critical field.

The remaining task consists of properly estimating the pinning volume $V_c = R_c^2 L_c^b$, which – in general – is anisotropic and depends on the collective pinning length L_c and radius R_c.[6] A proper account of this is given in [29], and one finds

$$J_c \sim (n_p a_0 \xi^2)^2 (\xi/\lambda)^2 (f_p/f_{Lab})^4 J_{dp} \tag{54}$$

for the most relevant case of large vortex bundles with $R_c > \lambda$. Here, the Labusch force [402,403] $f_{Lab} \equiv \xi\bar{C}$ defines the characteristic scale for strong pins (see Fig. 19), and the depairing current J_{dp} in Eq. (37) provides a theoretical upper bound for supercurrent transport.

The above expressions involve the vortex line energy $\varepsilon_0 = \Phi_0^2/(4\pi\mu_0\lambda^2)$ and an effective elastic constant $\bar{C} = [\int (d^3k/2\pi) G_{xx}(\mathbf{k})]^{-1} \approx \varepsilon_0/a_0$ from the elastic Green's function $G_{\alpha\beta}(\mathbf{k})$ (for in-depth details see Refs. [400], [404], and [405]). Note in particular that the weak collective pinning result scales *quadratically* with the defect density, i.e., $J_c \propto n_p^2$. Another important observation is the qualitative nature of these expressions (highlighted by the use of ∼ symbols). In fact, the statistical approach employed does not allow making quantitative statements. Rather, the strength of weak collective pinning theory is to differentiate field and temperature regimes in which pinning is active either on a single-vortex level or on the level of small or large vortex bundles. Therefore, in each regime, scaling relations can be derived for different observables, e.g., for the critical current density and the rate of thermally activated vortex motion, as has been explained in preceding sections. However, another analytically tractable case is the limit of a sparse distribution of strong defects, which will be studied below.

[6] Also called longitudinal and transverse correlation (Larkin) lengths.

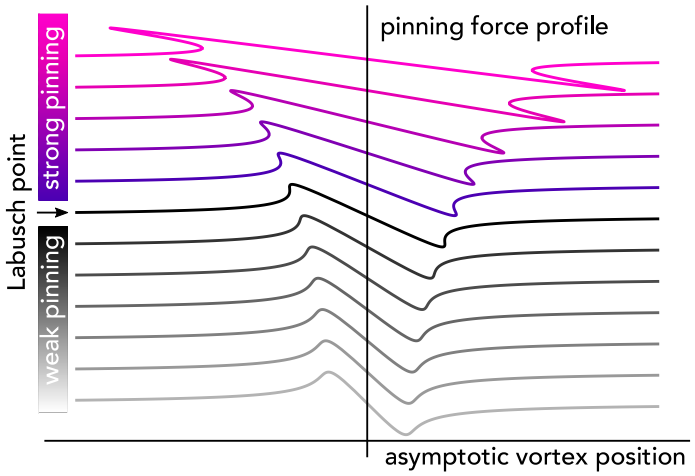

Fig. 20. Evolution of the effective pinning profile when approaching (gray levels) and crossing (color) the Labusch point upon changing the Labusch parameter $f_p\xi/\bar{C}$. In the strong-pinning regime, the pinning landscape becomes multivalued (bifurcation) and allows for a net average pinning force of individual defects. The bifurcation naturally leads to hysteretic effects as manifested, for instance, in the state-dependent ac (Campbell) response.
Source: Adapted with permission from [406].

5.1.2. Strong pinning theory

Under this framework, each defect is now capable of plastically deforming the vortex lattice and individually producing a net pinning force f_p capable of retaining the vortices at their sites. Correlations between defects can, to leading order, be neglected such that the pinning problem can be reduced to that of a single defect interacting with a vortex lattice. As derived by Labusch [402], such a plastic deformation arises when the pinning force exceeds a critical strength $f_p > f_{Lab}$, corresponding to the fact that pinning wins over the lattice elasticity. A natural consequence of this limiting case is the linearity of observables with the defect density. For instance, under this scenario, the critical current density reads as

$$J_c = \nu(n_p a_0 \xi^2)(\xi/a_0)^2(f_p/f_{Lab})^2 J_{dp}, \tag{55}$$

with ν a numerical constant that can be evaluated from the geometrical averaging of defect positions. For a simple illustration of how this number is computed, we can decompose the problem in a longitudinal one (along the Lorenz force) and a transverse one (perpendicular to it). For the moment, let us consider the situation where the vortex impacts the defect head-on (no lateral impact distance). In this longitudinal direction, the microscopic force-balance equation reads as

$$\bar{C}u = f(x+u), \tag{56}$$

with x being the asymptotic position coordination of the vortex, u its maximal deformation at the height of the defect, and $f(r)$ the bare pinning landscape (that would act on an infinitely stiff vortex with $x = r$).

Thus, on the one hand, for weak defects the non-linearity in Eq. (56) is negligible, and the deformation of the vortex at the defect height is approximately $u \approx f(x)/\bar{C}$. The effective force profile $f[x+u(x)]$ remains single-valued (see the gray lines in Fig. 20), which displays the pinning profile in the strong versus weak pinning regimes. Then, upon sampling over all realizations of vortex–defect separations, the total pinning force averages to zero, and hence necessitates considering collective effects in this weak-pinning regime. On the other hand, in the strong pinning regime – formally when $\bar{C} < \max_r \partial_r f(r)$ – the non-linear self-consistency equation for u possesses multiple solutions $u_F(x)$ $[u_p(x)]$ that are asymptotically free (or pinned) as shown in Fig. 20 (colored lines). Notice that in the critical state, the occupation of these solutions is asymmetric, with the free branch populated to the left of the defect and the pinned branch to the right. Therefore, the average force results from evaluating:

$$\langle f \rangle \equiv (t_\perp/a_0^2)\int_{-a_0/2}^{a_0/2} dx f[x + u_{occ}(x)], \tag{57}$$

over the occupied branches u_{occ}.

Vortices approaching the defect with a finite transverse displacement constitute a secondary aspect of the problem. In Eq. (57), this is accounted for by a transverse impact ratio $t_\perp/a_0 \approx 2\xi/a_0$. Moreover, in the limit $\bar{C} \ll \max_r \partial_r f(r)$, the above integral simplifies to $f_p^2/\bar{C}$, for f_p being the maximal pinning force in $f(r)$. Thus, inserting the expression for $\bar{C}$, one arrives at the expression for J_c in Eq. (55) with $\nu = 3\sqrt{3}/2$, which highlights that – in distinction to weak collective pinning – the strong pinning theory has a quantitative character.

The theory of strong vortex pinning, in its simplest form, thus accounts for a distribution of dilute and strong defects. Its framework has enabled calculations of analytic expressions for the critical current density, the zero-temperature current–voltage ($I - V$) characteristics, the (state-dependent) Campbell penetration depth, and the effect of thermally activated motion (creep)

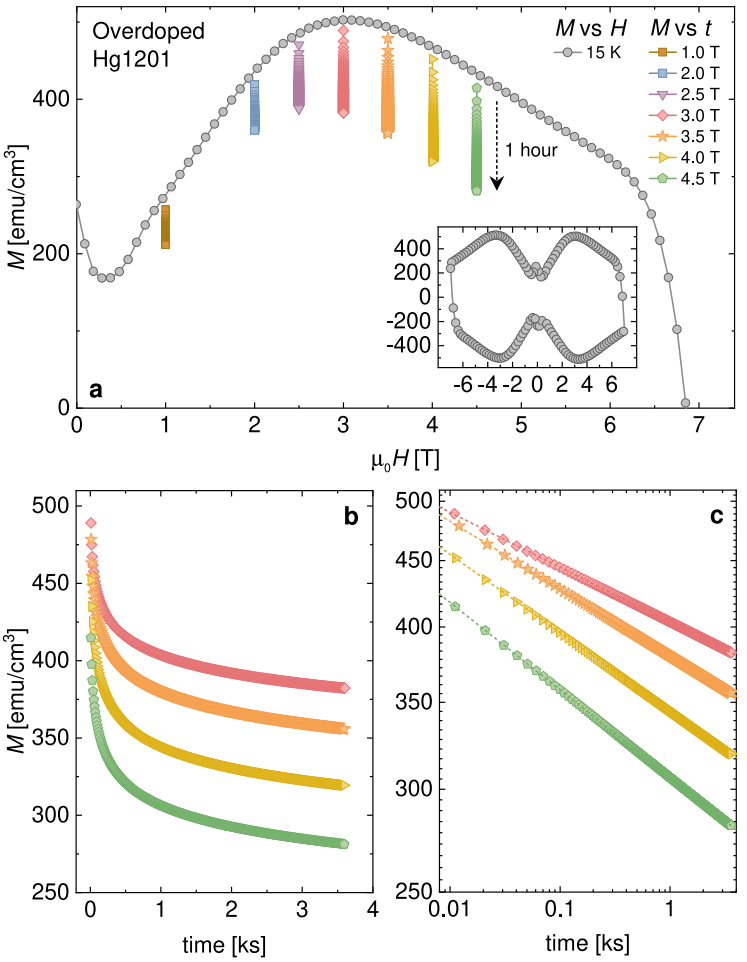

Fig. 21. **a.** Gray curve shows magnetic field-dependent irreversible magnetization in a $HgBa_2CuO_{4+x}$ (Hg1201) single crystal, measured at 15 K. The colored points show repeated measurements of the magnetization M collected for 1 h at fixed magnetic fields noted in the legend, capturing magnetic relaxation. Inset shows full magnetization loop $M(H)$. **b.** Magnetization plotted as a function of time at 15 K and in magnetic fields of 3–3.5 T, after the critical state has been established at each field. **c.** Data from (b) plotted as on a log–log scale. Linear fits demonstrate approximately (first-order) power-law behavior. It is common to parameterize creep S as the slope of $\log M$ vs. $\log t$.
Source: Adapted with permission from [418].

on the $I - V$ and Campbell characteristics [400,403–405,407–411]. Consequently, the success of the theory is evidenced by its consistency with experimental studies of materials containing strong pinning centers [406,412–414]. Beyond its standard framework, the theory of strong pinning has been expanded in different directions: First, for considering cluster pinning [415], an intermediate regime between weak collective pinning and strong pinning is assumed, where the rare events of a cluster of weak defects effectively produce a strong pin. A second extension has considered the limit of very strong defects, capable of pinning more than one vortex at a time [413]. This phenomenon is accompanied by a new type of peak effect at a critical field in which a defect becomes capable of pinning two (or more) vortices. Finally, a third extension – currently under investigation – considers the case in which the pinning theory for generalized pins breaks its cylindrical symmetry, for which the Hessian character of the pinning landscape would play a crucial role [416].

5.1.3. Thermally-activated vortex motion

Up to now, we have described how defects create effective energy barriers that pin vortices. However, under the action of driving or demagnetizing currents, this pinned state is metastable and vortices can hop out of their pinning site, energized by thermal energy, a phenomenon that is known as vortex creep. The associated hopping rate follows the Arrhenius law $\Gamma = e^{-U_{act}/k_B T}$. Through the energy barrier $U_{act}(T, H, J)$, creep itself depends on the interplay between vortex–vortex interactions, vortex–defect interactions, vortex elasticity, and anisotropy [29,193,417]. An early description of the creep process modeled vortices as non-interacting rigid objects hopping out of potential energy wells of depth $U_{act} \propto U_p|1 - J/J_c|$, with U_p being the energy barrier for $J = 0$ [29].

Proposed by Anderson and Kim, this description often sufficiently captures dynamics at low temperatures and magnetic fields. While the linear vanishing of U_{act} at J_c remains purely conjectured in their work, microscopic calculations have derived a different

power-law $U_{act} \propto (1 - J/J_c)^{3/2}$ in the strong pinning regime [409]. At higher temperatures, elasticity becomes more prominent. Moreover, vortex–vortex interactions become non-negligible as increasing magnetic fields reduce vortex separation. These properties significantly change the picture. Notably, current-induced forces can lengthen a vortex over time, and vortex deformation engenders distinctly different phases, such as glassy phases of decoupled or entangled vortices [419–421]. Considering vortex elasticity, collective creep theories predict the current dependence of the energy barrier $U_{act}(J) = U_p[(J_c/J)^{\mu} - 1]$, where μ is the glassy exponent related to the size and dimensionality of the vortex bundle that hops during the creep process [193,422]. Note that this distinctly differs from the Anderson-Kim model in that it considers an inverse power law relationship (instead of linear) between the energy barrier and current. Note also that, as $J \to 0$, the energy barrier diverges, predictive of glassy phases that do not arise under the premises of the Anderson-Kim model alone.

In order to interpolate between the low-temperature (Anderson-Kim) and collective creep regimes, the relationship $U_{act}(J) = (U_p/\mu)\left[(J_c/J)^{\mu} - 1\right]$ is commonly invoked [417], where $\mu \to -1$ recovers the Anderson-Kim prediction. Combining this interpolation formula with the creep frequency $1/t = 1/t_0 e^{U_{act}(J)/k_B T}$, we find that creep causes the persistent current to decay over time as

$$J(t) = J_{c0}[1 + (\mu k_B T/U_p)\ln(t/t_0)]^{-1/\mu}, \tag{58}$$

and parameterize thermal vortex creep as

$$S \equiv \left|\frac{d\ln J}{d\ln t}\right| = \frac{k_B T}{U_p + \mu k_B T \ln(t/t_0)}, \tag{59}$$

where, on the one hand, t_0^{-1} is a microscopic attempt frequency which is estimated to be 10^6-10^{10} Hz for a single flux line [410,423]; and, on the other hand, experimental time frames t for capturing creep are typically of the order of 1 h, such that $\ln(t/t_0) \sim$ 25-30 [424].

Because the magnetization $M \propto J$, creep is often readily measured by repeatedly recording the magnetization over time using a magnetometer and capturing its decay induced by dissipation from the creep process. Example $M(t)$ data collected on a $HgBa_2CuO_{4+x}$ crystal is shown in Fig. 21. From this data set, Eq. (59) is used to extract $S(T, H)$ and subsequently U_p and μ. Consequently, the utility of creep measurements extends beyond simply understanding the rate of decay in the persistent current, also revealing the size of the energy barrier, its dependence on current, field, and temperature, and whether the dynamics are glassy or plastic. Identifying creep as a decay in the magnetization applies under the conditions of an induced current. When there is an applied current, creep manifests as a rounding in the $I - V$ curves near the critical current I_c such that $I \sim V^n$, for which creep is parameterized by the so-called n-value and $S \sim 1/(n-1)$. Thus, note that magnetization and transport measurements provide information on the creep barrier $U_{act}(J)$ in different current ranges, although typical voltages probed during transport measurements are 5–6 orders of magnitude larger than voltages accessed via magnetic relaxation (magnetization) studies [31].

Evidently, for applications, creep should be minimized. In this sense, Eley et al. [425] have already predicted that the minimum achievable thermal creep rate in a material can be expressed by $S \sim Gi^{1/2} \cdot (t_c)$, where $Gi = (\gamma^2/2)(k_B T_c/\varepsilon_{sc})^2$ is the so-called Ginzburg–Levanyuk number, sometimes for simplicity just called the Ginzburg number [29]. This number is the ratio of the thermal energy at $T = T_c$ to the superconducting condensation energy $\varepsilon_{sc} = (\Phi_0^2/2\pi\mu_0\xi^2\lambda^2)\xi^3$, i.e., a dimensionless number that measures the possibility to use the GL theory up to the temperature when the fluctuation corrections become comparable to the value of the corresponding physical quantities. A summary of experimental data supporting this finding is presented in Fig. 22. Nevertheless, it is to be noticed that the applicability of this result is limited to the Anderson-Kim regime; therefore, at low temperatures and fields, we see that the minimum creep rate positively correlates with the material's Ginzburg number. This is consistent with observations that high T_c superconductors, which often have high Gi compared to low-T_c materials, also tend to exhibit much faster creep. In fact, creep is often inconsequential in low-T_c materials.

Quantum creep. In addition to thermal activation over an energy barrier, vortices can quantum-tunnel through it, referred to as quantum creep. In the weak collective pinning regime, the effective quantum creep rate [422,426,427] is predicted to be

$$|S_q| = \begin{cases} \dfrac{e^2}{\hbar}\dfrac{\rho_n}{\varepsilon\xi}\sqrt{\dfrac{J_c}{J_{dp}}}, & \text{if } L_c < a_0, \\ \dfrac{e^2}{\hbar}\dfrac{\rho_n}{\lambda}\left(\dfrac{a_0}{\lambda}\right)^4\left(\dfrac{a_0}{\xi}\right)^9\left(\dfrac{J_c}{J_{dp}}\right)^{9/2}, & \text{if } L_c > a_0, \end{cases} \tag{60}$$

where L_c is the length of the vortex segment (or bundle) that tunnels and ρ_n is the normal state resistivity [29]. In the case of depinning from columnar defects [427,428], the quantum creep rate is similarly defined as

$$|S_q| = \begin{cases} \dfrac{e^2}{\hbar}\dfrac{\rho_n}{\varepsilon\xi}\sqrt{\dfrac{J_c}{J_{dp}}}\left(\dfrac{\xi}{R}\right)^{5/2}, & \text{anisotropic}, \\ \dfrac{e^2}{\hbar}\dfrac{\rho_n}{d}\left(\dfrac{\xi}{R}\right)^2, & \text{layered}. \end{cases} \tag{61}$$

Notice how for anisotropic materials, S_q similarly depends on $\sqrt{J_c/J_{dp}}$ in the cases of weak collective pinning landscape and from columnar defects. At sufficiently low temperatures, there is a crossover to a regime in which quantum creep dominates over thermal creep. The crossover temperature was derived in [429] as $t_0 = \left(N_2\hbar V_o/\eta_l R^2\right)\cdot\sqrt{1 - J/J_c}$, where V_o and R are the height and the extent of the pinning potential at $J = 0$, $N_2 = 5/8\pi$, and $\eta_l = \Phi_0^2/2\pi c^2\xi^2\rho_n$ is the friction coefficient.

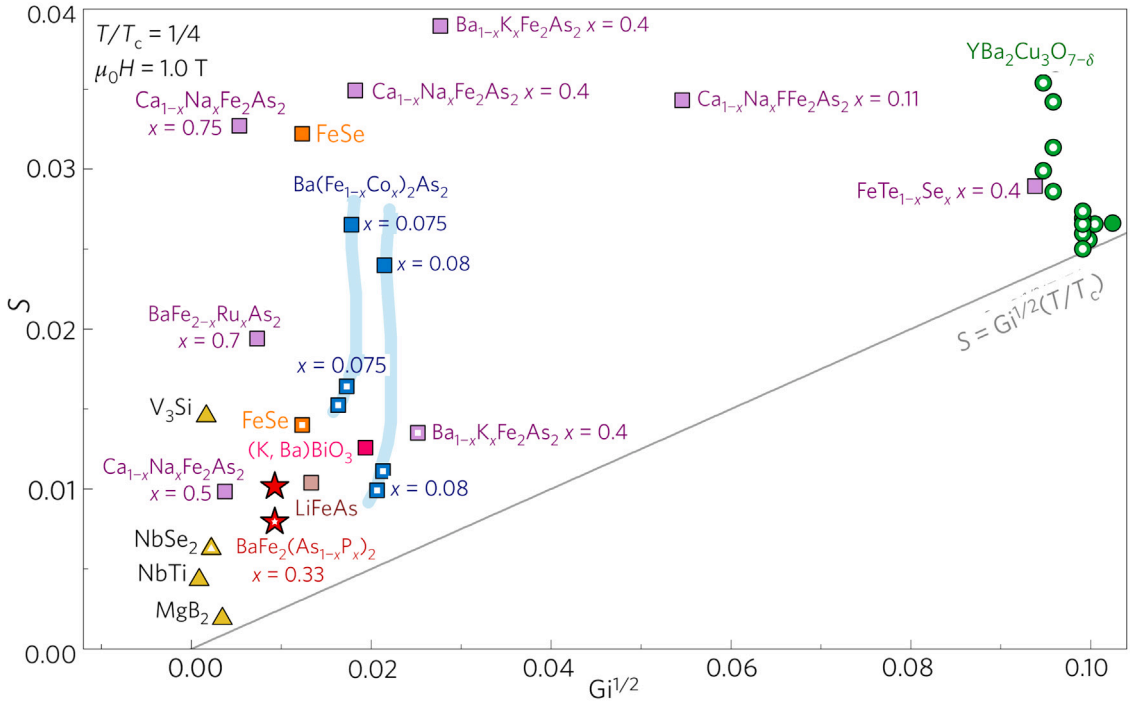

Fig. 22. Creep measured at reduced temperature $t_c = 1/4$ in a magnetic field of $\mu_0 H = 1$ T for different superconductors plotted versus $Gi^{1/2}$, where Gi is the Ginzburg–Levanyuk number. The open symbols indicate materials for which the microstructure has been modified either by irradiation or incorporation of inclusions. The solid gray line represents a proposed lower limit set by $Gi^{1/2}(t_c)$. The result predicts that the creep problem in yet-to-be-discovered high-T_c superconductors may counteract the benefits of high operating temperatures.
Source: Adapted with permission from [425].

However, experimental measurements of quantum creep are somewhat limited, predominately focusing on cuprates. This is not surprising, as according to Eq. (60) superconductors with high normal-state resistivity ρ_n and low ξ, such as high-T_c cuprates, are simply the best candidates for having measurable quantum creep rates. In these materials, crossovers have been identified in readily accessible temperature ranges of $\sim 8.5-11$ K in YBCO films [430–432], or $1.5-2$ K in YBCO crystals [431,433], as well as $5-6$ K in Tl2212 films [433,434], 17 K in Tl1212 [430], and 30 K in Hg1212 [430]. Additionally, Klein et al. [435] studying an iron-based superconductor found also a crossover around 1 K in Fe(Te,Se).

5.1.4. Correlated disorder

In previous sections, we considered how 'zero-dimensional' defects, such as point defects and interstitials, trap one-dimensional flux lines. However, with a difference in dimensionality between the pinning site and the pinned object, only a finite density of pins guarantees a non-vanishing pinning force *per unit length*. Thus, in this section, we consider one-dimensional defects (columnar defects, dislocations) and two-dimensional defects (grain boundaries, stacking faults), which are individually capable of applying a force on the entire vortex line. The increased dimension of the defect adds various new phenomena to the pinning problem, first and foremost, a strong dependence on the relative angle between vortex lines and the defect: A field parallel to the defect line (or plane) is much more strongly pinned than a field orthogonal to it. Also, the flux lines can discontinuously align to the defect line (plane) even if the field direction is slightly misaligned, known as a lock-in transition [436,437]. A third noteworthy phenomenon is the matching effect for columnar defects [438,439], where the critical current acquires pronounced features whenever the vortex density B/Φ_0 (now aligned with the columnar defects) reaches an integer multiple of the defect density n_d. At the first matching field $B_\Phi = \Phi_0 n_d$, each defect can accommodate one vortex, whereas above that, vortices outnumber the defects.

At first sight, these correlated defects seem tremendously more efficient in pinning lines of flux, as compared to the pinning capability of the zero-dimensional defects [172]. However, the benefit is limited by several downsides: first, as previously mentioned, columnar defects and grain boundaries produce a highly field-angle-dependent pinning profile [440,441], i.e., for fields away from the principal defect orientation, vortex pinning becomes very weak due to a translational invariance. This effect is often mitigated by considering an angular distribution of columnar defects or a mixture of defects, as exemplified in Fig. 23. Second, vortices trapped by a linear (or planar) defect depin by nucleating a critical half-loop excitation [442] (vortex segment leaving the defect) which then causes the rest of the trapped vortex to zip out of the defect, see Fig. 24. This mechanism involves a depinning energy that does not scale with the length of the trapped vortex and, hence, does not dimensionally outperform point-like defects. These topics are treated in detail elsewhere and we refer the interested reader, e.g., to the reviews of Blatter et al. [29] as well as Nelson and Vinokur [281].

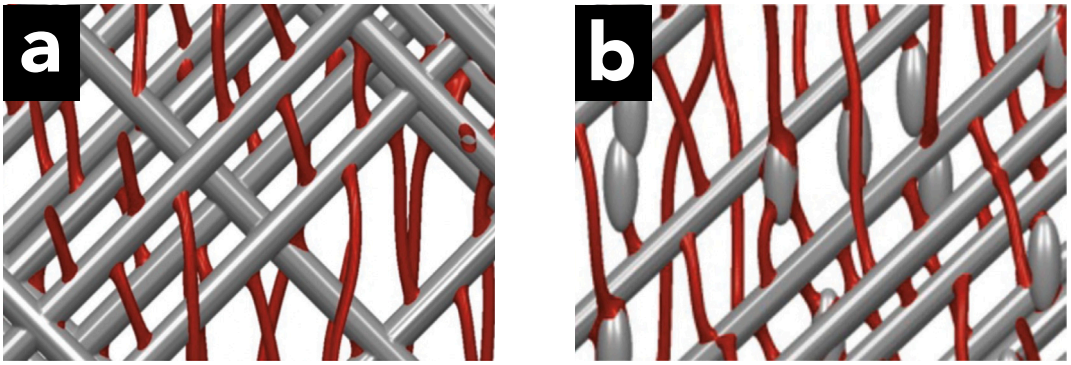

Fig. 23. Optimization of pinning performance for vortices (red) misaligned with a pinning landscape that consists of columnar defects (gray cylinders): Panel (a) shows a simulation snapshot of splayed columnar defects and (b) a mixed pinning landscape including columnar defects and elongated nanoparticles (gray ellipses). These simulation snapshots are reprinted with permission from [32] (Copyright Wiley-VCH GmbH).

In consequence, it should not come as a surprise that the most effective pinning is usually obtained when multiple pinning mechanisms and defect types are working jointly [443], which unfortunately leaves little room for accurate analytic treatment. Therefore, aiming for quantitative accuracy in the presence of mixed pinning landscapes usually requires resorting to numerical methods, such as the ones discussed in Section 5.2.

5.2. Simulating vortex–defect interactions

Due to the doping of high-T_c superconductors, which strongly affects the properties of these materials, the description of its meso- to macroscopic properties such as J_c also requires a realistic treatment of inhomogeneities from the microscopical perspective. Since the energy gaps can become comparable to the Fermi energy, it is useful to consider a unified treatment of normal and superconducting aspects influencing band structure, densities, gap functions, coherence lengths, and London penetration depths from first principles. Specifically, molecular dynamics simulations treat vortices as interacting particles, or strings of particles, under the influence of competing forces from a current, pinning sites, and thermal fluctuations. In this framework, vortices are introduced during initialization, and the resulting velocity–force curves can directly inform on the electrical transport characteristics and expected vortex phases. An alternative and more computationally intensive approach is to run time-dependent Ginzburg Landau simulations (TDGL), in which vortices naturally emerge when energetically favorable. We follow our discussion of vortex–defect interactions by introducing these microscopic simulation schemes and their predictive powers.

5.2.1. First principles computations: DFT & the Bogoliubov–de Gennes equations

Density functional theory (DFT) provides a convenient way to describe the electronic structure of materials. DFT is based on the Hohenberg–Kohn theorem stating that the ground state of the many-body system is a unique functional of the electron density. The complex many-body problem is therefore reduced to the search for a universal functional of the density. However, DFT cannot be used unless an approximation for the universal functional is available. For example, a review by Barbiellini [444] proposed a combination of DFT calculations and positron annihilation spectroscopy experiments to identify defects in $YBa_2Cu_3O_{7-\delta}$. Practical implementations of DFT involve solving a set of one-electron Schrödinger-like equations known as the Kohn–Sham equations. So far, the standard DFT approach – called the generalized gradient approximation (GGA) – has failed to describe the correct electronic structure of cuprate superconducting materials. Fortunately, the more accurate Strongly-Constrained and Appropriately-Normed (SCAN) functional has provided an approximation that correctly predicts the antiferromagnetic band gap (or absence thereof) and the spin moments of the undoped and doped cuprate HTS materials, without free parameters [445]. These advanced DFT calculations are ideal for the treatment of inhomogeneities such as stripes [446] and other defects that can pin vortices. Recently, the DFT/GGA approach has been used to calculate the electronic structure of the $BaFeAs_2$ compound [447] (a member of the 112-type family, AFeAs$_2$ [448]). These calculations predict an electronic structure that appears similar to ARPES measurements of the 122 compounds, which are also in agreement with DFT results obtained from standard approximations [449].

Also, the so-called superconducting density functional theory (SCDFT) generalizes the DFT by an additional density describing the order parameter of the superconducting condensate [450]. The implementation of the SCDFT framework leads to equations of the Kohn–Sham type that incorporate exchange and correlation effects into the Bogoliubov–de Gennes equations for an inhomogeneous superconductor. These equations [450] are (in atomic units)

$$\begin{aligned} \left[-\frac{\nabla^2}{2}+v^{\mathrm{e}}(\mathbf{r})\right]u_i(\mathbf{r})+\int d^3\mathbf{r}'\Delta(\mathbf{r},\mathbf{r}')v_i(\mathbf{r}') &= E_i\,u_i(\mathbf{r}),\\ \left[\frac{\nabla^2}{2}-v^{\mathrm{e}}(\mathbf{r})\right]v_i(\mathbf{r})+\int d^3\mathbf{r}'\Delta^*(\mathbf{r},\mathbf{r}')u_i(\mathbf{r}') &= E_i\,v_i(\mathbf{r}), \end{aligned} \tag{62}$$

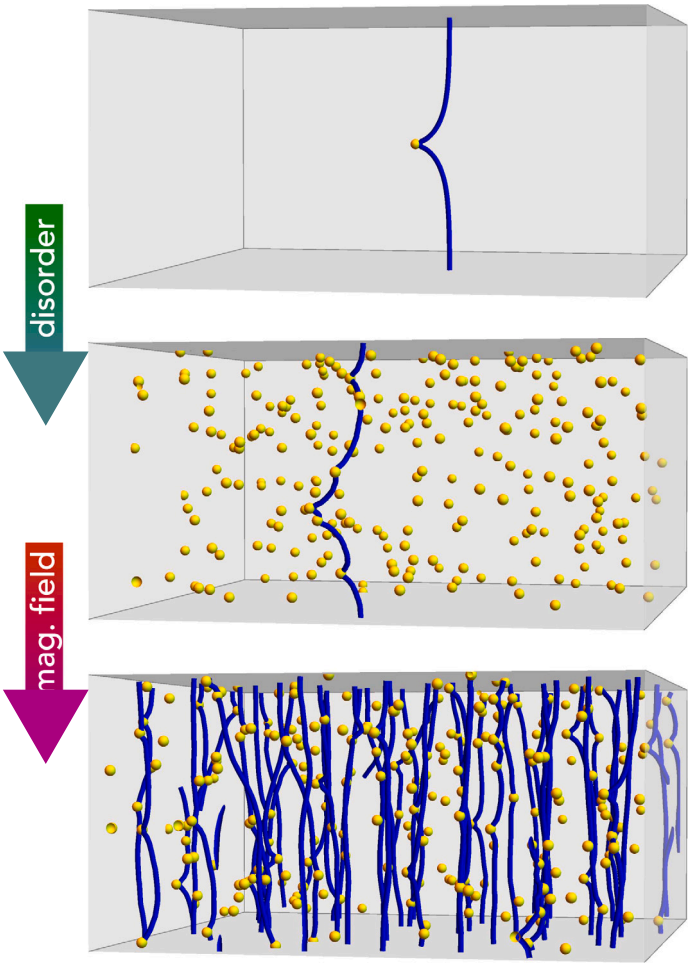

Fig. 24. Rendering of three simulation settings of the TDGL solver: (top) single-vortex single-defect limit, (middle) 1D strong pinning, (bottom) 3D strong pinning. This simplified hierarchy only illustrates two tuning parameters, namely the defect density and magnetic field strength. Other properties of the pinning characteristics (size distribution, shape, type), of the vortices (field-angle), and of the material (anisotropy) remain unchanged.
Source: Adapted with permission from [425]

where $u_i(\mathbf{r})$ and $v_i(\mathbf{r})$ are the particle and hole amplitudes while $v^{\mathrm{e}}(\mathbf{r})$ and $\Delta(\mathbf{r},\mathbf{r}')$ are the Kohn–Sham potential and the superconducting kernel, respectively.

Similarly, Berthod et al. [451] introduced a scalable method to solve the Bogoliubov–de Gennes equations that can rationalize scanning tunneling microscopy (STM) experiments in the presence of vortices. The method can be generalized to include multiple bands and competing orders such as antiferromagnetism or charge-density waves described by the SCAN DFT calculations [446]. Finally, the well-known equations of the GL theory for superconductors, correctly describing vortex dynamics, can also be derived from the same Bogoliubov–de Gennes equations [452]. Therefore, the first-principles framework discussed here evolves into a parameter-free approach that is only based on physical fundamental constants and elemental material properties.

5.2.2. *Time-dependent Ginzburg–Landau simulations*

As discussed above, first-principles calculations take a microscopic approach to the pinning problem, achieving atomic resolution. On the mesoscopic scale, the time-dependent Ginzburg–Landau (TDGL) approach treats vortices as topological singularities of a superconducting wave function $\psi(\mathbf{r},t)$ that varies in space and time according to the TDGL equation (in dimensionless units):

$$\tau(\partial_t + i\mu)\psi = \varepsilon(\mathbf{r})\psi - |\psi|^2\psi + \sum_{\alpha=x,y,z} \xi_\alpha^2(\partial_\alpha - iA_\alpha)^2\psi\,. \tag{63}$$

Under this framework, the time-evolution is characterized by a relaxation rate τ and the electrical potential μ, with A_α being the components of the vector potential. Thus, the superconducting properties are predominantly captured by the components of the anisotropic coherence length ξ_α, whilst pinning sites can be characterized by material defects that impose a spatially varying local critical temperature $\varepsilon(\mathbf{r})$ (δT_{c} pinning). Alternatively, pinning can be captured by spatial modulations of the coherence length

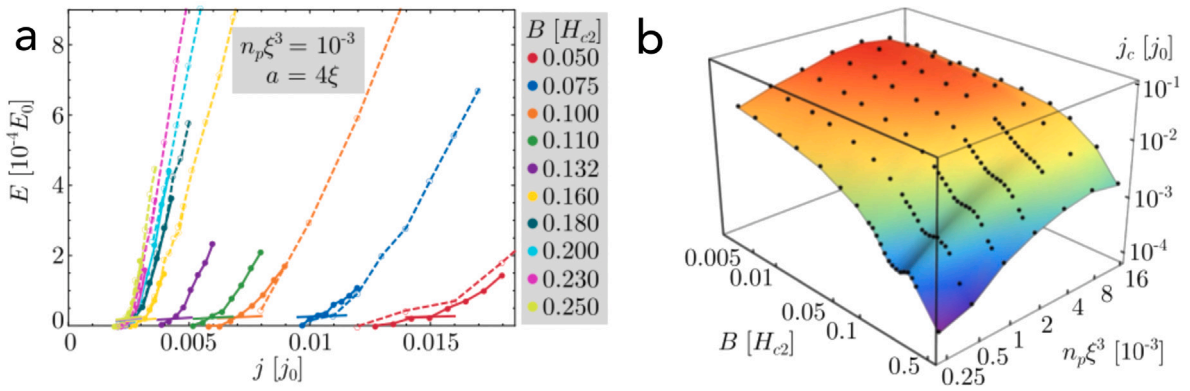

Fig. 25. (a) Current–voltage (I–V) characteristics for a fixed density of metallic defects (diameter $a = 4\xi$) for different fields as obtained from TDGL simulations. A faster scan (open symbols) allows rapid identification of the region of interest, while a longer simulation run increases the results' precision. The critical current, measured at 2% of flux flow voltage, is extracted from the simulated $I - V$ curves. Panel (b) shows the critical current map as a function of field strength and defect density. An optimal density of pinning sites is found near $n_p\xi^3 \sim 5 \times 10^{-3}$ and a new peak effect (non-monotonic $J_c(B)$) was discovered at low defect densities.
Source: Adapted with permission from [401].

components ($\delta\ell$ pinning). To account for thermal noise, the above equation can be augmented by a Langevin-force term $\zeta(\mathbf{r}, t)$, with $\langle\zeta^*(\mathbf{r}, t)\zeta^*(\mathbf{r}', t')\rangle = \tau t_c \delta(\mathbf{r} - \mathbf{r}')\delta(t - t')$, where t_c is the reduced temperature. Thus, close to the critical temperature T_c, the TDGL framework is rigorously rooted in the microscopic theory of superconductivity by Bardeen, Cooper, and Schrieffer [453], allowing it to account for realistic pinning mechanisms while capturing the elastic properties of vortices. Consequently, the TDGL approach fulfills the essential requirements to describe pinning phenomena with a high degree of fidelity at acceptable computational costs.

At an early stage, the TDGL approach was limited to small two-dimensional systems, yet allowed investigations of single vortices interacting with grain boundaries and domain walls as well as pinning of ~100 vortices by columnar defects in thin films [454–456]. At the turn of the century, three-dimensional simulations allowed for the first realistic descriptions of flux lines [457]. Another leap was achieved in 2015 when Koshelev and co-workers reached an unprecedented simulation volume of nearly $10^6\,\xi^3$ based on a parallelized solver of the TDGL equations implemented on graphics processing units (GPUs) [458,459].

In conclusion, due to the physical soundness of the TDGL formulations and the continuous advance on either the parallelization of computing workloads through accelerated GPUs or via CPU architectural innovations with faster clock speeds, today TDGL simulations present unique opportunities to investigate vortex dynamics in realistic pinning landscapes, e.g., as those observed in Dy-doped YBCO films [32,460,461]. Likewise, they can be used as a tool to optimize the defect landscape and therefore maximize the critical current of engineered HTS materials [31,32,459,462–464], or to investigate the regimes and boundaries of pinning components [401,465], as can be seen in Figs. 24 and 25.

5.2.3. Molecular dynamics simulations

As explained above, the DFT for superconductors can be mapped to the TDGL theory. Similarly, the GL approach can be coarse-grained to arrive at the classical molecular dynamics (MD) and stochastic Langevin descriptions by using multi-scale techniques. For example, classical forces can be derived from the many-body wave function of a vortex in a superconductor, as shown by Ao and Thouless in [466].

Compared to TDGL simulations, a less computationally intensive option for modeling vortex dynamics is to use MD-based simulations. These simulations are often invoked to study dynamics in a variety of seemingly disparate systems that can effectively be modeled as particles under the influence of external drives interacting with themselves and quenched disorder: this includes soft matter systems such as colloids and proteins, as well as hard condensed matter systems such as magnetic skyrmions and superconducting vortices [467]. These simulations are on the macroscopic scale and, unlike TDGL, are unable to resolve phenomena on the order of the superconducting coherence length ξ.

Whereas vortices naturally emerge in the TDGL approach, in MD simulations, a single vortex is simulated as either a single particle or a chain of particles attached via an elastic band or spring [467]. Thus, the pinning site particles are fixed and used to exert an attractive pinning force on the vortices. More specifically, MD simulations of vortex motion are typically guided by a particle-based equation of motion of the general form,

$$\mathbf{F}_i = \eta \mathbf{v}_i = \mathbf{F}_D + \mathbf{F}_i^{vv} + \mathbf{F}_i^{p} + \mathbf{F}^{T}, \tag{64}$$

with $\mathbf{F}_i$ being the total force acting on a vortex i, with its position and velocity given by $\mathbf{r}_i$ and $\mathbf{v}_i = d\mathbf{r}_i/dt$, respectively, and η being the vortex drag coefficient of the Bardeen–Stephen viscous drag model [468], which can be a function of the vortex velocity [469]. Notice also that the main contributions to this total force, as described by Eq. (64), include the current-induced Lorentz-like driving force $\mathbf{F}_D = |\mathbf{J}_c \times \mathbf{B}|$, the vortex–vortex interaction force $\mathbf{F}_i^{vv}$, a term for including the thermal fluctuations $\mathbf{F}^T$, and the vortex–defect

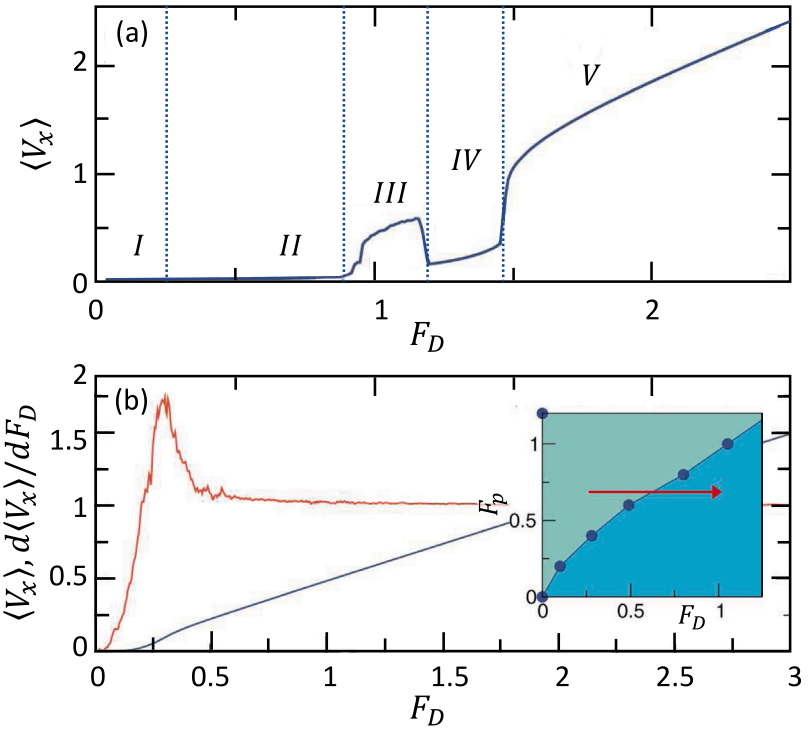

Fig. 26. (a) Velocity–force curve $\langle V_x \rangle$ vs F_D for a system with a square pinning array at a filling of $f = N_v/n_p = 1.0368$ for $\eta = 1.0$ and $f_p = 1.5$ based on [471]. The labeled phases are: I (pinned), II (interstitial flow), III (disordered liquid), IV (soliton motion), and V (moving smectic). (b) Velocity–force curve (blue) for a 2D system of vortices moving through quenched disorder for a non-dimensional vortex density $n_v = 1$, defect density $n_p = 0.5$, pinning force $f_p = 0.4$, and pinning radius $r_p = 0.3$. Derivative $d\langle V \rangle / dF_D$ of the velocity–force curve, useful for distinguishing pinning regimes and vortex phase transitions, is shown in red. The inset shows f_p versus F_D, identifying the disordered phase (light blue region) and the dynamically ordered phase (dark blue). All data are based on molecular dynamics simulations.
Source: Adapted with permission from (a) [471] and (b) [472].

interaction force $\mathbf{F}_i^p$. These dynamics are fundamentally overdamped because the vortex core encompasses single electrons, which behave dissipatively, serving as a source of damping. Then, to model the vortex–vortex interaction force, it is possible to use the approximation of Reichhardt et al. [467], who use the relationship $\mathbf{F}_i^{vv} = \sum_{j=1}^{N} F_0 K_1(r_{ij}/\lambda)\hat{\mathbf{r}}_{ij}$, where $F_0 = \Phi_0^2/2\pi\mu_0\lambda^3$, $\mathbf{r}_{ij} = |\mathbf{r}_i - \mathbf{r}_j|$ is the vortex separation, and K_1 is the modified Bessel function, which decays exponentially for $\mathbf{r}_{ij} > \lambda$. Consequently, vortex–vortex interactions can be negated at sufficiently large separations compared to the penetration depth λ, as has been proven recently by simulations on 2D systems of rigid vortices with cut-off vortex–vortex interactions at $\mathbf{r}_{ij}/\lambda > 6$ [470].

To simulate pinning sites, defects are treated as attractive and modeled as deep wells in an otherwise flat potential. For example, point-like pinning sites are typically described as randomly placed parabolic or Gaussian-shaped traps of extent r_p that can exert a maximum force f_p on a vortex [467,470]. Similarly, columnar defects have been modeled as parabolic potentials of radius r_p and magnitude f_p, where $F_i^p = -\sum_{k=1}^{n_p} f_p(r_{ik}/r_p)\Theta(r_p - r_{ik})\mathbf{r}_{ik}$, with $r_{ik} = |\mathbf{r}_i - \mathbf{r}_k|$ being the distance between the vortex i and pin k at r_k, and Θ being the Heaviside step function. In addition, MD simulations may consider adding further terms to Eq. (64) such as the Magnus force and inertia $m\ddot{\mathbf{r}}_i$. However, these contributions can typically be disregarded, on the one hand, owing to the negligible equivalent mass m of the vortex and, on the other hand, to the fact that the current transverse to the Lorentz force tends to be very small for superconducting vortices.

Implementing the simulations involves setting initial conditions such as the system size L, the number of vortices N_v (from the vortex density $n_v = N_v/L^2$), and the number of defects N_p (from the defect density $n_p = N_p/L^2$), as well as preparing the vortex ground state using an energy minimization protocol or simulated annealing. For example, to prepare a system similar to field-cooled experiments, the vortices are first placed into the system under the influence of thermal fluctuations (high temperatures), and the system is slowly cooled to $T = 0$ [473]. After initialization, to produce velocity–force curves, the simulations track the average vortex velocity $V_x = (1/N_v)\sum_1^{N_v} v_x$ in response to an incrementally increasing driving force F_D in the $\hat{x}$ direction. As the driving force is simply the Lorentz force resulting from an applied current J in the $\hat{y}$ direction, the results can be compared to experimental $I - V$ curves produced by current sweeps. Examples of such velocity–force curves are shown in Fig. 26.

The velocity–force curves provide information on critical parameters, such as the critical force F_c, i.e., the maximum driving force for which vortices remain pinned. Similarly, the critical current (depinning current) can be determined from the current corresponding to the driving force at which V_x rises to a particular metric, e.g., 0.03 in [473]. Velocity–force curves produced

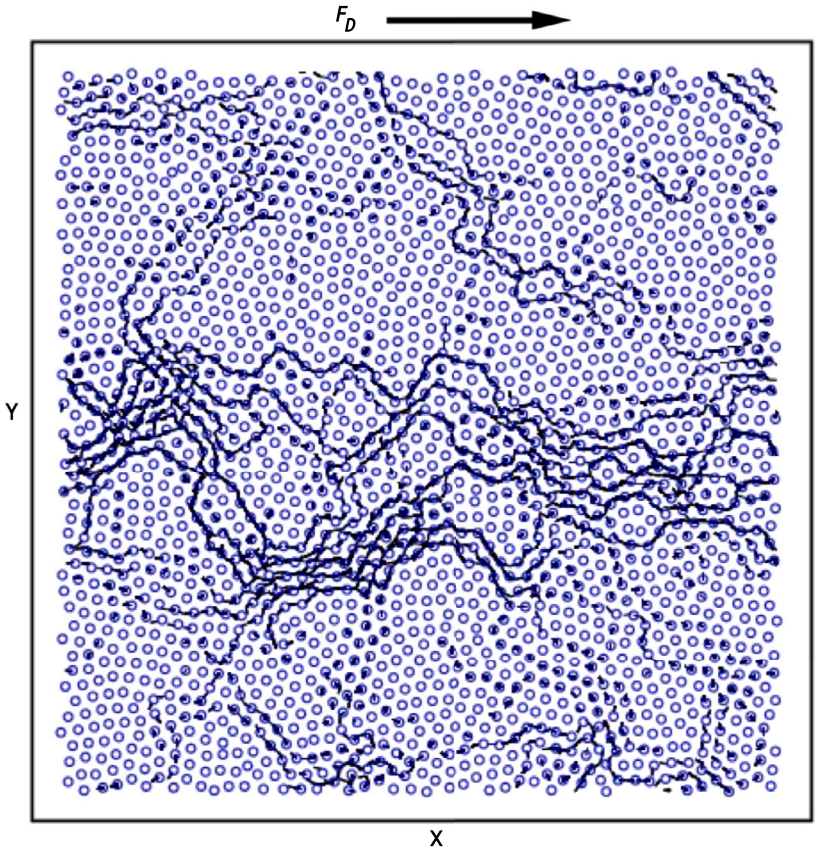

Fig. 27. MD simulations of the vortex response to a pulsed driving force along the x-direction in a system with $n_p = 1$ and $f_p = 1.0$ under driving of magnitude $F_D = 0.045$. A combination of pinned and moving vortices are shown: vortex positions are shown as circles and trajectories as lines. Pinning sites are not shown. *Source:* Reprinted with permission from [470].

under various conditions can also be scaled and the scaling exponents are subsequently used to identify phases. In addition, these simulations produce diagrams of vortex trajectories, as shown in Fig. 27, which can be used to study ordering and disordering of the vortex lattice. They have also provided insight into the formation and configurations of a range of glassy states, the motion of dislocations during plastic flow, and conditions under which a moving solid may form, in which vortex motion is fast and vortex–vortex interactions dominate over vortex–defect interactions [467]. For example, dV/dF_D is thought to saturate in the elastic regime, whereas plastic dynamics may induce a peak as the vortex lattice transitions from a strongly disordered to a more ordered state with increasing $\mathbf{F}_D$ [467,474].

Notice that because in this formalism the vortex itself is treated as a particle or rigid rod, in most studies its applicability is limited to 2D systems of thickness less than the penetration depth. However, recent works have modeled the vortex as a chain of particles connected by elastic strings [467] or springs [475,476], both allowing in principle the consideration of 3D systems.

Another approach to modeling 3D vortex dynamics through MD simulations is by means of the Langevin molecular dynamics algorithm. To model 3D dynamics, vortices are described as three-dimensional elastic lines through the trajectory $\mathbf{r}_i$, with the 2D ab-plane position vector defined as a function of the z coordinate, which simultaneously corresponds to the direction of the applied magnetic field. These lines are then placed in a 3D space with periodic boundary conditions in the xy plane and with free boundary conditions along the z direction. Dynamics is then determined by numerically solving the overdamped Langevin equation:

$$\eta \mathbf{v}_i = \eta \partial \mathbf{r}_i(t,z)/\partial t = -\frac{\delta H[\mathbf{r}_i(t,z)]}{\delta \mathbf{r}_i(t,z)} + \mathbf{f}_i(t,z) \tag{65}$$

for the velocity of the ith vortex, $\mathbf{v}_i$, where $\mathbf{f}_i(t,z)$ represents thermal stochastic forces, modeled as uncorrelated Gaussian white noise of zero mean $\langle \mathbf{f}_i(t,z) \rangle = 0$. Then, to represent the free energy term, Ref. [478] uses the Hamiltonian

$$H[\mathbf{r}_i] = \sum_{i=1}^{N} \int_0^L dz \left[\frac{\tilde{\varepsilon_1}}{2} \left| \frac{d\mathbf{r}_i(z)}{dz} \right|^2 + U_D(\mathbf{r}_i(z), z) + \frac{1}{2} \sum_{j \neq i}^{N} V\left(\left| \mathbf{r}_i(z) - \mathbf{r}_j(z) \right| \right) \right], \tag{66}$$

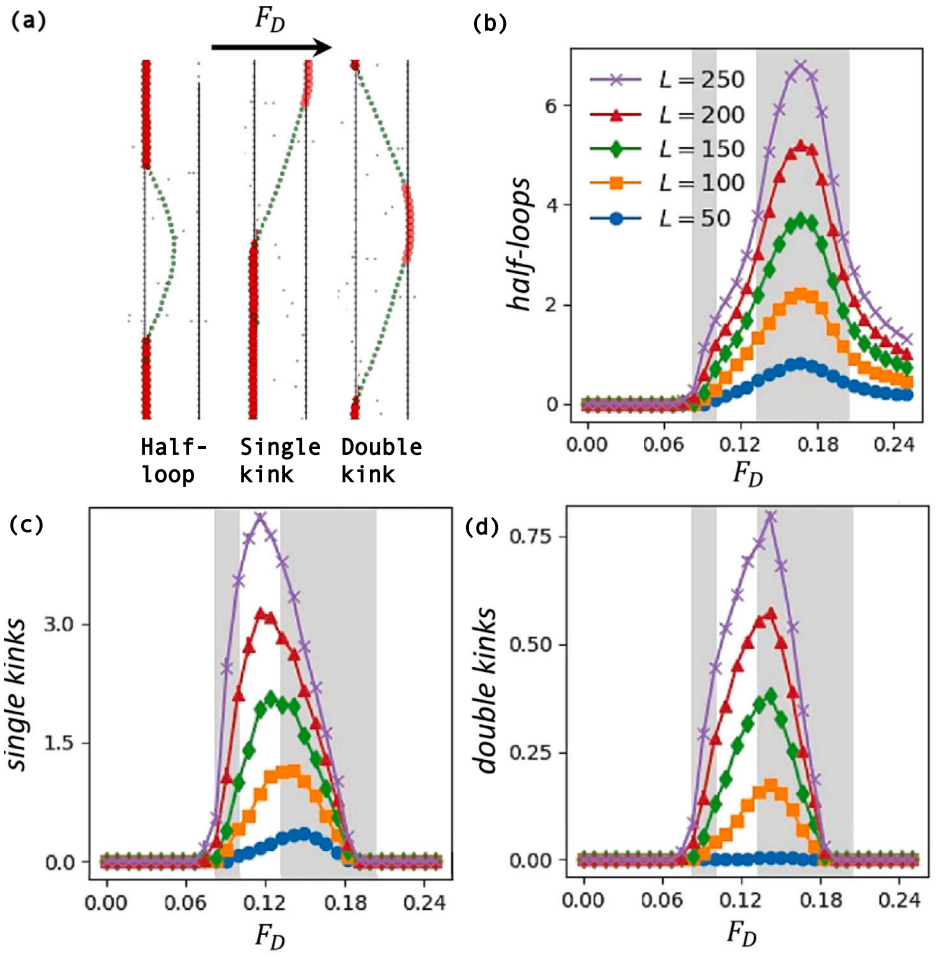

Fig. 28. (a) xz-plane projection of particle-based 3D Langevin molecular dynamics simulations showing three different excitations formed by flux lines interacting with planar defects: half-loop (left), single kink (middle), double kink (right). The green dotted lines represent flux lines, the red dotted sections show part of the flux line pinned to a planar defect, the gray dots are point defects, and the black vertical lines are planar defects. Steady-state number of (b) half-loops, (c) single kinks, and (d) double kinks as a function of drive F_D (units of ε_0) for interacting flux lines in the presence of two planar defects, in samples of thickness L (units of pinning potential width b_0).
Source: Adapted with permission from [477].

whose first term considers the elastic vortex line tension, an attractive potential U_D created by the pinning centers, and the repulsive vortex–vortex interaction potential $V(r)$. Here, $\tilde{\varepsilon_1} \approx \gamma^{-2}\varepsilon_0 \ln(\lambda_{ab}/\xi_{ab})$ is the elastic line stiffness (tilt modulus), N is the number of vortices, and $\varepsilon_0 = \Phi_0^2/(4\pi\mu_0\lambda_{ab}^2)$ is the vortex line energy. Then, the in-plane vortex–vortex interaction potential can be defined by $V(r) = 2\varepsilon_0 K_0(r/\lambda_{ab})$, where K_0 is the zeroth-order modified Bessel function, which, just as when used to describe vortex–vortex interactions in Eq. (64), it represents a logarithmic repulsion that is exponentially screened at the scale λ. Finally, point defects are defined by the potential

$$U_D(\mathbf{r}, z) = -\sum_{\alpha=1}^{n_d} \frac{b_0}{2} p\delta(z - z_\alpha)\left[1 - \tanh\left(5\frac{|\mathbf{r} - \mathbf{r}_\alpha| - b_0}{b_0}\right)\right], \tag{67}$$

where n_d is the number of point defects, b_0 is the pinning potential width, and $\mathbf{r}_\alpha$ and z_α represent the strength of the pinning potential in-plane and in the z direction, respectively. Thus, in order to define a potential for columnar defects, identical potential wells are placed at all positions $z = z_\alpha$ for select in-plane positions $\mathbf{r} = \mathbf{r}_\alpha$.

As shown in Fig. 28, Langevin MD simulations have recently predicted and studied the formation and dynamics of excitations, such as half-loops, single kinks, and double kinks, which emerge when vortices interact with planar and columnar defects [477]. Furthermore, such studies have determined correlation lengths [479], extracted time scales related to pinning and depinning [480], and determined the frequency dependence of voltage noise [481] related to driven vortices navigating different disorder landscapes.

More recently, another example of 3D vortex modeling is the work of Paturi et al. [475], who applied MD to simulate the vortices in superconductors containing nanorods. In this work, as well as others [482], Paturi models 3D dynamics by treating vortices as a

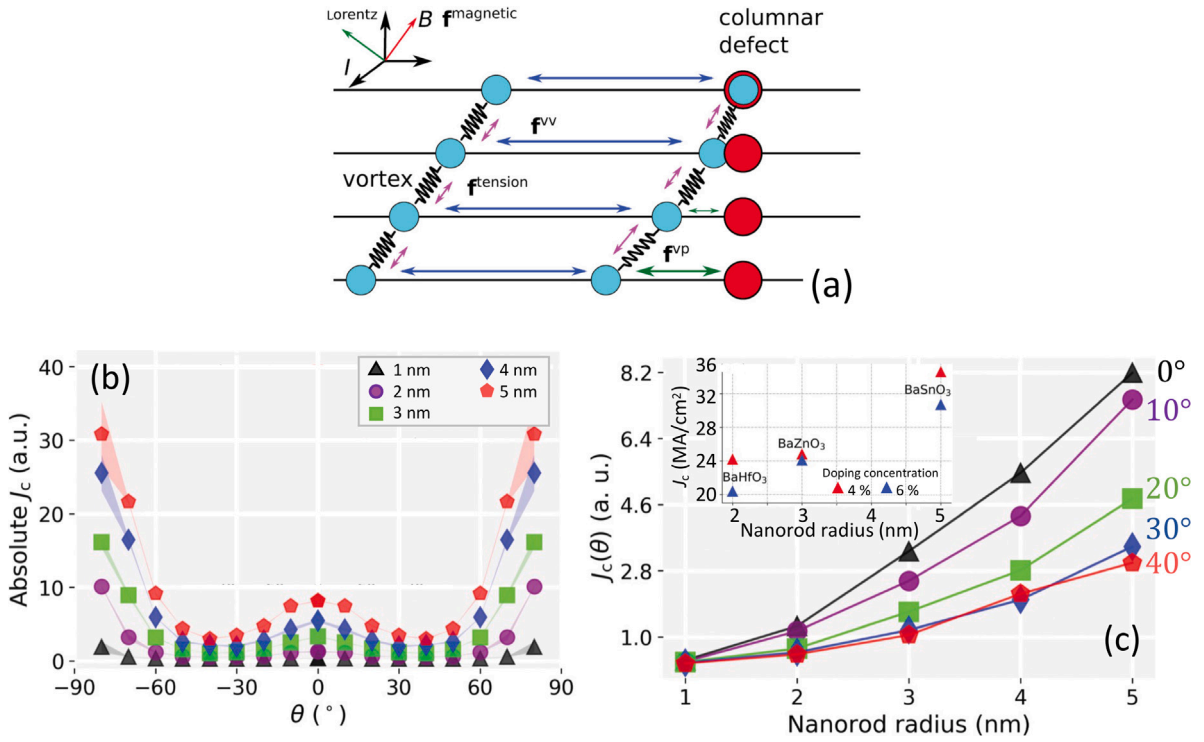

Fig. 29. MD simulations of vortices in a YBCO film containing nanorods. (a) Schematics of a 3D model where vortices are represented by turquoise circles connected with a spring-like force, and pinning sites are depicted as stationary red circles. Interactions are shown with arrows. Reprinted with permission of [475] (b) The simulated dependence of the critical current on applied field orientation for 0.5 T in a YBCO film containing 50 nanorods of varying radius oriented along the *c*-axis. (c) Simulated J_c versus nanorod radius for different applied field orientations. Inset shows experimental measurements of J_c of YBCO films containing nanoparticle dopants at 10 K in a 1 T magnetic field oriented along the *c*-direction.
Source: Adapted with permission from [482].

chain of vortex particles attached to one another via a spring-like force that depends on the magnetic field, see Fig. 29(a), allowing us to conclude that, notably, MD simulations can reproduce the correct anisotropic behavior in the angular dependence of the critical current, as shown in Fig. 29(b–d), whilst simultaneously disclosing the effect of considering different excitations formed by flux lines interacting with planar defects.

6. Engineering J_c for the next generation of applied superconductors

Soon after the discovery of HTS materials such as YBCO and BSCCO in the late 1980s with critical temperatures above the boiling point of LN2 (~ 77 K), or after 2001 when the superconducting properties of MgB_2 with $T_c \approx 39$ K were discovered (nearly doubling the boiling point of LH2, ~ 20 K); and more recently, after the discovery of Fe-based superconductors in 2006, world-wide research efforts have continued pursuing the demonstration of such materials with optimal use of their properties, and for enabling the deployment of a wide range of applications inaccessible to use of conventional conductors. They are based on both thin films (cryo-electronic devices) and on wires, tapes, and coated conductors (power devices), with the potential to make a huge impact on science, technology, sustainable growth, and energy transition. However, a few serious problems still remain to be solved.

6.1. *Milestones in the development of HTS wires and tapes*

One of the primary objectives in the field of superconductivity is the production of long, durable, and flexible conductors for use in various power applications, such as magnetic coils [1,2,483,484]. The fabrication of HTS wires, however, presents significant challenges for two key reasons: the ceramic and brittle nature of most HTS materials, including cuprates, which makes them difficult to handle, and the necessity of achieving biaxial texture in these materials to ensure optimal properties. Nevertheless, several techniques have been developed over recent decades to address these challenges on the superconducting precursors to be discussed below.

6.1.1. BSCCO

The initial method for producing superconducting HTS tapes led to the development of what are known as 'first-generation tapes' which are fabricated using BSCCO through the Powder-in-Tube (PIT) method. This method had been well-known from wire fabrication of low-temperature superconductors, especially Nb_3Sn [485,486], where crushed Sn powder was filled into Nb tubes. Here, sintered BSCCO is placed inside a sealed silver tube, which is then repeatedly rolled and thermally processed in a controlled oxygen atmosphere. The rolling and heating steps are carried out multiple times until the final tape attains the appropriate texture and density of the superconducting core, eliminating various defects (such as pores and cracks) for enhancing grain connectivity and critical current density [487]. While these first-generation tapes exhibit satisfactory self-field performance at 77 K, their in-field performance at elevated temperatures was insufficient for most applications due to the high anisotropy and hence low irreversibility fields of BSCCO [488–490]. Furthermore, the silver sheaths necessary for effective oxygen loading of the superconducting core make these tapes and wires rather expensive. Nevertheless, research on Bi2223 wires is ongoing, and there are several application possibilities for these materials. Ref. [491] gives a comprehensive overview over recent activities. Also Bi2212 wires have recently gained renewed interest due to their possible round shape and macroscopic electronic anisotropy, which is preferred for magnet applications [492].

6.1.2. REBCO

To enhance the in-field performance, an alternative approach was introduced, replacing the superconducting material BSCCO with REBCO compounds. For REBCO, the PIT method turned out not to be successful anymore because for this less anisotropic material a sufficiently sharp texture could hardly be achieved and hence large-angle grain boundaries were blocking the current flow. Paturi et al. nevertheless reached 3.3 kA/cm^2 at 77 K for nano-grained YBCO in silver sheath tapes [493,494]. Recently, REBCO PIT wires gained some interest again due to their potentially round shape, which is preferential for magnet applications. Zhang et al. investigated $YbBa_2Cu_3O_7$ in Ag sheaths by a novel melt-texturing method yielding compact cores [495,496]. Geng et al. reached 46 kA/cm^2 at 4.2 K in self-field and 33 kA/cm^2 in 14 T in YBCO round wires with a similar method [497,498].

Nevertheless, the use of these REBCO compounds basically resulted in the development of the so-called second-generation tapes, or Coated Conductors (CCs) [9,483,499], which were first reported as early as in 1991 [500]. The fabrication of coated conductors (CCs) faces challenges similar to those encountered for first-generation tapes, such as the brittleness of REBCO compounds and the requirement for a sharp biaxial texture to achieve optimal properties. Moreover, the microstructure and morphology of REBCO films are primarily influenced by the deposition process [9,33]. The specific characteristics of the crystallization process in each method result in a unique pinning landscape.

Briefly, there are two main categories of growth techniques, both highly effective in the challenging task of achieving biaxial texture in REBCO films: simultaneous deposition and growth techniques (commonly called 'in-situ growth techniques'), and sequential deposition and growth techniques (also referred to as 'ex-situ growth techniques').

The in-situ growth techniques involve the formation of the REBCO phase occurring directly during the deposition process. In this scenario, deposition and growth are concurrent processes. The growth mode is typically layer-by-layer due to a non-equilibrium process where surface diffusion plays a crucial role. Techniques included in this category are Physical Vapor Deposition (PVD) methods [501] such as Pulsed Laser Deposition (PLD) [502–504]; Pulsed Electron Deposition (PED) [505,506]; Magnetron- [507] and Radio-frequency Sputtering [508]; Liquid Phase Epitaxy (LPE) [509] including Hybrid-LPE [510]; Transient Liquid Assisted Growth (TLAG) [33,511]; as well as (Metal–Organic) Chemical Vapor Deposition (CVD) [512,513] including Laser-CVD [514]. These well-established techniques are widely recognized not only in the field of superconductivity but also in other areas [507,515–518], and generally result in high-quality films.

The ex-situ growth techniques involve a different approach. Here, the REBCO phase is not formed immediately after deposition. Instead, a subsequent annealing process is required to achieve the desired phase, often in a different environment than the deposition (ex situ). Consequently, deposition and growth of the REBCO phase are sequential processes. Most ex-situ growth techniques are solution-based, allowing for continuous deposition over large areas at atmospheric pressure, which significantly reduces costs. Techniques such as Chemical Solution Deposition (CSD) [519], Reactive Co-Evaporation (RCE) [520,521], and the BaF_2 process [522–524] belong to this group.

The architecture of CCs comprises a multilayered structure, consisting of a biaxially textures template, an epitaxial REBCO superconducting film, and protective metallic cap layers. The template consists of a metallic tape and buffer layers that are grown with biaxial texture. Metallic tapes are employed for their superior mechanical properties as well as their availability in long lengths. The buffer layers provide a continuous, smooth, and chemically inert surface, preventing the diffusion of metallic ions from the tape and oxygen to the tape, and facilitating the biaxially textured growth of REBCO films by texture transfer and reducing lattice misfit. Lastly, the protective cap layers serve to protect the superconducting layer from environmental exposure. Among the various steps in this process, procuring the biaxial texture for the optimal growth of the superconducting film is probably the most important one. There are two different strategies: textured metallic tapes, i.e. the Rolling-Assisted Biaxially Textured Substrate (RABiTS) method, and textured buffer layers on an untextured metallic tape, i.e. Ion Beam Assisted Deposition (IBAD) or Inclined Substrate Deposition (ISD).

In the RABiTS approach, which was introduced by Goyal et al. in 1996 [525], the metallic substrate is directly textured. Cube texturing is achieved through a series of rolling and annealing processes applied to an initially untextured metallic substrate, usually NiW while Ag and Cu had also been investigated. Following this, epitaxial buffer layers (typically consisting of a seed layer, a barrier layer, and a cap layer), are grown. The REBCO film is then deposited onto these buffer layers, and a final cap layer is added to protect the superconducting material [526]. Nowadays, flexible substrate ribbons 75 μm thick and more than 1 km long made of

Ni5at%W can be produced. On the other hand, the IBAD technique creates a preferred texture in one of the oxide buffer layers, thus eliminating the need for a pre-textured substrate, typically stainless steel or Hastelloy. Two materials have been employed: Initially, Ytria Stabilized Zirconia (YSZ) was textured by a simultaneous inclined ion beam in a growth selection process within thicknesses of around 1 μm [500]. Later, MgO was used [527,528], which is instead textured by a nucleation selection process within the first 5–10 nm. This process is very fast, making MgO the predominant choice used today.

A third texturing method applied by manufacturers is Inclined Substrate Deposition (ISD). Here, MgO is deposited (e.g. by e-beam deposition) on Hastelloy tapes that are inclined by a certain angle (typically 20°-30°) [529]. By a growth-selection process, MgO is growing biaxially oriented toward the incoming material beam, i.e., is inclined with respect to the substrate normal. This leads to an inclined growth of the epitaxially growing REBCO layer and hence typically skewed angular J_c dependencies, e.g. [530,531]. As a side remark, ISD has also been shown for fluoride films [532], which may interesting as buffer layers for IBS [533].

Once the template is prepared to ensure proper biaxial growth, the REBCO films are deposited. The chosen template as well as REBCO deposition method strongly influence the microstructure and hence the macroscopic properties of the final CC. RABiTS templates have relatively large grains of around 20 μm and usually GB grooves [534], while IBAD templates are usually smoother with grain sizes of the order of 1 μm [535]. ISD templates show typically a very faceted and tilted surface. Solution-based deposition methods show typically a lamellar growth, whereas deposition from the gas phase as PLD show a columnar growth. This influences the transparency and pinning properties of grain boundaries [536]. Perovskite nanoparticles (see next sections) usually grow biaxially textured in physical deposition methods but randomly oriented in solution-based methods, which strongly influences the strain states. These nanostructures can be grown as very well aligned and correlated nanocolumns in physical methods [135] in contrast to solution-based methods. Also on ISD templates due to their tilted geometry are elongated nanostructures hard to achieve [531]. The in-plane orientation of the REBCO layer may influence the strain sensitivity of J_c of the final CC [537]. Needless to say, the choice of template and buffer system determines the mechanical properties of the CC, such as delamination strength, stiffness, bending tolerance etc.

6.1.3. MgB_2 & Fe-based superconductors

For MgB_2 wires, the PIT method has also proven to be successful since grain boundaries are not necessarily current-limiting defects due to the relatively large coherence length. Two methods are possible, in-situ and ex-situ PIT process. In the former, boron (usually powder) and magnesium (in different forms) are filled in the tubes and react to MgB_2 during heat treatment; in the latter, pre-reacted MgB_2 powder is filled in the tubes. A recent review of the current challenges for producing MgB_2 films, bulks, and wires can be found in Ref. [107].

For the Fe-based superconductors, being the latest class of application-relevant superconducting materials, both methods, PIT and coated conductors are investigated. First wire samples of IBS were fabricated by PIT not long after discovery for the three major families 1111, 122, and 11 [538]. Whereas a certain degree of texture within the individual filaments is needed for BSCCO compounds, this is not necessarily the case for IBS because the grain boundaries do not as severely affect the superconducting current flow [539], as it will be shown in Section 6.4. However, grain boundaries are still an issue not so much due to the GB angle but due to foreign phases between the grains that widen the GB regions and limit the superconducting current flow. Several groups are working now on improving the GB transparency and the density of such wires, especially for K-doped 122 wires. For instance, in 2017, a K-doped Sr122 wire of around 100 m length has been demonstrated [540], which still holds the record for length. For reviews of the early development of IBS PIT wires and tapes, refer to [541–543].

IBS coated conductor samples have been prepared so far as mere proof-of-principle studies on basically the same templates as used for cuprate coated conductors [544]. As early as 2011, PLD-grown films of Fe(Se,Te) [545] and Co-doped $BaFe_2As_2$ [546,547] (and later P-doped $BaFe_2As_2$ [548]) were demonstrated with reasonable quality, followed by MBE-grown NdFeAs(O,F) films in 2014 [549]. Most of these films were deposited on IBAD-MgO templates, with PLD-Fe(Se,Te) [550] and electro-deposited FeSe [551] also being deposited on RABiTS templates. This electro-deposition route [552] as well as CSD-grown buffer layers [553] are currently being investigated by Italian groups to reduce the fabrication costs of IBS coated conductors. Moreover, in 2023, Liu et al. demonstrated the first continuously deposited 1 m long IBS coated conductor, prepared as Fe(Se,Te) on a CeO_2-buffered IBAD-MgO template using PLD in a multiturn reel-to-reel system [554], which was recently surpassed by 10 m and even 120 m long IBS CC samples [555].

6.2. Advanced optimization strategies

Paramount to guide the design of the next generation of HTS materials is to find alternatives informed either by theoretical models, numerical simulations, or by in-situ or ex-situ experimental approaches that could lead to a proper engineering of J_c for applications with specific temperature, field, and geometry of operation. Several of these alternatives have already been revised in previous sections, but we have been mostly focused on the in-situ properties of the HTS material at different length scales, i.e., where the vortex dynamics of type-II superconductors can be understood as a statistical average of a bundle of vortices in the macroscopic approach or, from the interaction between individual vortices with other vortices and defects in a more mesoscopic approach. However, in practical terms, J_c can also be engineered by ex-situ approaches which, although less predictable, can be one of the most notorious options in the absence of a unified theory.

In a broader sense, one of the primary tasks for engineering J_c is to avoid or minimize all material defects that hinder or diminish the supercurrent flow, such as large foreign phases, voids, large-angle grain boundaries (GBs), and radiation damage. Texturing of BSCCO tapes and REBCO coated conductors, as well as densification of power-in-tube wires and tapes, fall into this category.

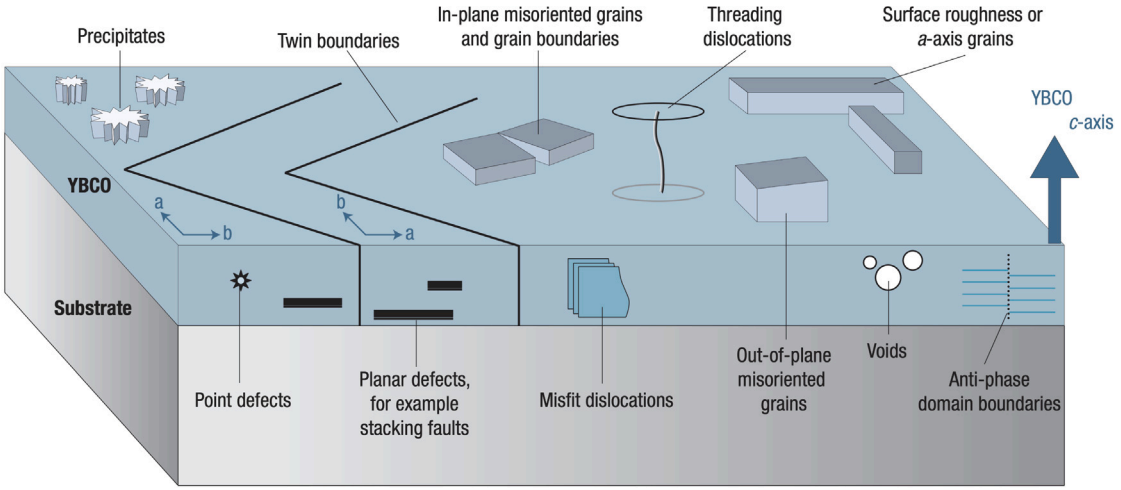

Fig. 30. Illustration of the many thin film defects that have been proposed as flux pinning sites in YBCO. Anything that locally disturbs the crystalline perfection over a scale of 0.1 – 1 nm is a candidate.
Source: Apdapted with permissions from of [556].

Somewhat more sophisticated, another closely related method is to increase J_c by optimizing and utilizing natural growth defects as effective pinning centers, e.g., dislocations, low-angle GBs, nano-precipitates, stacking faults, anti-phase boundaries, etc. (see Fig. 30); especially controlling their size and distribution by adjusting the preparation methods. A further optimization regarding the magnitude and anisotropy of J_c is the intended introduction of artificial pinning centers (APCs), i.e., radiation tracks or defects and (typically self-assembled) non-superconducting nanoparticles or nanocolumns, which is usually regarded as J_c engineering in the narrow sense.

Superconducting nanocomposites are created by introducing APCs to enhance the pinning performance of REBCO films. Initial attempts to produce these nanocomposites were made using in-situ growth techniques, i.e., involving the simultaneous deposition and growth of both the REBCO phase and the APCs. A common feature of nanocomposite thin films produced with in-situ techniques, which promote heterogeneous nucleation, is the presence of coherent interfaces between the embedded nanoparticles and the superconducting matrix. Additionally, this heterogeneous nucleation often leads to a self-assembly process of nanoparticles into uniformly dispersed vertical nanostructures or nanorods with diameters less than 5 nm [557,558]. The weaker pinning when the magnetic field is parallel to the *c*-axis is consequently enhanced by the interaction between nanorods and these vortices.

As discussed earlier, in the case of ex-situ growth techniques the growth process differs as these techniques are characterized by sequential deposition and growth steps. For nanocomposites, the growth process is also sequential, as the formation of the REBCO phase and the nanoparticles occurs at different stages rather than simultaneously. This sequential deposition and growth process promotes homogeneous nucleation of the nanoparticles, typically resulting in a random and uniform distribution within the matrix. Consequently, incoherent interfaces between the NPs and the REBCO phase are more prevalent with ex-situ techniques compared to in-situ methods, generally leading to a more isotropic pinning landscape [559]. This is a significant observation because isotropic wires are generally preferred. This preference arises not only because the wire's performance is independent of the field direction but also because the design and construction of magnets [2] can leverage the extensive experience gained from using low-temperature superconducting conductors in well-established technologies like NMR and MRI magnets [17]. Additionally, achieving nanoparticles with a size less than 10 nm is particularly challenging when using ex-situ growth techniques. Consequently, the pinning mechanism in films produced by ex-situ growth techniques differs from that in films grown using in-situ methods. The ultimate goal is *critical currents by design* [32], i.e., the design and optimization of pinning landscapes for the needs of a given application based on established models (see previous sections).

Finally, as discussed in Section 5, pinning being an interaction depends on the properties of both the pinning centers and the flux lines, either individually or as an ensemble. Therefore, J_c can also be increased by strengthening the vortex matter, somehow increasing the Cooper pair density (which deepens the pinning potentials), increasing the critical fields (H_{c2} and H_{irr}), and reducing anisotropy together with thermal fluctuations. Specifically, the J_c of practical superconductors can be improved by grain boundary engineering or controlling the hole doping level in cuprates (given its impact on the superfluid density), adding APCs in the form of material dopants, and even by changing or inflicting new defect morphologies by irradiation effects. These are the different phenomena to which we will devote the final sections of this review due to their paramount importance. In particular, we will focus on the engineering of REBCO and IBS thin films, including polycrystalline BSCCO and MgB_2 samples, for which the engineering of the J_c properties result less dependent on the mechanical properties of their granular counterparts. Therefore, for a dedicated review of superconducting bulks and their state-of-the-art technology, the reader is referred to Refs. [172,560–562].

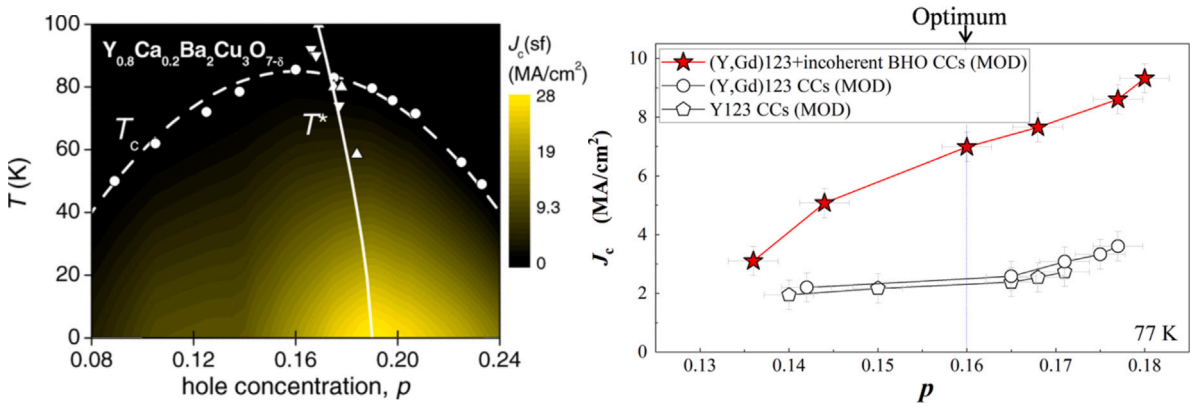

Fig. 31. (Top pane) Dome behavior of T_c as a function of doping and color plot of self-field (sf) critical current density J_c as a function of doping and temperature [Reprinted with permissions from [563]. (Bottom pane) Experimental data showing the doping dependence of the sf critical current density for standard (Y,Gd)$Ba_2Cu_3O_7$ and (Y,Gd)$Ba_2Cu_3O_7$ containing $BaHfO_3$ nanoparticle inclusions.
Source: Adapted with permissions from [564].

6.3. Engineering J_c by charge carrier doping

As discussed above, the engineering of HTS materials for applications is generally focused on understanding of microstructural modifications that can render improved pinning conditions and, therefore, greater J_c. However, this results in cumbersome scenarios where the electronic properties of the superconductors cannot be easily linked with the rather anisotropic behavior of the critical current density, $\mathbf{J}_c(\mathbf{B}, T)$, despite it is well known that they have a great impact on its intensity. For instance, in addition to material defects, electron and hole doping have an indirect effect on J_c, generally because doping affects the superfluid density to which the penetration depth is sensitive. In fact, in the case of cuprates, i.e., where the dominant superconducting features of the material lie in the electronic structure of the CuO_2 planes, the material can exhibit from antiferromagnetic insulating properties to a normal metal behavior just by changing charge carrier concentration, p, i.e., the number of holes per Cu ion in the CuO_2 planes.

Although adding atomic dopants or microstructural defects into the REBCO compounds or any other HTS material is probably one of the most promising and extensive alternatives for improving the pinning conditions of any practical superconductor, these alternatives usually demand large amounts of dopants, which can also lead to a strong suppression of the T_c, with no clear way yet on how to systematically reduce the dissipative flux motion for increasing J_c. However, if, at least for cuprates, we analyze the more fundamental route for engineering J_c, which refers to controlling and understanding the influence of p, some more general conclusions can be drawn. In this sense, we want to recall the work by Talantsev and co-workers [565], who experimentally investigated the hole-doping dependence of the self-field critical current density J_c^{sf} in $YBa_2Cu_3O_{7-\delta}$. They found that J_c^{sf} follows a common trend for the hole doping, rising to a sharp peak on the slightly overdoped side of the parabola for T_c versus p, as illustrated in Fig. 31. Tallon [563] subsequently explained these results using general arguments based on thermodynamics. In particular, he showed that thermodynamic properties related to J_c^{sf} predominantly depend on the superfluid density ρ_s and scales as $J_c \sim \rho_s T_c$.

On the other hand, concerning T_c optimization, Zaanen [566] explained that T_c becomes high in $YBa_2Cu_3O_{7-\delta}$ since one approaches the Planckian dissipation limit connecting viscosity to entropy in quantum liquids [567], where one can show that the pseudogap phase reduces ρ_s [568]. In fact, in hole-doped cuprates, the pseudogap is still present at the optimal doping where T_c reaches its peak [563]. Therefore, one must overdope the samples to a level around 0.19 holes per Cu atom where the pseudogap closes to reach the predicted peak in the doping dependent $\rho_s T_c$ as shown in the top pane of Fig. 31. Similarly, Stangl et al. [569] have recently presented an experimental study of oxygen doping in underdoped, optimally doped, and overdoped $YBa_2Cu_3O_{7-\delta}$ thin films, finding direct correlations among the charge carrier density n_H, the hole doping p, and the critical current density J_c. These results demonstrate a significant increase in J_c with n_H, as we approach the quantum critical point due to an increase in the superconducting condensation energy. The critical current reached a high value of 90 MA/cm^2 at 5 K, which corresponds to about 64% of the maximum depairing current density of d-wave superconductors recently predicted in Ref. [266]. Consequently, overdoping $YBa_2Cu_3O_{7-\delta}$ is a promising route to enhance J_c. Moreover, very recently, Miura et al. [564] combined Tallon's thermodynamic route for increasing the ρ_s with their established methods of incorporating incoherent $BaHfO_3$ nanoparticles, where their results clearly show (see bottom pane of Fig. 31) that thermodynamic improvements can work in parallel with APCs.

Analogously, at the high-temperature spectrum for superconducting applications, i.e., at or over the liquid nitrogen (LN2) boiling temperature of 77 K, the iron-based superconductors (IBS) are the other kind of materials where attaining a proper understanding of the charge carrier doping on the $J_c(B, \theta, T)$ dynamics is of utter importance. This is because in IBS materials, J_c also depends strongly on the doping level, and the maxima of J_c and T_c are not necessarily coinciding. This has been systematically investigated by Song, Ishida et al. [570,571] for $BaFe_2As_2$ (Ba122) compounds with different kinds of doping, such as single crystals of $Ba_{1-x}K_xFe_2As_2$ (K-Ba122), $BaFe_2(As_{1-x}P_x)_2$ (P-Ba122), and $Ba(Fe_{1-x}Co_x)_2As_2$ (Co-Ba122), either for hole, electron, and isovalent doping, respectively. In all cases, the maximum of J_c is in the slightly underdoped to the nearly optimally doped region of the phase diagram, most

pronounced for K doping. The reasons are minima of the penetration depth and coherence length near optimum T_c (i.e. near a quantum critical point) [571–574] and a concomitant strong maximum of the vortex line energy, large values of dT_c/dx and hence strong δT_c pinning, large normal state resistivities supporting δl pinning, and the vicinity to magnetically ordered phases. Indeed, record-high J_c values have been measured for P-Ba122 thin films [575][533] without any considerable pinning centers visible in TEM.

For Fe(Se,Te), the superconducting properties not only depend on the Se:Te stoichiometry (see e.g. [576]), but also on the Fe off-stoichiometry, i.e., vacancies or excess iron which can be regulated [577], e.g. by oxygen annealing with which a doubling of J_c can be achieved [578]. For a review on such annealing effects, see [579].

Similarly, for *Ln*FeAsO compounds (*Ln* lanthanide; typically Nd, Sm), the maximum of J_c seems to lie in the overdoped region. This has been revealed recently in studies on NdFeAs(O,H) films. Whereas F doping is only possible up to 20% with respect to O, levels up to 80% are possible with H doping [580]. Also here, a possible quantum critical point (QCP) has been identified by temperature-dependent and anisotropy measurements of the normal state resistivity [581], where T_c remains at high levels in a wide doping range while the electronic anisotropy decreases [582], leading to an upward shift of the irreversibility line. Macroscopically clean H-doped samples show similarly high J_c values ($F_{p,max} \sim 90$ GN/m^3 at $B \parallel c$, 4 K) as a F-doped film of similar thickness with highly complex microstructure [583]. Again, by combining optimizing the charge carrier density and introducing APCs, Miura et al. were recently able to quadruple the critical current density in overdoped SmFeAs(O,H) thin films treated by proton irradiation [584].

6.4. Grain boundary engineering

Due to the extremely small coherence lengths of $\xi_{ab} \sim 2$ nm in cuprates and IBS, the structurally disturbed regions in otherwise clean large-angle grain boundaries constitute weak links, or Josephson contacts. Under this scenario, the critical current density has shown to decrease exponentially with grain boundary misorientation angle for many different cuprates [585], and more recently for Fe-based superconductors [539]. This is easily explained by the exponential decrease of tunnel currents with barrier thickness plus a more or less linear increase of grain boundary thickness with the misorientation angle. Also, even low-angle grain boundaries with GB angles above a certain critical value θ_c may act as weak links in cuprates due to the strong strain dependence of J_c, band-bending near dislocations, and oxygen disorder near the GB plane. This critical angle θ_c is below 5° for cuprates (depending on film quality) but around 9° in IBS [539] due to differences in strain dependence and coherence length. Also the exponential decay of J_c is slower than for cuprates. That means IBS with reasonable properties may be producible with lower degrees of texture than cuprates and hence via powder-in-tube or on cheaper coated conductor templates.

Eisterer [586] recently developed a model for the critical current density of polycrystalline HTS samples based on the abundance of GB angles (i.e., degree and kind of texture) and their transparency (i.e., the angle dependence of J_c), and Hecher et al. [587] determined with a related model that a small grain size is actually beneficial for current transport and magnetization behavior in polycrystalline IBS samples, even though the GBs are current-limiting. The current–voltage curves $V(I)$ across grain boundaries are usually linear with offset, showing the so-called non-ohmic differentially linear behavior [588], which may even be segmented, as shown by Diaz et al. [589]. This is due to extremely high electrical fields across the grain boundary and hence this region being in the flux-flow regime (linear dissipation) rather than in the flux-creep regime (non-linear dissipation). This strong limitation of J_c by grain boundaries was the main obstacle for the manufacture of HTS wires and tapes based on cuprate superconductors with sufficiently high current carrying capability, since strong biaxial texture is needed.

For sufficiently small fields, low angle grain boundaries may also act as pinning centers, as shown e.g., by Horide and Matsumoto on YBCO bicrystal films [590] with 5° tilt GB. Due to the larger critical angle, this effect is even more important for IBS. For them, it has been shown that low angle GBs in Co- [547], P- [548], and K-doped Ba122 [591] as well as in NdFeAs(O,F) [592] are beneficial for J_c. In fact, the K-doped Ba122 films have shown J_c values close to the depairing J_c [591], holding the record for IBS at the moment for a field of 10 T applied parallel to the *c*-direction [593], only surpassed by Pb-ion-irradiated K-Ba122 single crystals [594]. Also, it turned out that depending on the misorientation angle or texture quality, as well as the pinning properties of the grains and morphology of the GBs, there is a certain crossover in magnetic field between a region of GB limitation of J_c at low magnetic fields and a region of pinning limitation at high fields [588,595]. This means that J_c cannot be improved in the high-field region by GB engineering, and, from a theoretical point of view, describing the field-dependence of the critical current density $J_c(B)$ with a pinning force analysis, e.g. following Dew-Hughes [596] or similar models, is only reasonable at high-fields in samples with GB networks acting as weak links [597]. This cross-over field has also been recently identified for IBS films on technical substrates [598]. Whether J_c is indeed limited by weak links in layered superconductors, can be estimated by a 2D-fluctuation-based criterion as developed by Talantsev and Crump [599].

Due to the strongly increased texture quality of coated conductor samples as well as the meandering grain boundaries, e.g., in MOD-derived YBCO films, the cross-over field is shifted to lower and lower values (between 1 T and 4 T at 77 K), where the pinning improvement gains in importance. In this sense, pioneering research mainly involving PLD has shown that J_c can indeed be considerably improved by either substrate decoration [600] or by the insertion of perovskite nanoparticles such as $BaZrO_3$ [601], $BaIrO_3$ [602], Yttria-Stabilized Zirconia (YSZ) [603] or Y_2O_3 nanoparticles [604]. In fact, substantial work has been conducted along this line of research by many groups worldwide, inspecting the growth and properties of such microstructures by insertion of non-superconducting nanoparticulate phases, such as perovskites, double-perovskites, pyrochlores, etc., for which we refer our readers to a further review presented in [605].

6.5. Artificial pinning in advanced superconductors

As described in previous sections, due to Lorentz-like forces and thermal fluctuations that lead to the movement of vortices, J_c is usually strongly depressed by magnetic fields, especially as temperature increases, but such movement can be suppressed by sufficiently strong pinning centers. Therefore, fundamental studies on the effects of engineering the microstructure of advanced superconducting materials by the addition of APCs, while avoiding current-limiting defects such as GBs, voids, cracks, large precipitates, etc., result of great importance to conceive the optimization and market penetration of superconducting devices. Thus, we devote this section to present a brief but comprehensive summary of the most notable experimental efforts in introducing such artificial pinning centers in HTS cuprates and other superconducting materials for practical applications such as MgB_2 and IBS compounds. For similarly important and ongoing work on LTS materials, foremost Nb-Ti and Nb_3Sn, the reader may refer to the abundance of textbooks and reviews on these materials (see e.g., Refs. [46,47,606–610]).

6.5.1. REBCO grown by PLD

As mentioned above, very soon after the discovery of YBCO, single crystals and epitaxial thin films were fabricated and used for studies of fundamental properties of this new material. It was a great surprise that the critical current densities in thin films are two orders of magnitude larger than in single crystals, and those two orders of magnitude larger than in sintered powder samples. The reason for the former is the very different nature and densities of defects in the two morphologies, and the reason for the latter is the weak-link behavior of grain boundaries of sufficiently large angle [585,611].

Initially, almost all efforts to grow films were through physical in-situ methods, like co-evaporation, magnetron sputtering, molecular beam epitaxy (MBE), and PLD, i.e., methods involving a deposition chamber with a vacuum-controlled atmosphere. It soon became clear that PLD offers many advantages over the other methods. So, most of the 'pioneering' work on artificial pinning centers at the beginning of this century has been done almost exclusively using PLD.

While in single crystals there are only low densities of weak point-like defects due to oxygen vacancies and few twins, in YBCO thin films there are a large number of different defects depending on the fabrication process. Considering the much larger thermal energy at LN2 temperature (77 K) compared with the use of LHe (4.2 K) for LTS materials, in YBCO the pinning energy must overcome both the Lorentz-like forces and the thermal energy, hence the paramount importance of the pinning centers. In fact, in YBCO thin films, the so-called natural pinning centers may occur during deposition or in the target itself, and these can be point defects, vacancies, interstitials, atomic substitutions, columnar defects, dislocations, nanorods, antiphase boundaries, twin boundaries, stacking faults, precipitates etc. [556], as illustrated in Fig. 30.

However, especially in high magnetic fields, natural pinning centers are not sufficient and/or not strong enough to overcome the large Lorentz-like forces. Therefore, for using YBCO in high magnetic field applications, nano-engineering of APCs is needed. The first cost-effective method for fabricating APCs was the so-called substrate decoration [612,613], proposed initially for Tl-based superconducting films grown by sputtering and post-annealing on substrates decorated with Ag nano-islands; followed later by the same method applied to YBCO films grown by PLD [600]. The improvement of J_c could be further increased by a proper choice of the film architecture, e.g., using a multilayer structure in which YBCO layers are separated by thin insulating layers such as CeO_2 [614].

The next step forward was the deposition from a composite target, e.g., YBCO with perovskite nano-inclusions, e.g., perovskites, $BaZrO_3$ (BZO) [601] or double-perovskites, such as $RE_2Ba{-}4CuMO_y$ (M: W, Zr, Nb) [615,616] and Ba_2YNbO_6 [617,618], or rare-earth tantalates [619], where one specific type of pinning centers was sought.

Whether such non-superconducting additions grow as more or less round nanoparticles, as (usually c-axis-)correlated nano-columns, or as ab-parallel platelets, as well as their diameters, is strongly governed by the strain states at the interfaces among nanoparticle, matrix, and substrate [621]. These strain states around coherent nanoparticles/nanocolumns are also responsible for a typical small T_c decrease in PLD-grown nanocomposites (in contrast to CSD, where the nanoparticles are randomly oriented and incoherent), which is explained by a reduction in oxygen content in the strained regions [622]. This may be alleviated by Ca doping [623], very similar to the Ca doping of grain boundaries [624].

Recent approaches are targeting several types of pinning centers by using double-doping, for example, with BZO and Y_2O_3 [625, 626], Gd_3TaO_7 and Ba_2YNbO_6 [627] (mainly leading to $Ba_2(Y,Gd)(Nb,Ta)O_6$ precipitates though), $BaSnO_3$ and Y_2O_3 [628], or $LaAlO_3$ and YBa_2NbO_6 [629].

Mixed double perovskites, typically $Ba_2Y(Nb,Ta)O_6$ (BYNTO), offer with the ratio of Nb and Ta another degree of freedom, which determines the morphology of the nanocolumns, especially their diameter, straightness, and interface quality. Ercolano et al. [627] showed an unusual pinning landscape consisting of $Ba_2(Y/Gd)(Nb/Ta)O_6$ segmented nanorods parallel to the c-axis and $(Y/Gd)_2O_3$ plate-like nanoparticles parallel to the ab-plane together with large pinning forces and matching effects. Similarly promising properties with large matching and irreversibility fields by addition of BYNTO were reported by Rizzo et al. [630,631] and Opherden et al. [135], a small review on YBCO/BYNTO can be found in [632]. In this case, the films exhibit a complex microstructure composed of pinning centers that vary in size, shape, and orientation. This leads to a large enhancement of the J_c values and of the pinning force density at 77 K. Moreover, for magnetic fields up to several Tesla, the critical current density displays values that are nearly constant so demonstrating the strength of the new pinning configuration. The field dependence of the pinning force density $F_p(B)$ has its maximum at the matching field showing different behaviors below and above it. In fact, below the matching field it is demonstrated that the sample is dominated by the creation of half loop and double kink structures while above the matching field the sample exhibits typical flux creep processes because the pinning centers are weaker and uncorrelated [135].

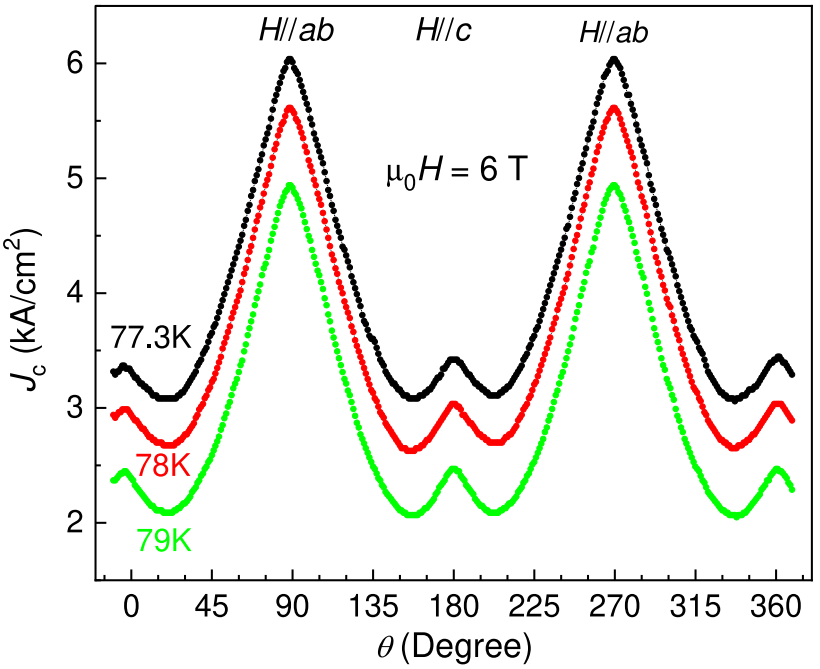

Fig. 32. Angular dependence of the critical current density regarding field orientation at 6 T and three temperatures for a (15 pulses Ag/450 nm YBCO)×10 multilayer film at three temperatures (15 pulses on the Ag target per layer led to the best quasi-layer of Ag nano-islands).
Source: Adapted with permission from [620].

The combination of the three methods: substrate decoration, BZO nano-inclusions, and quasi-multilayer architecture, brings together the advantages of each approach, creating a very complex landscape of synergetic pinning centers. By a combination of substrate decoration with Ag nanodots (that increased critical current density, allowed the growth of thicker films without the usual drastic decrease in J_c and proved to promote columnar growth of YBCO) with BZO doping, BZO nanorods and nanoparticles act as effective pinning centers for magnetic field in both directions: along the *c*-axis and in the *ab*-plane [633,634].

Additionally, in PLD-grown films, nano-engineering of pinning centers can also change the anisotropy of J_c with respect to the direction of the magnetic field, i.e., the $J_c(B,\theta)$ function. For example, the introduction of substrate decoration and quasi-multilayer approach involving Ag nano-islands that proved to induce a columnar growth of YBCO also induces a secondary maximum in the angle dependence of the critical current density, for the field parallel to the *c*-axis, as can be seen in Fig. 32 for a high magnetic field of 6 T. Also, for the artificial pinning centers obtained by using YBCO targets with a BZO secondary phase, the substrate temperature and the frequency of the laser pulses play a crucial role. For instance, it was discovered that lower substrate temperature and higher pulse frequency led mostly to the formation of BZO nanoparticles (with critical current larger for fields parallel to the *ab*-planes), while higher substrate temperature and lower pulse frequency led to self-assembled BZO nanorods parallel to the *c*-axis, leading to a larger critical current for field in the *c*-axis direction, as shown in Fig. 33.

Similarly, in a DC field of 1 T, BZO-doped YBCO films deposited at 780 °C and 8 Hz have the maximum J_c at field orientations close to the *ab*-plane, and a rather flat minimum range for orientations close to the *c*-axis. There are now several types of pinning centers, natural and artificial, introduced by BZO doping, of which a large number are nanoparticles, and a minority are *c*-axis correlated extended defects. However, a higher deposition temperature (800 °C) and a smaller repetition rate (longer time for diffusion) gives sufficient energy and time for the BZO to self-assemble into *c*-axis oriented nanorods, leading to a maximum in J_c at field orientations parallel to the *c*-axis. Similar dependencies were found for YBCO-BZO quasimultilayers, where high deposition temperatures and thin YBCO layers lead to BZO nanocolumns rather than nanoparticles, which can be explained by the nanoparticle/-rod formation being a diffusion-driven process [635]. On the other hand, when using a BZO-doped YBCO target together with Ag nano-islands, synergetic pinning centers can be obtained, which are quite effective in increasing critical currents for all DC field orientations. This can be seen in Fig. 34, which shows the $J_c(\theta)$ dependencies of a 0.4 μm thick Ag-decorated BZO-doped YBCO film at several fields between 0.5 T and 5 T at 77.3 K.

Finally, at fields smaller than 3 T the maximum J_c is obtained for DC fields parallel to the *c*-axis, Fig. 34, meaning that both the *c*-axis correlated artificial pinning centers created by the Ag-induced columnar growth of YBCO together with the BZO self-assembled nanorods provide a very strong pinning landscape for the flux lines. When the field is increased, the number of *c*-axis correlated pinning centers is not sufficient, so the system now depends on the natural anisotropy of YBCO, with maximum J_c for fields parallel to the *ab*-plane. For fields larger than 3.5 T, J_c is largest for fields parallel to the *ab*-plane, while there still exists a local maximum for fields parallel to the *c*-axis due to BZO columnar defects. However, for a field window between 1.5 T and 3.5 T, the anisotropy

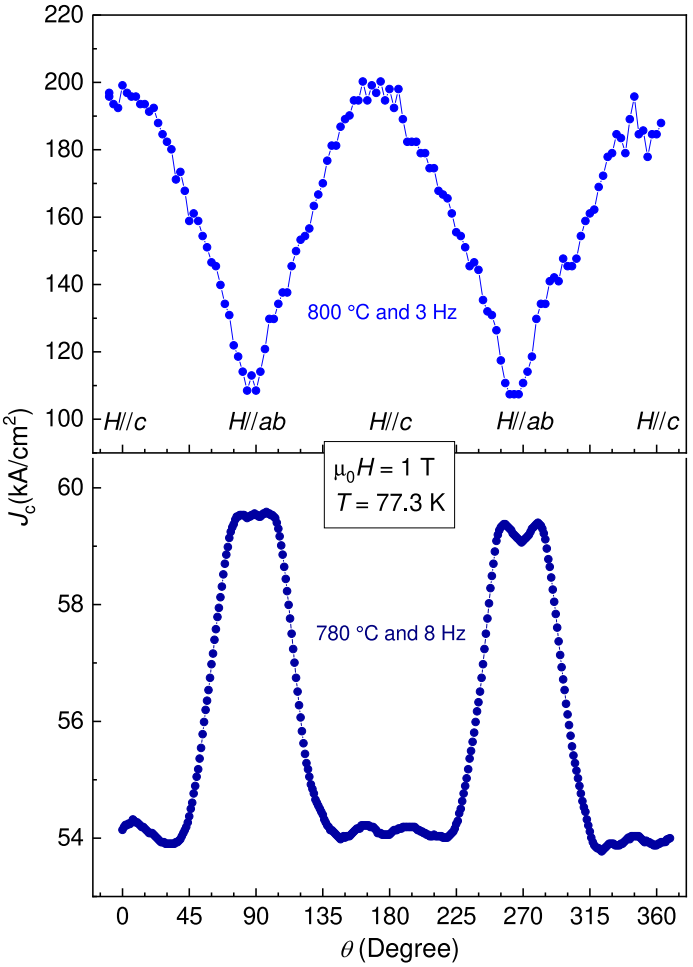

Fig. 33. Angular dependence of J_c at 1 T, 77.3 K of BZO-doped YBCO films deposited at 800 °C and 3 Hz (light blue) compared to 780 °C and 8Hz (dark blue).
Source: Adapted with permission from [620].

of the critical current density is rather small, which is beneficial for a large number of applications in coils and solenoids in which various parts of the coil feels the magnetic field at a different orientation.

6.5.2. REBCO grown by CSD / MOD

Although PLD produces excellent REBCO films with artificial pinning centers as described above, the need for vacuum chambers can severely restrict the fabrication of long-lengths of coated conductors. Maximum achieved lengths until now of several hundred meters are still rather expensive in terms of $/A·m. Therefore, manufacturing by much more cost-effective alternatives such as Chemical Solution Deposition (CSD) results of utter interest.

CSD, one of the MOD (metal–organic decomposition) methods, comprises four steps: preparation of the precursor solution (mixing salts in desired stoichiometry in adequate solvents), deposition (e.g., spin coating, bar coating, slot-die coating, and inkjet printing), pyrolysis (to remove all the organic content), and growth (crystallization and oxygenation).

The particularities of the crystallization process, being a sequential or 'ex-situ' growth technique, cause a characteristically different pinning landscape compared to PLD. In CSD, immediately after the deposition, there is no REBCO phase formed yet; the deposition and the growth of the REBCO phase are sequential processes. This leads to a laminar microstructure in comparison to rather columnar microstructures for PLD. Furthermore, the development of the REBCO matrix does not happen at the same time as the NPs as in PLD. Here, the NPs usually grow after homogeneous nucleation in an amorphous environment and afterwards, the REBCO matrix around them after heterogeneous nucleation at the substrate. This leads to usually randomly oriented NPs with incoherent interfaces, in contrast to highly oriented, self-assembled nanoparticles/nanocolumns with usually coherent interfaces as in PLD. Importantly, to achieve NPs with a size < 10 nm is very difficult in ex-situ growth techniques.

Furthermore, choosing adequate NPs is very important. Criteria are: (*i*) high stability at the REBCO crystallization temperatures, (*ii*) no chemical reactivity with REBCO or intermediate phases, and (*iii*) no cationic substitution into REBCO, which would

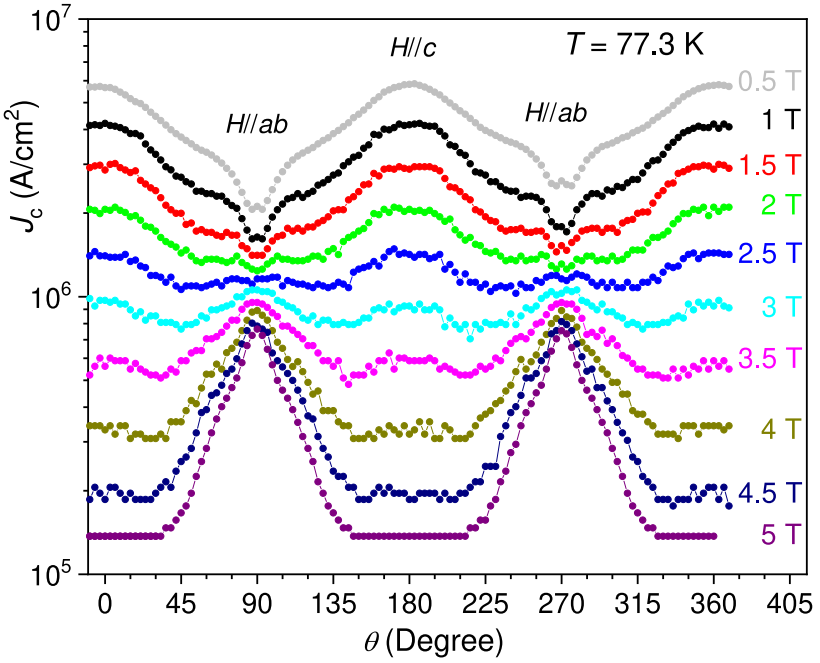

Fig. 34. Angular dependence of J_c of a 0.4 μm thick Ag-decorated BZO-doped YBCO film at 77.3 K in applied fields between 0.5 and 5 T. *Source:* Adapted with permission from [620].

diminish T_c. Multiple different NPs were employed in recent years, e.g. the barium perovskites (BaMO_3, M = Zr, Sn and Hf) [229,231,636,637], binary rare-earth oxides (RE_xO_y, RE = Y, Gd, Ho, Er, Dy) and their solid solutions [638], and double perovskites (Ba$_2RE$(Ta,Nb)O$_6$, RE = Y, Yb, Gd, Er) [639].

While CSD is an ex-situ growth technique, the preparation of CSD-grown nanocomposites can be further distinguished regarding the formation of the NPs: 'in-situ' and 'ex-situ'. In the 'in-situ' approach, the NPs spontaneously segregate during crystallization from solutions containing also the precursor salts for the NPs. Excellent superconducting properties and pinning performance has been shown for this method [229,231,636,637,639,640]. The complex NP growth mechanisms with kinetic and thermodynamic effects hinder a proper control of their nucleation and growth, leading to a limitation in achievable pinning performances. In the 'ex-situ' approach, pre-formed NPs are suspended in a colloidal solution, which is mixed with the REBCO precursor solution. The NPs are embedded in the REBCO matrix during the thermal processes. A key advantage of this novel approach is the precise control of the composition, size, and concentration of the NPs.

The NPs themselves are effective pinning centers if their size is similar to the coherence length of the REBCO compound, i.e., 2-5 nm. If much larger, they generally do not improve J_c, and often even decrease it. Such 2-5 nm NPs are relatively easy to achieve using in-situ growth techniques like PLD, but are much more challenging to produce with CSD. Some years ago it was discovered that the NPs in CSD can create additional pinning centers, e.g., by a certain freedom to modify the features of the NPs by controlling the nucleation process [641]. The nucleation of the NPs can be tuned by changing the crystallization processing parameters.

As described by Llordés et al. [231], the interface NPs/REBCO is usually incoherent, which generates interfacial energy in these local regions, which, if sufficiently large, is released by the formation of extra Cu–O chains or stacking faults (SFs) [229,231]. The partial dislocations in their perimeter create nanoscale strained regions that prevent the Cooper-pair formation and, thus, form effective pinning centers [231,642], Fig. 35, which was proved by correlating the pinning force with the nanostrain ε [231,639]. Considering all this, this SFs scenario is key for the pinning performance and properties of 'in-situ' CSD nanocomposite films, as supported by several works [231,638,639,643]. Most of the work on the pinning properties of such nanocomposite films concerns randomly oriented NPs, especially well studied for YBCO–BZO samples [229,231,644]. An exhaustive analysis of the H-T phase diagrams has demonstrated that the isotropic-strong defect contribution controls the pinning, especially at intermediate temperatures and low magnetic fields [645], and lies indeed at the origin of their enhanced properties, see Fig. 36.

The SFs lead to a significant increase in the isotropic-strong contribution, particularly relevant at intermediate fields and temperatures. They also increase the anisotropic-strong contribution for $H \parallel ab$, making them a decisive defect to analyze and understand the pinning properties of 'in-situ' nanocomposites [641,644]. The effective pinning anisotropy γ_{eff}, hence, decreases with increasing the nanostrain associated to the stacking faults. This entails a much smoother dependence of J_c with the orientation of the magnetic field but is not related to a change in the intrinsic anisotropy of REBCO compounds [646]. In addition, stacking faults affect the twin boundary landscape by breaking their vertical coherence, rendering them into pinning centers instead of channeling planes. At low temperatures, the twin boundaries, therefore, lose their ability to act as vortex channels, and there is no decay in the $J_c(B,\theta)$ in specific current/field configurations where channeling effects may govern the vortex dynamics [647,648].

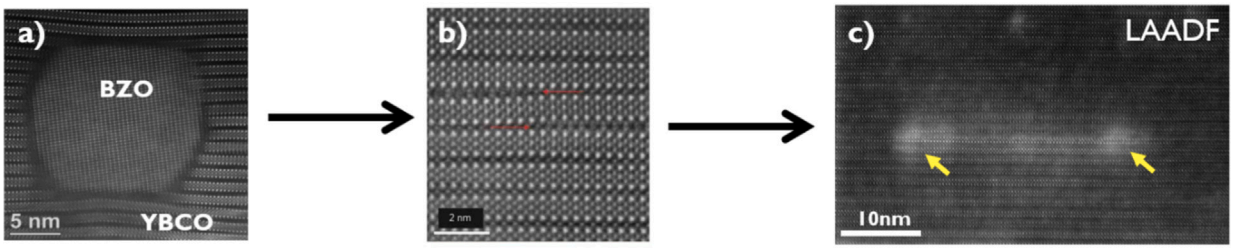

Fig. 35. TEM images summarizing the SFs formation due to the presence of large nanoparticles (> 5 nm). (a) The embedded NPs create a distortion in the YBCO matrix, which causes an interfacial energy. (b) This energy is released by adding extra Cu–O chains or stacking faults. Adapted with permission from [231] (c) At the perimeter of these intergrowths, very strained nanoscale regions appear in the low-angle annular dark-field scanning electron microscopy (LAADF) images, i.e., bright contrast regions indicated with yellow arrows, which act as normal regions that pin the vortices.
Source: Adapted with permission from [649].

The SFs also affect thermal activation of flux motion and, hence, offer the chance to reduce flux creep. For incoherent NPs, the elastic-to-plastic creep crossover line shifts to higher temperatures, resulting in lower creep rates S compared to pristine films. The extended elastic creep region correlates with the increase of isotropic nanostrain, which is responsible for the major isotropic-strong pinning in YBCO nanocomposites [136,650]. This scenario of dominant pinning by stacking faults is widely accepted, but alternative perspectives exist. Some authors have reported on 'in-situ' nanocomposite films exhibiting excellent performance at different magnetic fields without significant SF densities [651–653], which suggests other pinning mechanisms, at least under certain conditions.

In the 'ex-situ' approach, the use of simple oxide NPs like CeO_2 or ZrO_2 leads to the formation of $BaCeO_3$ or $BaZrO_3$ during the crystallization process as a result of the reaction with the Ba present in the precursors [654–656]. In this case, and also for the case of preformed $BaMO_3$ NPs [657,658], pinning is comparable to the 'in-situ' approach. TEM images show a high density of SFs originating from the randomly oriented NPs in the 'ex-situ' films [654,655,657,658] with microstructures very similar to the 'in-situ' films. Therefore, the pinning mechanisms described above are still valid for the 'ex-situ' films, as evidenced by the correlation of the crossover magnetic field, $\mu_0 H^*$, with the nanostrain for different types of 'ex-situ' nanocomposites (see Fig. 37(a)). The field $\mu_0 H^*$, also called accommodation field and usually determined at 90% of J_c in self-field, is a measure for the transition between single-vortex pinning to collective pinning. The incorporation of NPs in the 'ex-situ' films causes a large increase in nanostrain and consequently $\mu_0 H^*$, just as in the 'in-situ' nanocomposites. This translates into a similar trend of strong and weak pinning contributions [641], following also the same trend with the NP concentration (see e.g., Fig. 37(b)).

One of the advantages of the 'ex-situ' approach is the possibility to reduce the size of the NPs. In this sense, an increase in the strong pinning contribution in samples with NPs in the range of 5 nm has been recently reported [658]. Thus, under this scenario and considering this NP size, it is very likely that the NPs themselves are associated in a synergetic manner to the partial dislocations to enhance vortex pinning because their mean diameter is close to the coherence length (ξ), hence offering a new pinning scenario in CSD nanocomposite films.

6.5.3. BSCCO compounds

As for REBCO, similar non-superconducting foreign phases have been tested for BSCCO compounds as strong pinning centers including simple oxides (mainly MgO), perovskites (mainly $SrZrO_3$), and the formation of double perovskites. All these investigations started somewhat earlier (in the mid-90s) than the development of coated conductors, basically in parallel to the development of the 1st generation of superconducting wires and tapes. Besides those, elemental substitutions have been successfully tested as well, such as Y or Gd for Ca [659,660], Ni or Cr for Cu [661,662], F for O [663], and Lu for Sr [664]. For instance, in the case of Pb-doped Bi2212 samples with Lu substitutions, such as $Bi_{1.6}Pb_{0.5}Sr_{2-x}Lu_xCa_{1.1}Cu_{2.1}O_{8+\delta}$ [664], it is noteworthy that these samples reach significantly higher T_c (95.8 K) and J_c (ranging from ~1.4 to 14×10^6 A/m^2 at 64 K for $x \simeq 0-0.1$) compared to their pure Pb-Bi2212 counterparts (T_c = 80.7 K, x = 0). This enhancement is believed to result from a crossover from an overdoped to an optimally doped condition in the hole density at the CuO_2 planes. However, as the Lu doping level increases beyond x = 0.1, J_c begins to decrease due to reduced grain size, increased porosity, and grain misorientation. Similarly, in the case of Gd substitutions, $Bi_{1.6}Pb_{0.4}Sr_2Ca_{1-x}Gd_xCu_2O_{8+\delta}$ samples with Gd doping at x = 0.1 exhibit enhanced grain boundary weak-links and flux pinning centers, achieving a critical temperature of approximately 90.22 K and a self-field critical current density of 4.7×10^8 A/m^2 at 5 K [660].

However, in contrast to REBCO, all this has been kept as a side topic despite significant efforts to improve their J_c are still ongoing [665]. The reasons for it are varied, but mainly due to the much lower irreversibility fields of BSCCO at elevated temperatures compared to REBCO (e.g., at 0.25 T vs. 10 T at 77 K with $B \parallel c$), what makes BSCCO only useful either at low fields (e.g. for power cables at 77 K) or low temperatures (e.g. in magnet coils at 4 K). Therefore, other microstructural aspects remained more important for optimizing J_c in these polycrystalline yet textured wires and tapes, such as phase formation improvement by Pb doping, grain boundary issues and texturing as well as macroscopic defects such as sausaging of filaments, voids and cracks. Eventually, the APC investigations were therefore taken over by REBCO in the early 2000's, when grain boundary issues were mainly solved for those materials.

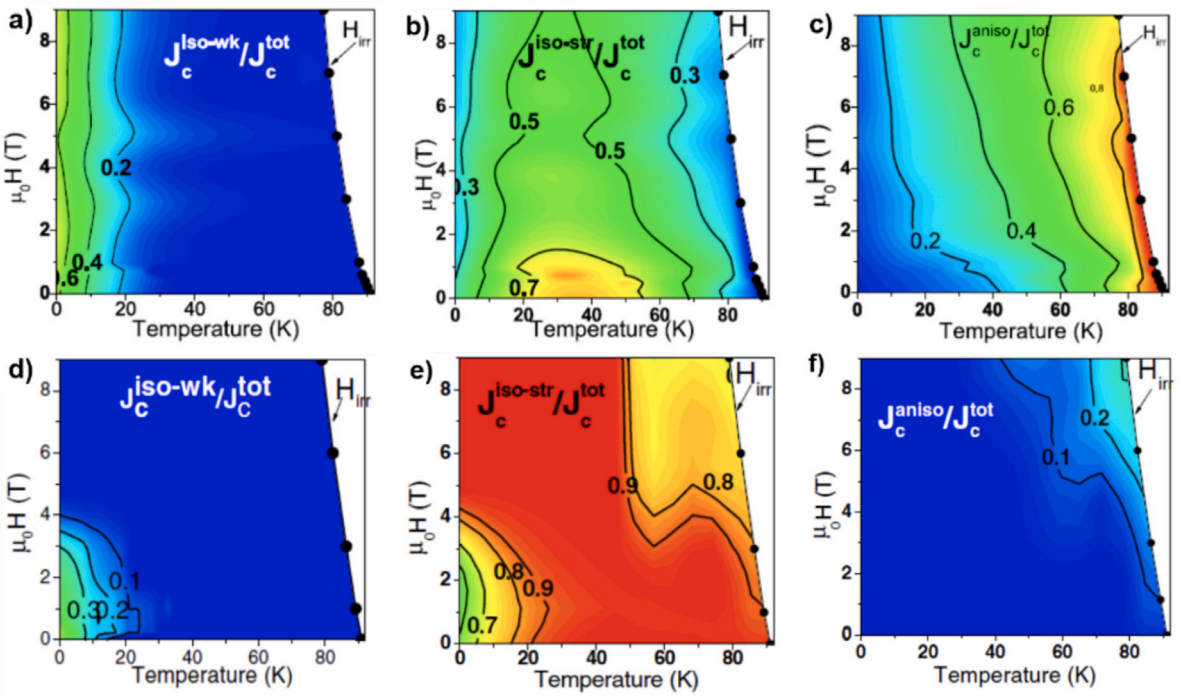

Fig. 36. Pinning phase diagrams corresponding to (a) J_c^{iso-wk}/J_c^{tot} ratio, (b) $J_c^{iso-str}/J_c^{tot}$ ratio and (c) J_c^{aniso}/J_c^{tot} ratio as a function of B and T for a standard TFA–YBCO film and (d) J_c^{iso-wk}/J_c^{tot} ratio, (e) $J_c^{iso-str}/J_c^{tot}$ ratio and (f) J_c^{aniso}/J_c^{tot} ratio as a function of B and T for a YBCO-BZO nanocomposite film. Numbers indicate the relative weight. Also shown is the irreversibility line, $B_{irr}(T)$.
Source: Panels adapted with permission from [644].

Due to the polycrystalline nature of most of the investigated samples, the APCs have several effects. They are not only growing within the grains as pinning centers but can also agglomerate between the grains, which may lead either to current blockage or to improved grain connectivity, depending on the chosen material combination. Furthermore, some of the additives are not stable, e.g. MgO has been found to form $Mg_{1-x}Cu_xO$ [666], and Al_2O_3 to turn into $(Sr,Ca)_3Al_2O_6$ [667], which changes the stoichiometry of the matrix. Furthermore, transition metals may also dope on the Cu side, usually leading to T_c decrease. With this regard, TiO_2 [668], NiO [669], but also sulphides [670] and rare-earth oxides [671] were found to be detrimental to BSCCO. Nevertheless, CdO has been recently found to be more stable if doped with 5% of Mn or Fe [672,673]. Takahira et al. doped Pb-containing Bi2223 films with Y_2O_3 and Al_2O_3 [674]. Both additions lead to a significant increase in the Bi2212 phase, characterized by intergrowths and stacking faults. However, this also resulted in a substantial reduction of T_c, to about one-tenth of that observed in (Bi,Pb)2223 thin films without Al_2O_3, and even much lower for samples with Y_2O_3. Although J_c was improved compared to a Bi2223 tape, the addition of oxides ultimately reduced J_c due to the formation of several foreign phases.

Besides APCs (see Table 2), also growth-related defects, such as Bi-2201 intergrowths [675] and Ca_2PbO_4 particles by thermal treatment [676] have been investigated. In contrast to REBCO, no self-assembled nanocolumns in BSCCO have been reported so far, which may be due to the more different growth rates in the *ab*-plane and the *c*-directions, or the weaker layer coupling and hence a more pronounced overgrowth of particles by the matrix. However, it is known that with MgO nanorods aligned parallel to *c* or *ab* in a Bi2212 thick film, B_{irr} and J_c for $B \parallel c$ can be significantly increased [677].

Finally, while Bi2212 single crystals and bulks have a very low critical current density in self field, J_c^{sf}, it becomes substantially larger in thin films. For instance, for a 100 nm thin film $J_c^{sf} \simeq 0.06\,MA/cm^2$ has been reported [678], and for a 50 nm film $J_c^{sf} = 1.0\,MA/cm^2$ [679], both at 50 K and films grown by PLD. Yamasaki et al. showed 0.09 MA/cm^2 and 0.6 MA/cm^2 for 110 nm and 280 nm thick MOCVD-grown Bi2212 films, respectively [680]. Keppert et al. recently reached 2.2 MA/cm^2 in a phase-pure and very smooth PLD-grown 50 nm thick film on LAO [681]. Similar values have been achieved for Bi2223 thin films with 5 MA/cm^2 at 50 K [682]. The much stronger pinning observed in BSCCO thin films is mostly caused by the usual growth defects, such as dislocation cores, domain boundaries, antiphase boundaries, and stacking faults; and possibly also by nanostrain, known to enhance vortex pinning in HTS cuprates [658].

6.5.4. MgB_2

Unlike most REBCO materials, the grain boundaries are not a problem in the case of MgB_2 due to its usually much larger coherence length (10 – 40 nm), which is about one order of magnitude greater than in the case of YBCO [706,707]. In fact, grain boundaries can be effective pinning centers [708], but even in this case pinning engineering plays an important role in improving the performance of the material, mainly by modifying the density and the quality of grain boundaries.

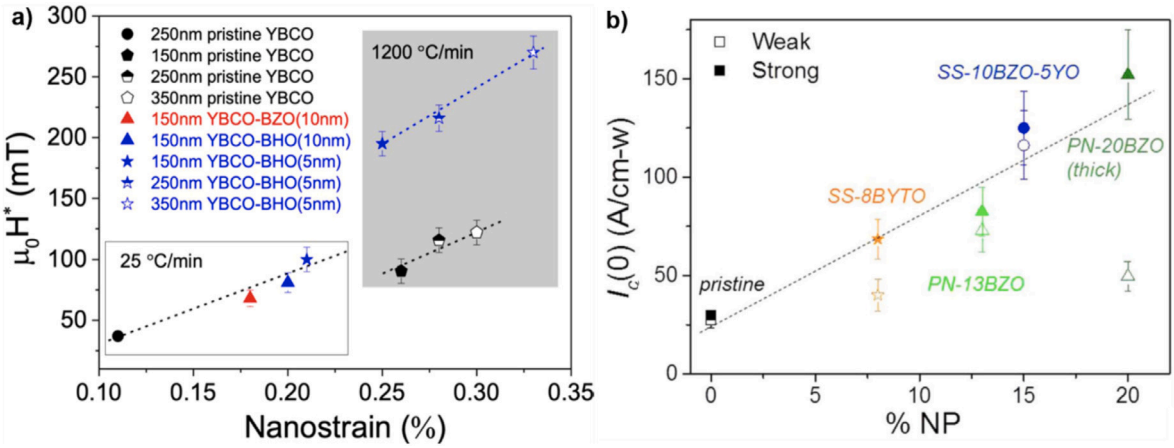

Fig. 37. (a) Dependence of $\mu_0 H^*$ at 5 K on the nanostrain for pristine YBCO and different ex-situ YBCO-BMO nanocomposite (panel reprinted from [658]) and (b) weak and strong contributions to $I_c(0)$ (extrapolated values of I_c at 0 K) for different in-situ (SS in the graph) and ex-situ (PN in the graph) nanocomposite films.
Source: Panels adapted with permission from [641].

Table 2
Selected work on artificial pinning centers (APCs) in BSCCO. All Bi2223 samples, as well as the Bi2212 samples marked by ∗ are Pb-doped. sf: self-field, poly: polycrystalline bulk or powder.

Matrix	APC	Sample	J_c/J_c^{prist}	conditions	remarks	Refs.
Bi2223	Ni on Cu	tapes	2.7	77 K, 400 mT		[661]
	Cr on Cu	tapes	3.4	77 K, 400 mT		[662]
	CdO	poly	5.9	30 K, sf	2212–2223 mixture	[683,684]
	MgO	tapes	3.2	5 K(?), sf	in GBs	[685,686]
	ZnO	poly	2.4	77 K, sf		[687]
	ZrO_2	tapes	1.3	5 K, 1 T		[688]
	Cr_2O_3	poly	1.7	77 K, sf	slight T_c increase	[689]
	Al_2O_3	poly	2.2	77 K, 0.3 T	slight T_c increase	[667,690]
	SiC	tapes	1.2	77 K, sf		[691]
Bi2212	Ag doping	film	1.25	5 K, 1 T	Ag in GBs	[692]
	F on O	poly	2	5 K, 1 T		[663]
	Y on Ca	film	1.8	70 K, sf	resistivity decreased	[659]
	Gd on Ca	poly*	1.75	5 K, sf	T_c increase	[660]
	Lu on Sr	poly*	10	64 K, sf	T_c and B_{irr} increase	[664]
	CdO	poly*	up to 2.9	60 K, sf	T_c increase	[672,673,693]
	MgO	tapes	3.0	20 K, 1 T		[694–697]
	MgO	poly	15	60 K, 90 mT		[666]
	MgO	film	1.8	40 K, 0.4 T		[698]
	MgO	thick film	3.8	20 K, 0.5 T	MgO nanorods	[677]
	BaO_2	tape	2	4.2 K, sf		[699]
	Re_2O_3	film	1.5	10 K, sf	*Re*:Y,Er	[700]
	AeIrO_3	film	up to 3.2	0.85T_c, sf	*Ae*:Ca,Sr,Ba; T_c decrease	[701,702]
	$SrZrO_3$	poly	1.6	5 K, 1 T		[703,704]
	$SrHfO_3$	poly	5	5 K, 1 T		[704]
	$SrZrO_3$	tapes	~2	60 K, sf	–	[705]
	$SrZrO_3$	film	–	–	TEM study	[665]
	Sr_2CaMoO_6	poly	1	5 K, 1 T	improvement at 60 K	[704]
	Sr_2CaWO_6	poly	3.5	5 K, 1 T		[704]

A higher density of grain boundaries is obtained by nanostructuring of the grains. Fabrication of MgB_2 with nano-grains depends on raw materials and processing technology. In general, processing of MgB_2 is classified into two groups of methods: in-situ and ex-situ routes. In the first one, the MgB_2 phase is formed by the reaction between Mg and B, while in the second one the MgB_2 compound is straightforwardly used. There are advantages and disadvantages. For example, the in-situ route applies lower processing temperatures, typically between 650 and 850 °C, but one has to deal with a high vapor pressure of Mg and its high reactivity, e.g., with oxygen. These aspects influence not only the quality but also the reproducibility since processing control is difficult. Some improvements are obtained when using the ex-situ route, but processing temperatures are higher, usually above 1000 °C. High temperatures are needed because sintering of MgB_2 starts at 850-950 °C. The high vapor pressure of Mg, apart from the problems

of Mg evaporation and MgO formation, leads to the production of materials with poor density, especially in the in-situ routes. Pressure-assisted processing techniques were successful in tackling these issues. For bulk fabrication, spark plasma sintering (SPS) gained recognition as a versatile and reproducible method. This technique simultaneously applies a uniaxial pressure and a current on the powders placed within a die system. The current has a pulsed component and, although still under debate, there is evidence that, apart from resistive heating, it can promote activation processes far away from equilibrium, such as the formation of hot spots, electro-diffusion, grain boundary cleaning, sparks formation accompanied by plasma states, and heating from inside to outside as in the microwave heating [709–712]. As a consequence, sintering temperature and time in SPS are often found to be decreased while highly dense materials are obtained. In addition, SPS is a flexible technique allowing high heating and cooling rates, which are very useful features to avoid grain coarsening, and thus to obtain nanostructured materials. It is noteworthy that SPS influences especially grain boundaries. Therefore, this observation suggests that the SPS of MgB_2 deserves attention for pinning control. In this framework, the very recent use of non-conventional spark plasma sintering [713] is worth mentioning. In fact, if a sintering temperature equal to 750 °C under 300 MPa is used, the grain connectivity is improved, and the density of the sample is enhanced with respect to the one obtained by conventional solid-state sintering methods. Due to the improved grain size refinement, the J_c values show a 67% improvement compared to the ones obtained with traditional fabrication techniques.

Grain boundaries and grains can be modified by the introduction of additives. Formation of nano-precipitates or their effect on microstructure by the introduction of new interfaces, defects, or strain can all contribute to pinning if their size is comparable with ξ. For example, it has been reported how Ni nanoparticles act as further pinning centers [714]. This, together with the more uniformly refined MgB_2 grains and increased grain boundaries, enhances the J_c values at high applied fields with a significant enhancement also of the irreversibility fields $B_{irr}(T)$. Even in this case, when the temperature is increased too much (above 500 °C) during the fabrication process, the intergranular connectivity worsens implying a depressed critical current density inside the superconductor.

Another approach is to use additives as sources of elements that act as substitutes in the crystal lattice of MgB_2. Then, triggered by crystal structure modification, the electronic structure also changes having an impact on the intrinsic pinning properties of the material, possibly caused by the variation in the local strain with a modification of interfaces between the particles with different substitution levels. In fact, many additives can induce effective pinning in what can be described as MgB_2-matrix composites with precipitates, but the situation is rather different regarding chemical substitutions. Only a few elements can act as substitutes in the crystal lattice of MgB_2 for reasonably high and detectable solubility limits. An interesting example is Zr doping on MgB_2 bulk synthesized by solid state method [715]. Generally, the heat treatment temperature is crucial in order to obtain refined grain size and improved grain connectivity. In MgB_2 bulk samples, if this temperature is varied from 650 °C and 800 °C, Zr does not occupy the atomic sites inside the MgB_2 crystal structure, instead it produces ZrB_2 particles within the MgB_2 matrix. In this way, the J_c values are enhanced due to the good grain connectivity detectable analyzing the sample microstructure. It is also worth underlining in this context that a different heating rate during the fabrication process can bring changes in the microstructure and the morphology of the sample which modify its superconducting properties [716]. In particular, a low heating rate such as 5 K/min has shown a better MgB_2 grain connectivity improving the critical current density behavior in high magnetic fields. On the other hand, a high heating rate like 30 K/min causes a degeneration of the superconducting properties since the grain connectivity is largely worsened due to the creation of many vacancies in the sample. From a practical viewpoint, only carbon substituting for boron has high solubility and has been proven to produce a strong pinning effect [717]. Nevertheless, the higher the substitution level with carbon is, the lower the critical temperature becomes. Hence, co-additives, e.g., a mixture of additives providing carbon for substitution and those promoting the formation of the nanostructured composite, can prove rewarding in the control and enhancement of pinning and, therefore, J_c. To do so, the influence of additives individually, in combination, and in the context of a certain technology and raw materials has to be considered.

In the case of ex-situ SPS, various additives have already been investigated. In particular, the magnetic field dependence of the critical current density is of interest, which has been measured in several MgB_2 samples with an optimum amount of additives at 20 K, Fig. 38. Clearly, the optimum amount of an additive A is within a narrow range and corresponds approximately to a stoichiometry defined as $(MgB_2)_{0.9}A_{0.01}$. This is due to the interplay between opposing effects on J_c of enhanced pinning and lower connectivity for higher additive amounts introduced in the superconducting MgB_2 matrix. In fact, on the one hand, the additives of Fig. 38 as well as B_4C, Ge, GeO_2 and RE_2O_3 (RE = Ho, Eu, La) enhance J_c at high magnetic fields up to ~ 60%, while there is often a decrease at low magnetic fields. There are also other additives that boost J_c when added individually or as a pair, e.g. Ho_2O_3+Te. However on the other hand, there are additives such as Sb, Bi, Sb_2O_5, hexagonal boron nitride (h-BN), and graphene (G), or co-additives such as C_{60}+cBN and $Ge_2C_6H_{10}O_7$+cBN that do not improve J_c at all. Remarkably, for the indicated co-additives, J_c is enhanced if one of the component additives is used separately.

Thus, to understand the influence of additives on the pinning and J_c characteristics of MgB_2, we have classified the additives into 5 main groups: (i) Type-1 additives such as h-BN and G which are *almost* not reactive with MgB_2; (ii) Type-2 enclosing RE_2O_3 additives reacting with MgB_2 as well as the formation of impurity boride M_uB_v phases with M being a metal from the additive; (iii) Type-3 additives such as Sb, Sb_2O_3, Sb_2O_5, Bi, Bi_2O_3, Te, TeO_2, Ge, and GeO_2, all reacting with MgB_2 and, the formation of impurity Mg_mM_n phases; (iv) Type-4 additives such as fullerene (F), F + c-BN, SiC + Te, $Ge_2H_{10}C_6O_7$, and B_4C as sources of C for substituting boron in the crystal lattice of MgB_2; and finally (v) Type-5 such as Ho_2O_3+Te co-additives, which could be understood within the Type-2 + Type-3 families. For additives of Type-4, besides the 'substitution' effects, the 'composite' effects for Type-1 and 3 are also active. Therefore, it can be considered that a F-additive is purely Type-4, whilst (F + c-BN) is a Type 4+1, (Te + SiC) and $Ge_2H_{10}C_6O_7$ a type 4+3, and B_4C is approximately of Type 4+1 or 4+3.

The pinning details for the as-defined types of additives are commonly investigated within the pinning force scaling law [719], $f_p = Kh^p(1-h)^q$, where f_p is the reduced pinning force density, $F_p/F_{p,max}$, with $F_{p,max}$ being the maximum pinning force, and h being

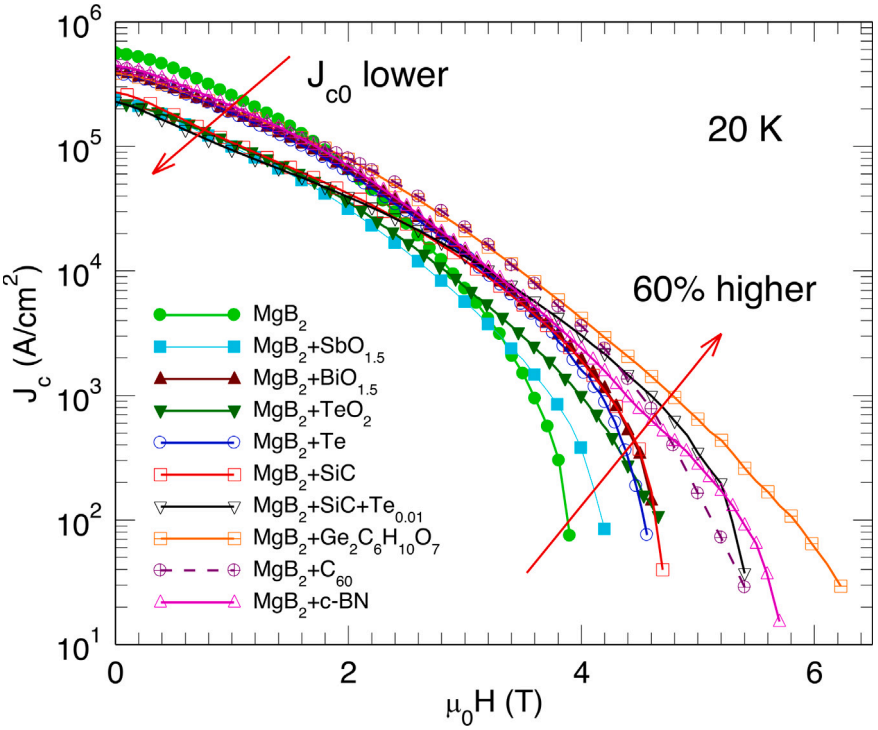

Fig. 38. Dependence of critical current density on the magnetic field at 20 K of several MgB_2 samples with different additives obtained by ex-situ SPS. Starting compositions are: MgB_2, $MgB_2(SbO_{1.5})_{0.01}$, $MgB_2(BiO_{1.5})_{0.01}$, $MgB_2(TeO_2)_{0.01}$, $MgB_2(Te)_{0.01}$, $MgB_2(SiC)_{0.025}$, $MgB_2(SiC)_{0.025}Te_{0.01}$, $MgB_2(Ge_2C_6H_{10}O_7)_{0.0014}$, $MgB_2(C_{60})_{0.015}$, and MgB_2(cubic-BN)$_{0.01}$.
Source: Adapted with permission from [718].

here the ratio between the applied magnetic field, H, and the irreversibility field, H_{irr}, which is a widely adopted generalization of the original work, where $h = H/H_{c2}$ [596,719], for strong-fluctuation superconductors. Then, p and q are statistical parameters that can be extracted by fitting experimental data to $f_p(h)$ curves at $5-35$ K. The maximum pinning force, at $f_p = 1$, is reached at the reduced field $h_0 = p/(p+q)$. According to Dew-Hughes [596], surface pinning (grain boundary pinning in the case of MgB_2) is active when $h_0 = 0.2$, $p = 0.5$ and $q = 2$, while pinning on point defects is active for $h_0 = 0.33$, $p = 1$, and $q = 2$. These are the main mechanisms theoretically contributing to pinning in MgB_2. In this sense, it is worth noticing that by representing the parameters h_0, p, and q as a function of the amount z of carbon substituting for boron in $Mg(B_{1-z}C_z)_2$, it has also been found that carbon substitution has a strong influence on the pinning-force-related parameters [718,720], where the values of z can be determined via the variation of the MgB_2 lattice parameter [721,722].

The influence of the additives of Type-1 to Type-3 on pinning force parameters is significant at low substitutional carbon amounts, i.e., for $z \leq 0.018$. But in this z-range, p and q can take abnormally high values (p up to ~ 2 and q up to ~ 5.6) very different from the theoretically predicted values. Abnormal values with h_0 as low as 0.13 were observed for samples of Type-2 and Type-5. Unusually low values of h_0 were reported also by other authors [723,724]. Thus, the validity of the scaling analysis procedure to correctly assess pinning when applied to MgB_2 is questionable. Samples of the so-called Type-5, such as $(MgB_2)_{0.99}(Te_x(HoO_{1.5})_y)_{0.01}$, with $x/y = 0/0$, $0.73/0.27 = 2.7$, $0.57/0.43 = 1.32$, $0.4/0.6 = 0.67$, $0.31/0.69 = 0.45$, $0.27/0.75 = 0.33$ have shown the possibility to tune the self-field critical current density J_c^{sf} depending on the ratio x/y. In this sense, it was found that the maximum values of $F_{p,max}$ and therefore J_c^{sf} for these samples are for $x/y = 0.67$, more specifically, with $F_{p,max} = 9.2$ GN/m^3 at 5 K, 6.4 GN/m^3 at 15 K, and 4.4 GN/m^3 at 20 K.

More interesting is that for $x < 0.67$, the $f(h)$ curves present a kink and inflection points as shown in Fig. 39. It is worth noticing that these were randomly oriented samples, although the kink effect has also been observed in other cases, e.g., in c-axis-oriented samples [725]. Therefore, as a consequence of the additives, the non-uniformities specific to the microstructure (grain size and distribution), defects, local strain, non-stoichiometry, orientation and anisotropy features can all impact the shape of the pinning force. The presence of kinks and inflection points generates difficulties in fitting the reduced pinning force curves. Even without an obvious kink, there are fitting problems, and pinning force parameters can deviate significantly from the theoretical values. Poor fitting, though with p and q parameters closer to theoretical values, was encountered for C-rich samples ($z > 0.018$).

Furthermore, the shape and maximum position of the $f(h)$ curve change with temperature. This can be seen in Fig. 39, where h_0 shifts to higher values for increasing temperatures (compare curves at 5 K and 20 K for a given sample, noticing the shift of the h_0-position and the position of the arrows indicating the kinks). Thus, following the pinning force scaling law analysis under

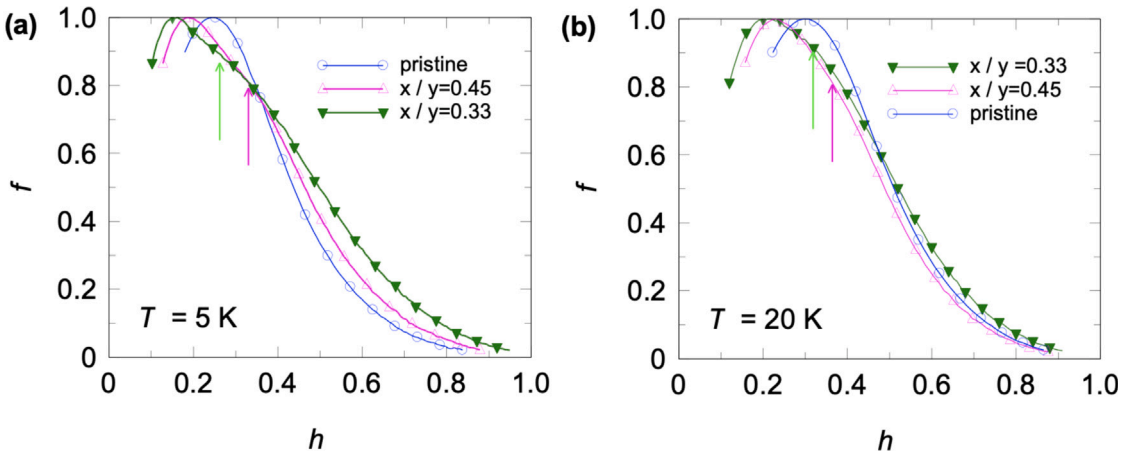

Fig. 39. Reduced pinning force versus reduced magnetic field at (a) 5 K and (b) 20 K for pristine (without additive) sample and for samples of Type 5, $(MgB_2)_{0.99}(Te_x\ (HoO_{1.5})_y)_{0.01}$, with $x/y = 0.45$ and $0.27/0.75 = 0.33$. Arrows indicate kinks.
Source: Adapted with permission from [720].

the Dew-Hughes approach, this would suggest a change in the pinning mechanism from major grain boundary pinning at low temperatures to point defect pinning at high temperatures. However, further analysis led to the identification of several issues. On the one hand, (i) If activation of a pinning mechanism at a crossover temperature would occur, this could be accounted, according to literature [726–729], by using an additive expression such as $f = \sum_i K_i h^{p_i}(1-h)^{q_i}$ with p_i and q_i taking values according to Dew-Hughes approximation [596], and with each term being ascribed to one mechanism. In fact, in the Dew-Hughes interpretation, there are six terms, three related to the dimensionality of the pinning centers for each of the two types of pinning centers, i.e., for normal (or ΔT_c) pinning due to local changes in the critical temperature, and Δk pinning due to local changes in the mean free path of the carriers. Nevertheless, not only the physics beneath such a model with a direct summation of different mechanisms is somehow questionable, but more importantly, our attempts to apply it on the MgB_2 composites above mentioned failed since the parameters p_i and q_i resulting from the fitting process were abnormal. For instance, some p_i values were found to be negative, or the values of p_i and q_i were up to extremely high values of 10 and 44, respectively. It is worth noting, however, that a purely statistical description within the maximum entropy model, Section 3.3.4, yields the same dependencies on reduced field [246] without microscopic constraints on the fit parameters p_i and q_i. On the other hand, (ii) as addressed before, the dominant pinning elements in MgB_2 are the grain boundaries, and obviously, they do not disappear with increasing temperature, but the flux lines change their properties, and so does the interaction with the defects. Thus, the presented results and the arguments (i) and (ii) serve to highlight the limitations of the indicated pinning force models and the need to accommodate and integrate all observations of an experimental nature within a new one.

Nonetheless, considering the percolation model discussed in Section 3.2.3 (Eq. (24)) for determining the flux pinning force [730–732], the scaling expression $f_p = h^{1/2}(1-h)^2 g(h,T)$ has recently been derived [733]. Under this approach, the proposed model preserves the framework of the grain boundary pinning in the entire temperature domain, with $g(h,T)$ being defined as a field-dependent coupling factor. In fact, in polycrystalline samples, the function $g(h,T)$ can account for the revealed peculiarities of f_p, such as the peak shift, where broadening and other effects emerge as a consequence of the percolative nature of the supercurrent. The fitting process of the experimental curves indicated that $g(h,T)$ is either a single or a double-peaked distribution function that depends on the sample composition and fabrication technique. Distribution functions were either Gaussian or lognormal. The reason for such a dependence is not clear, and further investigations are required. The challenges are to quantify microstructural differences at nano, micron, and larger scales of the MgB_2 sample and to correlate them with their measurement of J_c. In turn, their structural and microstructural details depend on processing routes and raw materials [734]. In fact, in most of the cases when an increase in pinning ergo J_c has been observed, it is usually linked with the presence of nano-precipitates of secondary phases with at least one dimension comparable to the coherence length ξ of MgB_2. Interestingly, there are also cases when precipitates are much larger than ξ that still enhance J_c. One such example is MgB_2 added with cubic BN [735]. In this composite, BN does not react with MgB_2 but has a convenient lattice matching presumably inducing a pinning-enhancing microstrain at the interface.

6.5.5. *Fe-based superconductors*

The search for effective pinning centers in Fe-based superconductors (IBS) had a kick-start from the corresponding work done on cuprates earlier, especially on REBCO films. Already in the early days of IBS and parallel to the attempts of growing high-quality films [736,737], making wires [108,738] or coated conductors [544], and understanding the grain boundary issues [539], the effects of natural growth defects and the introduction or self-assembly of APCs was studied. In fact, very similar structures (nanocolumns and nanoparticles, planar intergrowths, dislocation cores) and dopant materials were successfully tested. Also, for IBS, oxide nanostructures turned out to be effective APCs, whereas the actual analog, non-superconducting arsenides [739] or selenides [740], have not been successful so far, most likely due to their low melting temperature and hence chemical stability.

In this sense, Tarantini et al. found that growth-related oxide nanocolumns in Co-Ba122 films on STO-buffered CaF_2 substrates [741] are responsible for strong pinning in *c*-direction. These defects were later identified as $BaFeO_2$ [742], and the combination with isotropic defects (nanoparticles) yielded pinning force densities comparable to optimized Nb_3Sn [743]. Analogously, Lee et al. [744] combined these *c*-axis-oriented defects with planar intergrowths in artificial multilayers, finding that whereas the single-layer Co-Ba122 which contained the above-mentioned nanocolumns shows only a strong *c*-axis peak, the STO-buffered Co-Ba122 multilayer shows a strong *ab*-peak. Here, nanocolumns were not formed, possibly because the residual oxygen was used up in the STO interlayers. A multilayer of Co-Ba122 and oxygen-rich Ba122 showed both the *c*-axis and the *ab*-peak. Here, oxide nanocolumns and interplanar defects were forming, and the J_c anisotropy can be regarded as a summation of the two other cases. On the other hand, Sato et al. were able to tailor vertical defects in P-Ba122 films by the deposition rate [745], finding that whereas high deposition rates of 3.9 Å/s lead to tilted extended defects (most likely domain boundaries), a lower deposition rate of 2.7 Å/s lead to short *c*-axis-oriented defects, which were related to dislocations and yielded the higher J_c values. Similar nanocolumns with corresponding *c*-axis peaks were also found in Fe(Se,Te) films on bare STO by Braccini et al. whereas similar films on CaF_2 showed more or less isotropic defects with a rather angle-independent J_c [746]. Recently, further isotropic defects, namely rectangular-shaped nanodomains of differing Se:Te ratio or in-plane orientation, were also identified in Fe(Se,Te)/CaF_2 films, whose domain boundaries contribute to pinning [387].

Kauffmann-Weiss et al. [583] measured pinning force densities as high as 95 GN/m^3 at 4.2 K $B \parallel c$ in thin NdFeAs(O,F) films, a record value at that time. They attributed it to the complex microstructure of natural growth defects, such as nanoscale As-Nd disorder, Fe-rich nanoparticles, F-rich interlayers, MgF_2 formation at the interface, strain as well as the layered crystal structure and the surfaces. For $CaKFe_4As_4$ singles crystals, Ishida et al. [747] measured surprisingly high J_c values, which were surpassing even optimized film samples of Co-Ba122 and NdFeAs(O,F), especially for $B \parallel ab$. This was related to a unique defect structure, namely a combination of two types of *ab*-oriented Ca122 intergrowths: non-superconducting, large, thick and low-T_c, small, thin. A pronounced peak effect for $B \parallel c$ at 20 K was found and explained by the temperature dependence of the condensation energy of matrix and defects.

Miura et al. [748] introduced 1 mol% and 3 mol% $BaZrO_3$ in $BaFe_2(As_{0.66}P_{0.33})_2$ films and achieved up to 3.2 times increased pinning force densities. The field of maximum enhancement was found to be *T*-independent and to depend on the nanoparticle density as $H(\Delta J_{c,max}) \sim n^{1/3\sim1/2}$, which was explained by the similarity of mean particle distance and mean vortex separation. Later, the same group was able to fit the temperature, field, and angular dependencies of the critical current density of these films by a model without free parameters, involving the creep-free J_c and comparing particle diameter with (anisotropic) coherence length [749]. These particles lead to a reduction of the creep rate half-way to the theoretical lower limit, $Gi(T/T_c)$, where *Gi* is the Ginzburg–Levanyuk parameter. On the other hand, Lee et al. [750] incorporated BZO particles (2, 4, and 8 mol%) in optimally Co-doped Ba122 films, where 2 mol% showed the best performance, i.e. 170 GN/m^3 at 4.2 K $B \parallel c$, i.e., achieving a 14-times increase in its pinning force density. Here, BZO formed short nm-sized *c*-axis-oriented nanorods, instead of round nanoparticles as for the P-doped samples. This is most likely due to a different strain state at the interfaces. More recently, Meyer et al. introduced $BaHfO_3$ nanoparticles in Co-Ba122 films in a multi-layering technique [751], finding a 10-times increase in its pinning force density (46 GN/m^3 at 5 K $B \parallel c$).

On the other hand, the effect of $SrTiO_3$ incorporation in Fe(Se,Te) by a sector-target method [740] depends strongly on the doping amount. 3% STO did not lead to a nanocomposite microstructure of clearly visible nanoparticles or nanocolumns. In contrast, a 10% sample showed clear STO nanocolumns but also a strong suppression of T_c. CeO_2 as interlayer [752], buffer layer, or cap layer [753], have all shown to increase J_c by a factor of 10-15 at 4 K, as in the case of 10% $CoFe_2O_4$ doping leading to additional magnetic pinning [754]. Reasons may be additional nanoclusters of differing Se-Te stoichiometry, interfacial defects, strain, and elemental doping. Multilayering Co-doped and undoped Ba122 [755] lead to equal J_c values for $B \parallel c$ and $B \parallel ab$ at all temperatures, i.e. to an increased density of surprisingly *c*-axis-aligned defects. 3D behavior and δl pinning were measured for these films and attributed to the large coherence length compared to the interlayer thickness.

Microstrain is a very effective method for creating additional pinning in IBS due to the strong strain and pressure sensitivity of their superconducting properties. In this sense, Ozaki et al. [756] showed that proton irradiation of Fe(Se,Te) films leads to a simultaneous increase of T_c from 18 K to 18.5 K, and a J_c increase at 4.2 K by a factor 1.6 in self-field or $B \parallel c$ conditions, whilst a factor of 2 for $B \parallel ab$ (further details on the use of irradiation techniques are discussed in the forthcoming section). However, at 12 K, the increase is one order of magnitude, with the F_p maxima shifted to higher fields for both directions, indicating effective strong pinning. A remarkable maximum pinning force density of 120 GN/m^3 was measured for $B \parallel ab$ at 4.2 K. This was explained by nanostrain around the irradiation defects in combination with the pressure dependence of T_c. Seo et al. [757] created such nanoscale strain defects later by multilayering Fe(Se,Te) and CeO_2. Here, T_c decreased continuously with increasing amount of CeO_2 in the interlayers, controlled by pulse number. The sample with the lowest pulse number $p = 2$ on the CeO_2 target showed a layered nanoscale strained pinning landscape and enhanced J_c values, whereas larger pulse numbers lead to real multilayers and decreased J_c values. The sample with $p = 2$ showed a J_c increase by 3.8 at 6 K and $F_p^{max} = 58$ GN/m^3 at 10 T, even surpassing the irradiated films mentioned above despite the decreased T_c.

Sivakov et al. [758] have shown how the growth conditions are essential to obtain good performances in terms of critical temperature, critical current density, and critical fields. In particular, they showed how, by varying the growth velocity of two $FeSe_{0.35}Te_{0.65}$ crystals, it is possible to influence their superconducting transport properties: the sample obtained with the longer formation time shows a modified microstructure characterized by additional pinning centers and weak links that are more metallic, and hence a better grain connectivity. These features lead to lower resistivities and higher J_c values. It is also possible to modify the morphology and the microstructure of Fe(Se,Te) through a melting procedure exposed to several annealing treatments. These

strongly affect the secondary phases dispersed in the tetragonal matrix such as the trigonal, non-superconducting Fe_7Se_8 phase. Masi et al. [759] have illustrated that an Fe(Se,Te) sample shows low critical current densities when it is quenched from high temperature. Contrarily, samples exposed to controlled cooling annealing procedures indicate that their superconducting behavior is improved by showing J_c values much higher than the pristine sample ones. Zhang et al. [760] have shown that the sintering temperature has an influence on the morphology and microstructure of bulk samples in the 122 family of iron based superconductors, which is one of the most promising for power applications of superconductivity. In particular, $Sr_{0.6}K_{0.4}Fe_2As_2$ bulk samples present the best J_c values when the sintering temperature is above 850 °C because of the disappearance of the impurity phases. If the temperature is raised above 850 °C, the J_c shows a very weak dependence on the applied magnetic field indicating that the pinning strength of the sample is increasing due to the formation of large grains with fewer impurities.

Another example for the influence of microstructural factors on the transport properties is ball-milling of Co-doped $BaFe_2As_2$ as shown by Shimada et al. [761]. The authors showed that an increased ball milling energy leads to smaller grain size and consequently to ultra-fine grained Ba122 bulks. However, these higher ball energies deteriorate the connectivity between the grains via a reduction of neck area leading to reduced critical current densities. In a similar study, Tokuta and Yamamoto [762] showed that an increased ball milling energy leads to strain in the samples decreasing the *a*-axis and increasing the *c*-axis lattice parameter. This leads to a slight reduction in T_c but an increase in the upper critical fields, very comparable to strained thin films.

Similar to MgB_2, spark-plasma sintering (SPS) has also been employed for producing highly dense IBS bulks. Ahn and Oh showed, e.g., in 2013 that SPS yields the highest J_c values among other hot-consolidation methods for pristine as well as B- and C-doped Fe(Se,Te) samples [763] due to a high degree of densification and the cleanliness of the superconducting phase. Puneet et al. used SPS to investigate graphene doping of Fe(Se,Te), finding an improved J_c for 0.5 wt% graphene [764]. Recently, Iebole et al. [765] used such SPS-prepared Fe(Se,Te) samples as PLD targets for the growth of thin films on CaF_2 substrates with excellent properties, T_c = 16 K, J_c = 0.1 MA/cm^2 at 5 K and 16 T. Zaikina et al. introduced SPS for Ba122 superconductors as a very fast preparation technique—'superconductors in an hour'—by using BaH_2 as both Ba and H source [766]. Yamamoto et al. [767] recently optimized such SPS-prepared (Ba,K)Fe_2As_2 bulk samples by deep-learning methods [768]. They reached J_c values around 10^5 A/cm^2 and trapped fields of 2.8 T at 5 K. A high density of planar defects with associated strain fields [769] may be responsible for effective pinning and hence such high J_c values in such samples besides the optimized grain connectivity.

6.6. Radiation effects on the J_c properties

The study of radiation effects on the superconducting properties of type-II superconductors, and in particular on their critical current density, J_c, has been for decades a very active field of research. This is probably because radiation sources are commonly used as a tool for the optimization or enhancement of the electronic transport properties of diverse materials, including superconductors [31], and more recently because to effectively utilize the HTS technology in clean energy sources such as fusion reactors, the radiation hardness of the HTS materials became a crucial issue to be studied [770–772]. For these reasons, the modification of T_c and J_c as well as the shift of the irreversibility line resulting from the exposition of the superconductor to energetic ions, neutrons, electrons, and photons have been subject of intense characterization [31,417,773–775]. Consequently, we consider it important to finish this review by presenting a comprehensive discussion of notorious irradiation experiments carried out on HTS tapes and coated conductors—considered the leading candidates for applications in radiation-harsh environments—, with a clear analysis of how the dependence of the radiation effects on the shape of the material (e.g., single crystal, polycrystal, or epitaxial film) and on the substrate (insulator or metallic) can influence our understanding of J_c. Additionally, also recent irradiation experiments investigating the fundamental properties and optimization of J_c in MgB_2 and IBS compounds will be reviewed.

First, we will outline the different kinds of defects that can be formed in the superconducting compound during or as a result of irradiation, revealing the morphology of defects induced by different sources of radiation and energy levels, and highlighting relevant findings on whether a specific irradiation technique could lead to either an improvement or deterioration of J_c. Then, due to its current technological importance, we will finish this chapter by introducing our most recent knowledge of radiation damage in HTS conductors for fusion technologies. In this sense, we call our readers' attention to the fact that although the list of works cited below is not exhaustive but rather focused on HTS tapes and coated conductors, it is our understanding that the discussion presented in the following subsections captures the main features of irradiation experiments on advanced superconductors, when categorized in terms of the projectile particle or irradiation technique.

6.6.1. Radiation defect morphology

Irradiation has been proven to be a versatile and very efficient tool for tailoring the electromagnetic properties of HTS tapes and coated conductors, making them functional for specific applications. Defects play a double role [776,777]: (i) Firstly, acting as scattering centers for carriers, lowering the critical temperature and greatly affecting the order parameter (especially in multiband systems) [778,779] and the intrinsic anisotropy [780]. (ii) Secondly, as pinning centers for fluxons changing the overall pinning landscape and its angular behavior with the consequent change of the critical current density [781,782]. In this regard, the defect morphology can be controlled by suitably choosing the type and energy of the striking particles, while the defect density can be modulated by tuning the irradiation fluence [783].

As sketched in Fig. 40(a), electrons in the range of MeV create only point defects consisting of an interstitial atom and its corresponding lattice vacancy, also called 'Frenkel pairs' [784]. In the same energy range, a similar damage is produced by protons, which introduce some nm-sized clusters. Protons of higher energy, light ions, and neutrons produce point defects and a larger number of small cascades of defect clusters [774], which can act as isotropic pinning centers [31] as illustrated in Fig. 40(b). All these defects

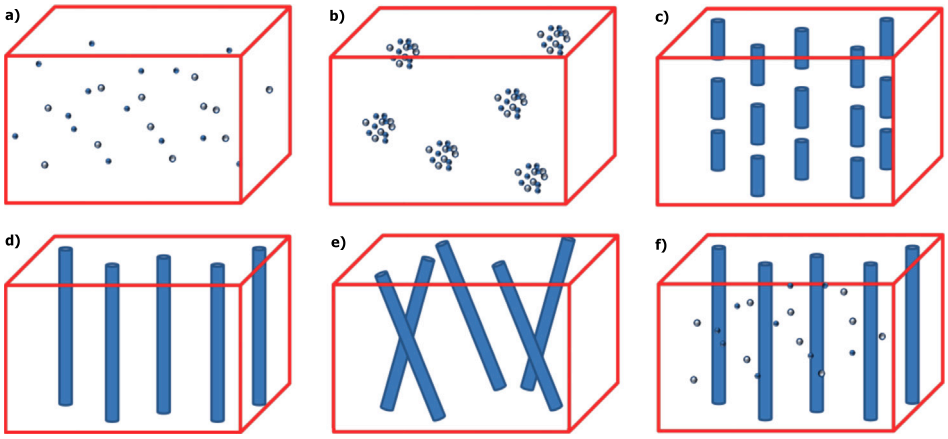

Fig. 40. Sketches of possible morphologies of radiation-induced defects depending on the irradiation conditions. (a) Electron and proton-induced defects. (b) MeV energy proton, neutron and MeV heavy ion induced defects. (c) Discontinuous correlated defects from ~ 100MeV heavy ions. (d) Columnar defects from high energy heavy ions. (e) Splayed columnar defects generated by heavy fission fragments or by irradiations at different angles. (f) Combined columnar and pointlike defects from a double irradiation process for composite pinning landscapes.

can be ascribed to the elastic scattering of the striking particles against the target nuclei and to avoid immediate recombination, with a transferred energy high enough to overcome the binding energy of the lattice atoms. This threshold displacement energy is, in principle, characteristic of each atomic species, material, lattice position, displacement direction and temperature [785]. It is generally of the order of a few eV to a few tens of eV, where a reference value typically employed in calculations is 25 eV, i.e., 1000 times the thermal energy of an electron at room temperature.

Nevertheless, in cuprates, the easiest atom to displace is certainly the loosely bound oxygen [776,786], whose content strongly influences T_c. Thus, if the transferred energy barely allows the displacement of a target atom, Frenkel pairs are created. In contrast, if the transferred energy is much larger, the primary displaced atom starts an avalanche process of defect production, resulting in the formation of what is called a 'collision cascade'. In the case of neutron irradiation, they consist of spheroidal defects where the lattice is completely disrupted [787] surrounded by a larger area with a deformed lattice [788], and of individual lattice defects decreasing the lattice periodicity [789]. In addition, due to the small collision cross-section of neutrons, these defects are homogeneously distributed across the target. However, some inhomogeneity in the defect distribution was observed in neutron-irradiated MgB_2 samples where an important damage mechanism consists of low-energy neutron capture by the ^{10}B isotope with the consequent emission of an α particle and a ^{7}Li nucleus [790], which in turn create displacement damage. Therefore, the large cross-section of this reaction results in a very disordered region close to the sample surface and induces a defects distribution gradient in thick samples. Either the use of cadmium shields before the sample [790] or the preparation of samples with boron isotopically enriched in 11B [791], both can partially solve this inhomogeneity problem. Analogously, a high density of point-like defects is created by thermal neutrons in GdBCO or SmBCO coated conductors for the high neutron capture cross-sections of gadolinium and samarium, respectively [792].

Randomly distributed nanoclusters of defects have also been detected in superconducting samples irradiated with MeV heavy ions [793,794]. Nonetheless, by increasing the mass and the energy of the impinging particles, the energy transfer by electronic scattering becomes the prevailing source of damage and extended anisotropic defects occur. They consist of continuous or discontinuous amorphous tracks along the particle path, in dependence of the energy release and on the target material [795] (See Fig. 40(d) and (c), respectively), behaving as anisotropic pinning centers [796]. A crossover between elongated discontinuous columnar tracks and slightly elongated clusters was found by comparing TEM images of (Y,Dy)BCO coated conductors, irradiated with 100 MeV and 50 MeV Ag ions, respectively [797]. However, the threshold electronic energy loss for creating columnar defects in a metallic compound, such as MgB_2 or iron-based superconductors, is much higher than the one occurring in cuprates [776,798,799].

An alternative radiation technique for generating crossed columnar tracks in Bi-based tapes consists of bombarding the samples with high energy (e.g., ~ 0.8 GeV) protons. This causes the fission of the Bi nuclei and the production of two heavy ions (e.g. Xe or Kr) with energies of the order of 100 MeV each, i.e. high enough to produce randomly oriented columnar tracks [800,801], Fig. 40(e). Likewise, for the study of irradiation effects with very high neutron energies, as the ones of interest for nuclear fusion technology, neutron absorption/capture reactions are also relevant. These reactions can result in point defects, additional cascades, and the presence of transmutation elements such as H and He [802]. These can also be introduced by combined irradiations for a better control of the defect morphology and distribution, Fig. 40(f). From a contrasting viewpoint, high-energy photons (X-rays and Gamma rays) can also introduce damage in HTS conductors. Depending on the conditions of the experimental setup, they can heat the sample locally [803], or directly induce the generation of high-energy electrons that then can displace atoms in the crystal [786].

6.6.2. Photons, electrons, and neutrons

From this perspective, certain distinction needs to be made in terms of the energy levels of the light or other radiation used, as well as on the dimensions of the HTS sample. For instance, in the case of *photon irradiation*, we will refer mostly to high-intensity

beams with fluences as low as 10^{12} photons/s, which can be obtained from light sources that range from UV lamps or lasers with energies in the range 5–40 eV, X-rays with energies of up to a few tens of keV, or even Gamma-ray photons with energies above 100 keV [804]. The use of photon irradiation or any other particle irradiation for the study of a single or a few monolayer HTS films with thicknesses of ~ 0.2 nm each will not be considered in this review as they lay out of the scope of the CCs emphasized in this section.

The above is also because at these dimensions, the bombarding particles, e.g., photons, can interact directly with the valence electrons of the HTS material in its normal state or, with the quasiparticles (Cooper pairs) that lie over their Fermi surface at the superconducting state, in such way that excited 'electrons' can escape the HTS material before being affected by inelastic collisions. Therefore, for samples with thicknesses ranging from one to a few monolayers, the photon irradiation technique is mostly referred to photoemission spectroscopies aimed for the study of the electronic structure of the superconducting crystal [264,805], but not for the improvement of the macroscopic properties of HTS films whose minimal thickness is about 1 μm. This also applies to particles with mass such as electrons, protons, and neutrons, which, bombarded to samples of dimensions similar to a single atomic layer (monolayer), can be used for fundamental crystallographic or energy particle dispersion experiments [806–808].

Limiting our discussion to HTS thin films for high-field/current applications, and especially to the optimization of their macroscopic properties, e.g., J_c or T_c, photon irradiation experiments are particularly relevant for X-ray studies at high-intensity facilities, and also for applications where gamma-ray irradiation is expected, e.g., at space and in nuclear fusion reactors. Nevertheless, to date, only a limited number of experiments have been carried out in this direction, starting with the seminal work of K. Tanabe's group, who studied the effects of photoinduced hole doping on YBCO thin films [809]. Since then, it is known that if an enhancement of both J_c and T_c in REBCO thin films is seen by photo-irradiation, such enhancement will be rather dependent on the photon dose than on the oxygen content of the SC sample. Consequently, this phenomenon complicates the reproducibility and practical deployment of this technique for the large-scale manufacturing of HTS tapes, which has strongly limited the interests of our community on this subject. However, this topic has recently recovered certain interest due to its potential use at high-energy particle facilities, where we expect a significant increment in the study of commercial 2G-HTS tapes under large doses of gamma radiation. An example of such research is the work conducted for the construction of the muon beamline of the Japan Proton Accelerator Research Complex, where the absorbed dose of the high-field pion capture solenoids can reach up to 130 MGy in 10 years. With this in mind, the commercially available SCS4050 tape manufactured by SuperPower Inc. [257] has been tested already. Several of these samples have been irradiated by a ^{60}Co Gamma-ray source, with up to a maximum dose of 27.4 MGy and an average dose rate of 5.7 kGy/h at ambient temperature [810], finding that the artificial pinning centers of the SCS4050 tape show an almost negligible (≤5%) degradation in their superconducting properties (T_c, and J_c). This, in fact is a remarkable result as it was previously thought that despite the Gamma rays, seemingly not modifying the T_c of YBCO (the constituent SC layer of SuperPower tapes), may lead to a significant decrease in its J_c at doses higher than 0.4 MGy [811]. However, the response of the SCS4050 tape to neutron irradiation was not as promising as for fluences above 8.23×10^{21} n/m^2, both J_c and T_c deteriorated, leading to the destruction of the superconducting state at fluences above 4.11×10^{22} n/m^2. Still, a vast room for research remains open for the testing of this and other commercial 2G-HTS tapes with HTS films based on YBCO, GdBCO, or EuBCO, where it is also known that ad hoc post heat treatments can help to recover and reinforce the SC state on photon and neutron irradiated REBCO samples [812,813].

In respect of *electron irradiation* treatments, it is worth reminding that the point defects induced by this technique are generally distributed in a homogeneous way across the HTS sample. This means that, although this technique results useful for fundamental studies of the pairing state [814], it offers little insight into how the pinning properties of practical superconductors can be enhanced. Consequently, there is very little literature about the impact of electron irradiation on the J_c properties of HTS tapes, although it is well known that in YBCO tapes subjected to a 23 MeV electron irradiation up to a fluence of 3×10^{18}/cm^2, both T_c and J_c remain unaffected [815].

However, considering the use of *neutron irradiation* techniques over REBCO thin films, these can offer a better insight into how the formation of defects can affect the critical temperature and transport current properties of superconductors. Nevertheless, the behavior of the critical current density with the neutron irradiation dose is not trivial, and the use of this technique for the optimization of J_c and T_c of commercial HTS tapes has resulted in scenarios that are still open to great debate. On the one hand, fast (fission) neutron irradiation experiments ($E > 0.1$ MeV) have been carried out already on a large set of commercial REBCO coated conductors such as the YBCO tapes fabricated by SuperPower Inc., e.g., on the SCS4050 tape which contains a ~1 μm-YBCO film [816], or the American Superconductor AMS-344 tape [258] with a ~0.8 μm YBCO film [817], and the 2.5 μm-YBCO concept-tape developed by Bruker EST [816]. Similar studies have been seen also on a broad set of GdBCO tapes [818] manufactured by SuNAM [256], Superpower [257], and SuperOx [260]. In all these cases, not only the thickness of the superconducting layer is different, but more importantly, the method and template used for the deposition of the REBCO film are different. Thus, although a certain consensus exists on the statement that fast neutrons can introduce effective pinning sites, which in turn might enhance the J_c properties of the REBCO layer, there is no consensus on what will be an effective fluence. For instance, although the T_c in all samples decreases linearly with increasing neutron fluence [782], the same fluence (2.1×10^{22} n/m^2) can either enhance, reduce, or have no effect on the tape's pinning structure, at different magnetic field ranges and different temperatures [818,819]. In fact, no monotonic trend has been found leading to a direct correlation between the critical current density and the neutron fluence, as remarkable differences on the $J_c(B, \theta)$ function have been found, depending on the pristine or defective state of the SC samples [820]. This is possibly due to the fact that cascades can act as rather efficient pinning centers for fields perpendicular to the layered structure of REBCO, but can also damage the planes, decreasing their pinning efficiency for parallel fields. Still, a post-irradiation annealing in Ar or O_2 atmospheres has evidenced a partial J_c recovery in irradiation-damaged coated-conductors with $BaZrO_3$ nanoparticles [821]. In contrast, further J_c improvements in addition to those produced by neutron irradiation have been found

Table 3
Change in the $J_c(B,\theta)$ anisotropy in selected samples irradiated with different particles. $J_{c,max}$ and $J_{c,min}$ are the maximum and minimum J_c values measured by changing the tilt angle of the applied field B.

Material	Irradiation (particles – energy – fluence)	$J_{c,max}/J_{c,min}$ pristine	$J_{c,max}/J_{c,min}$ irradiated	B (T)	T (K)	Ref.
$FeSe_{0.5}Te_{0.5}$	Protons - 190 keV - 1×10^{19} m^{-2}	3.8	1.9	15	4.2	[830]
$FeSe_{0.5}Te_{0.5}$	Au ions - 6 MeV - 1×10^{16} m^{-2}	1.10	1.10	5	4.2	[793]
YBCO	Fast Neutrons - > 0.1 MeV - 1×10^{21} m^{-2}	2	1.5	6	64	[816]
(Y,Dy)BCO	Au ions - 25 MeV - 1×10^{15}-1×10^{16} m^{-2}	2.2	1.5	1	77	[831]
(Y,Dy)BCO	Ag ions - 50 MeV - 2×10^{15} m^{-2}	1.4–1.9	1.2–1.5	1–5	65	[797]
(Y,Dy)BCO	Ag ions - 100 MeV - 2×10^{15} m^{-2}	1.4–1.9	1.6–2.2	1–5	65	[797]
Zr-YBCO	Au ions - 25 MeV - 1×10^{15}-10^{16} m^{-2}	1.7	1.9	1	77	[831]
GdBCO	Xe ions - 80 MeV - 6.5×10^{14} m^{-2} Tri-modal irrad. ($\parallel$ to c, $\pm$ 45°)	1.8	1.3	4	70	[796]
BZO-added REBCO	Pb ions - 1.4 GeV - 5×10^{14} m^{-2} Bi-modal irrad. ($\pm$ 45°)	2.6	1.3	1	77	[32]
U-added Bi2223	Thermal neutrons - <0.55 eV - 4×10^{19} m^{-2} Fission splayed tracks	25–30	3.5	0.5	77	[825]

in CCs without additional pre-irradiation artificial pinning centers. Nonetheless, in both cases, the J_c modulation is not monotonic with the annealing temperature, probably due to a competition between the simultaneous increase of the superfluid density and the reduction in the number of efficient pinning centers. Neutron irradiations were also reported to significantly change the sensitivity of the critical current to applied stress in the GdBCO/IBAD systems, whereas nearly no change was observed in YBCO/RABiTS [792]. In addition, it has been found that the normalized critical temperature ($T_c/T_{c,0}$) vs fluence depends neither on the pristine critical temperature value, $T_{c,0}$, nor on the specifics of the coated conductor at least up to fluences about 5×10^{22} n/m^2 [782]. These results can be interpreted in light of the prominent role played by small defects in suppressing both T_c and J_c combined with the beneficial effect of larger defects acting as pinning centers [822], possibly opening a way to predictive models of irradiation induced superconducting performance suppression [823].

Bombardment with thermal neutrons ($E < 0.55$ eV) was also employed to induce artificial defects in Uranium-added Bi2223/Ag tapes [824]. In this case, the induced fission of ^{235}U by thermal neutron irradiation produces two ions with a total kinetic energy of 162 MeV propagating in opposite directions. These ions create discontinuous tracks of defects with random orientation that become effective in increasing J_c above a certain magnetic field threshold, depending on both working temperature and field orientation, i.e., in the region where J_c is limited by a weak pinning landscape in the pristine samples. Remarkably, a reduction of J_c anisotropy by about one order of magnitude was found with fission track densities of 4×10^{19} [825] (see Table 3).

Neutron irradiation of MgB_2 wire at a fluence of 4.75×10^{18} n/m^2 suppressed T_c below 5 K [826]. This decrease is much larger than that observed in $Mg^{11}B_2$-enriched bulk samples [827], thus highlighting that the neutron capture reaction plays a significant role in suppressing superconductivity. However, a subsequent annealing processes allowed T_c recovering its undamaged values. Contextually, the in-field critical current density that dropped to zero after irradiation overcomes the non-irradiated sample value after 24 h annealing at temperatures $\geq$ 400 °C and shows a fishtail behavior. This could imply that the irradiation-induced defects still present after annealing act as effective pinning sites. On the contrary, a J_c improvement was directly observed in Cu/MgB_2 wire irradiated at lower neutron fluence [790,828]. In this case, the authors attributed the enhancement to an increase of the upper critical field rather than to radiation induced defects. However, the J_c enhancement obtained by irradiation are always much lower than that achievable with carbon or C-based compound doping [829].

6.6.3. Protons and heavier ions

As for the case of neutron irradiation, the pristine sample texture and the defect distribution are both known to affect T_c and J_c of most HTS materials when subjected to proton or heavier ion irradiation at certain fluences. Heavier ions with MeV energy generate randomly distributed spheroidal defects that act as isotropic pinning centers not too different from the neutron-generated ones [794]. However, their production rate is significantly higher, making this irradiation technique applicable to optimizing the pinning properties of HTS tapes at an industrial scale [832,833][834]. Moreover, in contrast to other linear pinning centers such us BZO nanorods, irradiation-induced columnar defects can be introduced at arbitrary angles (Fig. 40e), which therefore allow better control of the J_c anisotropy by combining irradiation along different directions (see Table 3).

Reel-to-reel irradiation of REBCO coated conductors with 16–18 MeV Au ions evidenced the same critical current enhancement as obtained on short static samples [832], and the maximum J_c enhancement (over 2-fold at 27 K) was achieved with a fluence of 6×10^{15} Au ions/m^2. The presence of secondary phase particles such as $BaZrO_3$ and $(Dy,Y)_2O_3$, acting as strong flux pinning centers, makes YBCO coated conductors less affected by ion irradiation compared to the undoped conductors [831], even though the additional radiation-induced defects decreased the J_c anisotropy of the pristine samples as evidenced in Table 3.

Notice also in Table 3 that protons with a few hundred keV of kinetic energy, and a fluence of 1×10^{19} p/m^2, have also been proved to be very efficient in improving the in-field J_c features of iron-based superconducting films, even reducing their magnetic anisotropy when compared with pristine samples [830]. However, for the case of cuprate-based films, there is no consensus yet on what conditions could lead to the enhancement of J_c. For example, it has been seen that although the critical current density can be doubled by proton irradiation, e.g., in Dy-doped YBCO coated conductors at 27 K and magnetic fields ranging between 3 T to

6 T [835], or on GdBCO coated conductors irradiated with 3.5 MeV protons up to a fluence of 6×10^{20} p/m^2 [836], in the latter case the irradiation also induced a systematic J_c suppression in the self-field conditions, and a larger T_c decrease. Overall, one should keep in mind that the J_c improvement occurring at high field is often at the cost of decreasing the transition temperature and the self-field/low-field J_c properties of the cuprate [832,837]. This reduction can be ascribed to an oxygen deficiency in the damaged areas, which can be partially recovered by post-irradiation annealing process in oxygen atmosphere, which results not only in an effective restoration of the oxygen concentration, but of T_c and the self-field J_c properties of HTS tapes, without annihilating the defect nanoclusters [794]. Likewise, it has been found that the irradiation temperature also affects the defect migration to the grain boundaries [838], which act as defect sinks, thus providing a grain decoupling less relevant in low-temperature irradiations.

Moreover, the morphology of the radiation defects caused by high energy particles is known to affect the magneto-angular anisotropy $J_c(B,\theta)$ of the superconducting thin film. This is particularly evident for high-energy ions (able to deposit at least 8 MeV/μm) that produce defects, which are linearly correlated although discontinuous, up to the point (above 20 MeV/μm) where the defects become continuous [839]. In fact, continuous columnar defects created by high-energy heavy ions behave as strong flux pinning centers when the magnetic field is directed along their axis, and the J_c improvement is predicted to be maximum when the density of the columnar defects matches that of the vortices. For this reason, the ion fluence is often given in terms of the dose-equivalent field B_ϕ, i.e., of the magnetic field at which the density of vortices matches the number of ion tracks. Moreover, the J_c vs. H curves of the irradiated conductors show a peak whose position depends on B_ϕ and an increase of anisotropy (Table 3). For instance, the comparison of the J_c vs. H curves of DyBCO coated conductors obtained before and after irradiation with different heavy ions (320 MeV Au ions and 200 MeV Ni ions) revealed that the J_c improvement rises at the increase of the electronic energy lost by the impinging ions, i.e., with the radius of the columnar defects [840].

In the case of the commercially produced (Y,Dy)BCO coated conductors by American Superconductor [258], different behaviors have been seen depending on the energy of the projectile particle (Table 3). For instance, with a fluence of 1×10^{15}/m^2, Au ions of 25 MeV (that produce uncorrelated spheroidal defects) have been seen to strongly reduce J_c at 77 K, when a magnetic field of 1 T is applied along the irradiation direction [831]. Nevertheless, at double fluence and in the same field conditions, when using 50 MeV Ag ions (introducing correlated defects), a J_c improvement appears over the entire angular range [797]. Conversely, for 100 MeV Ag ions, a significant J_c enhancement occurs just for fields applied parallel to the irradiation direction, whereas there is a strong J_c reduction for a range of angles orthogonal to this direction. Interestingly, by decreasing the temperature, it has been recently shown that the J_c of the conductor irradiated with the 100 MeV Ag ions shows an almost isotropic behavior [841]. Analogously, Kihlstrom at al. [443] reported on the synergistic effect of a composite pinning landscape, Fig. 40(f), resulting from sequential irradiations with 250 MeV Au ions (at $B_\phi = 3$ T) and 4 MeV protons (at the fluence of 4×10^{20} p/m^2) that, against a T_c reduction of about 3.5 K, yields J_c values larger than achievable by irradiating with only one species. This highlights how, in the temperature-field regime relevant for applications, the presence of randomly distributed nanoclusters of defects created by protons can be effective in preventing the flux-line jumping between columnar defects and in catching stray flux lines. Besides, the creation of correlated pinning along the c-axis also mitigates the J_c anisotropy.

A crossover from a sequence of ellipsoidal defects via nearly continuous to totally continuous tracks was detected in YBCO coated conductors irradiated with 46, 77, and 167 MeV Xe ions [795]. Similarly, in GdBCO coated conductors irradiated with 80 MeV Xe ions [842], a noticeable change in the defect microstructure against the irradiation angles was also observed. This was due to their anisotropic thermal diffusivity, i.e., ions incoming along the c-axis produced shortly segmented columnar tracks, whereas columnar defects were formed when the ion beam was tilted at an angle $\geq 20°$ from the c-axis. Analogously, a mixing of discontinuous tracks parallel to the c-axis and of columnar defects tilted at ±45° was reported for the same samples when using 270 MeV Xe ions [843]. Remarkably, the J_c values measured in 80 MeV irradiated samples overcome the pristine values in a wide angular range and are higher than those measured on samples irradiated by ions of 270 MeV. Moreover, recent studies on Fujikura GdBCO coated conductors [844] irradiated with 2 MeV He^+ ions have started to shed light on defect annealing and the influence of working conditions on radiation effects [845]. From this standpoint, both T_c and J_c values of patterned tracks degrade with irradiation dose, but more importantly, room temperature annealing of 'in-situ' irradiated samples can result in a significant recovery of the superconducting properties.

Thus, in conclusion, the choice of the fluence is crucial for J_c optimization, although its dependence is not monotonic. For instance, in Gd-doped YBCO coated conductors irradiated with a 1.9 GeV Ta-ion beam parallel to the c-axis [846], the maximum J_c has been seen to double as the fluence increases from 5×10^{13} to 5×10^{14} ions/m^2, but decreases thereafter. In fact, under the same irradiation a similar behavior was noted in other YBCO coated conductors doped with different elements, where a J_c improvement by 4.4 times was attained at 30 K and at $B_{appl} = B_\phi = 1.0$ T [847]. Likewise, by irradiation with 1.4 GeV Pb ions at angles close to ±45 ° from the c-axis, a strong reduction of the J_c anisotropy has been seen in several coated conductors [32]. Conversely, the superimposition of 1.4 GeV Pb-ion induced columnar defects tilted by 45° from the c-axis to BZO nanorods also aligned along the c-axis (both with the same estimated density), produced just a single J_c peak at 45°. This means that the irradiation made the pinning action of the BZO nanorods ineffective.

Regarding bismuth-based cuprate conductors, strong J_c enhancements of up to one order of magnitude at 50 K and in applied fields higher than 0.2 T have been measured in both mono- and multi-filamentary Bi2223 tapes irradiated with 0.25 and 4.2 GeV Au ions, respectively [848,849]. This is the case when the ion beam and the magnetic field are both applied parallel to the c-axis. The Au-ion irradiation also caused a marked reduction of the anisotropy of the irreversibility field. Similarly, splayed columnar defects produced by induced fission fragments irradiating Bi2223 tapes with 0.8 GeV protons led to a smaller field dependence of J_c than in a virgin sample in applied fields above B_ϕ. As a consequence, over twice the pristine J_c value can be achieved in correspondence to B_ϕ at 55 K and $H \parallel c$ [850]. Interestingly, the J_c enhancement occurs regardless of whether the magnetic field is applied parallel

or perpendicularly to the *ab*-plane of the tape. Analogous results were achieved on Bi2212 tapes irradiated with 0.8 GeV protons, where an areal density of tracks of about $6.4 \times 10^{14}/m^2$ (corresponding to $B_\phi \sim 1.35$ T) led to a J_c enhancement of nearly three orders of magnitude at 1 T and 20 K [851].

In contrast, irradiation tests on Fe(Se,Te) films, preliminary to the study of Fe(Se,Te) coated conductors, evidenced cascade defects followed by the formation of a strain field around them [756], increasing T_c by about 0.8 K after irradiation with 0.19 MeV protons [793]. Remarkably, an improvement in self-field J_c of up to one order of magnitude was observed, with positive effects in the whole investigated range of applied fields and also, with negligible or very modest T_c changes measured after irradiations with 3.5 MeV protons and 6 MeV Au ions, respectively [793,852,853]. Likewise, a significant J_c increment up to a factor of 5 was obtained in Co-Ba122 ($x = 0.08$) thin films irradiated with 0.6 MeV He ions at a fluence of 5×10^{17} ions/m^2 [854].

6.6.4. Radiation damage in HTS for nuclear fusion technology

One of the key enabling technologies for the development of fusion reactors lies in the use of highly radiation-resistant conductors for their high-field magnets. For large Tokamak facilities such as ITER [855], low-T_c superconductors can suffice to achieve the task since the required field is below 10 T [856]. However, for the development of much more compact reactors, the use of HTS tapes and coated conductors is the only viable option [771].

The development of 'compact' D-shaped ($R_0 = 1.85$ m, $a = 0.57$ m) HTS magnets with record strength ($B_0 = 12.2$ T) was recently demonstrated within the SPARC project [857], and although this is a major milestone for fusion technology, there are still many challenges the HTS materials need to overcome before enabling break-even fusion production, such as those referred to the radiation hardness of HTS materials [858–860].

Thus, despite having found that Fe-based superconductors are expected to be more resistant to radiation [542,852], showing interesting features from their multigap nature [861,862], the production of long lengths of commercial HTS tapes with IBS precursors is still to be seen. Nevertheless, these are already available in the case of cuprates, i.e., in what we have been calling the 2G-HTS tapes, but due to the *d*-wave nature of cuprate superconductors [266,863], these are known to be very sensitive to particle irradiation. Yet, their excellent superconducting properties [864], combined with the possibility to partially screen the plasma radiation via a careful reactor design, promise to allow their use for the required lifetime [858].

In more detail, an operating fusion Tokamak produces the highest neutron rate from the deuterium–tritium (DT) reaction that generates a 3.5 MeV α particle and a 14.1 MeV neutron [865]. However, these energetic neutrons will interact with several materials of the first wall, vacuum chamber, cooling system, etc., before reaching the superconducting coil [772,866]. These interactions will slow down the neutrons and eventually generate secondary particles that will, in turn, travel and interact with the HTS materials. For these reasons, the radiation environment experienced by the HTS tape might strongly differ from one reactor design to another. Clearly, these interactions will help to somehow protect the magnets from radiation damage (the larger the reactor, the more protected the magnets), but it also makes it more difficult to estimate and experimentally evaluate the need for additional screening or even the suitability and lifetime of the HTS material for the task [772].

For instance, for the radial neutron camera on ITER the down-scattered DT spectral count at 2.5 MeV is expected to be strongly attenuated with respect to the first wall, with particle counts 30 times fewer than the counts at the DT peak [867], allowing us to suggest that the radiation level in the superconducting coils at ITER is bearable [868]. However, the situation might be very different in compact reactors or in situations with very high energy density and neutron rates. As an example of this, we have noticed that for the case of SPARC, only 4 times fewer DT counts at 2.5 MeV compared to 14.1 MeV have been found [866]. In fact, in this case, the majority of down-scattered neutrons are presumed to come from reflections off the far wall along the spectrometer line-of-sight [869], but even by removing that part of the wall, the expected DT count is not reduced, as new simulations have shown [866]. Still, a rough estimate of the lifetime of poloidal field HTS coils in SPARC has been reported [858], using a value of 3×10^{18} n/cm^2 as the threshold for damage level. The authors suggested that 25 cm of additional ZrH_2 shielding might grant achieving the desired 10 years lifetime of the coil, but further studies based on the HTS damage rather than on the expected neutron fluence are strongly needed. A first attempt in this direction comes from a computational study that focuses on the comparison between the expected radiation damage in ARC with the achievable damage from fission reactor experiments, considering neutron spectra, displacement per atom (dpa), morphology of the defects, and thermal aspects [772].

The examples above clearly show the need for specific estimates of both the radiation environment and resulting damage in HTS coils in fusion reactors and also for experimental studies on the influence of fusion radiation on HTS properties. However, the neutron spectrum at the magnet position is non-trivial, and clearly, it is not possible to reproduce it exactly in an experiment [772]. In addition, currently no high flux of 14.1 MeV neutron source facility is available [802], therefore, experimental investigations need to be carried out under the view of the best approximation available. Thus, in order to design appropriate experiments, simulations of the expected radiation environment, damage levels, and defects typology are required. In this regard, several pre-compiled codes such as MCNP6 [870], PHITS [871], GEANT4 [872], TRIPOLI-4 [873], and FLUKA [874] can be employed for this aim. Such investigations have recently begun, providing a thorough characterization of the HTS radiation environment in ARC-class reactors [875,876] and examining the impact of ion heating on HTS cable performance [877]. These studies emphasize the need for careful neutron shielding designs to ensure a magnet lifetime sufficient for commercial fusion projects.

Finally, from the point of view of experimental facilities, several experiments have taken advantage of the broad neutron spectrum of fission reactors for research, although the 14.1 MeV component is still missing [772]. Nevertheless, 14.1 MeV neutron beams can be obtained by hitting suitable targets with light ion beams, but high fluences are currently not achievable [878]. In consequence, carefully designed ion irradiation experiments (possibly with multiple beams [879]) might get close to reproducing the damage expected from the exposition to high-energy neutrons. This is based on the initial assessment of J_c changes in commercial

REBCO tapes, where the displacement damage induced by MeV heavy ions serves to emulate the neutron effects in fusion reactor environments [880]. Yet, bear in mind that in the real application of HTS coils in fusion projects, the HTS material will be exposed not only to neutron radiation but will be operating at cryogenic temperatures whilst sustaining intense electrical currents. This implies that the generation and recombination of defects might be different with respect to that studied in irradiated samples at room temperature and without transport current; hence, experimental studies are extensively needed but are remarkably challenging. A recent comprehensive review on these topics can be found in Ref. [881].

7. Conclusions and outlook

Having discussed the concept of critical current density in high-temperature superconductors under the apparently different lenses of the macroscopic, mesoscopic, and microscopic worlds, a broad range of knowledge connections have been established which will benefit not only the next generations of researchers in the rather broad field of superconductivity, but are anticipated to lead the development of advance superconductors for the high-current and high-field applications that are currently paving the way for the future of the fusion energy, transportation, and energy resilience sectors.

Starting from the macroscopic concept of critical current density as a material law, which relates to the most commonly sought parameter in the practical specifications of cables, magnets, and any other large-scale applications for the so-called high-temperature superconductors, J_c establishes a common language that joins engineers, material scientists, experimentalists, and theoreticians, all with the common goal of tailoring these HTS materials in advancing their applications. Undoubtedly, for the world of HTS applications a well-grounded material law in terms of the macroscopic fields $\mathbf{E}(\mathbf{J})$ with $\mathbf{J}$ scaled in terms of the *material parameter* J_c, i.e.: $\mathbf{E}(\mathbf{J}/J_c)$, is the essential tool for solving many of the purely electromagnetic, magneto-thermal, or electro-mechanical problems daily faced in the development of such technologies.

Thus, to begin within a common frame of understanding, in Section 2, we commenced our discussion by introducing the seminal contribution to the concept of J_c by C. P. Bean [49,50], who proposed the simplest possible model of the $\mathbf{E}(\mathbf{J})$ law in superconductivity, even without explicit mention of the electric field (though implicitly recalled). Remarkably, this model, which is strictly valid for isothermal 1D systems, captures in a simple but very effective manner the main physics behind the characteristics of type-II superconductors to maintain large amounts of carrying current and magnetic field, i.e., the flux pinning. Then, over the decades, numerous extensions of the model have allowed dealing with more and more complex situations, including the solutions of 2D and 3D problems, and including the incorporation of relaxation effects, anisotropies, material defects, and coupling to thermal or mechanical modes. Thus, although stated in terms of macroscopic fields that are defined over length scales many orders of magnitude above the size of the fundamental objects (flux tubes typically spanning over tens of nanometers), the deep understanding of the Critical State model has allowed us to identify valid expressions that connect to the vortex physics.

In brief, one may use a thermodynamic approach that generalizes Bean's model but still keeps a minimal structure for describing the superconducting physics on a large scale. Essentially, by re-stating the problem in terms of minimum entropy production with a dedicated (geometric) interpretation of the $\mathbf{E}(\mathbf{J})$ law, one can incorporate the pinning and vortex–vortex interactions that involve arbitrary size effects, hysteretic losses, magnetization and demagnetization phenomena, and complex configurations with rotating magnetic flux lines, all being common situations experienced in the design and operation of actual HTS applications. Hence, while our comprehension of J_c from a macroscopic perspective is almost complete, its microscopic origin and influence on vortex dynamics at a mesoscopic scale pose more intricate challenges.

Coherence with mesoscopic theories has been tested in dedicated experiments with controlled artificial pinning centers in thin films. Much work also exists on phenomenological expressions for samples in large-scale applications, mainly developed for the practical use of advanced superconductors currently in the commercial pipeline. However, some unexplored corners still exist. In particular, the investigation of "quasi-force-free" configurations where $\mathbf{B}$ has some component along the induced $\mathbf{J}$. This scenario has been explored in very limited instances, primarily involving ideal slab geometries or short samples of straight HTS conductors, where the mechanism of flux cutting comes into play. Essentially, this mechanism constrains the J_c threshold parallel to the lines of the magnetic field within the superconductor. However, its implications on the energy efficiency of helicoidally wound superconducting tapes, as seen in CORC cables, or on the U-turn of D-shaped or racetrack coils utilized in high-field magnets, remain relatively uncharted. This knowledge gap presents an opportunity for further optimization of advanced superconductors, particularly from a macroscopic perspective.

In order to improve the energy efficiency and the performances of the superconductors, in particular for electric current transport, it is important to analyze the correlations between their crystalline structure and the vortex lattice characteristics from real-life scenarios. This can be done by analyzing the behavior of the J_c measurements performed at different temperatures and magnetic fields, which, however, present various experimental issues as discussed in Section 3. Among these, it is necessary to underline the difficulty in the evaluation of the correct value of J_c in the $E(J)$ law, due for example to the sample inhomogeneities, thermal effects, and different anisotropies. Moreover, each measurement technique needs the use of specific criteria that define the threshold for the evaluation of the involved physical parameter. In other words, it is necessary to specify some peculiar measurement parameters, e.g., the sweep rate of the field in DC magnetic measurements or the frequency of the magnetic field or transport current in AC measurements, if a correct interpretation of the scope of J_c for real applications is given.

One of the most interesting aspects concerning the critical current is the possibility to have high values at high fields as it appears in the case of the Second Magnetization Peak (SMP) phenomenon, measured with DC magnetic techniques. The presence of the SMP phenomenon in a superconductor is attractive for the applications also because J_c is strictly correlated with the irreversibility field above which no pinning force acts on the vortices. In this framework, an optimized fabrication process plays a fundamental role

in determining the morphology and the pinning landscape of the material, and so it can allow tuning of the features of the SMP phenomenon in order to maximize the superconducting and the transport capabilities of the cuprates at their working temperatures. In order to indirectly correlate the critical current to the measured macroscopic physical properties, several models are available. Unfortunately, they have different degrees of approximation and can be rigorously applied in particular conditions only, determined by the type of sample, its shape, dimensionality, orientation, etc., and within a given experimental technique. In this context, a more universal model that also puts the macroscopic variables in close correlation with the microscopic ones would be desirable.

The discussion of critical currents in superconductors is incomplete without mentioning their behavior at super-critical current densities, which has been the focus of Section 4. This operational zone of high power dissipation and intense currents is crucial in applications such as fault current limiters and fusion energy magnets. Two phenomena can occur when the critical current – *defined by a very low threshold voltage* – is surpassed. Exploring the current–voltage characteristics to much higher currents and electric fields reveals either a sudden switch into the normal state or, particularly in low external magnetic fields and in self-field, a strongly non-linear behavior caused by the suppression of thermodynamic fluctuations of the superconducting order parameter. High electric fields exert a comparable influence on the configuration of the superconducting transition, akin to the impact of strong magnetic fields. The transition phase is significantly prolonged toward lower temperatures, a phenomenon substantiated by both theoretical computations and experimental observations involving high-intensity, brief current pulses, strategically employed to avert the nucleation of thermal hotspots. As a result, resistance increases even quicker in the supercritical domain than anticipated by thermal models, which are generally based on transition curves observed at low electric fields. Since the impacts of high electric and magnetic fields are not additive, the additional influence of a strong electric field becomes much weaker in the external magnetic fields of several teslas.

Likewise, we have explained how in moderate and high magnetic fields, a discontinuous jump into the high resistive or normal state can occur due to flux-flow instability, FFI. The flux-flow instability occurs at the instability current, which is typically smaller than the pairbreaking current, thus being a crucial factor to take into account in applications where superconductors are exploited in the presence of magnetic fields. The flux-flow instability also prevents realizing regimes of fast (a few km/s to a few tens of km/s) vortex velocities. This restriction is essential for the development of fast fluxonic devices with potential applications in information processing. Thus, while the capability of HTS materials to detect single optical and infrared-range photons is attracting increasing attention, we anticipate that this question will be addressed in detail in the years to come.

The use of the FFI as a tool also reveals a sensitive method to explore the anisotropy of a superconductor. Competitive high-field superconductors should achieve not only the highest critical currents but also the most isotropic ones, so pushing toward the operating limits of any superconducting device. In fact, sustaining the robust current-carrying capacity of these materials within varying fields and temperatures is imperative. Consequently, a comprehensive investigation into the mechanisms underpinning the instability of the vortex lattice, concomitant with the quenching of the superconducting state, becomes indispensable. Depending on the nature of the quenching from the superconducting to the normal state, the difference between the instability current and the critical current can be significant or not, thus it may be totally reasonable to assess the instability current as the actual critical current of the superconducting material. Such scrutiny is essential to avert adverse dissipations and to judiciously select the suitable material for a given application.

Actualizing J_c-by-design requires modeling vortex dynamics via a multi-scale approach in which (i) the elemental interactions with defects are understood on a microscopic scale, (ii) the phenomenology of vortex matter is accurately captured at a mesoscopic level (of the order of the coherence length ξ), and (iii) this knowledge is extended to a macroscopic scale describing the full field-penetrated state under the action of currents in wires and coils as well as devices for sensing and computing. This forms the core subject of Section 5, where we reviewed theoretical, experimental, and numerical aspects of vortex matter research that have advanced the technological progress on this multi-scale path. These include vortex pinning theories, thermally activated vortex motion and quantum creep, tuning fundamental superconducting parameters, and subsequently, the J_c and creep mechanisms using electron/hole doping, and multi-scale simulation tools.

While pinning theories have effectively elucidated dependencies witnessed in experimental data, their application remains fragmented, often confined to specific temperatures and field ranges with specific sample orientations. Achieving comprehensive replication of the $J_c(T, B, \theta)$ function or creep across an expansive spectrum of conditions – encompassing temperatures, magnetic fields, and field orientations – still poses a challenge. This is particularly notable in instances involving non-monotonic characteristics like the second magnetization peaks.

Fully analytical approaches are complicated by a composite of different defect dimensionalities involved in the problem. Consequently, molecular dynamics and time-dependent Ginzburg–Landau simulations have been implemented and successfully predicted J_c in certain materials, e.g., YBCO films containing nanoparticle inclusions as well as the local peak in $J_c(T, B, \theta)$ for YBCO films containing nanorods. Another current limitation is our incomplete knowledge about the material structure, which requires advances in microscopy to, e.g., measure point defect densities and image interactions between elastic vortex lines and defects through the material thickness. This will improve our microscopic understanding of structure–property relationships, which can subsequently inform next-generation simulations for engineering J_c. A promising approach for these next-generation simulations is to develop and apply self-adjusting machine-learning algorithms using neural networks. See, e.g., Ref. [882] for a discussion of this and other transformative opportunities in vortex physics.

From an engineering standpoint, we can state that the operational temperature range for HTS materials in practical applications comfortably aligns with the capabilities of contemporary cryogenic systems. However, due to the pronounced depression of the critical current density resulting from magnetic fields, predominantly due to the interplay of Lorentz-like forces and thermally-activated flux line movement, understanding the presence of nanostructural defects inherent in the fabrication process of advanced

superconductors results of utter importance. Yet, these defects might prove insufficient in both volume density and pinning potential to yield the desired effects. Consequently, we have devoted our final chapter, Section 6, to exploring the different avenues for engineering J_c in the next generation of advanced superconductors. This entails delving into charge carrier doping, manipulation of grain boundaries, and deliberate introduction of artificial pinning centers. Furthermore, we investigated the effects of radiation techniques on J_c to elucidate their potential influence on the defects' morphology, as well as the related challenge for fusion energy systems.

The predominant focus of experimental endeavors in this domain has centered around YBCO (REBCO) films and coated conductors. In terms of fabrication processes, pulsed laser deposition (PLD) notably stands out among the in-situ methods, offering significant advantages over alternative approaches. Consequently, much of the pioneering work concerning APCs was conducted utilizing PLD. Over time, progress in this area followed a gradual trajectory. It commenced with substrate decoration, followed by the adoption of a quasi-multilayer approach and the utilization of composite targets for deposition. Intriguingly, under specific conditions, the application of composite targets facilitated the emergence of self-assembled correlated nanoscale pinning centers.

Recent advancements have demonstrated the most promising outcomes for enhancing critical currents across diverse field and temperature conditions through the synergy of multiple pinning centers, achieved via a combination of different techniques and various types of nano-inclusions, such as double-doping, mixed double perovskites, and intermediate nanolayers. This intricate pinning landscape can also be tailored by manipulating the thermodynamic growth parameters. An illustrative instance is the case of barium zirconate (BZO), which forms mostly nanoparticles in the HTS matrix at elevated rates of laser pulses and marginally reduced growth temperatures, while for the slower process (higher temperature and lower laser pulse frequency), BZO self-assembles in *c*-axis-correlated nanorods.

A more cost-effective alternative to PLD coated conductors is the fabrication of REBCO tapes by chemical solution deposition (CSD). Here, two approaches of inserting perovskite nanoparticles (mostly BZO and BHO) have been successfully tested, in-situ and ex-situ phase formation of the perovskites. Whereas for the former the solutions seem to be more stable, the latter offers larger freedom of material combinations as well as potentially smaller nanoparticles. Contrary to PLD, where heterogeneous nucleation is promoted, leading to a self-assembling process of the NPs that create homogeneously dispersed vertical nanostructures or nanorods, in CSD the perovskite nanoparticles usually grow randomly oriented due to the sequential growth process of the REBCO phase and the NPs. The sequential deposition and growth processes favor the homogeneous nucleation of the NPs, generally resulting in a random and homogeneous distribution in the matrix. Consequently, the appearance of incoherent interfaces between the NPs and the REBCO phase is much more common in CSD than for in-situ growth techniques.

The conventional in-situ approach for the nanocomposite preparation has been shown to significantly increase the pinning force and, consequently, J_c of CSD-grown films. Since in this case the size of the NPs is larger than the coherence length, the pinning-relevant defects are rather stacking faults associated with the incoherent interfaces between the REBCO phase and the NPs. Similar improvements in the transport properties have been observed for the ex-situ approach with preformed NPs. Also here, the pinning mechanism relies on the stacking faults in the vicinity of the NPs. Recently, YBCO nanocomposite films with NPs in the range of 5 nm were reported, leading to a strong increase of the pinning contribution, which is likely a synergistic association of the stacking faults and the NPs themselves since their mean diameter is close to the coherence length.

For BSCCO, the addition of APCs has always been a side topic of academic interest, even though followed by several groups. The same systems as for REBCO, i.e. oxides and (double-)perovskites, have been tested. The nanoparticles often occur also in grain boundaries and voids, which complicates a clear distinction between different possible effects. Typical J_c enhancements are of the order of 2-3, often measured at 77 K self-field or 5 K, 1 T. So far, nanocolumns have not been reported for BSCCO compounds.

MgB_2 has the advantage of a coherence length roughly one order of magnitude larger than for the HTS cuprates, thus enabling grain boundaries as effective pinning centers. This is deemed advantageous, as it eliminates the need for the fabrication of epitaxial single-crystal-like materials, a requirement prevalent in the case of REBCO to attain high critical current densities. Consequently, less sophisticated and cheaper technologies will easily generate polycrystalline MgB_2 with controlled and maximized critical current density. In practice, the sensitivity of MgB_2 to specifics of processing, raw materials, additives, and impurities is also high. This is because they impact anisotropy, defects, homogeneity, chemical substitution into the MgB_2 lattice, local strain, grain boundaries, nano- and microstructures, and all these material details are known to influence the pinning efficiency and the quality of the superconductor. Therefore, pinning engineering is also of paramount importance for the development of MgB_2, which, as for REBCO, is not trivial. In fact, the mentioned sensitivity of MgB_2 is reflected in the field dependencies of the pinning force densities. Namely, these curves may show peculiar profiles (e.g. broadening, peak shift, kink occurrence) so that fitting with a universal pinning force scaling law is uncommon. Moreover, the scaling models based on additive expressions are also shown to fail in MgB_2, because the pinning force factors extracted by fitting the experimental curves are usually far away from the theoretical ones. Nevertheless, a scaling model for the grain boundary pinning can work well in the entire temperature domain if a field-dependent coupling factor is introduced. This coupling factor can account for the revealed peculiarities of the pinning force and, as indicated by the fitting process, is either a single- or double-peaked Gaussian or log-normal function.

Concomitantly, the strategies for enhancing J_c in Fe-based superconducting films have been found to be very similar to the work done on cuprates, e.g., deepening the pinning potentials by appropriate doping, avoiding J_c-limiting defects such as large-angle GBs, utilizing natural growth defects such as low-angle GBs and dislocation networks, and introducing APCs from oxide nanoparticles, especially in Ba122 compounds, or by irradiation. Typical high values of maximum pinning force densities for $B \parallel c$ at 4–5 K are around 100 GN/m^3, as seen for such different systems as pristine and Mn-doped (Li,Fe)OHFeSe, impinged defects in thin NdFeAs(O,F) films, and K-doped Ba122 films. Worth mentioning are two methods for IBS: GB engineering for GB angles close to the critical angle of $\sim 9°$ and strain engineering by epitaxy and irradiation. For the former, several groups have shown enhanced J_c values for slightly

lower degrees of texture (in contrast to the cuprates); the latter has, e.g., been shown for inducing superconductivity in undoped parent compounds by epitaxial strain as well as for enhancing both T_c and J_c simultaneously by ion irradiation.

Gaining a comprehensive understanding of radiation-induced damage mechanisms and their impact on T_c and J_c of HTS materials is indeed challenging, given the multifaceted nature of the contributing parameters. Nevertheless, such understanding holds the potential to expedite the optimization process for superconducting tapes and, of paramount significance, assumes a pivotal role in advancing compact fusion technology. Thus, we have revisited prominent irradiation experiments on advanced superconductors, with a specific emphasis on evaluating the repercussions of damage radiation on coated conductors and HTS tapes intended for real-world applications. Consequently, our investigations have revealed that the morphology of irradiation-induced defects can be governed by judiciously selecting the type and energy of impacting particles. This spectrum ranges from point defects in the case of electrons to columnar defects arising from high-energy heavy ion irradiations. Moreover, the density and orientation of defects can be finely tuned through the adjustment of irradiation fluence and direction. The data consistently reveals overarching trends as damage escalates: a gradual decline in T_c and a non-monotonic pattern in J_c, attributed to the interplay of defect-induced scattering (detrimental) and enhanced vortex pinning (favorable). The dual role of defects renders the prediction of radiation effects on superconducting properties notably challenging.

Furthermore, irradiation has demonstrated its efficacy in adjusting the J_c anisotropy. This adjustment manifests as a decrease when isotropically distributed defects are introduced (as seen in irradiations with MeV-energy protons, neutrons, or heavy ions) or when irradiation-induced defects render the as-grown anisotropic pinning centers ineffective. Notably, the controlled introduction of pinning centers via particle irradiation endows it with exceptional utility as a tool for the development and refinement of pinning models. Likewise, we anticipate that a significant surge in irradiation experiments will be directed toward comprehending the behavior of HTS conductors within the fusion environment, as this field holds paramount importance for the HTS technology and its potential growth. However, achieving this objective will demand a multitude of intricate experiments, spanning a wide spectrum of fluence ranges and energy levels, where a significant emphasis will be placed on conducting such experiments under both, *in-situ* irradiation and *operando* conditions, given their potential to yield insights of paramount significance.

In conclusion, as the demand for advanced superconductors continues to surge in the context of the energy transition, wherein the exceptional current-carrying and magnetic field capabilities of HTS materials are critical for the widespread adoption of compact fusion energy systems, hydrogen-cryocooled powertrains for aviation and long-haul trucking industries, and lightweight MW power drives for the wind energy sector, among other large scale applications, we anticipate a substantial upsurge in research endeavors aimed at increasing J_c through the diverse engineering strategies outlined in Section 6. Concurrently, there will be a concerted effort to enhance our comprehension of vortex–defect interactions in applied superconductors, as elucidated in Section 5. Additionally, a deeper understanding of flux-flow instability regimes in these materials, as explored in Section 4, will be sought from fundamental perspectives. These pursuits will collectively aim to maximize and optimize the utilization of these materials in real-world scenarios, as discussed in Section 3, guided by robust macroscopic approaches that steer the advancement of superconducting machines, magnets, and cables within the energy industry, as elaborated in Section 2. Finally, we note recent efforts to establish a dynamic database compiling key material properties relevant to HTS-based applications [883]. This includes critical current densities, magnetic and thermal parameters, and mechanical and electrical characteristics of structural and auxiliary materials. Such a resource is expected to support future design and modelling of advanced superconducting systems.

CRediT authorship contribution statement

H.S. Ruiz: Writing – review & editing, Writing – original draft, Visualization, Validation, Supervision, Project administration, Investigation, Conceptualization. **J. Hänisch:** Writing – original draft, Visualization, Resources, Investigation, Conceptualization. **M. Polichetti:** Writing – original draft, Visualization, Resources, Investigation, Conceptualization. **A. Galluzzi:** Writing – original draft, Visualization, Resources, Investigation. **L. Gozzelino:** Writing – original draft, Visualization, Resources, Investigation, Conceptualization. **D. Torsello:** Writing – original draft, Visualization, Resources, Investigation. **S. Miloševič-Govedarović:** Writing – original draft, Visualization, Resources, Investigation, Conceptualization. **J. Grbović-Novaković:** Writing – original draft, Visualization, Resources, Investigation, Conceptualization. **O.V. Dobrovolskiy:** Writing – original draft, Visualization, Resources, Investigation, Conceptualization. **W. Lang:** Writing – original draft, Visualization, Resources, Investigation, Conceptualization. **G. Grimaldi:** Writing – original draft, Visualization, Resources, Investigation, Conceptualization. **A. Crisan:** Writing – original draft, Visualization, Resources, Investigation, Conceptualization. **P. Badica:** Writing – original draft, Visualization, Resources, Investigation, Conceptualization. **A.M. Ionescu:** Writing – original draft, Visualization, Resources, Investigation, Conceptualization. **P. Cayado:** Writing – original draft, Visualization, Resources, Investigation, Conceptualization. **R. Willa:** Writing – original draft, Visualization, Resources, Investigation, Conceptualization. **B. Barbiellini:** Writing – original draft, Visualization, Resources, Investigation, Conceptualization. **S. Eley:** Writing – original draft, Visualization, Resources, Investigation, Conceptualization. **A. Badía–Majós:** Writing – original draft, Visualization, Resources, Investigation, Conceptualization.

Declaration of competing interest

The authors declare the following financial interests/personal relationships which may be considered as potential competing interests: Harold S. Ruiz reports administrative support and travel were provided by European Cooperation in Science and Technology (COST). If there are other authors, they declare that they have no known competing financial interests or personal relationships that could have appeared to influence the work reported in this paper.

Acknowledgments

This review paper is result of the international and multidisciplinary collaboration funded by the European Cooperation in Science and Technology (COST) action CA19108: High-Temperature Superconductivity for Accelerating the Energy Transition, https://www.cost.eu/actions/CA19108/.

All authors thank the COST action for enabling funds for the discussion and publication of this paper. Additionally, HSR's work was supported by the UK Research and Innovation, Engineering and Physical Sciences Research Council (EPSRC), Grant Refs. EP/S025707/1 and EP/2438289. JH acknowledges support by the German Research Foundation (DFG), grant number HA 6407/4-1. LG and DT acknowledge the support by the Italian Ministry of Education, University, and Research (Project PRIN HIBiSCUS, Grant No. 201785KWLE) and by the Istituto Nazionale di Fisica Nucleare (Experiment SAMARA). DT acknowledges the support by the Ministry of Education, Universities and Research "Programma Operativo Nazionale (PON) Ricerca e Innovazione 2014–2020". OD acknowledges support by the Austrian Science Fund (FWF), project I6079-N, and by the German Research Foundation (DFG) under Germany's Excellence Strategy, project EXC-2123 QuantumFrontiers – 390837967. WL acknowledges support by the Austrian Science Fund (FWF), project I4865-N. GG acknowledges support by the Italian Ministry of Education, University, and Research, PON Research and Competitiveness 2007–2013, under grant agreement PON NAFASSY (PONa3-00007). AC, PB and AMI acknowledge the support of the European Regional Development Fund, Operational Program Competitiveness, project POC 28/2016, and the support of Romanian Ministry of Research, Innovation and Digitization through Programs PC2-PN23080202 and 35PFE/2021. RW acknowledges funding support from the Heidelberger Akademie der Wissenschaften through its WIN initiative (8. Teilprogramm). BB acknowledges funding support from the INERCOM platform at LUT University and computational resources from the CSC-IT Center for Science, Finland. BB is also grateful for useful discussions with Dr. Tiina Salmi (Tampere University) and Prof. Petriina Paturi (Turku University). SE acknowledges support from the National Science Foundation DMR-1905909 and DMR-2046925. SGM and JGN acknowledge support from the MSTDI of Republic of Serbia under grant 451-03-68/2022-14/200017. ABM acknowledges the financial support from Spanish MCIN/ AEI/ 10.13039/501100011033 (project PID2020-113034RB-I00), Spanish MCIU/ AEI/ 10.13039/501100011033 (project PID2023-146041OB-C21) and Gobierno de Aragón (research group T54_23R).

Data availability

No hitherto unpublished data was used for this article.

References

[1] Molodyk A, Larbalestier DC. The prospects of high-temperature superconductors. Science 2023;380(6651):1220–2.
[2] Godeke A. High temperature superconductors for commercial magnets. Supercond Sci Technol 2023;36(11):113001.
[3] Patel I, Shah A, Shen B, Wei H, Hao L, Hu J, et al. Stochastic optimisation and economic analysis of combined high temperature superconducting magnet and hydrogen energy storage system for smart grid applications. Appl Energy 2023;341:121070.
[4] Papageorgiou PG, Oureilidis KO, Christoforidis GC. A systematic review of hybrid superconducting magnetic/battery energy storage systems: Applications, control strategies, benefits, limitations and future prospects. Renew Sustain Energy Rev 2023;183:113436.
[5] Stryczewska HD, Boiko O, Stępień MA, Lasek P, Yamazato M, Higa A. Selected materials and technologies for electrical energy sector. Energies 2023;16(12).
[6] Chen Y, Fu L, Chen X, Jiang S, Chen X, Xu J, et al. Ultra-low electrical loss superconducting cables for railway transportation: Technical, economic, and environmental analysis. J Clean Prod 2024;445:141310.
[7] Sadeghi A, Morandi A, Yazdani-Asrami M. Feasibility of high temperature superconducting cables for energy harvesting in large space-based solar power satellite applications: Electromagnetic, thermal and cost considerations. Energy Rep 2024;11:4523–36.
[8] Kingham D, Gryaznevich M. The spherical tokamak path to fusion power: Opportunities and challenges for development via public–private partnerships. Phys Plasmas 2024;31(4):042507.
[9] MacManus-Driscoll JL, Wimbush SC. Processing and application of high-temperature superconducting coated conductors. Nat Rev Mater 2021;6(7):587–604.
[10] Bednorz JG, Müller KA. Possible high T_c superconductivity in the Ba-La-Cu-O system. Z Phys B Condens Matter 1986;64(2):189–93.
[11] Testardi L, Wernick J, Royer W. Superconductivity with onset above 23° K in Nb_3Ge sputtered films. Solid State Commun 1974;15(1):1–4.
[12] Wu MK, Ashburn JR, Torng CJ, Hor PH, Meng RL, Gao L, et al. Superconductivity at 93 K in a new mixed-phase Y-Ba-Cu-O compound system at ambient pressure. Phys Rev Lett 1987;58:908.
[13] Maeda H, Tanaka Y, Fukutomi M, Asano T. A new high-T_c) oxide superconductor without a rare earth element. Japan J Appl Phys 1988;27(2A):L209.
[14] Nagamatsu J, Nakagawa N, Muranaka T, Zenitani Y, Akimitsu J. Superconductivity at 39 K in magnesium diboride. Nature 2001;410(6824):63–4.
[15] Kamihara Y, Watanabe T, Hirano M, Hosono H. Iron-based layered superconductor $La[O_{1-x}F_x]FeAs$ (x = 0.05-0.12) with T_c = 26 K. J Am Chem Soc 2008;130(11):3296–7.
[16] Manso Jimeno M, Vaughan JT, Geethanath S. Superconducting magnet designs and MRI accessibility: A review. NMR Biomed 2023;36(9):e4921.
[17] Wikus P, Frantz W, Kümmerle R, Vonlanthen P. Commercial gigahertz-class NMR magnets. Supercond Sci Technol 2022;35(3):033001.
[18] Kraemer H-P, Bauer A, Frank M, van Hasselt P, Kummeth P, Wohlfart M, et al. ASSiST - A superconducting fault current limiter in a public electric power grid. IEEE Trans Power Deliv 2022;37(1):612–8.
[19] Dong F, Hao L, Park D, Iwasa Y, Huang Z. On the future sustainable ultra-high-speed maglev: An energy-economical superconducting linear thrusting system. Energy Convers Manage 2023;291:117247.
[20] Li X, Palazzolo A. A review of flywheel energy storage systems: state of the art and opportunities. J Energy Storage 2022;46:103576.
[21] Mitchell N, Zheng J, Vorpahl C, Corato V, Sanabria C, Segal M, et al. Superconductors for fusion: a roadmap. Supercond Sci Technol 2021;34(10):103001.
[22] Cooper BE, Hadfield RH. Viewpoint: Compact cryogenics for superconducting photon detectors. Supercond Sci Technol 2022;35(8):080501.
[23] Ybanez L, Colle A, Nilsson E, Berg F, Galla G, Tassisto M, et al. ASCEND: The first step towards cryogenic electric propulsion. IOP Conf Ser: Mater Sci Eng 2022;1241(1):012034.

[24] Stautner W. Cryocoolers for superconducting generators. In: Cryocoolers: Theory and applications. Cham: Springer International Publishing; 2020, p. 121–54.
[25] Demko J, Fesmire J, Shu Q-S. Cryogenic heat management: Technology and applications for science and industry. 1st ed. CRC Press; 2022.
[26] Liu J, Wang Q, Qin L, Zhou B, Wang K, Wang Y, et al. World record 32.35 tesla direct-current magnetic field generated with an all-superconducting magnet. Supercond Sci Technol 2020;33(3):03LT01.
[27] Patel A, Baskys A, Mitchell-Williams T, McCaul A, Coniglio W, Hänisch J, et al. A trapped field of 17.7 T in a stack of high temperature superconducting tape. Supercond Sci Technol 2018;31(9):09LT01.
[28] Zhou D, Srpcic J, Huang K, Ainslie M, Shi Y, Dennis A, et al. Reliable 4.8 T trapped magnetic fields in Gd–Ba–Cu–O bulk superconductors using pulsed field magnetization. Supercond Sci Technol 2021;34(3):034002.
[29] Blatter G, Feigel'man MV, Geshkenbein VB, Larkin AI, Vinokur VM. Vortices in high-temperature superconductors. Rev Modern Phys 1994;66:1125–388.
[30] McHenry ME, Sutton RA. Flux pinning and dissipation in high temperature oxide superconductors. Prog Mater Sci 1994;38:159–310.
[31] Kwok W-K, Welp U, Glatz A, Koshelev AE, Kihlstrom KJ, Crabtree GW. Vortices in high-performance high-temperature superconductors. Rep Progr Phys 2016;79(11):116501.
[32] Sadovskyy IA, Jia Y, Leroux M, Kwon J, Hu H, Fang L, et al. Toward superconducting critical current by design. Adv Mater 2016;28(23):4593.
[33] Puig T, Gutierrez J, Obradors X. Impact of high growth rates on the microstructure and vortex pinning of high-temperature superconducting coated conductors. Nat Rev Phys 2024;6(2):132–48.
[34] Pardo E, Kapolka M. 3D computation of non-linear eddy currents: Variational method and superconducting cubic bulk. J Comput Phys 2017;344:339–63.
[35] Yazdani-Asrami M, Song W, Morandi A, Carne GD, Murta-Pina J, Pronto A, et al. Roadmap on artificial intelligence and big data techniques for superconductivity. Supercond Sci Technol 2023;36(4):043501.
[36] Plakida N. High-temperature cuprate superconductors: Experiment, theory, and applications. In: Springer series in solid-state sciences, Springer Berlin Heidelberg; 2010.
[37] Rao CNR, Nagarajan R, Vijayaraghaven R. Synthesis of cuprate superconductors. Supercond Sci Technol 1993;6(1):1.
[38] Kamihara Y, Hiramatsu H, Hirano M, Kawamura R, Yanagi H, Kamiya T, et al. Iron-based layered superconductor: LaOFeP. J Am Chem Soc 2006;128(31):10012–3.
[39] Putti M, Pallecchi I, Bellingeri E, Cimberle MR, Tropeano M, Ferdeghini C, et al. New Fe-based superconductors: properties relevant for applications. Supercond Sci Technol 2010;23(3):034003.
[40] Biswal G, Mohanta K. A recent review on iron-based superconductor. Mater Today: Proc 2021;35:207–15.
[41] Muralidhar M, Shadab M, Srikanth AS, Jirsa M, Noudem J. Review on high-performance bulk MgB_2 superconductors. J Phys D: Appl Phys 2023;57(5):053001.
[42] Prikhna T, Sokolovsky V, Moshchil V. Bulk MgB_2 Superconducting Materials: Technology, Properties, and Applications. Materials 2024;17(11):2787.
[43] Josephson BD. Macroscopic field equations for metals in equilibrium. Phys Rev 1966;152:211–7.
[44] Campbell AM, Evetts J. Critical currents in superconductors. In: Monographs on physics: Taylor and Francis, London: Taylor & Francis; 1972.
[45] Tinkham M. Introduction to superconductivity: Second edition (Dover Books on Physics) (Vol 1). 2nd ed. New York: Dover Publications; 2004.
[46] Orlando TP, Delin KA. Foundations of applied superconductivity. Reading, Massachusets: Addison-Wesley; 1991.
[47] Matsushita T. Flux pinning in superconductors. In: Springer series in solid-state sciences, vol. 178, Heidelberg: Springer; 2014.
[48] Badía-Majós A. Macroscopic Superconducting Phenomena. 2053-2563, IOP Publishing; 2021.
[49] Bean CP. Magnetization of hard superconductors. Phys Rev Lett 1962;8:250–3.
[50] Bean CP. Magnetization of high-field superconductors. Rev Modern Phys 1964;36:31–9.
[51] Luzuriaga J, Badía-Majós A, Nieva G, Giordano J, López C, Serquis A, et al. Magnetic relaxation induced by transverse flux shaking in MgB_2 superconductors. Supercond Sci Technol 2008;22(1):015021.
[52] Liang F, Qu T, Zhang Z, Sheng J, Yuan W, Iwasa Y, et al. Vortex shaking study of REBCO tape with consideration of anisotropic characteristics. Supercond Sci Technol 2017;30(9):094006.
[53] Baghdadi M, Ruiz HS, Coombs TA. Crossed-magnetic-field experiments on stacked second generation superconducting tapes: Reduction of the demagnetization effects. Appl Phys Lett 2014;104(23):232602.
[54] Baghdadi M, Ruiz HS, Coombs TA. Nature of the low magnetization decay on stacks of second generation superconducting tapes under crossed and rotating magnetic field experiments. Sci Rep 2018;8(1):1342.
[55] Mikitik GP. Critical states in thin planar Type-II superconductors in a perpendicular or inclined magnetic field (Review). Low Temp Phys 2010;36(1):13–38.
[56] Mikheenko P, Kuzovlev Y. Inductance measurements of HTSC films with high critical currents. Phys C: Supercond 1993;204(3):229–36.
[57] Brandt EH, Indenbom M. Type-II-superconductor strip with current in a perpendicular magnetic field. Phys Rev B 1993;48:12893–906.
[58] Prigozhin L. Solution of thin film magnetization problems in Type-II superconductivity. J Comput Phys 1998;144(1):180–93.
[59] Clem JR, Perez-Gonzalez A. Flux-line-cutting and flux-pinning losses in Type-II superconductors in rotating magnetic fields. Phys Rev B 1984;30:5041–7.
[60] Brandt EH, Mikitik GP. Unusual critical states in Type-II superconductors. Phys Rev B 2007;76:064526.
[61] Kashima Y. On the double critical-state model for Type-II superconductivity in 3D. ESAIM Math Model Numer Anal 2008;42(3):333–74.
[62] Pecher R, McCulloch M, Chapman L, Elliot C. 3D modelling of bulk Type-II superconductors using unconstrained H-formulation. Inst Phys Conf Ser 2003;81:1418.
[63] Grilli F, Stavrev S, Le Floch Y, Costa-Bouzo M, Vinot E, Klutsch I, Meunier G, Tixador P, Dutoit B. Finite-element method modeling of superconductors: from 2-D to 3-D. IEEE Trans Appl Supercond 2005;15(1):17–25.
[64] Grilli F, Brambilla R, Sirois F, Stenvall A, Memiaghe S. Development of a three-dimensional finite-element model for high-temperature superconductors based on the H-formulation. Cryogenics 2013;53:142–7.
[65] Stenvall A, Lahtinen V, Lyly M. An H-formulation-based three-dimensional hysteresis loss modelling tool in a simulation including time varying applied field and transport current: the fundamental problem and its solution. Supercond Sci Technol 2014;27(10):104004.
[66] Pardo E, Kapolka M. 3D magnetization currents, magnetization loop, and saturation field in superconducting rectangular prisms. Supercond Sci Technol 2017;30(6):064007.
[67] Kapolka M, Zermeño VMR, Zou S, Morandi A, Ribani PL, Pardo E, et al. Three-dimensional modeling of the magnetization of superconducting rectangular-based bulks and tape stacks. IEEE Trans Appl Supercond 2018;28(4):1–6.
[68] Kapolka M, Pardo E. 3D modelling of macroscopic force-free effects in superconducting thin films and rectangular prisms. Supercond Sci Technol 2019;32(5):054001.
[69] Kapolka M, Pardo E, Grilli F, Baskys A, Climente-Alarcon V, Dadhich A, et al. Cross-field demagnetization of stacks of tapes: 3D modelling and measurements. Supercond Sci Technol 2019.
[70] Prigozhin L, Sokolovsky V. Fast Fourier transform-based solution of 2D and 3D magnetization problems in type-II superconductivity. Supercond Sci Technol 2018;31(5):055018.
[71] Fareed MU, Kapolka M, Robert BC, Clegg M, Ruiz HS. 3D FEM modeling of CORC commercial cables with Bean's like magnetization currents and its AC-losses behavior. IEEE Trans Appl Supercond 2022;32(4):1–5.

[72] Fareed MU, Kapolka M, Robert BC, Clegg M, Ruiz HS. 3D modelling and validation of the optimal pitch in commercial CORC cables. IOP Conf Ser: Mater Sci Eng 2022;1241(1):012030.
[73] Clegg M, Ruiz H. Electromagnetic analysis and AC losses of triaxial cables with multiple 2G-HTS layers per phase. Superconductivity 2023;5:100039.
[74] Clegg M, Ruiz HS. Practical forecasting of AC losses in multi-layer 2G-HTS cold dielectric conductors. IEEE Trans Appl Supercond 2023;33(5):1–6.
[75] Xing W, Heinrich B, Zhou H, Fife AA, Cragg AR. Magnetic flux mapping, magnetization, and current distributions of $YBa_2Cu_3O_7$ thin films by scanning Hall probe measurements. J Appl Phys 1994;76(7):4244–55.
[76] Grigorenko AN, Bending SJ, Gregory JK, Humphreys RG. Scanning Hall probe microscopy of flux penetration into a superconducting $YBa_2Cu_3O_{7-\delta}$ thin film strip. Appl Phys Lett 2001;78(11):1586–8.
[77] Fang L, Jia Y, Mishra V, Chaparro C, Vlasko-Vlasov VK, Koshelev AE, et al. Huge critical current density and tailored superconducting anisotropy in $SmFeAsO_{0.8}F_{0.15}$ by low-density columnar-defect incorporation. Nat Commun 2013;4.
[78] Johansen TH, Baziljevich M, Bratsberg H, Galperin Y, Lindelof PE, Shen Y, et al. Direct observation of the current distribution in thin superconducting strips using magneto-optic imaging. Phys Rev B 1996;54(22):16264–9.
[79] Jooss C, Warthmann R, Forkl A, Kronmüller H. High-resolution magneto-optical imaging of critical currents in $YBa_2Cu_3O_{7-\delta}$ thin films. Phys C: Supercond 1998;299(3):215–30.
[80] Jooss C, Albrecht J, Kuhn H, Leonhardt S, Kronmüller H. Magneto-optical studies of current distributions in high-T_c superconductors. Rep Progr Phys 2002;65(5):651–788.
[81] Sánchez A, Navau C. Critical-current density from magnetization loops of finite high-T_c superconductors. Supercond Sci Technol 2001;14(7):444–7.
[82] Ruiz HS, Badía-Majós A. Exotic magnetic response of superconducting wires subject to synchronous and asynchronous oscillating excitations. J Appl Phys 2013;113(19):193906.
[83] Badía-Majós A. Understanding stable levitation of superconductors from intermediate electromagnetics. Am J Phys 2006;74(12):1136–42.
[84] Quéval L, Liu K, Yang W, Zermeño VMR, Ma G. Superconducting magnetic bearings simulation using an H-formulation finite element model. Supercond Sci Technol 2018;31(8):084001.
[85] Hohenberg P, Krekhov A. An introduction to the Ginzburg–Landau theory of phase transitions and nonequilibrium patterns. Phys Rep 2015;572:1–42.
[86] Schmid A. A time dependent Ginzburg-Landau equation and its application to the problem of resistivity in the mixed state. Phys Kondens Mater 1966;5(4):302–17.
[87] Grigorishin KV. Extended time-dependent Ginzburg–Landau theory. J Low Temp Phys 2021;203(3):262–308.
[88] Badía-Majós A, López C. Electromagnetics close beyond the critical state: Thermodynamic prospect. Supercond Sci Technol 2012;25(10):104004.
[89] Landau LD, Lifshitz EM. Electrodynamics of continuous media: Vol 8. (Course of Theoretical Physics) Butterworth-Heinemann; 1984.
[90] Prigogine I. Introduction to thermodynamics of irreversible processes. New York: Interscience; 1967.
[91] Clem JR, Weigand M, Durrell JH, Campbell AM. Theory and experiment testing flux-line cutting physics. Supercond Sci Technol 2011;24(6):062002.
[92] Badía-Majós A, López C. Modelling current voltage characteristics of practical superconductors. Supercond Sci Technol 2015;28(2):024003.
[93] Conn A, Gould G, Toint P. Lancelot: A fortran package for large-scale nonlinear optimization (Release A). Springer-Verlag Berlin Heidelberg; 1992, p. 332.
[94] Matsushita T. Measurement methods for critical current density. In: Flux pinning in superconductors. Berlin, Heidelberg: Springer Berlin Heidelberg; 2007, p. 209–31.
[95] Ekin JW. Experimental techniques for low-temperature measurements: Cryostat design, material properties and superconductor critical-current testing. Oxford University Press; 2006, p. 673.
[96] Yeshurun Y, Malozemoff AP. Giant flux creep and irreversibility in an Y-Ba-Cu-O crystal: An alternative to the superconducting-glass model. Phys Rev Lett 1988;60:2202–5.
[97] Talantsev EF, Strickland NM, Wimbush SC, Crump WP. The onset of dissipation in high-temperature superconductors: Self-field experiments. AIP Adv 2017;7(12):125230.
[98] Pan AV, Golovchanskiy IA, Fedoseev SA. Critical current density: Measurements vs. reality. Europhys Lett 2013;103(1):17006.
[99] Ekin JW. Offset criterion for determining superconductor critical current. Appl Phys Lett 1989;55(9):905–7.
[100] Cooley LD, Lee PJ, Larbalestier DC. Processing of low T_c conductors: The alloy Nb–Ti. In: Cardwell D, Larbalestier D, Braginski A, editors. Handbook of superconductivity: processing and cryogenics, vol. 2. CRC Press; 2021, p. 26.
[101] Banno N. Low-temperature superconductors: Nb_3Sn, Nb_3Al, and NbTi. Superconductivity 2023;6:100047.
[102] Pong I. Processing of low T_c conductors: The compound Nb_3Sn. In: Cardwell D, Larbalestier D, Braginski A, editors. Handbook of superconductivity: processing and cryogenics, vol. 2. CRC Press; 2021, p. 63.
[103] Jiang J, Hellstrom EE. Processing of high T_c conductors: The compound Bi-2212. In: Cardwell D, Larbalestier D, Braginski A, editors. Handbook of superconductivity: processing and cryogenics, vol. 2. CRC Press; 2021, p. 19.
[104] Oloye TA, Matras M, Jiang J, Hossain SI, Su Y, Trociewitz UP, et al. Correlation of critical current density to quasi-biaxial texture and grain boundary cleanliness in fully dense Bi-2212 wires. Supercond Sci Technol 2021;34(3):035018.
[105] Horvat J, Yeoh WK, Kim JH, Dou SX. Transport and magnetic critical current in superconducting MgB_2 wires. Supercond Sci Technol 2008;21(6):065003.
[106] Kim J, Dou S, Matsumoto A, Choi S, Kiyoshi T, Kumakura H. Correlation between critical current density and n-value in MgB_2/Nb/Monel superconductor wires. Phys C: Supercond Appl 2010;470(20):1207–10.
[107] Carvalho de Castro Sene F. Review on the state-of-the-art and challenges in the MgB_2 component manufacturing for superconducting applications. Superconductivity 2024;9:100083.
[108] Yao C, Ma Y. Recent breakthrough development in iron-based superconducting wires for practical applications. Supercond Sci Technol 2019;32(2):023002.
[109] Zhang X, Ma Y. Progress in the development of the 122-type IBS wires. Superconductivity 2022;2:100010.
[110] Jaroszynski J, Constantinescu A-M, Miller G, Xu A, Francis A, Murphy T, et al. Rapid assessment of REBCO CC angular critical current density $J_c(B, T = 4.2\ \mathrm{K}, \theta)$ using torque magnetometry up to at least 30 Tesla. Supercond Sci Technol 2022;35(9):095009.
[111] Zola D, Gömöry F, Polichetti M, Strýček F, Seiler E, Hušek I, et al. A study of coupling loss on Bi-columnar BSCCO/Ag tapes through AC susceptibility measurements. Supercond Sci Technol 2004;17(3):501.
[112] Gömöry F. Characterization of high-temperature superconductors by AC susceptibility measurements. Supercond Sci Technol 1997;10(8):523.
[113] Polichetti M, Adesso M, Pace S. Third harmonics of the AC magnetic susceptibility: a method for the study of flux dynamics in high temperature superconductors. Eur Phys J B-Condens Matter Complex Syst 2003;36(1):27–36.
[114] Campbell AM. The response of pinned flux vortices to low-frequency fields. J Phys C: Solid State Phys 1969;2(8):1492–501.
[115] Qvarford M, Heeck K, Lensink JG, Wijngaarden RJ, Griessen R. Microtorquemeter for magnetization measurements on small superconducting samples. Rev Sci Instrum 1992;63(12):5726–32.
[116] Graef MD. Magnetic imaging and its applications to materials. In: Experimental methods in the physical sciences, vol. 36, San Diego ; London: Academic Press; 2001.
[117] Budker D, Jackson Kimball DF. Optical magnetometry. New York: Cambridge University Press; 2013, http://dx.doi.org/10.1038/nphys566.
[118] Johansen TH, Shantsev DV. Magneto-optical imaging. In: II. Mathematics, physics and chemistry-vol. 142, Nato Science Series; 2004.

[119] Meltzer AY, Levin E, Zeldov E. Direct reconstruction of two-dimensional currents in thin films from magnetic-field measurements. Phys Rev Appl 2017;8:064030.
[120] Amorós J, Duran A, Carrera M, López J, Granados X. Singular spectrum analysis filtering and Fourier inversion: an efficient and fast way to improve resolution and quality of current density maps with low-cost Hall scanning systems. Meas Sci Technol 2018;30(1):015010.
[121] Broadway D, Lillie S, Scholten S, Rohner D, Dontschuk N, Maletinsky P, et al. Improved current density and magnetization reconstruction through vector magnetic field measurements. Phys Rev Appl 2020;14:024076.
[122] Boyer R, Fillion G, LeBlanc MAR. Hysteresis losses and magnetic phenomena in rotating disks of type-II superconductors. J Appl Phys 1980;51(3):1692–701.
[123] Badía-Majós A, López C, Ruiz HS. General critical states in type-II superconductors. Phys Rev B 2009;80:144509.
[124] Ruiz HS, Badía-Majós A. Smooth double critical state theory for type-II superconductors. Supercond Sci Technol 2010;23(10):105007.
[125] Sirois F, Grilli F, Morandi A. Comparison of constitutive laws for modeling high-temperature superconductors. IEEE Trans Appl Supercond 2019;29(1).
[126] Warnes W, Larbalestier D. Critical current distributions in superconducting composites. Cryogenics 1986;26(12):643–53.
[127] Edelman HS, Larbalestier DC. Resistive transitions and the origin of the n value in superconductors with a Gaussian critical-current distribution. J Appl Phys 1993;74(12):3312.
[128] Yamafuji K, Kiss T. Current-voltage characteristics near the glass-liquid transition in high-T_c superconductors. Phys C: Supercond 1997;290(1):9–22.
[129] Yamafuji K, Kiss T. A new interpretation of the glass-liquid transition of pinned fluxoids in high-T_c superconductors. Phys C: Supercond 1996;258(3):197–212.
[130] Kiss T, Nakamura T, Takeo H, Kuroda K, Matsumoto Y, Irie F. Flux creep characteristics in the presence of a pinning distribution for $Y_1Ba_2Cu_3O_{7-\delta}$ superconducting thin films. IEEE Trans Appl Supercond 1995;5(2):1363–6.
[131] Riva N, Sirois F, Lacroix C, Pellerin F, Giguere J, Grilli F, Dutoit B. A wide range E-J constitutive law for simulating REBCO tapes above their critical current. Supercond Sci Technol 2021;34(11):115014.
[132] Griessen R. Relaxation effects, I-V curves and irreversibility lines in high-T_c superconductors. Phys C: Supercond 1991;175(3):315–23.
[133] Caplin AD, Cohen LF, Perkins GK, Zhukov AA. The electric field within high-temperature superconductors: mapping the E-J-B surface. Supercond Sci Technol 1994;7(6):412–22.
[134] Taylor DMJ, Hampshire DP. Relationship between the *n*-value and critical current in Nb_3Sn superconducting wires exhibiting intrinsic and extrinsic behaviour. Supercond Sci Technol 2005;18(12):S297–302.
[135] Opherden L, Sieger M, Pahlke P, Huhne R, Schultz L, Meledin A, et al. Large pinning forces and matching effects in $YBa_2Cu_3O_{7-\delta}$ thin films with $Ba_2Y(Nb/Ta)O_6$ nano-precipitates. Sci Rep 2016;6(1).
[136] Valles F, Palau A, Rouco V, B. Mundet XO, Puig T. Angular flux creep contributions in $YBa_2Cu_3O_{7-\delta}$ nanocomposites from electrical transport measurements. Sci Rep 2018;8(3):5924.
[137] Iida K, Hänisch J, Reich E, Kurth F, Hühne R, Schultz L, et al. Intrinsic pinning and the critical current scaling of clean epitaxial Fe(Se,Te) thin films. Phys Rev B 2013;87:104510.
[138] Civale L, Maiorov B, MacManus-Driscoll J, Wang H, Holesinger T, Foltyn S, et al. Identification of intrinsic ab-plane pinning in $YBa_2Cu_3O_7$ thin films and coated conductors. IEEE Trans Appl Supercond 2005;15(2):2808–11.
[139] Robert BC, Fareed MU, Ruiz HS. How to choose the superconducting material law for the modelling of 2G-HTS coils. Materials 2019;12(17):2679.
[140] Zhang X, Zhong Z, Geng J, Shen B, Ma J, Li C, et al. Study of critical current and *n*-values of 2G HTS tapes: Their magnetic field-angular dependence. J Supercond Nov Magn 2018;31(12):3847–54.
[141] Zhang X, Zhong Z, Ruiz HS, Geng J, Coombs TA. General approach for the determination of the magneto-angular dependence of the critical current of YBCO coated conductors. Supercond Sci Technol 2017;30(2):025010.
[142] Kim YB, Hempstead CF, Strnad AR. Critical persistent currents in hard superconductors. Phys Rev Lett 1962;9:306–9.
[143] Xu M, Shi D, Fox RF. Generalized critical-state model for hard superconductors. Phys Rev B 1990;42:10773–6.
[144] Richardson RA, Pla O, Nori F. Confirmation of the modified Bean model from simulations of superconducting vortices. Phys Rev Lett 1994;72:1268–71.
[145] Thakur KP, Raj A, Brandt EH, Kvitkovic J, Pamidi SV. Frequency-dependent critical current and transport AC loss of superconductor strip and Roebel cable. Supercond Sci Technol 2011;24(6):065024.
[146] Wimbush SC, Strickland NM. Utilising angle-dependent critical current data in the electromagnetic modelling of HTS coils. Supercond Sci Technol 2022;35(2):024004.
[147] Zermeno VMR, Abrahamsen AB, Mijatovic N, Jensen BB, Sørensen MP. Calculation of alternating current losses in stacks and coils made of second generation high temperature superconducting tapes for large scale applications. J Appl Phys 2013;114(17):173901.
[148] Ionescu A, Miu D, Crisan A, Miu L. Pinning-induced vortex-system disordering at the origin of the second magnetization peak in superconducting single crystals. J Supercond Nov Magn 2018;31(8):2329–37.
[149] Galluzzi A, Buchkov K, Tomov V, Nazarova E, Leo A, Grimaldi G, et al. Evidence of pinning crossover and the role of twin boundaries in the peak effect in FeSeTe iron based superconductor. Supercond Sci Technol 2018;31(1):015014.
[150] Gordeev SN, Jahn W, Zhukov AA, Küpfer H, Wolf T. Comparative study of the peak effect in $YBa_2Cu_3O_{7-\delta}$ single crystals by transport and magnetic measurements. Phys Rev B 1994;49:15420–3.
[151] Yang G, Shang P, Sutton SD, Jones IP, Abell JS, Gough CE. Competing pinning mechanisms in $Bi_2Sr_2CaCu_2O_y$ single crystals by magnetic and defect structural studies. Phys Rev B 1993;48:4054–60.
[152] Kodama Y, Oka K, Yamaguchi Y, Nishihara Y, Kajimura K. Relation between the second peak in the magnetization curves and magnetic relaxation of $La_{2-x}Sr_xCuO_4$ single crystals. Phys Rev B 1997;56(10):6265.
[153] Abulafia Y, Shaulov A, Wolfus Y, Prozorov R, Burlachkov L, Yeshurun Y, et al. Plastic vortex creep in $YBa_2Cu_3o_{7-x}$ crystals. Phys Rev Lett 1996;77:1596–9.
[154] Nishizaki T, Naito T, Kobayashi N. Anomalous magnetization and field-driven disordering transition of a vortex lattice in untwinned $YBa_2Cu_3O_y$. Phys Rev B 1998;58(17):11169.
[155] Li D, Lin P-J, Rosenstein B, Shapiro BY, Shapiro I. Influence of quenched disorder on the square-to-rhombohedral structural transformation of the vortex lattice of Type-II superconductors. Phys Rev B 2006;74(17):174518.
[156] Safar H, Gammel P, Bishop D, Mitzi D, Kapitulnik A. SQUID picovoltometry of single crystal $Bi_2Sr_2CaCu_2O_{8+\delta}$: Observation of the crossover from high-temperature Arrhenius to low-temperature vortex-glass behavior. Phys Rev Lett 1992;68(17):2672.
[157] Küpfer H, Gordeev S, Jahn W, Kresse R, Meier-Hirmer R, Wolf T, et al. Phase diagram of flux creep in melt-textured and single-crystalline $YBa_2Cu_3O_{7-\delta}$. Phys Rev B 1994;50(10):7016.
[158] Lotnyk D, Vovk R, Obolenskii M, Zavgorodniy A, Kováč J, Antal V, et al. Evolution of the Fishtail-effect in pure and Ag-doped MG-YBCO. J Low Temp Phys 2010;161(3):387–94.
[159] Daeumling M, Seuntjens J, Larbalestier D. Oxygen-defect flux pinning, anomalous magnetization and intra-grain granularity in $YBa_2Cu_3O_{7-\delta}$. Nature 1990;346(6282):332–5.
[160] Prozorov R, Ni N, Tanatar M, Kogan V, Gordon R, Martin C, et al. Vortex phase diagram of $Ba(Fe_{0.93}Co_{0.07})_2As_2$ single crystals. Phys Rev B 2008;78(22):224506.
[161] Zhou W, Xing X, Wu W, Zhao H, Shi Z. Second magnetization peak effect, vortex dynamics and flux pinning in 112-type superconductor $Ca_{0.8}La_{0.2}Fe_{1-x}Co_xAs_2$. Sci Rep 2016;6(1):1–10.

[162] Lopes PV, Sundar S, Salem-Sugui S, Hong W, Luo H, Ghivelder L. Second magnetization peak, anomalous field penetration, and Josephson vortices in $KCa_2Fe_4As_4F_2$ bilayer pnictide superconductor. Sci Rep 2022;12(1):20359.
[163] Poole C, Farach H, Creswick R, Prozorov R. Superconductivity. Amsterdam: Academic Press; 2007.
[164] Shantsev DV, Koblischka MR, Galperin YM, Johansen TH, Půst L, Jirsa M. Central peak position in magnetization loops of high-T_c superconductors. Phys Rev Lett 1999;82:2947–50.
[165] Polichetti M, Galluzzi A, Buchkov K, Tomov V, Nazarova E, Leo A, et al. A precursor mechanism triggering the second magnetization peak phenomenon in superconducting materials. Sci Rep 2021;11(1):1–9.
[166] Stamopoulos D, Pissas M. A DC magnetization and local permeability study of the $HgBa_2CuO_{4+\delta}$ superconductor. Supercond Sci Technol 2001;14(10):844.
[167] Shen B, Cheng P, Wang Z, Fang L, Ren C, Shan L, et al. Flux dynamics and vortex phase diagram in $Ba(Fe_{1-x}Co_x)_2As_2$ single crystals revealed by magnetization and its relaxation. Phys Rev B 2010;81(1):014503.
[168] Stamopoulos D, Niarchos D. Relaxation measurements in the regime of the second magnetization peak in Nb films. Phys C: Supercond 2004;417(1–2):69–76.
[169] Zhukov A, Küpfer H, Perkins G, Cohen L, Caplin A, Klestov S, et al. Influence of oxygen stoichiometry on the irreversible magnetization and flux creep in $RBa_2Cu_3O_{7-\delta}$ (R Y,Tm) single crystals. Phys Rev B 1995;51(18):12704.
[170] Klein L, Yacoby E, Yeshurun Y, Erb A, Müller-Vogt G, Breit V, et al. Peak effect and scaling of irreversible properties in untwinned Y-Ba-Cu-O crystals. Phys Rev B 1994;49(6):4403.
[171] Cohen L, Laverty J, Perkins G, Caplin A, Assmus W. Fishtails, scales and magnetic fields. Cryogenics 1993;33(3):352–6.
[172] Murakami M. Melt-processing of high temperature superconductors. Prog Mater Sci 1994;38:311–57.
[173] Reissner M, Lorenz J. Comparison of results of different methods for the analysis of flux creep behavior in a melt-textured $YBa_2Cu_3O_{7-x}$ sample showing a fishtail effect. Phys Rev B 1997;56(10):6273.
[174] Küpfer H, Wolf T, Lessing C, Zhukov A, Lancon X, Meier-Hirmer R, et al. Peak effect and its evolution from oxygen deficiency in $YBa_2Cu_3O_{7-\delta}$ single crystals. Phys Rev B 1998;58(5):2886.
[175] Miu L, Noji T, Koike Y, Cimpoiasu E, Stein T, Almasan C. Crossover from elastic to plastic vortex creep across the second magnetization peak of high-temperature superconductors. Phys Rev B 2000;62(22):15172.
[176] Giller D, Abulafia Y, Prozorov R, Wolfus Y, Shaulov A, Yeshurun Y. Local voltage-current characteristics in high-T_c superconductors. Phys Rev B 1998;57(22):R14080.
[177] Pissas M, Moraitakis E, Kallias G, Bondarenko A. Onset of the fishtail peak in an untwinned $YBa_2Cu_3O_{7-\delta}$ crystal. Phys Rev B 2000;62(2):1446.
[178] Gokhfeld D, Semenov S, Balaev D, Yakimov I, Dubrovskiy A, Terentyev KY, et al. Establishing of peak effect in YBCO by Nd substitution. J Magn Magn Mater 2017;440:127–8.
[179] Antal V, Volochová D, Kavečanskỳ V, Kováč J, Diko P. Influence of annealing in oxygen and argon on the superconducting properties of Li-doped YBCO single-grain bulks. Phys C: Supercond Appl 2017;541:22–9.
[180] Vojtkova L, Diko P, Kovac J, Vojtko M. Influence of Sm_2O_3 microalloying and Yb contamination on Y211 particles coarsening and superconducting properties of IG YBCO bulk superconductors. Supercond Sci Technol 2018;31(6):065003.
[181] Marchiori E, Bending SJ. Mapping the flux penetration profile in a 2G-HTS tape at the microscopic scale: deviations from a classical critical state model. Supercond Sci Technol 2019;32(2):025009.
[182] Galstyan E, Pratap R, Majkic G, Kochat M, Mohan V, Selvamanickam V. Correlation between microstructure and in-field performance of Zr-added REBCO coated conductors made by advanced MOCVD. IEEE Trans Appl Supercond 2019;29(5):1–6.
[183] Koblischka M, van Dalen A, Schuster T, Leghissa M, Jirsa M. Large fishtail effect in $DyBa_2Cu_3O_{7-\delta}$ single crystals containing columnar defects. Phys C: Supercond 1994;235:2839–40.
[184] Van Dalen A, Koblischka M, Griessen R, Jirsa M, Kumar GR. Dynamic contribution to the fishtail effect in a twin-free $DyBa_2Cu_3O_{7-\delta}$ single crystal. Phys C: Supercond 1995;250(3–4):265–74.
[185] Jirsa M, Pust L, Dlouhỳ D, Koblischka M. Fishtail shape in the magnetic hysteresis loop for superconductors: Interplay between different pinning mechanisms. Phys Rev B 1997;55(5):3276.
[186] Jirsa M, Koblischka M, Van Dalen A. Relaxation and scaling of magnetization around the fishtail minimum in single crystal with columnar tracks. Supercond Sci Technol 1997;10(7):484.
[187] Pissas M, Moraitakis E, Kallias G, Terzis A, Niarchos D, Charalambous M. Irreversibility line in superconducting $HgBa_2CuO_{4+\delta}$ single crystals. Phys Rev B 1998;58:9536–42.
[188] Pissas M, Stamopoulos D, Moraitakis E, Kallias G, Niarchos D, Charalambous M. Magnetic relaxation measurements in the region of the second magnetization peak in a $HgBa_2CuO_{4+\delta}$ single crystal. Phys Rev B 1999;59(18):12121.
[189] Eley S, Willa R, Chan MK, Bauer ED, Civale L. Vortex phases and glassy dynamics in the highly anisotropic superconductor $HgBa_2CuO_{4+\delta}$. Sci Rep 2020;10(1):1–11.
[190] Saif M, Tripathi D. Thermoelectric properties of Sr-doped LSCO for energy harvesting applications below room temperature. Energy Storage 2022;5(2):e2393.
[191] Rodríguez JE. LSCO ceramics as possible thermoelectric material for low temperature applications. MRS Online Proc Libr 2008;1044(1):619.
[192] Anderson PW, Kim YB. Hard superconductivity: Theory of the motion of Abrikosov flux lines. Rev Modern Phys 1964;36:39–43.
[193] Feigel'man MV, Geshkenbein VB, Larkin AI, Vinokur VM. Theory of collective flux creep. Phys Rev Lett 1989;63:2303–6.
[194] Sutjahja I, Nugroho A, Tjia M, Menovsky A, Franse J. Peak effects and the solid vortex phase of a T*-phase $SmLa_{0.8}Sr_{0.2}CuO_{4-\delta}$ single crystal. Phys Rev B 2001;64(13):134502.
[195] Tamegai T, Iye Y, Oguro I, Kishio K. Anomalous peak effect in single crystal $Bi_2Sr_2CaCu_2O_{8+y}$ studied by Hall probe magnetometry. Phys C: Supercond Appl 1993;213(1–2):33–42.
[196] Kalisky B, Shaulov A, Tamegai T, Yeshurun Y. Time evolution of the second magnetization peak in $Bi_2Sr_2CaCu_2O_{8+\delta}$. J Appl Phys 2003;93(10):8659–61.
[197] Khaykovich B, Zeldov E, Majer D, Li T, Kes P, Konczykowski M. Vortex-lattice phase transitions in $Bi_2Sr_2CaCu_2O_8$ crystals with different oxygen stoichiometry. Phys Rev Lett 1996;76(14):2555.
[198] Miu L, Cimpoiasu E, Stein T, Almasan C. Plastic vortex creep above the second magnetization peak in $Bi_2Sr_2CaCu_2O_{8+\delta}$ single crystals. Phys C: Supercond 2000;334(1–2):1–6.
[199] Sun YP, Hsu YY, Lin BN, Luo HM, Ku HC. Anomalous variation of second magnetization peak and onset field in overdoped $(Bi,P)_2Sr_2CaCu_2O_{8+\delta}$ single crystals. Phys Rev B 2000;61:11301–4.
[200] Sun Y, Song W, Du J, Ku H. Magnetic relaxation measurements on a heavily Pb-doped $Bi_2Sr_2CaCu_2O_{8+\delta}$ single crystal. Phys Rev B 2002;66(10):104520.
[201] Brandstätter G, Sauerzopf F, Weber H. Magnetic properties and critical currents in Tl-based high-T_c superconducting single crystals. Phys Rev B 1997;55(17):11693.
[202] Singh M, Prajapat C, Dogra A, Kumar R, Yashwant G, Ravikumar G, et al. Effect of Ag^{15+} and Li^{3+} ion irradiation on superconducting $Tl_2Ca_2Ba_2Cu_3O_{10}$ single crystals. Nucl Instruments Methods Phys Res Sect B: Beam Interactions Mater Atoms 2011;269(10):1117–20.
[203] Zehetmayer M, Eisterer M, Krutzler C, Jun J, Kazakov S, Karpinski J, et al. Order–disorder transition in the flux line lattice of superconducting MgB_2 single crystals with artificially introduced defects: comparison with theory. Supercond Sci Technol 2007;20(9):S247.

[204] Wisniewski A, Puzniak R, Judek J, Krutzler C, Eisterer M, Weber HW, et al. Comparison of the influence of carbon substitution and neutron-induced defects on the upper critical field and flux pinning in MgB_2 single crystals. Supercond Sci Technol 2007;20(3):256.
[205] Pissas M, Lee S, Yamamoto A, Tajima S. Peak effect in single crystal MgB_2 superconductor for H ‖ c-axis. Phys Rev Lett 2002;89:097002.
[206] Zehetmayer M, Eisterer M, Jun J, Kazakov SM, Karpinski J, Birajdar B, et al. Fishtail effect in neutron-irradiated superconducting MgB_2 single crystals. Phys Rev B 2004;69:054510.
[207] Stamopoulos D, Speliotis A, Niarchos D. From the second magnetization peak to peak effect. A study of superconducting properties in Nb films and MgB_2bulk samples. Supercond Sci Technol 2004;17(11):1261.
[208] Krutzler C, Zehetmayer M, Eisterer M, Weber HW, Zhigadlo N, Karpinski J. Comparative study of neutron irradiation and carbon doping in MgB_2 single crystals. Phys Rev B—Condens Matter Mater Phys 2007;75(22):224510.
[209] Cai Q, Liu Y, Ma Z, Cardwell DA. Fishtail effects and improved critical current density in polycrystalline bulk MgB_2 containing carbon nanotubes. Phys C: Supercond 2013;492:6–10.
[210] Koblischka MR, Muralidhar M. Pinning force scaling analysis of Fe-based high-T_c superconductors. Internat J Modern Phys B 2016;30(32):1630017.
[211] Kopeliansky R, Shaulov A, Shapiro BY, Yeshurun Y, Rosenstein B, Tu JJ, et al. Possibility of vortex lattice structural phase transition in the superconducting pnictide $Ba(Fe_{0.925}Co_{0.075})_2As_2$. Phys Rev B 2010;81:092504.
[212] Shen B, Cheng P, Wang Z, Fang L, Ren C, Shan L, et al. Flux dynamics and vortex phase diagram in $Ba(Fe_{1-x}Co_x)_2As_2$ single crystals revealed by magnetization and its relaxation. Phys Rev B 2010;81:014503.
[213] Pramanik AK, Harnagea L, Singh S, Aswartham S, Behr G, Wurmehl S, et al. Critical current and vortex dynamics in single crystals of $Ca(Fe_{1-x}Co_x)_2As_2$. Phys Rev B 2010;82:014503.
[214] Meng Y, Sun Y, Xing X, Tamegai T, Shi Z. Anomalously small magnetic relaxation rate of $Ca_{10}(Pt_3As_8)(Fe_{2-x}Pt_xAs_2)_5$ superconductor. Supercond Sci Technol 2023;36(8):085022.
[215] Zhigadlo N, Weyeneth S, Katrych S, Moll P, Rogacki K, Bosma S, et al. High-pressure flux growth, structural, and superconducting properties of *Ln*FeAsO (*Ln* = Pr, Nd, Sm) single crystals. Phys Rev B—Condens Matter Mater Phys 2012;86(21):214509.
[216] Singh SJ, Bristow M, Meier WR, Taylor P, Blundell SJ, Canfield PC, et al. Ultrahigh critical current densities, the vortex phase diagram, and the effect of granularity of the stoichiometric high-T_c superconductor $CaKFe_4As_4$. Phys Rev Mater 2018;2(7):074802.
[217] Bonura M, Giannini E, Viennois R, Senatore C. Temperature and time scaling of the peak-effect vortex configuration in $FeTe_{0.7}Se_{0.3}$. Phys Rev B—Condens Matter Mater Phys 2012;85(13):134532.
[218] Pramanik AK, Harnagea L, Nacke C, Wolter AUB, Wurmehl S, Kataev V, et al. Fishtail effect and vortex dynamics in LiFeAs single crystals. Phys Rev B 2011;83:094502.
[219] Tang M, Dong C, Xu Z, Liu C, Yang P, Tu C, et al. Transition of vortex pinning behaviour induced by an artificial microstructure design in $Ba(Fe_{0.94}Co_{0.06})_2As_2$ pnictide superconductor. Mater Today Phys 2022;27:100783.
[220] Sundar S, Lopes PV, Salem-Sugui S, Li ZZ, Hong WS, Luo HQ, et al. Order–disorder phase transition and elastic-to-plastic vortex creep crossover in a triclinic iron pnictide superconductor $(Ca_{0.85}La_{0.15})_{10}(Pt_3As_8)(Fe_2As_2)_5$. Sci Rep 2023;13(1):16273.
[221] Blatter G, Geshkenbein VB, Larkin AI. From isotropic to anisotropic superconductors: A scaling approach. Phys Rev Lett 1992;68:875–8.
[222] Kogan VG, Clem JR. Uniaxial Type-II superconductors near the upper critical field. Phys Rev B 1981;24:2497–505.
[223] Hao Z, Clem JR. Reversible magnetization and torques in anisotropic high-κ Type-II superconductors. Phys Rev B 1991;43:7622–30.
[224] Kumar GR, Koblischka M, Martinez J, Griessen R, Dam B, Rector J. Angular scaling of critical current measurements on laser-ablated $YBa_2Cu_3O_{7-\delta}$ thin films. Phys C: Supercond 1994;235–240:3053–4.
[225] Xu X, Fang J, Cao X, Li K. The critical current density and the pinning mechanism of epitaxial $YBa_2Cu_3O_{7-\delta}$ thin films. Solid State Commun 1995;93(4):291–3.
[226] Xu XJ, Fang J, Cao XW, Li K. A scaling formula of critical current density for anisotropic superconductors. J Phys D: Appl Phys 1996;29(9):2473–5.
[227] Guryev VV, Shavkin SV, Kruglov VS. Method for critical current angular dependencies analysis of superconducting tapes. J Phys: Conf Ser 2021;2103(1):012096.
[228] Civale L, Maiorov B, Serquis A, Willis JO, Coulter JY, Wang H, et al. Understanding high critical currents in $YBa_2Cu_3O_7$ thin films and coated conductors. J Low Temp Phys 2004;135:87–98.
[229] Gutiérrez J, Llordés A, Gázquez J, Gibert M, Romà N, Ricart S, et al. Strong isotropic flux pinning in solution-derived $YBa_2Cu_3O_{7-x}$ nanocomposite superconductor films. Nat Mater 2007;6:367–73.
[230] Malmivirta M, Palonen H, Inkinen S, Yao LD, Tikkanen J, Huhtinen H, et al. Dirty limit scattering behind the decreased anisotropy of doped $YBa_2Cu_3O_{7-\delta}$ thin films. Supercond Sci Technol 2016;28(4):175702.
[231] Llordés A, Palau A, Gázquez J, Coll M, Vlad R, Pomar A, et al. Nanoscale strain-induced pair suppression as a vortex-pinning mechanism in high-temperature superconductors. Nat Mater 2012;11(4):329–36.
[232] Fastampa R, Sarti S, Silva E, Milani E. Scaling in the angular dependence of the critical current and temperature-dependent anisotropy ratio in $Bi_2Sr_2CaCu_2O_8$. Phys Rev B 1994;49:15959–64.
[233] Wimbush SC, Strickland NM, Long NJ. Low-temperature scaling of the critical current in 1G HTS wires. IEEE Trans Appl Supercond 2015;25(3):1–5.
[234] Kidszun M, Haindl S, Thersleff T, Hänisch J, Kauffmann A, Iida K, et al. Critical current scaling and anisotropy in oxypnictide superconductors. Phys Rev Lett 2011;106:137001.
[235] Iida K, Hänisch J, Thersleff T, Kurth F, Kidszun M, Haindl S, et al. Scaling behavior of the critical current in clean epitaxial $Ba(Fe_{1-x}Co_x)_2As_2$ thin films. Phys Rev B 2010;81:100507.
[236] Matsui H, Ogiso H, Yamasaki H, Sohma M, Yamaguchi I, Kumagai T, et al. Dimpling in critical current density vs. magnetic field angle in $YBa_2Cu_3O_7$ films irradiated with 3-MeV gold ions. J Appl Phys 2013;114(23):233911.
[237] Mishev V, Zehetmayer M, Fischer DX, Nakajima M, Eisaki H, Eisterer M. Interaction of vortices in anisotropic superconductors with isotropic defects. Supercond Sci Technol 2015;28(10):102001.
[238] Watanabe K, Awaji S, Kobayashi N, Yamane H, Hirai T, Muto Y. Angular dependence of the upper critical field and the critical current density for $Y_1Ba_2Cu_3O_{7-\delta}$ films. J Appl Phys 1991;69(3):1543–6.
[239] van der Beek CJ, Konczykowski M, Prozorov R. Anisotropy of strong pinning in multi-band superconductors. Supercond Sci Technol 2012;25(8):084010.
[240] Li Y, Kang G, Gao Y. Scaling rules for critical current density in anisotropic biaxial superconductors. Phys B 2016;491:70–8.
[241] Backmeister L, Aichner B, Karrer M, Wurster K, Kleiner R, Goldobin E, et al. Ordered bose glass of vortices in superconducting $YBa_2Cu_3O_{7-\delta}$ thin films with a periodic pin lattice created by focused helium ion irradiation. Nanomaterials 2022;12(19):3491.
[242] Aichner B, Backmeister L, Karrer M, Wurster K, Kleiner R, Goldobin E, et al. Angle-dependent magnetoresistance of an ordered Bose glass of vortices in $YBa_2Cu_3O_{7-\delta}$ thin films with a periodic pinning lattice. Condens Matter 2023;8(2):32.
[243] Tachiki M, Takahashi S. Anisotropy of critical current in layered oxide superconductors. Solid State Commun 1989;72(11):1083–6.
[244] Long N. Model for the angular dependence of critical currents in technical superconductors. Supercond Sci Technol 2008;21(2):025007.
[245] Wimbush SC, Long NJ. The interpretation of the field angle dependence of the critical current in defect-engineered superconductors. New J Phys 2012;14(8):083017.
[246] Long NJ. Maximum entropy distributions describing critical currents in superconductors. Entropy 2013;15(7):2585–605.

[247] Knibbe R, Strickland NM, Wimbush SC, Puichaud A-H, Long NJ. Structure property relationships in a nanoparticle-free SmBCO coated conductor. Supercond Sci Technol 2016;29(6):065006.
[248] Petrisor T, Mos R, Nasui M, Gabor M, Augieri A, Celentano G, et al. The vortex path model analysis of the field angle dependence of the critical current density in nanocomposite $YBa_2Cu_3O_{7-x}$-$BaZrO_3$ films obtained by low fluorine chemical solution deposition. J Supercond Nov Magn 2014;27(11):2493–500.
[249] Malmivirta M, Yao LD, Inkinen S, Huhtinen H, Palonen H, Jha R, et al. The angular dependence of the critical current of $BaCeO_3$ doped $YBa_2Cu_3O_{6+x}$ thin films. IEEE Trans Appl Supercond 2015;25(3):1–5.
[250] Seiler E, Gömöry F, Ries R, Vojenčiak M. Analysis of critical current anisotropy in commercial coated conductors in terms of the maximum entropy approach. Supercond Sci Technol 2019;32(9):095004.
[251] Mineev N, Baskakov A, Rudnev I. Critical current anisotropy of Zr doped MOCVD coated conductor in magnetic fields up to 8 T. Phys Procedia 2015;71:406–11.
[252] Gömöry F, Šouc J, Vojenčiak M, Klinčok B. Phenomenological description of flux pinning in non-uniform high-temperature superconductors in magnetic fields lower than the self-field. Supercond Sci Technol 2007;20(9):S271–7.
[253] Hilton DK, Gavrilin AV, Trociewitz UP. Practical fit functions for transport critical current versus field magnitude and angle data from (RE)BCO coated conductors at fixed low temperatures and in high magnetic fields. Supercond Sci Technol 2015;28(7):074002.
[254] Leys PM, Klaeser M, Schleissinger F, Schneider T. Angle-dependent $U(I)$ measurements of HTS coated conductors. IEEE Trans Appl Supercond 2013;23(3):8000604.
[255] Leys PM, Klaeser M, Schleissinger F, Schneider T. Analysis of the anisotropic critical current behaviour of HTS coated conductors. J Phys: Conf Ser 2014;507(2):022013.
[256] SuNAM. Superconductor, nano and advanced materials. 2022, Technical information available at http://www.i-sunam.com/.
[257] SuperPower. SuperPower®2G HTS wire. 2022, Technical information available at http://www.superpower-inc.com/content/{2}g-hts-wire.
[258] AMSC. American superconductor, AMSC amperium®HTS wire. 2022, Technical information available at http://www.amsc.com/solutions-products/hts_wire.html.
[259] SHSC. Shangai Superconductor Technology Co. Ltd. 2G HTS strip. 2022, Technical information available at http://www.shsctec.com/.
[260] SuperOx. SuperOx 2G HTS wire. 2022, Technical information available at http://www.SuperOx.ru/en/products/.
[261] Hu D, Ainslie MD, Raine MJ, Hampshire DP, Zou J. Modeling and comparison of in-field critical current density anisotropy in high-temperature superconducting (HTS) coated conductors. IEEE Trans Appl Supercond 2016;26(3):1–6.
[262] Fietz WA, Beasley MR, Silcox J, Webb WW. Magnetization of superconducting Nb-25%Zr wire. Phys Rev 1964;136:A335–45.
[263] Ginzburg VL, Landau LD. On the theory of superconductivity. In: On superconductivity and superfluidity: a scientific autobiography. Berlin, Heidelberg: Springer Berlin Heidelberg; 2009, p. 113–37.
[264] Kordyuk AA, Borisenko SV. ARPES on high-temperature superconductors: Simplicity vs. complexity (Review Article). Low Temp Phys 2006;32(4):298–304.
[265] Ruiz HS, Badía-Majós A. Nature of the nodal kink in angle-resolved photoemission spectra of cuprate superconductors. Phys Rev B 2009;79:054528.
[266] Millán JS, Millán J, Pérez LA, Ruiz HS. Critical current density in d-wave Hubbard superconductors. Materials 2022;15(24):8969.
[267] Sun Y, Ohnuma H, Ayukawa S-y, Noji T, Koike Y, Tamegai T, et al. Achieving the depairing limit along the c axis in $Fe_{1+y}Te_{1-x}Se_x$ single crystals. Phys Rev B 2020;101:134516.
[268] Bardeen J. Critical fields and currents in superconductors. Rev Modern Phys 1962;34:667–81.
[269] Kupryanov MY, Lukichev VF. Temperature dependence of pair-breaking current in superconductors. Sov J Low Temp Phys (Engl Transl); (United States) 1980;6(4).
[270] Clem JR, Bumble B, Raider SI, Gallagher WJ, Shih YC. Ambegaokar-Baratoff–Ginzburg-Landau crossover effects on the critical current density of granular superconductors. Phys Rev B 1987;35:6637–42.
[271] Albrecht J, Djupmyr M, Brück S. Universal temperature scaling of flux line pinning in high-temperature superconducting thin films. J Phys: Condens Matter 2007;19(21):216211.
[272] Talantsev EF, Tallon JL. Universal self-field critical current for thin-film superconductors. Nat Commun 2015;6(1):7820.
[273] Silsbee FB. A note on electrical conduction in metals at low temperatures. J Wash Acad Sci 1916;6:597.
[274] Silsbee FB. Current distribution in supraconductors. Proc Natl Acad Sci 1927;13(7):516–8.
[275] London F, London H, Lindemann FA. The electromagnetic equations of the supraconductor. Proc R Soc Lond Ser A - Math Phys Sci 1935;149(866):71–88.
[276] Talantsev E, Crump WP, Tallon JL. Thermodynamic parameters of single- or multi-band superconductors derived from self-field critical currents. Ann Phys, Lpz 2017;529(12):1700197.
[277] Talantsev EF, Iida K, Ohmura T, Matsumoto T, Crump WP, Strickland NM, et al. p-wave superconductivity in iron-based superconductors. Sci Rep 2019;9(1):14245.
[278] Griessen R, Hai-hu W, van Dalen AJJ, Dam B, Rector J, Schnack HG, et al. Evidence for mean free path fluctuation induced pinning in $YBa_2Cu_3O_7$ and $YBa_2Cu_4O_8$ films. Phys Rev Lett 1994;72:1910–3.
[279] Li MT, Fang YF, Sun Z, Zhang JC, Lin CT. Evidence for weak collective pinning and δl pinning in topological superconductor $Cu_xBi_2Se_3$. J Phys: Condens Matter 2018;30(31):31LT01.
[280] Wen H, Zhao Z, Xiao Y, Yin B, Li J. Evidence for flux pinning induced by spatial fluctuation of transition temperatures in single domain $(Y_{1-x}Pr_x)Ba_2Cu_3O_{7-\delta}$ samples. Phys C: Supercond 1995;251(3):371–8.
[281] Nelson DR, Vinokur VM. Boson localization and correlated pinning of superconducting vortex arrays. Phys Rev B 1993;48:13060–97.
[282] Hwa T, Le Doussal P, Nelson DR, Vinokur VM. Flux pinning and forced vortex entanglement by splayed columnar defects. Phys Rev Lett 1993;71:3545–8.
[283] Moshchalkov VV, Metlushko VV, Güntherodt G, Goncharov IN, Didyk AY, Bruynseraede Y. Irradiation-induced crossover from point defects to correlated disorder pinning in $Bi_2Sr_2CaCu_2O_x$ single crystals. Phys Rev B 1994;50:639–42.
[284] van der Beek CJ, Konczykowski M, Vinokur VM, Li TW, Kes PH, Crabtree GW. Vortex line pinning and Bose-Glass dynamics in heavy-ion irradiated $Bi_2Sr_2CaCu_2O_{8+\delta}$ single crystals. Phys Rev Lett 1995;74:1214–7.
[285] Yu R, Sandiumenge F, Martinez B, Vilalta N, Obradors X. Interface pinning in high T_c-high J_c $Nd_{1+x}Ba_{2-x}Cu_3O_y$ directionally solidified in air. Appl Phys Lett 1997;71(3):413–5.
[286] Martínez B, Obradors X, Gou A, Gomis V, Piñol S, Fontcuberta J, et al. Critical currents and pinning mechanisms in directionally solidified $YBa_2Cu_3O_7$-Y_2BaCuO_5 composites. Phys Rev B 1996;53:2797–810.
[287] Polat O, Sinclair JW, Zuev YL, Thompson JR, Christen DK, Cook SW, et al. Thickness dependence of magnetic relaxation and $E-J$ characteristics in superconducting (Gd-Y)-Ba-Cu-O films with strong vortex pinning. Phys Rev B 2011;84:024519.
[288] Lao M, Willa R, Meledin A, Rijckaert H, Chepikov V, Lee S, et al. In-field performance and flux pinning mechanism of pulsed laser deposition grown $BaSnO_3$/$GdBa_2Cu_3O_{7-\delta}$ nanocomposite coated conductors by SuperOx. Supercond Sci Technol 2019;32(9):094003.
[289] Plain J, Puig T, Sandiumenge F, Obradors X, Rabier J. Microstructural influence on critical currents and irreversibility line in melt-textured $YBa_2Cu_3O_{7-x}$ reannealed at high oxygen pressure. Phys Rev B 2002;65:104526.
[290] Brandt EH. The flux-line lattice in superconductors. Rep Progr Phys 1995;58(11):1465–594.
[291] Larkin AI, Ovchinnikov YN. Nonlinear conductivity of superconductors in the mixed state. Sov Phys JETP 1975;41:960.
[292] Larkin AI, Ovchinnikov YN. Nonequilibrium superconductivity. Elsevier, Amsterdam; 1986, p. 493.

[293] Doettinger SG, Huebener RP, Gerdemann R, Kühle A, Anders S, Träuble TG, et al. Electronic instability at high flux-flow velocities in high-T_c superconducting films. Phys Rev Lett 1994;73:1691–4.
[294] Doettinger S, Huebener R, Kühle A. Electronic instability during vortex motion in cuprate superconductors regime of low and high magnetic fields. Physica C 1995;251(3):285–9.
[295] Doettinger SG, Kittelberger S, Huebener RP, Tsuei CC. Quasiparticle energy relaxation in the cuprate superconductors. Phys Rev B 1997;56:14157–62.
[296] Xiao ZL, Ziemann P. Vortex dynamics in YBCO superconducting films: Experimental evidence for an instability in the vortex system at high current densities. Phys Rev B 1996;53:15265–71.
[297] Xiao ZL, Voss-de Haan P, Jakob G, Adrian H. Voltage jumps in current-voltage characteristics of $Bi_2Sr_2CaCu_2O_{8+\delta}$ superconducting films: Evidence for flux-flow instability under the influence of self-heating. Phys Rev B 1998;57:R736–9.
[298] Xiao ZL, Andrei EY, Ziemann P. Coexistence of the hot-spot effect and flux-flow instability in high-T_c superconducting films. Phys Rev B 1998;58:11185–8.
[299] Xiao ZL, Voss-deHaan P, Jakob G, Kluge T, Haibach P, Adrian H, et al. Flux-flow instability and its anisotropy in $Bi_2Sr_2CaCu_2O_{8+\delta}$ superconducting films. Phys Rev B 1999;59:1481–90.
[300] Xiao ZL, Andrei EY, Shuk P, Greenblatt M. Joule heating induced by vortex motion in a type-II superconductor. Phys Rev B 2001;64:094511.
[301] Kunchur MN. Unstable flux flow due to heated electrons in superconducting films. Phys Rev Lett 2002;89:137005.
[302] Knight JM, Kunchur MN. Energy relaxation at a hot-electron vortex instability. Phys Rev B 2006;74:064512.
[303] Koshelev AE, Vinokur VM. Dynamic melting of the vortex lattice. Phys Rev Lett 1994;73:3580–3.
[304] Maza J, Ferro G, Veira JA, Vidal F. Transition to the normal state induced by high current densities in $YBa_2Cu_3O_{7-\delta}$, thin films: A thermal runaway account. Phys Rev B 2008;78:094512.
[305] Larkin A, Varlamov A. Theory of fluctuations in superconductors. Oxford: Clarendon Press; 2005.
[306] Varlamov AA, Galda A, Glatz A. Fluctuation spectroscopy: From Rayleigh-Jeans waves to Abrikosov vortex clusters. Rev Modern Phys 2018;90:015009.
[307] Lang W, Göb W, Kula W, Sobolewski R. Anisotropic magnetoresistance in the normal state of oxygen-deficient $YBa_2Cu_3o_{7-\delta}$ thin films induced by superconducting fluctuations. Z Phys B Condens Matter 1995;98(4):453–6.
[308] Ullah S, Dorsey AT. Effect of fluctuations on the transport properties of type-II superconductors in a magnetic field. Phys Rev B 1991;44(1):262–73.
[309] Puica I, Lang W. Critical fluctuation conductivity in layered superconductors in a strong electric field. Phys Rev B 2003;68(5):54517.
[310] Aslamazov L, Larkin A. Effect of fluctuations on the properties of a superconductor above the critical temperature. Sov Phys Solid State 1968;10(4):875–80.
[311] Lawrence WE, Doniach S. Theory of layer structure superconductors. In: Kanda E, editor. Proceedings of the 12th international conference on low temperature physics. Keigaku; 1971, p. 361–2.
[312] Bu Y, Fujita M, Lin S. Ginzburg-Landau effective action for a fluctuating holographic superconductor. J High Energy Phys 2021;2021(9):168.
[313] Ikeda R, Ohmi T, Tsuneto T. Renormalized fluctuation theory of resistive transition in high-temperature superconductors under magnetic field. J Phys Soc Japan 1989;58(4):1377–86.
[314] Ikeda R, Ohmi T, Tsuneto T. Theory of broad resistive transition in high temperature superconductors under magnetic field. J Phys Soc Japan 1991;60(3):1051–69.
[315] Hurault J. Nonlinear effects on the conductivity of a superconductor above its transition temperature. Phys Rev 1969;179(2):494–6.
[316] Tsuzuki T. Nonlinear response above superconducting transition point. 3. Ginzburg-Landau-Gorkov approximation. Progr Theoret Phys 1970;43(2):286–302.
[317] Kajimura K, Mikoshiba N. Nonlinear excess conductivity in superconducting aluminum films above the transition temperature. Solid State Commun 1970;8:1617–9.
[318] Thomas G, Parks R. Momentum depairing in the paraconductivity regime. Physica 1971;55:215–23.
[319] Varlamov AA, Reggiani L. Nonlinear fluctuation conductivity of a layered superconductor - crossover in strong electric fields. Phys Rev B 1992;45(2):1060–3.
[320] Tinh BD, Li DP, Rosenstein B. Electrical conductivity beyond a linear response in layered superconductors under a magnetic field. Phys Rev B 2010;81(22):224521.
[321] Mishonov T, Posazhennikova A, Indekeu J. Fluctuation conductivity in superconductors in strong electric fields. Phys Rev B 2002;65(6):064519.
[322] Dorsey AT. Linear and nonlinear conductivity of a superconductor near T_c. Phys Rev B 1991;43(10):7575–85.
[323] Puica I, Lang W. Non-ohmic critical fluctuation conductivity of layered superconductors in a magnetic field. Phys Rev B 2003;68(21):212503.
[324] Puica I, Lang W. Out-of-plane fluctuation conductivity of layered superconductors in strong electric fields. Phys Rev B 2006;73(2):024502.
[325] Puica I, Lang W, Siraj K, Pedarnig JD, Bäuerle D. Non-Ohmic Hall resistivity observed above the critical temperature in the high-temperature superconductor $YBa_2Cu_3O_{7-\delta}$. Phys Rev B 2009;79(9):094522.
[326] Mishonov TM, Varonov AM, Chikina I, Varlamov AA. Generation of terahertz oscillations by thin superconducting film in fluctuation regime. Eur Phys J B 2019;92(7):158.
[327] Chen T, Liang SC, Zhang H, Sun YX, Yan SL, Yan SS. Non-linear I-V characteristics of a c-axis-oriented $Tl_2Ba_2Ca_2Cu_3O_x$ thin film. Solid State Commun 1990;76(3):345–7.
[328] Soret JC, Ammor L, Martinie B, Lecomte J, Odier P, Bok J. Non-ohmic conductivity, fluctuations and dimensional crossover in YBaCuO. Europhys Lett 1993;21(5):617–22.
[329] Gorlova IG, Zybtsev SG, Pokrovskii VY. Nonlinear conductivity of $Bi_2Sr_2CaCu_2O_x$ whiskers near the superconducting transition. JETP Lett 1995;61(10):839–45.
[330] Kunchur MN, Christen DK, Phillips JM. Observation of free flux flow at high dissipation levels in $YBa_2Cu_3O_{7-\delta}$ epitaxial films. Phys Rev Lett 1993;70(7):998–1001; Phys Rev Lett 1993;70:2356 (erratum).
[331] Fruchter L, Sfar I, Bouquet F, Li ZZ, Raffy H. Nonlinear excess conductivity of $Bi_2Sr_2Ca_{n-1}Cu_nO_{2n+4+x}$ $n = (1, 2)$ thin films. Phys Rev B 2004;69(14):144511.
[332] Puica I, Lang W, Peruzzi M, Von Lemmermann K, Pedarnig JD, Bauerle D. High electric field study of the superconducting transition of $YBa_2Cu_3O_{7-x}$. Supercond Sci Technol 2004;17(9):S543–7.
[333] Huebener RP. The Abrikosov vortex lattice: Its discovery and impact. J Supercond Nov Magn 2019;32(3):475–81.
[334] Dobrovolskiy OV. Fast dynamics of vortices in superconductors. In: Encyclopedia of Condensed Matter Physics. Elsevier; 2024, p. 735–54.
[335] Cherpak NT, Lavrinovich AA, Gubin AI, Vitusevich SA. Direct-current-assisted microwave quenching of $YBa_2Cu_3O_{7-x}$ coplanar waveguide to a highly dissipative state. Appl Phys Lett 2014;105(2):022601.
[336] Puica I, Lang W, Durrell JH. High velocity vortex channeling in vicinal YBCO thin films. Physica C 2012;479:88–91.
[337] Xiao ZL, Häring J, Heinz B, Ziemann P. Influence of He ion bombardment at medium energies on the vortex instability at high current densities observed in YBaCuO films. J Low Temp Phys 1996;105(5):1159–64.
[338] Yu AB, Lin CT, Zhang XF, You LX. Extremely fast vortex dynamics in $Bi_2Sr_2Ca_2Cu_3O_{10+\delta}$ crystalline nanostrip. Chin Phys B 2023;32(6):067402.
[339] Stoll OM, Kaiser S, Huebener RP, Naito M. Intrinsic flux-flow resistance steps in the cuprate superconductor $Nd_{2-x}Ce_xCuO_y$. Phys Rev Lett 1998;81:2994–7.
[340] Huebener RP, Stoll OM, Kaiser S. Electronic vortex structure and quasiparticle scattering in the cuprate superconductor $Nd_{2-x}Ce_xCuO_y$. Phys Rev B 1999;59:R3945–7.
[341] Stoll OM, Huebener RP, Kaiser S, Naito M. Magnetic field and temperature dependence of the intrinsic resistance steps in the mixed state of the cuprate superconductor $Nd_{2-x}Ce_xCuO_y$. Phys Rev B 1999;60:12424–8.

[342] Kunchur MN, Wu C, Arcos DH, Ivlev BI, Choi E-M, Kim KHP, et al. Critical flux pinning and enhanced upper critical field in magnesium diboride films. Phys Rev B 2003;68:100503.
[343] Lyatti M, Wolff MA, Savenko A, Kruth M, Ferrari S, Poppe U, et al. Experimental evidence for hotspot and phase-slip mechanisms of voltage switching in ultrathin $YBa_2Cu_3O_{7-x}$ nanowires. Phys Rev B 2018;98:054505.
[344] Rouco V, Massarotti M, Stornaiuolo D, Papari GP, Obradors X, Puig T, et al. Vortex lattice instabilities in $YBa_2Cu_3O_{7-x}$ nanowires. Materials 2018;11:211.
[345] Leo A, Nigro A, Braccini V, Sylva G, Provino A, Galluzzi A, et al. Flux flow instability as a probe for quasiparticle energy relaxation time in Fe-chalcogenides. Supercond Sci Technol 2020;33(10):104005.
[346] Grimaldi G, Leo A, Nigro A, Pace S, Braccini V, Bellingeri E, et al. Angular dependence of vortex instability in a layered superconductor: the case study of Fe(Se,Te) material. Sci Rep 2018;8:4150.
[347] Wördenweber R, Hollmann E, Schubert J, Kutzner R, Panaitov G. Regimes of flux transport at microwave frequencies in nanostructured high-T_c films. Phys Rev B 2012;85:064503–1–6.
[348] Zhou X, Lee W-S, Imada M, Trivedi N, Phillips P, Kee H-Y, et al. High-temperature superconductivity. Nat Rev Phys 2021;3(7):462–5.
[349] Demsar J. Non-equilibrium phenomena in superconductors probed by femtosecond time-domain spectroscopy. J Low Temp Phys 2020;201(5):676–709.
[350] Tajima S. Optical studies of high-temperature superconducting cuprates. Rep Progr Phys 2016;79(9):094001.
[351] Fultz B. Vibrational thermodynamics of materials. Prog Mater Sci 2010;55(4):247–352.
[352] Vodolazov DY, Peeters FM. Rearrangement of the vortex lattice due to instabilities of vortex flow. Phys Rev B 2007;76:014521.
[353] Embon L, Anahory Y, Jelic ZL, Lachman EO, Myasoedov Y, Huber ME, et al. Imaging of super-fast dynamics and flow instabilities of superconducting vortices. Nat Commun 2017;8(1):85.
[354] Dobrovolskiy OV, Bevz VM, Begun E, Sachser R, Vovk RV, Huth M. Fast dynamics of guided magnetic flux quanta. Phys Rev Appl 2019;11:054064.
[355] Dobrovolskiy OV, Vodolazov DY, Porrati F, Sachser R, Bevz VM, Mikhailov MY, et al. Ultra-fast vortex motion in a direct-write Nb-C superconductor. Nat Commun 2020;11(1):3291.
[356] Budinská B, Aichner B, Vodolazov DY, Mikhailov MY, Porrati F, Huth M, et al. Rising speed limits for fluxons via edge-quality improvement in wide MoSi thin films. Phys Rev Appl 2022;17:034072.
[357] Bezuglyj AI, Shklovskij VA, Budinská B, Aichner B, Bevz VM, Mikhailov MY, et al. Vortex jets generated by edge defects in current-carrying superconductor thin strips. Phys Rev B 2022;105:214507.
[358] Bevz V, Mikhailov M, Budinská B, Lamb-Camarena S, Shpilinska S, Chumak A, et al. Vortex counting and velocimetry for slitted superconducting thin strips. Phys Rev Appl 2023;19:034098.
[359] Porrati F, Barth S, Sachser R, Dobrovolskiy OV, Seybert A, Frangakis AS, et al. Crystalline niobium carbide superconducting nanowires prepared by focused ion beam direct writing. ACS Nano 2019;13(6):6287–96.
[360] Korneeva YP, Manova N, Florya I, Mikhailov MY, Dobrovolskiy O, Korneev A, et al. Different single-photon response of wide and narrow superconducting Mo_xSi_{1-x} strips. Phys Rev Appl 2020;13:024011.
[361] Córdoba R, Mailly D, Rezaev RO, Smirnova EI, Schmidt OG, Fomin VM, et al. Three-dimensional superconducting nanohelices grown by He^+-focused-ion-beam direct writing. Nano Lett 2019;19:8597.
[362] Babaev E. Vortices with fractional flux in two-gap superconductors and in extended Faddeev model. Phys Rev Lett 2002;89:067001.
[363] Silaev MA. Stable fractional flux vortices and unconventional magnetic state in two-component superconductors. Phys Rev B 2011;83:144519.
[364] Guikema JW, Bluhm H, Bonn DA, Liang R, Hardy WN, Moler KA. Two-dimensional vortex behavior in highly underdoped $YBa_2Cu_3O_{6+x}$ observed by scanning Hall probe microscopy. Phys Rev B 2008;77:104515.
[365] Iguchi Y, Shi RA, Kihou K, Lee C-H, Barkman M, Benfenati AL, et al. Superconducting vortices carrying a temperature-dependent fraction of the flux quantum. Science 2023;380(6651):1244–7.
[366] Pokusinskyi AO, Kasatkin AL. Dissociation of composite Abrikosov vortices in two-band superconductors in a strong rf field. Low Temp Phys 2024;50(2):111–6.
[367] Vodolazov DY. Single-photon detection by a dirty current-carrying superconducting strip based on the kinetic-equation approach. Phys Rev Appl 2017;7:034014.
[368] Korneeva YP, Vodolazov DY, Semenov AV, Florya IN, Simonov N, Baeva E, et al. Optical single-photon detection in micrometer-scale NbN bridges. Phys Rev Appl 2018;9:064037.
[369] Charaev I, Morimoto Y, Dane A, Agarwal A, Colangelo M, Berggren KK. Large-area microwire MoSi single-photon detectors at 1550 nm wavelength. Appl Phys Lett 2020;116(24):242603.
[370] Chiles J, Buckley SM, Lita A, Verma VB, Allmaras J, Korzh B, et al. Superconducting microwire detectors based on WSi with single-photon sensitivity in the near-infrared. Appl Phys Lett 2020;116(24):242602.
[371] Shibata H, Akazaki T, Tokura Y. Fabrication of MgB_2 nanowire single-photon detector with meander structure. Appl Phys Express 2013;6(2):023101.
[372] Cherednichenko S, Acharya N, Novoselov E, Drakinskiy V. Low kinetic inductance superconducting MgB_2 nanowires with a 130 ps relaxation time for single-photon detection applications. Supercond Sci Technol 2021;34(4):044001.
[373] Ejrnaes M, Parlato L, Arpaia R, Bauch T, Lombardi F, Cristiano R, et al. Observation of dark pulses in 10 nm thick YBCO nanostrips presenting hysteretic current voltage characteristics. Supercond Sci Technol 2017;30(12):12LT02.
[374] Lyatti M, Wolff MA, Gundareva I, Kruth M, Ferrari S, Dunin-Borkowski RE, et al. Energy-level quantization and single-photon control of phase slips in $YBa_2Cu_3O_{7-x}$ nanowires. Nat Commun 2020;11(1):763.
[375] You L. Superconducting nanowire single-photon detectors for quantum information. Nanophotonics 2020;9(9):2673–92.
[376] Charaev I, Bandurin DA, Bollinger AT, Phinney IY, Drozdov I, Colangelo M, et al. Single-photon detection using high-temperature superconductors. Nature Nanotechnology 2023;18(4):343–9.
[377] Bezuglyj A, Shklovskij V. Effect of self-heating on flux flow instability in a superconductor near T_c. Phys C: Supercond 1992;202(3):234–42.
[378] Kes PH, Aarts J, Vinokur VM, van der Beek J. Dissipation in highly anisotropic superconductors. Phys Rev Lett 1990;64:1063.
[379] Larkin AI, Ovchinnikov YN. Electrodynamics of inhomogeneous Type-II superconductor. Zh Eksp Teor Fiz 1973;65:1704; Sov Phys JETP 1974;38:854.
[380] Kossler WJ, Dai Y, Petzinger KG, Greer AJ, Williams DL, Koster E, et al. Transparency of the *ab* planes of $Bi_2Sr_2CaCu_2O_{8+\delta}$ to magnetic fields. Phys Rev Lett 1998;80:592–5.
[381] Vanderbemden P, Hong Z, Coombs T, Denis S, Ausloos M, Schwartz J, et al. Behavior of bulk high-temperature superconductors of finite thickness subjected to crossed magnetic fields: Experiment and model. Phys Rev B 2007;75(17):174515.
[382] Vanderbemden P, Hong Z, Coombs T, Ausloos M, Babu NH, Cardwell D, et al. Remagnetization of bulk high-temperature superconductors subjected to crossed and rotating magnetic fields. Supercond Sci Technol 2007;20(9):S174.
[383] Baghdadi M, Ruiz HS, Fagnard JF, Zhang M, Wang W, Coombs TA. Investigation of demagnetization in HTS stacked tapes implemented in electric machines as a result of crossed magnetic field. IEEE Trans Appl Supercond 2015;25(3):1–4.
[384] Celebi S, Sirois F, Lacroix C. Collapse of the magnetization by the application of crossed magnetic fields: observations in a commercial Bi: 2223/Ag tape and comparison with numerical computations. Supercond Sci Technol 2015;28(2):025012.
[385] Li Q, Kwon C, Xi XX, Bhattacharya S, Walkenhorst A, Venkatesan T, et al. Effects of dimensional crossover on flux pinning in a model high-T_c superconductor: $YBa_2Cu_3O_{7-\delta}/(Pr_x\ Y_{1-x})Ba_2Cu_3O_{7-\delta}$ superlattices. Phys Rev Lett 1992;69:2713–6.

[386] Leo A, Marra P, Grimaldi G, Citro R, Kawale S, Bellingeri E, et al. Competition between intrinsic and extrinsic effects in the quenching of the superconducting state in Fe(Se,Te) thin films. Phys Rev B 2016;93:054503.
[387] Scuderi M, Pallecchi I, Leo A, Nigro A, Grimaldi G, Ferdeghini C, et al. Nanoscale analysis of superconducting Fe(Se,Te) epitaxial thin films and relationship with pinning properties. Sci Rep 2021;11:20100.
[388] Khan MR, Leo A, Nigro A, Galluzzi A, Polichetti M, Braccini V, et al. Effective magnetic field dependence of the flux pinning energy in $FeSe_{0.5}Te_{0.5}$ superconductor. Materials 2021;14:5289.
[389] Grimaldi G, Leo A, Sabatino P, Carapella G, Nigro A, Pace S, et al. Speed limit to the Abrikosov lattice in mesoscopic superconductors. Phys Rev B 2015;92:024513.
[390] Grimaldi G, Leo A, Avitabile F, Martucciello N, Galluzzi A, Polichetti M, et al. Vortex lattice instability at the nanoscale in a parallel magnetic field. Nanotechnology 2019;30:424001.
[391] Grimaldi G, Leo A, Nigro A, Pace S, Huebener RP. Dynamic ordering and instability of the vortex lattice in Nb films exhibiting moderately strong pinning. Phys Rev B 2009;80:144521—-10.
[392] Grimaldi G, Leo A, Zola D, Nigro A, Pace S, Laviano F, et al. Evidence for low-field crossover in the vortex critical velocity of type-II superconducting thin films. Phys Rev B 2010;82:024512.
[393] Grimaldi G, Leo A, Nigro A, Silhanek AV, Verellen N, Moshchalkov VV, et al. Controlling flux flow dissipation by changing flux pinning in superconducting films. Appl Phys Lett 2012;100(20):202601.
[394] Silhanek AV, Leo A, Grimaldi G, Berdiyorov GR, Milosevic MV, Nigro A, et al. Influence of artificial pinning on vortex lattice instability in superconducting films. New J Phys 2012;14(5):053006.
[395] Kalisky B, Aronov P, Koren G, Shaulov A, Yeshurun Y, Huebener RP. Flux-flow resistivity anisotropy in the instabilitu regime of the *a-b* plane of epitaxial superconducting $YBa_2Cu_3O_{7-\delta}$. Phys Rev Lett 2006;97:067003.
[396] Doval JM, Maza J, Torron C, Veira JA, Tello M, Vidal F. New measurements of the transition to the normal state induced by high current densities in high-T_c superconductor microbridges under thermal smallness conditions. Adv Sci Technol 2014;95:202.
[397] Grimaldi G, Leo A, Nigro A, Bruno E, Priolo F, Pace S. A study of current stability in the dissipative flux flow state of superconducting films. IEEE Trans Appl Supercond 2013;23:8200704.
[398] Leo A, Grimaldi G, Guarino A, Avitabile F, Marra P, Citro R, et al. Quenching current by flux-flow instability in iron-chalcogenides thin films. IEEE Trans Appl Supercond 2016;27:7300405.
[399] Larkin AI, Ovchinnikov YN. Pinning in type II superconductors. J Low Temp Phys 1979;34(3–4):409–28.
[400] Blatter G, Geshkenbein VB, Koopmann JAG. Weak to strong pinning crossover. Phys Rev Lett 2004;92:067009.
[401] Willa R, Koshelev AE, Sadovskyy IA, Glatz A. Strong-pinning regimes by spherical inclusions in anisotropic type-II superconductors. Supercond Sci Technol 2018;31:014001.
[402] Labusch R. Calculation of the critical field gradient in Type-II superconductors. Cryst Lattice Defects 1969;1:1.
[403] Koopmann JAG, Geshkenbein VB, Blatter G. Peak effect at the weak to strong pinning crossover. Physica C 2004;404:209.
[404] Willa R, Geshkenbein VB, Blatter G. Campbell penetration in the critical state of type-II superconductors. Phys Rev B 2015;92:134501.
[405] Willa R, Geshkenbein VB, Blatter G. Probing the pinning landscape in type-II superconductors via Campbell penetration depth. Phys Rev B 2016;93:064515.
[406] Willa R, Geshkenbein VB, Prozorov R, Blatter G. Campbell response in type-II superconductors under strong pinning conditions. Phys Rev Lett 2015;115:207001.
[407] Thomann AU, Geshkenbein VB, Blatter G. Dynamical aspects of strong pinning of magnetic vortices in type-II superconductors. Phys Rev Lett 2012;108:217001.
[408] Thomann AU, Geshkenbein VB, Blatter G. Vortex dynamics in type-II superconductors under strong pinning conditions. Phys Rev B 2017;96:144516.
[409] Buchacek M, Willa R, Geshkenbein VB, Blatter G. Persistence of pinning and creep beyond critical drive within the strong pinning paradigm. Phys Rev B 2018;98:094510.
[410] Buchacek M, Willa R, Geshkenbein VB, Blatter G. Strong pinning theory of thermal vortex creep in type-II superconductors. Phys Rev B 2019;100:014501.
[411] Gaggioli F, Blatter G, Geshkenbein VB. Creep effects on the Campbell response in Type-II superconductors. Phys Rev Res 2022;4:013143.
[412] Buchacek M, Xiao ZL, Dutta S, Andrei EY, Raychaudhuri P, Geshkenbein VB, et al. Experimental test of strong pinning and creep in current-voltage characteristics of type-II superconductors. Phys Rev B 2019;100:224502.
[413] Willa R, Marziali Bermúdez M, Pasquini G. Thermal hysteresis of the Campbell response as a probe for bulk pinning landscape spectroscopy. Phys Rev B 2018;98:184520.
[414] Jones SC, Miura M, Yoshida R, Kato T, Civale L, Willa R, et al. Designing high-performance superconductors with nanoparticle inclusions: Comparisons to strong pinning theory. APL Mater 2021;9:091105.
[415] Buchacek M, Geshkenbein VB, Blatter G. Role of rare events in the pinning problem. Phys Rev Res 2020;2:043266.
[416] Willa R, Geshkenbein VB, Blatter G. Hessian characterization of the pinning landscape in a Type-II superconductor. Phys Rev B 2022;105:144504.
[417] Yeshurun Y, Malozemoff AP, Shaulov A. Magnetic relaxation in high-temperature superconductors. Rev Modern Phys 1996;68:911–49.
[418] Cole HM, Venuti MB, Gorman B, Bauer ED, Chan MK, Eley S. Plastic vortex creep and dimensional crossovers in the highly anisotropic superconductor $HgBa_2CuO_{4+x}$. Phys Rev B 2023;107:104509.
[419] Fisher MPA. Vortex-glass superconductivity: A possible new phase in bulk high-T_c oxides. Phys Rev Lett 1989;62:1415.
[420] Vinokur VM, Kes PH, Koshelev AE. Flux pinning and creep in very anisotropic high temperature superconductors. Phys C: Supercond Appl 1990;168(1–2):29–39.
[421] Nelson DR, Vinokur VM. Boson localization and pinning by correlated disorder in high-temperature superconductors. Phys Rev Lett 1992;68(15):2398–401.
[422] Blatter G, Geshkenbein VB, Vinokur VM. Quantum collective creep. Phys Rev Lett 1991;66:3297.
[423] Brandt E. Thermal fluctuation of the vortex positions in high-T_c superconductors. Physica C 1989;162–164:1167–8.
[424] Embon L, Anahory Y, Suhov A, Halbertal D, Cuppens J, Yakovenko A, et al. Probing dynamics and pinning of single vortices in superconductors at nanometer scales. Sci Rep 2015;5(1):7598.
[425] Eley S, Miura M, Maiorov B, Civale L. Universal lower limit on vortex creep in superconductors. Nat Mater 2017;16:409–13.
[426] Blatter G, Geshkenbein V. Quantum collective creep: Effects of anisotropy, layering, and finite temperature. Phys Rev B 1993;47:2725–41.
[427] Smith CM, Caldeira AO, Blatter G. Classical and quantum creep of vortices from columnar defects. Czech J Phys 1996;46(SUPPL. 3):1739–40.
[428] Chudnovsky EM, Ferrera A, Vilenkin A. Quantum depinning of flux lines from columnar defects. Phys Rev B 1995;51:1181–4.
[429] Smith CM, Caldeira AO, Blatter G. Creep of vortices from columnar defects. Phys Rev B 1996;54:R784–7.
[430] Åkerman JJ, Venturini EL, Siegal MP, Yun SH, Karlsson UO, Rao KV. Two-stage crossover from thermal to quantum flux creep of dilute vortex ensembles in various high-T_c superconducting thin films. Phys Rev B 2001;64:094509.
[431] Landau I, Ott H. Crossover from thermally activated flux creep to quantum tunneling of vortices in a $YBa_2Cu_3O_{7-x}$ film. Physica C 2000;340(4):251–60.
[432] Luo S, Li C, He Y, Zhang G, Jin D, Chen Z, et al. Magnetic relaxation study of macroscopic quantum tunnelling in YBCO films. Supercond Sci Technol 2002;15(9):1300–3.
[433] Hoekstra AFT, Testa AM, Doornbos G, Martinez JC, Dam B, Griessen R, et al. Temperature and magnetic-field dependence of quantum creep in various high-T_c superconductors. Phys Rev B 1999;59:7222–37.

[434] Tejada J, Chudnovsky EM, García A. Quantum tunneling of vortices in the $Tl_2CaBa_2Cu_2O_8$ superconductor. Phys Rev B 1993;47:11552–4.
[435] Klein T, Grasland H, Cercellier H, Toulemonde P, Marcenat C. Vortex creep down to 0.3 K in superconducting Fe(Te,Se) single crystals. Phys Rev B 2014;89:014514.
[436] Silhanek A, Civale L, Candia S, Nieva G, Pasquini G, Lanza H. Evidence for vortex staircases in the whole angular range due to competing correlated pinning mechanisms. Phys Rev B 1999;59:13620–3.
[437] Taen T, Yagyuda H, Nakajima Y, Tamegai T, Ayala-Valenzuela O, Civale L, et al. Observation of lock-in phenomena in heavy-ion-irradiated single crystal of $Ba(Fe_{0.93}Co_{0.07})_2As_2$. Phys Rev B 2014;89:024508.
[438] Sadovskyy IA, Koshelev AE, Kwok W-K, Welp U, Glatz A. Targeted evolution of pinning landscapes for large superconducting critical currents. PNAS 2019;116:10291.
[439] Niebieskikwiat D, Silhanek A, Civale L, Nieva G, Levy P, Krusin-Elbaum L. Suppression of matching field effects by splay and pinning energy dispersion in $YBa_2Cu_3O_7$ with columnar defects. Phys Rev B 2001;63:144504.
[440] Maiorov B, Baily SA, Zhou H, Ugurlu O, Kennison JA, Dowden PC, et al. Synergetic combination of different types of defect to optimize pinning landscape using $BaZrO_3$-doped $YBa_2Cu_3O_7$. Nat Mater 2009;8(5):398–404.
[441] Eley S, Khilstrom K, Fotovat R, Xiao Z, Chen A, Chen D, et al. Glassy dynamics in a heavy ion irradiated $NbSe_2$ crystal. Sci Rep 2018;8.
[442] Sonin EB, Horovitz B. Thermal and quantum creep of vortices trapped by twin boundaries and columnar defects. Phys Rev B 1995;51:6526–30.
[443] Kihlstrom KJ, Civale L, Eley S, Miller DJ, Welp U, Kwok WK, et al. Large enhancement of the in-field critical current density of YBCO coated conductors due to composite pinning landscape. Supercond Sci Technol 2020;34(1):015011.
[444] Barbiellini B. High-temperature cuprate superconductors studied by x-ray Compton scattering and positron annihilation spectroscopies. J Phys: Conf Ser 2013;443(1):012009.
[445] Furness JW, Zhang Y, Lane C, Buda IG, Barbiellini B, Markiewicz RS, et al. An accurate first-principles treatment of doping-dependent electronic structure of high-temperature cuprate superconductors. Commun Phys 2018;1(1):1–6.
[446] Zhang Y, Lane C, Furness JW, Barbiellini B, Perdew JP, Markiewicz RS, et al. Competing stripe and magnetic phases in the cuprates from first principles. Proc Natl Acad Sci 2020;117(1):68–72.
[447] Gong Z, Zou J, Xu G. Structural, electronic, and magnetic properties of the possible pnictide superconductor $BaFeAs_2$. Phys Rev B 2024;110:085128.
[448] Ray SJ, Alff L. Superconductivity and dirac fermions in 112-phase pnictides. Physica Status Solidi (B) 2017;254(1):1600163.
[449] Fedorov A, Yaresko A, Haubold E, Kushnirenko Y, Kim T, Büchner B, et al. Energy scale of nematic ordering in the parent iron-based superconductor $BaFe_2as_2$. Phys Rev B 2019;100:024517.
[450] Oliveira L, Gross E, Kohn W. Density-functional theory for superconductors. Phys Rev Lett 1988;60(23):2430.
[451] Berthod C, Maggio-Aprile I, Bruér J, Erb A, Renner C. Observation of Caroli–de Gennes–Matricon vortex states in $YBa_2Cu_3O_{7-\delta}$. Phys Rev Lett 2017;119:237001.
[452] Cyrot M. Ginzburg-Landau theory for superconductors. Rep Progr Phys 1973;36(2):103.
[453] Gor'kov LP. Microscopic derivation of the Ginzburg-Landau equations in the theory of superconductivity. Sov Phys JETP 1959;9:1364–7.
[454] Gropp WD, Kaper HG, Leaf GK, Levine DM, Palumbo M, Vinokur VM. Numerical simulation of vortex dynamics in type-II superconductors. J Comput Phys 1995;123:254–66.
[455] Crabtree GW, Gunter DO, Kaper HG, Koshelev AE, Leaf GK, Vinokur VM. Numerical simulations of driven vortex systems. Phys Rev B 2000;61:1446–55.
[456] Palonen H, Jäykkä J, Paturi P. Modeling reduced field dependence of critical current density in $YBa_2Cu_3O_{6+x}$ films with nanorods. Phys Rev B 2012;85:024510.
[457] Winiecki T, Adams CS. Time-dependent Ginzburg-Landau simulations of the voltage-current characteristic of type-II superconductors with pinning. Phys Rev B 2002;65:104517.
[458] Sadovskyy IA, Koshelev AE, Phillips CL, Karpeev DA, Glatz A. Stable large-scale solver for Ginzburg-Landau equations for superconductors. J Comput Phys 2015;294:639.
[459] Koshelev AE, Sadovskyy IA, Phillips CL, Glatz A. Optimization of vortex pinning by nanoparticles using simulations of the time-dependent Ginzburg-Landau model. Phys Rev B 2016;93:060508.
[460] Herrera M, Ortalan V, Morgan DG, Browning ND, Rupich MW. Observation of the three-dimensional distribution of flux pinning centers in Dy-doped $YBa_2Cu_3O_{7-x}$ coated conductors. J Appl Phys 2008;103(8):084301.
[461] Ortalan V, Herrera M, Rupich MW, Browning ND. Three dimensional analyses of flux pinning centers in Dy-doped $YBa_2Cu_3O_{7-x}$ coated superconductors by STEM tomography. Physica C 2009;469(23–24):2052–9.
[462] Kimmel G, Sadovskyy IA, Glatz A. In silico optimization of critical currents in superconductors. Phys Rev E 2017;96:013318.
[463] Glatz A, Sadovskyy IA, Welp U, Kwok W-K, Crabtree GW. The quest for high critical current in applied high-temperature superconductors. J Supercond Nov Magn 2020;33(1):127.
[464] Dang HTM, Tinh BD. The critical current density of iron-based superconductors under magnetic field. Eur Phys J B 2022;95(10):177.
[465] Willa R, Koshelev AE, Sadovskyy IA, Glatz A. Peak effect due to competing vortex ground states in superconductors with large inclusions. Phys Rev B 2018;98:054517.
[466] Ao P, Thouless DJ. Berry's phase and the Magnus force for a vortex line in a superconductor. Phys Rev Lett 1993;70:2158–61.
[467] Reichhardt C, Reichhardt CJO. Depinning and nonequilibrium dynamic phases of particle assemblies driven over random and ordered substrates: a review. Rep Progr Phys 2016;80(2):26501.
[468] Bardeen J, Stephen MJ. Theory of the motion of vortices in superconductors. Phys Rev 1965;140:A1197–207.
[469] Gurevich A, Ciovati G. Dynamics of vortex penetration, jumpwise instabilities, and nonlinear surface resistance of Type-II superconductors in strong rf fields. Phys Rev B 2008;77:104501.
[470] Reichhardt C, Reichhardt CJO. Jamming, fragility and pinning phenomena in superconducting vortex systems. Sci Rep 2020;10(1):32669592.
[471] Reichhardt CJO, Reichhardt C. Dynamic phases and reentrant Hall effect for vortices and skyrmions on periodic pinning arrays. Eur Phys J B 2022;95(8):135.
[472] Reichhardt CJO, del Campo A, Reichhardt C. Kibble-Zurek mechanism for nonequilibrium phase transitions in driven systems with quenched disorder. Commun Phys 2022;5(1):173.
[473] Olson CJ, Reichhardt C, Bhattacharya S. Critical depinning force and vortex lattice order in disordered superconductors. Phys Rev B 2001;64:024518.
[474] Bhattacharya S, Higgins MJ. Dynamics of a disordered flux line lattice. Phys Rev Lett 1993;70:2617–20.
[475] Paturi P, Malmivirta M, Hynninen T, Huhtinen H. Angle dependent molecular dynamics simulation of flux pinning in YBCO superconductors with artificial pinning sites. J Phys: Condens Matter 2018;30(31):315902.
[476] Paturi P, Huhtinen H. Roles of electron mean free path and flux pinning in optimizing the critical current in YBCO superconductors. Supercond Sci Technol 2022;35(6):065007.
[477] Chaturvedi H, Galliher N, Dobramysl U, Pleimling M, Täuber UC. Dynamical regimes of vortex flow in Type-II superconductors with parallel twin boundaries. Eur Phys J B 2018;91(11):294.
[478] Dobramysl U, Assi H, Pleimling M, Täuber UC. Relaxation dynamics in type-II superconductors with point-like and correlated disorder. Eur Phys J B 2013;86(5):228.

[479] Pleimling M, Täuber UC. Characterization of relaxation processes in interacting vortex matter through a time-dependent correlation length. J Stat Mech Theory Exp 2015;2015(9).
[480] Dobramysl U, Pleimling M, Täuber UC. Pinning time statistics for vortex lines in disordered environments. Phys Rev E 2014;90:062108.
[481] Das J, Bullard TJ, Täuber UC. Vortex transport and voltage noise in disordered superconductors. Phys A 2003;318(1):48–54.
[482] Rivasto E, Huhtinen H, Hynninen T, Paturi P. Vortex dynamics simulation for pinning structure optimization in the applications of high-temperature superconductors. J Phys: Condens Matter 2022;34(23):235902.
[483] Wang K, Dong H, Huang D, Shang H, Xie B, Zou Q, et al. Advances in second-generation high-temperature superconducting tapes and their applications in high-field magnets. Soft Sci 2022;2(3).
[484] Prokopec R, Fischer DX, Weber HW, Eisterer M. Suitability of coated conductors for fusion magnets in view of their radiation response. Supercond Sci Technol 2015;28(1):014005.
[485] Kunzler JE, Buehler E, Hsu FSL, Wernick JH. Superconductivity in Nb_3Sn at high current density in a magnetic field of 88 kgauss. Phys Rev Lett 1961;6:89–91.
[486] Barzi E, Zlobin AV. Nb3Sn wires and cables for high-field accelerator magnets. Cham: Springer International Publishing; 2019, p. 23–51.
[487] Lei Z, Yao C, Guo W, Wang D, Ma Y. Progress on the fabrication of superconducting wires and tapes via hot isostatic pressing. Materials 2023;16(5).
[488] Briant CL, Hall EL, Lay KW, Tkaczyk IE. Microstructural evolution of the BSCCO-2223 during powder-in-tube processing. J Mater Res 1994;9(11):2789–808.
[489] Beales TP, Jutson J, Le Lay L, Mölgg M. Comparison of the powder-in-tube processing properties of two $(Bi_{2-x}Pb_x)Sr_2Ca_2Cu_3O_{10+\delta}$ powders. J Mater Chem 1997;7:653–9.
[490] Balachandran U, Iyer AN, Huang JY, Jammy R, Haldar P, Hoehn JG, et al. Recent advances in bismuth-based superconductors. JOM 1994;46(12):23–5.
[491] Sato K. Research, fabrication and applications of Bi-2223 HTS wires. World Scientific; 2016.
[492] Oz Y, Jiang J, Matras M, Oloye TA, Kametani F, Hellstrom EE, et al. Conundrum of strongly coupled supercurrent flow in both under- and overdoped Bi-2212 round wires. Phys Rev Mater 2021;5:074803.
[493] Paturi P, Raittila J, Grivel J-C, Huhtinen H, Seifi B, Laiho R, et al. Preparing superconducting nanopowder based YBCO/Ag tapes. Phys C: Supercond 2002;372–376:779–81.
[494] Paturi P, Kulmala T, Raittila J, Grivel J-C, Laiho R, Andersen N. Texture of YBCO/Ag PIT-tapes. Phys C: Supercond 2004;408–410:935–6, Proceedings of the International Conference on Materials and Mechanisms of Superconductivity. High Temperature Superconductors VII – M2SRIO.
[495] Zhang Z, Jiang J, Wang Q, Larbalestier DC, Hellstrom EE. Optimization of a novel melt-growth heat treatment of $YbBa_2Cu_3O_{7-\delta}$/Ag Tapes. IEEE Trans Appl Supercond 2018;28(4):1–4.
[496] Zhang Z, Jiang J, Tian H, Wang Q, Larbalestier DC, Hellstrom EE. Investigation of the melt-growth process of $YbBa_2Cu_3O_{7-\delta}$ powder in Ag-sheathed tapes. CrystEngComm 2019;21:1369–77.
[497] Geng Z, Oguro H, Awaji S. Melt growth of $YBa_2Cu_3O_{7-\delta}$ by using $BaCu_2O_2$ and Y_2BaCuO_5 in Ag-sheath. IEEE Trans Appl Supercond 2024;34(5):1–4.
[498] Geng Z, Oguro H. Development of high critical current density YBCO high temperature superconducting round wire. J Adv Sci 2024;36:36109.
[499] Obradors X, Puig T. Coated conductors for power applications: materials challenges. Supercond Sci Technol 2014;27:044003.
[500] Iijima Y, Tanabe N, Ikeno Y, Kohno O. Biaxially aligned $YBa_2Cu_3O_{7-x}$ thin film tapes. Phys C: Supercond 1991;185–189:1959–60.
[501] Wördenweber R. Physical vapor thin-film deposition techniques. In: Cardwell D, Larbalestier D, Braginski A, editors. Handbook of superconductivity: processing and cryogenics, vol. 2. CRC Press; 2021, p. 17.
[502] Igarashi M, Kakimoto K, Hanyu S, Tashita C, Hayashida T, Hanada Y, et al. Remarkable progress in fabricating RE123 coated conductors by IBAD/PLD technique at fujikura. J Phys: Conf Ser 2010;234(2):022016.
[503] Molodyk A, Samoilenkov S, Markelov A, Degtyarenko P, Lee S, Petrykin V, et al. Development and large volume production of extremely high current density $YBa_2Cu_3O_7$ superconducting wires for fusion. Sci Rep 2021;11(1):2084.
[504] Usoskin A, Knoke J, Garcia-Moreno F, Issaev A, Dzick J, Sievers S, et al. Large-area HTS-coated stainless steel tapes with high critical currents. IEEE Trans Appl Supercond 2001;11(1):3385–8.
[505] Harshavardhan KS, Strikovski M. Pulsed electron-beam deposition of high temperature superconducting films for coated conductor applications. In: Second-generation HTS conductors. Boston, MA: Springer US; 2005, p. 109–33.
[506] Ko KP, Moon SH, Song KJ, Park C, Yoo SI. High quality $SmBa_2Cu_3O_{7-\delta}$ thin films on $SrTiO_3$ (100) substrates deposited by pulsed electron beam deposition. IEEE Trans Appl Supercond 2005;15(2):3054–7.
[507] Li J, Ren G-K, Chen J, Chen X, Wu W, Liu Y, et al. Facilitating complex thin film deposition by using magnetron sputtering: A review. JOM 2022;74(8):3069–81.
[508] Raven MS. Radio frequency sputtering and the deposition of high-temperature superconductors. J Mater Sci, Mater Electron 1994;5(3):129–46.
[509] Qi X, MacManus-Driscoll J. Liquid phase epitaxy processing for high temperature superconductor tapes. Curr Opin Solid State Mater Sci 2001;5(4):291–300.
[510] Kursumovic A, Tomov RI, Hühne R, MacManus-Driscoll JL, Glowacki BA, Evetts JE. Hybrid liquid phase epitaxy processes for $YBa_2Cu_3O_7$ film growth. Supercond Sci Technol 2004;17(10):1215.
[511] Queraltó A, Sieger M, Gupta K, Meledin A, Barusco P, Saltarelli L, et al. Transient liquid assisted growth of superconducting $YBa_2Cu_3O_{7-x}$ films based on pulsed laser deposition. Supercond Sci Technol 2022;36(2):025003.
[512] Watson IM. Metal-organic CVD of the high-T_c superconductor $YBa_2Cu_3O_{7-\delta}$. Chem Vapor Depos 1997;3(1):9–26.
[513] Selvamanickam V, Galinski G, Carota G, DeFrank J, Trautwein C, Haldar P, et al. High-current Y-Ba-Cu-O superconducting films by metal organic chemical vapor deposition on flexible metal substrates. Phys C: Supercond 2000;333(3):155–62.
[514] Zhao P, Ito A, Tu R, Goto T. Fast epitaxial growth of *a*-axis- and *c*-axis-oriented $YBa_2Cu_3O_{7-\delta}$ films on (100) $LaAlO_3$ substrate by laser chemical vapor deposition. Appl Surf Sci 2011;257(9):4317–20.
[515] Sabzi M, Mousavi Anijdan SH, Shamsodin M, Farzam M, Hojjati-Najafabadi A, Feng P, et al. A review on sustainable manufacturing of ceramic-based thin films by chemical vapor deposition (CVD): Reactions kinetics and the deposition mechanisms. Coatings 2023;13(1).
[516] Yu J, Han W, Suleiman AA, Han S, Miao N, Ling FC-C. Recent advances on pulsed laser deposition of large-scale thin films. Small Methods 2024;8(7):2301282.
[517] Liguori A, Gualandi C, Focarete ML, Biscarini F, Bianchi M. The pulsed electron deposition technique for biomedical applications: A review. Coatings 2020;10(1).
[518] Liang F, Yang J, Zhao Y, Zhou Y, Yan Z, He J, et al. A review of thin film electrolytes fabricated by physical vapor deposition for solid oxide fuel cells. Int J Hydrog Energy 2022;47(87):36926–52.
[519] Malozemoff AP, Fleshler S, Rupich M, Thieme C, Li X, Zhang W, et al. Progress in high temperature superconductor coated conductors and their applications. Supercond Sci Technol 2008;21(3):034005.
[520] Oh SS, Ha HS, Kim HS, Ko RK, Song KJ, Ha DW, et al. Development of long-length SmBCO coated conductors using a batch-type reactive co-evaporation method. Supercond Sci Technol 2008;21(3):034003.
[521] Matias V, Rowley EJ, Coulter Y, Maiorov B, Holesinger T, Yung C, et al. YBCO films grown by reactive co-evaporation on simplified IBAD-MgO coated conductor templates. Supercond Sci Technol 2009;23(1):014018.
[522] Suenaga M, Solovyov VF, Wu L, Wiesmann HJ, Zhu Y. BaF_2 Post-Deposition Reaction Process for Thick YBCO Films. In: Second-generation HTS conductors. Boston, MA: Springer US; 2005, p. 135–47.

[523] Yoo J, Leonard KJ, Hsu HS, Heatherly L, List FA, Lee DF, et al. The growth of YBCO films with high critical current at reduced pressures using the BaF_2 ex situ process. Supercond Sci Technol 2004;17(10):1209.

[524] Christen HM, Lee DF, List FA, Cook SW, Leonard KJ, Heatherly L, et al. Pulsed electron deposition of fluorine-based precursors for $YBa_2Cu_3O_{7-x}$-coated conductors. Supercond Sci Technol 2005;18(9):1168.

[525] Goyal A, Norton DP, Budai JD, Paranthaman M, Specht ED, Kroeger DM, et al. High critical current density superconducting tapes by epitaxial deposition of $YBa_2Cu_3O_x$ thick films on biaxially textured metals. Appl Phys Lett 1996;69(12):1795–7.

[526] Goyal A, Paranthaman MP, Schoop U. The RABiTS approach: Using rolling-assisted biaxially textured substrates for high-performance YBCO superconductors. MRS Bull 2004;29(8):552–61.

[527] Wang CP, Do KB, Beasley MR, Geballe TH, Hammond RH. Deposition of in-plane textured MgO on amorphous Si_3N_4 substrates by ion-beam-assisted deposition and comparisons with ion-beam-assisted deposited yttria-stabilized-zirconia. Appl Phys Lett 1997;71(20):2955–7.

[528] Groves J, Arendt P, Foltyn S, DePaula R, Peterson E, Holesinger T, et al. Ion-beam assisted deposition of bi-axially aligned MgO template films for YBCO coated conductors. IEEE Trans Appl Supercond 1999;9(2):1964–6.

[529] Bauer M, Semerad R, Kinder H. YBCO films on metal substrates with biaxially aligned MgO buffer layers. IEEE Trans Appl Supercond 1999;9(2):1502–5.

[530] Lao M, Bernardi J, Bauer M, Eisterer M. Critical current anisotropy of GdBCO tapes grown on ISD–MgO buffered substrate. Supercond Sci Technol 2015;28(12):124002.

[531] Stafford BH, Sieger M, Ottolinger R, Meledin A, Strickland NM, Wimbush SC, et al. Tilted $BaHfO_3$ nanorod artificial pinning centres in REBCO films on inclined substrate deposited-mgo coated conductor templates. Supercond Sci Technol 2017;30(5):055002.

[532] Li H-F, Parker T, Tang F, Wang G-C, Lu T-M, Lee S. Biaxially oriented CaF_2 films on amorphous substrates. J Cryst Growth 2008;310(15):3610–4.

[533] Kurth F, Tarantini C, Grinenko V, Hänisch J, Jaroszynski J, Reich E, et al. Unusually high critical current of clean P-doped $BaFe_2As_2$ single crystalline thin film. Appl Phys Lett 2015;106(7):072602.

[534] Holleis S, Shipulin IA, Hühne R, Bernardi J, Eisterer M. Reduced granularity in BHO-doped YBCO films on RABiTS templates. Supercond Sci Technol 2022;35(10):104001.

[535] Matias V, Hammond RH. Ion beam induced crystalline texturing during thin film deposition. Surf Coat Technol 2015;264:1–8.

[536] Feldmann DM, Holesinger TG, Cantoni C, Feenstra R, Nelson NA, Larbalestier DC, et al. Grain orientations and grain boundary networks of $YBa_2Cu_3O_{7-\delta}$ films deposited by metalorganic and pulsed laser deposition on biaxially textured Ni-W substrates. J Mater Res 2006;21:923–34.

[537] Otten S, Kario A, Kling A, Goldacker W. Bending properties of different REBCO coated conductor tapes and Roebel cables at $T = 77$ K. Supercond Sci Technol 2016;29(12):125003.

[538] Togano K, Matsumoto A, Kumakura H. Fabrication and transport properties of ex situ powder-in-tube (PIT) processed $(Ba,K)Fe_2As_2$ superconducting wires. Solid State Commun 2012;152(8):740–6, Special Issue on Iron-based Superconductors.

[539] Iida K, Hänisch J, Yamamoto A. Grain boundary characteristics of Fe-based superconductors. Supercond Sci Technol 2020;33(4):043001.

[540] Zhang X, Oguro H, Yao C, Dong C, Xu Z, Wang D, et al. Superconducting properties of 100-m class $Sr_{0.6}K_{0.4}Fe_2As_2$ tape and pancake coils. IEEE Trans Appl Supercond 2017;27(4):1–5.

[541] Ma Y. Progress in wire fabrication of iron-based superconductors. Supercond Sci Technol 2012;25(11):113001.

[542] Pallecchi I, Eisterer M, Malagoli A, Putti M. Application potential of Fe-based superconductors. Supercond Sci Technol 2015;28(11):114005.

[543] Zhang X, Ma Y. Progress in the development of the 122-type IBS wires. Superconductivity 2022;2:100010.

[544] Iida K, Hänisch J, Tarantini C. Fe-based superconducting thin films on metallic substrates: Growth, characteristics, and relevant properties. Appl Phys Rev 2018;5(3):031304.

[545] Si W, Zhou J, Jie Q, Dimitrov I, Solovyov V, Johnson PD, et al. Iron-chalcogenide $FeSe_{0.5}Te_{0.5}$ coated superconducting tapes for high field applications. Appl Phys Lett 2011;98(26):262509.

[546] Iida K, Hänisch J, Trommler S, Matias V, Haindl S, Kurth F, et al. Epitaxial growth of superconducting $Ba(Fe_{1-x}Co_x)_2As_2$ thin films on technical ion beam assisted deposition MgO substrates. Appl Phys Express 2010;4(1):013103.

[547] Katase T, Hiramatsu H, Matias V, Sheehan C, Ishimaru Y, Kamiya T, et al. Biaxially textured cobalt-doped $BaFe_2As_2$ films with high critical current density over 1 MA/cm^2 on MgO-buffered metal-tape flexible substrates. Appl Phys Lett 2011;98(24):242510.

[548] Sato H, Hiramatsu H, Kamiya T, Hosono H. Enhanced critical-current in P-doped $BaFe_2As_2$ thin films on metal substrates arising from poorly aligned grain boundaries. Sci Rep 2016;6:36828.

[549] Iida K, Kurth F, Chihara M, Sumiya N, Grinenko V, Ichinose A, et al. Highly textured oxypnictide superconducting thin films on metal substrates. Appl Phys Lett 2014;105:1–4.

[550] Si W, Han SJ, Shi X, Ehrlich SN, Jaroszynski J, Goyal A, et al. High current superconductivity in $FeSe_{0.5}Te_{0.5}$-coated conductors at 30 Tesla. Nat Commun 2013;4:1347.

[551] Yamashita A, Matsumoto R, Tanaka M, Hara H, Iida K, Holzapfel B, et al. Observation of zero resistance in as-electrodeposited FeSe. Solid State Commun 2018;270:72–5.

[552] Piperno L, Celentano G, Sotgiu G. Electrodeposition of iron selenide: A review. Coatings 2023;13(11).

[553] Piperno L, Vannozzi A, Augieri A, Masi A, Mancini A, Rufoloni A, et al. High-performance Fe(Se,Te) films on chemical CeO_2-based buffer layers. Sci Rep 2023;13.

[554] Liu L, Ye J, Mou S, Zhu R, Miao C, Li Y, et al. Fabrication of meter-long class Fe(Se,Te)-coated conductors with high superconducting performance. Adv Eng Mater 2023;25(9):2201536.

[555] Liu L, Li Y, Mou S, Miao C, Zhu R, Li R, Ye J. Development of Fe(Se,Te) coated conductors by PLD process for high magnetic field applications. IEEE Transactions on Applied Superconductivity 2025;35(5):1–4.

[556] Foltyn SR, Civale L, MacManus-Driscoll JL, Jia QX, Maiorov B, Wang H, et al. Materials science challenges for high-temperature superconducting wire. Nat Mater 2007;6(9):631–42.

[557] Yamada Y, Takahashi K, Kobayashi H, Konishi M, Watanabe T, Ibi A, et al. Epitaxial nanostructure and defects effective for pinning in $Y(RE)Ba_2Cu_3O_{7-x}$ coated conductors. Appl Phys Lett 2005;87(13):132502.

[558] Matsumoto K, Mele P. Artificial pinning center technology to enhance vortex pinning in YBCO coated conductors. Supercond Sci Technol 2009;23(1):014001.

[559] Gutiérrez J, Llordés A, Gázquez J, Gibert M, Romà N, Ricart S, et al. Strong isotropic flux pinning in solution-derived $YBa_2Cu_3O_{7-x}$ nanocomposite superconductor films. Nat Mater 2007;6(5):367–73.

[560] Durrell JH, Ainslie MD, Zhou D, Vanderbemden P, Bradshaw T, Speller S, et al. Bulk superconductors: a roadmap to applications. Supercond Sci Technol 2018;31(10):103501.

[561] Namburi DK, Cardwell DA. Dense and robust (RE)BCO bulk superconductors for sustainable applications: Current status and future perspectives. In: High-t_c superconducting technology: towards sustainable development goals (1st ed.). Jenny Stanford Publishing; 2021, p. 58–74.

[562] Namburi DK, Shi Y, Cardwell DA. The processing and properties of bulk (RE)BCO high temperature superconductors: current status and future perspectives. Supercond Sci Technol 2021;34(5):053002.

[563] Tallon JL. Thermodynamics and critical current density in high-T_c superconductors. IEEE Trans Appl Supercond 2014;25(3):1–6.

[564] Miura M, Tsuchiya G, Harada T, Sakuma K, Kurokawa H, Sekiya N, et al. Thermodynamic approach for enhancing superconducting critical current performance. NPG Asia Mater 2022;14(1):1–12.
[565] Talantsev E, Strickland N, Wimbush S, Storey J, Tallon J, Long N. Hole doping dependence of critical current density in $YBa_2Cu_3O_{7-\delta}$ conductors. Appl Phys Lett 2014;104(24):242601.
[566] Zaanen J. Why the temperature is high. Nature 2004;430(6999):512–3.
[567] Kovtun PK, Son DT, Starinets AO. Viscosity in strongly interacting quantum field theories from black hole physics. Phys Rev Lett 2005;94(11):111601.
[568] Ahmad N, Naqib S. Estimation of Cooper pair density and its relation to the critical current density in Y(Ca)BCO high-T_c cuprate superconductors. Results Phys 2020;17:103054.
[569] Stangl A, Palau A, Deutscher G, Obradors X, Puig T. Ultra-high critical current densities of superconducting $YBa_2Cu_3O_{7-\delta}$ thin films in the overdoped state. Sci Rep 2021;11(1):1–12.
[570] Song D, Ishida S, Iyo A, Nakajima M, ichi Shimoyama J, Eisterer M, et al. Distinct doping dependence of critical temperature and critical current density in $Ba_{1-x}K_xFe_2As_2$ superconductor. Sci Rep 2016;6:26671.
[571] Ishida S, Song D, Ogino H, Iyo A, Eisaki H, Nakajima M, et al. Doping-dependent critical current properties in K, Co, and P-doped $BaFe_2As_2$ single crystals. Phys Rev B 2017;95:014517.
[572] Putzke C, Walmsley P, Fletcher J, Malone L, Vignolles D, Proust C, et al. Anomalous critical fields in quantum critical superconductors. Nat Commun 2014;5:5679.
[573] Almoalem A, Yagil A, Cho K, Teknowijoyo S, Tanatar MA, Prozorov R, et al. Dependence of the absolute value of the penetration depth in $(Ba_{1-x}K_x)Fe_2As_2$ on doping. Phys Rev B 2018;98:054516.
[574] Hashimoto K, Cho K, Shibauchi T, Kasahara S, Mizukami Y, Katsumata R, et al. A sharp peak of the zero-temperature penetration depth at optimal composition in $BaFe_2(As_{1-x}P_x)_2$. Science 2012;336(6088):1554–7.
[575] Sakagami A, Kawaguchi T, Tabuchi M, Ujihara T, Takeda Y, Ikuta H. Critical current density and grain boundary property of $BaFe_2(As,P)_2$ thin films. Phys C: Supercond 2013;494:181–4.
[576] Yeh K-W, Huang T-W, lin Huang Y, Chen T-K, Hsu F-C, Wu PM, et al. Tellurium substitution effect on superconductivity of the α-phase iron selenide. Europhys Lett 2008;84(3):37002.
[577] Zhang Y, Wang T, Wang Z, Xing Z. Effects of Te- and Fe-doping on the superconducting properties in $Fe_ySe_{1-x}Te_x$ thin films. Sci Rep 2022;12:391.
[578] Zhang C, Si W, Li Q. Doubling the critical current density in superconducting $FeSe_{0.5}Te_{0.5}$ thin films by low temperature oxygen annealing. Appl Phys Lett 2016;109(20):202601.
[579] Sun Y, Shi Z, Tamegai T. Review of annealing effects and superconductivity in $Fe_{1+y}Te_{1-x}Se_x$ superconductors. Supercond Sci Technol 2019;32(10):103001.
[580] Iida K, Hänisch J, Kondo K, Chen M, Hatano T, Wang C, et al. High J_c and low anisotropy of hydrogen doped NdFeAsO superconducting thin film. Sci Rep 2021;11:5636.
[581] Chen MY, Iida K, Kondo K, Hänisch J, Hatano T, Ikuta H. Inter- to intra-layer resistivity anisotropy of NdFeAs(O,H) with various hydrogen concentrations. Phys Rev Mater 2022;6:054802.
[582] Kondo K, Motoki S, Hatano T, Urata T, Iida K, Ikuta H. NdFeAs(O,H) epitaxial thin films with high critical current density. Supercond Sci Technol 2020;33(9):09LT01.
[583] Kauffmann-Weiss S, Iida K, Tarantini C, Boll T, Schneider R, Ohmura T, et al. Microscopic origin of highly enhanced current carrying capabilities of thin NdFeAs(O,F) films. Nanoscale Adv 2019;1:3036–48.
[584] Miura M, Eley S, Iida K, Hanzawa K, Matsumoto J, Hiramatsu H, Ogimoto Y, Suzuki T, Kobayashi T, Ozaki T, Kurokawa H, Sekiya N, Yoshida R, Kato T, Okada T, Okazaki H, Yamaki T, Hänisch J, Awaji S, Maeda A, Maiorov B, Hosono H. Quadrupling the depairing current density in the iron-based superconductor $SmFeAsO_{1-x}H_x$. Nature Materials 2024;23(5):1370–8.
[585] Hilgenkamp H, Mannhart J. Grain boundaries in high-T_c superconductors. Rev Modern Phys 2002;74:485–549.
[586] Eisterer M. Predicting critical currents in grain-boundary limited superconductors. Phys Rev B 2019;99:094501.
[587] Hecher J, Baumgartner T, Weiss JD, Tarantini C, Yamamoto A, Jiang J, et al. Small grains: a key to high-field applications of granular Ba-122 superconductors? Supercond Sci Technol 2015;29(2):025004.
[588] Verebelyi DT, Christen DK, Feenstra R, Cantoni C, Goyal A, Lee DF, et al. Low angle grain boundary transport in $YBa_2Cu_3O_{7-\delta}$ coated conductors. Appl Phys Lett 2000;76(13):1755–7.
[589] Díaz A, Mechin L, Berghuis P, Evetts JE. Observation of viscous flux flow in $YBa_2Cu_3O_{7-\delta}$ low-angle grain boundaries. Phys Rev B 1998;58:R2960–3.
[590] Horide T, Matsumoto K. Evaluation of vortex pinning across low angle grain boundary in $YBa_2Cu_3O_7$ film. Appl Phys Lett 2012;101(11):112604.
[591] Iida K, Qin D, Tarantini C, Hatano T, Wang C, Guo Z, et al. Approaching the ultimate superconducting properties of $(Ba,K)Fe_2As_2$ by naturally formed low-angle grain boundary networks. NPG Asia Mater 2021;13:68.
[592] Guo Z, Gao H, Kondo K, Hatano T, Iida K, Hänisch J, et al. Nanoscale texture and microstructure in a NdFeAs(O,F)/IBAD-MgO superconducting thin film with superior critical current properties. ACS Appl Electron Mater 2021;3(7):3158–66.
[593] Iida K, Hänisch J, Hata S, Yamamoto A. Recent progress on epitaxial growth of Fe-based superconducting thin films. Supercond Sci Technol 2023;36(6):063001.
[594] Fang L, Jia Y, Chaparro C, Sheet G, Claus H, Kirk MA, et al. High, magnetic field independent critical currents in $(Ba,K)Fe_2As_2$ crystals. Appl Phys Lett 2012;101(1):012601.
[595] Fernández L, Holzapfel B, Schindler F, de Boer B, Attenberger A, Hänisch J, et al. Influence of the grain boundary network on the critical current of $YBa_2Cu_3O_7$ films grown on biaxially textured metallic substrates. Phys Rev B 2003;67:052503.
[596] Dew-Hughes D. Flux pinning mechanisms in Type II superconductors. Philos Mag: A J Theor Exp Appl Phys 1974;30(2):293–305.
[597] Sieger M, Hänisch J, Pahlke P, Sparing M, Gaitzsch U, Iida K, et al. $BaHfO_3$-doped thick $YBa_2Cu_3O_{7-\delta}$ films on highly alloyed textured Ni-W tapes. IEEE Trans Appl Supercond 2015;25(3):1–4.
[598] Iida K, Sato H, Tarantini C, Hänisch J, Jaroszynski J, Hiramatsu H, et al. High-field transport properties of a P-doped $BaFe_2As_2$ film on technical substrate. Sci Rep 2017;7(1):39951.
[599] Talantsev EF, Crump WP. Weak-links criterion for pnictide and cuprate superconductors. Supercond Sci Technol 2018;31(12):124001.
[600] Ionescu M, Li AH, Zhao Y, Liu HK, Crisan A. Enhancement of critical current density in $YBa_2Cu_3O_{7-\delta}$ thin films grown using PLD on YSZ (001) surface modified with Ag nano-dots. J Phys D: Appl Phys 2004;37(13):1824–8.
[601] MacManus-Driscoll JL, Foltyn SR, Jia QX, Wang H, Serquis A, Civale L, et al. Strongly enhanced current densities in superconducting coated conductors of $YBa_2Cu_3O_{7-x}$ + $BaZrO_3$. Nat Mater 2004;3(7):439–43.
[602] Hänisch J, Cai C, Hühne R, Schultz L, Holzapfel B. Formation of nanosized $BaIrO_3$ precipitates and their contribution to flux pinning in Ir-doped $YBa_2Cu_3O_{7-\delta}$ quasi-multilayers. Appl Phys Lett 2005;86(12):122508.
[603] Yamada Y, Takahashi K, Kobayashi H, Konishi M, Watanabe T, Ibi A, et al. Epitaxial nanostructure and defects effective for pinning in $Y(RE)Ba_2Cu_3O_{7-x}$ coated conductors. Appl Phys Lett 2005;87(13):132502.
[604] Matsumoto K, Horide T, Ichinose A, Horii S, Yoshida Y, Mukaida M. Critical current control in $YBa_2Cu_3O_{7-\delta}$ films using artificial pinning centers. Japan J Appl Phys 2005;44(No. 7):L246–8.

[605] Mele P, Crisan A, Adam MI. Pinning-engineered $YBa_2Cu_3O_x$ thin films. In: Vortices and nanostructured superconductors, vol. 261. Cham: Springer International Publishing; 2017, p. 15–63.
[606] Ginzburg VL, Andryushin EA. Superconductivity (Revised Edition). Singapore: World Scientific Publishing Company; 2004, ID: 239231.
[607] Gurevich AV, Mints RG, Rakhmanov AL. Physics of composite superconductors. New York: Begell House; 1997, p. 348.
[608] Mousavi T, Grant PS, Speller SC, Grovenor C. New nanoscale artificial pinning centres for NbTi superconductors. Mater Des 2021;198:109285.
[609] Spina T, Ballarino A, Bottura L, Scheuerlein C, Flukiger R. Artificial pinning in Nb_3Sn wires. IEEE Trans Appl Supercond 2017;27(4):1–5.
[610] Dietderich D, Scanlan R. Nb_3Sn artificial pinning microstructures. IEEE Trans Appl Supercond 1997;7(2):1201–4.
[611] Ayache J. Grain boundaries in high temperature superconducting ceramics. Phil Mag 2006;86(15):2193–239.
[612] Crisan A, Fujiwara S, Nie JC, Sundaresan A, Ihara H. Sputtered nanodots: A costless method for inducing effective pinning centers in superconducting thin films. Appl Phys Lett 2001;79(27):4547–9.
[613] Crisan A, Badica P, Fujiwara S, Nie J-C, Sundaresan A, Iyo A, et al. Nanodots-induced pinning centers in thin films: effects on critical current density, activation energy and flux jump rate. IEEE Trans Appl Supercond 2003;13(2):3726–9.
[614] Foltyn SR, Wang H, Civale L, Jia QX, Arendt PN, Maiorov B, et al. Overcoming the barrier to 1000 A/cm width superconducting coatings. Appl Phys Lett 2005;87(16):162505.
[615] Kechik MMA, Mikheenko P, Sarkar A, Dang VS, Babu NH, Cardwell DA, et al. Artificial pinning centres in $YBa_2Cu_3O_{7-\delta}$ thin films by $Gd_2Ba_4CuWO_y$ nanophase inclusions. Supercond Sci Technol 2009;22(3):034020.
[616] Reich E, Thersleff T, Hühne R, Iida K, Schultz L, Holzapfel B. Structural and pinning properties of $Y_2Ba_4CuMO_y$ (M = Nb,Zr)/$YBa_2Cu_3O_{7-\delta}$ quasi-multilayers fabricated by off-axis pulsed laser deposition. Supercond Sci Technol 2009;22(10):105004.
[617] Feldmann DM, Holesinger TG, Maiorov B, Foltyn SR, Coulter JY, Apodaca I. Improved flux pinning in $YBa_2Cu_3O_7$ with nanorods of the double perovskite Ba_2YNbO_6. Supercond Sci Technol 2010;23(9):095004.
[618] Ercolano G, Harrington SA, Wang H, Tsai CF, MacManus-Driscoll JL. Enhanced flux pinning in $YBa_2Cu_3O_{7-\delta}$ thin films using Nb-based double perovskite additions. Supercond Sci Technol 2010;23(2):022003.
[619] Harrington SA, Durrell JH, Maiorov B, Wang H, Wimbush SC, Kursumovic A, Lee JH, et al. Self-assembled, rare earth tantalate pyrochlore nanoparticles for superior flux pinning in $YBa_2Cu_3O_{7-\delta}$ films. Supercond Sci Technol 2008;22(2):022001.
[620] Crisan A, Dang V-S, Mikheenko P. Nano-engineered pinning centres in YBCO superconducting films. Phys C: Supercond Appl 2017;533:118–32.
[621] Wu J, Shi J. Interactive modeling-synthesis-characterization approach towards controllable in situ self-assembly of artificial pinning centers in RE-123 films. Supercond Sci Technol 2017;30(10):103002.
[622] Cantoni C, Gao Y, Wee SH, Specht ED, Gazquez J, Meng J, et al. Strain-driven oxygen deficiency in self-assembled, nanostructured, composite oxide films. ACS Nano 2011;5(6):4783–9, PMID: 21604819.
[623] Wu JZ, Ogunjimi V, Sebastian MA, Zhang D, Jian J, Huang J, et al. Enabling coherent $BaZrO_3$ nanorods/$YBa_2Cu_3O_{7-x}$ interface through dynamic lattice enlargement in vertical epitaxy of $BaZrO_3$/$YBa_2Cu_3O_{7-x}$ nanocomposites. Supercond Sci Technol 2022;35(3):034001.
[624] Hammerl G, Schmehl A, Schulz RR, Goetz B, Bielefeldt H, Schneider CW, et al. Enhanced supercurrent density in polycrystalline $YBa_2Cu_3O_{7-\delta}$ at 77 K from calcium doping of grain boundaries. Nature 2000;407(9):162.
[625] Mele P, Matsumoto K, Horide T, Ichinose A, Mukaida M, Yoshida Y, et al. Incorporation of double artificial pinning centers in $YBa_2Cu_3O_{7-\delta}$ films. Phys C: Supercond 2008;468(15):1631–4.
[626] Zhou H, Maiorov B, Baily SA, Dowden PC, Kennison JA, Stan L, et al. Thickness dependence of critical current density in $YBa_2Cu_3O_{7-\delta}$ films with $BaZrO_3$ and Y_2O_3 addition. Supercond Sci Technol 2009;22(8):085013.
[627] Ercolano G, Bianchetti M, Wimbush SC, Harrington SA, Wang H, Lee JH, et al. State-of-the-art flux pinning in $YBa_2Cu_3O_{7-\delta}$ by the creation of highly linear, segmented nanorods of Ba_2(Y /Gd)(Nb/Ta)O_6 together with nanoparticles of $(Y/Gd)_2O_3$ and (Y/Gd)$Ba_2Cu_4O_8$. Supercond Sci Technol 2011;24(9):095012.
[628] Jha AK, Matsumoto K, Horide T, Saini S, Mele P, Ichinose A, et al. Tailoring the vortex pinning strength of YBCO thin films by systematic incorporation of hybrid artificial pinning centers. Supercond Sci Technol 2015;28(11):114004.
[629] Xu Y, Suo H, Qureishy T, Grivel J-C, Mikheenko P, Liu M, et al. Systematic research on the effect of both positive and negative mismatch dopants in double-doped YBCO superconducting films. J Eur Ceram Soc 2021;41(1):480–7.
[630] Rizzo F, Augieri A, Angrisani Armenio A, Galluzzi V, Mancini A, Pinto V, et al. Enhanced 77 K vortex-pinning in $YBa_2Cu_3O_{7-x}$ films with Ba_2YTaO_6 and mixed Ba_2YTaO_6 + Ba_2YNbO_6 nano-columnar inclusions with irreversibility field to 11 T. APL Mater 2016;4(6):061101.
[631] Celentano G, Rizzo F, Augieri A, Mancini A, Pinto V, Rufoloni A, et al. $YBa_2Cu_3O_{7-x}$ films with Ba_2Y(Nb,Ta)O_6 nanoinclusions for high-field applications. Supercond Sci Technol 2020;33(4):044010.
[632] Rizzo F, Augieri A, Kursumovic A, Bianchetti M, Opherden L, Sieger M, et al. Pushing the limits of applicability of REBCO coated conductor films through fine chemical tuning and nanoengineering of inclusions. Nanoscale 2018;10:8187–95.
[633] Mikheenko P, Sarkar A, Dang V-S, Tanner J, Abell J, Crisan A. c-axis correlated extended defects and critical current in $YBa_2Cu_3O_x$ films grown on Au and Ag-nano dot decorated substrates. Phys C: Supercond 2009;469(14):798–804.
[634] Mikheenko P, Dang V-S, Tse YY, Kechik MMA, Paturi P, Huhtinen H, et al. Integrated nanotechnology of pinning centers in $YBa_2Cu_3O_x$ films. Supercond Sci Technol 2010;23(12):125007.
[635] Kiessling A, Hänisch J, Thersleff T, Reich E, Weigand M, Hühne R, et al. Nanocolumns in $YBa_2Cu_3O_{7-x}$/$BaZrO_3$ quasi-multilayers: formation and influence on superconducting properties. Supercond Sci Technol 2011;24(5):055018.
[636] Erbe M, Hänisch J, Hühne R, Freudenberg T, Kirchner A, Molina-Luna L, et al. $BaHfO_3$ artificial pinning centres in TFA-MOD-derived YBCO and GdBCO thin films. Supercond Sci Technol 2015;28(11):114002.
[637] Cayado P, Erbe M, Kauffmann-Weiss S, Bühler C, Jung A, Hänisch J, et al. Large critical current densities and pinning forces in CSD-grown superconducting $GdBa_2Cu_3O_{7-x}$-$BaHfO_3$ nanocomposite films. Supercond Sci Technol 2017;30(9):094007.
[638] Chen Y, Selvamanickam V, Zhang Y, Zuev Y, Cantoni C, Specht E, et al. Enhanced flux pinning by $BaZrO_3$ and $(Gd,Y)_2O_3$ nanostructures in metal organic chemical vapor deposited GdYBCO high temperature superconductor tapes. Appl Phys Lett 2009;94(6):062513.
[639] Coll M, Guzman R, Garcés P, Gazquez J, Rouco V, Palau A, et al. Size-controlled spontaneously segregated Ba_2YTaO_6 nanoparticles in $YBa_2Cu_3O_7$ nanocomposites obtained by chemical solution deposition. Supercond Sci Technol 2014;27(4):044008.
[640] Cayado P, Erbe M, Kauffmann-Weiss S, Jung A, Hänisch J, Holzapfel B. Chemical solution deposition of $Y_{1-x}Gd_xBa_2Cu_3O_{7-\delta}$–$BaHfO_3$ nanocomposite films: combined influence of nanoparticles and rare-earth mixing on growth conditions and transport properties. RSC Adv 2018;8:42398–404.
[641] Palau A, Vallès F, Rouco V, Coll M, Li Z, Pop C, et al. Disentangling vortex pinning landscape in chemical solution deposited superconducting $YBa_2Cu_3O_{7-x}$ films and nanocomposites. Supercond Sci Technol 2018;31(3):034004.
[642] Deutscher G. Origin of weak-link behavior of grain boundaries in superconducting cuprates and pnictides. Appl Phys Lett 2010;96(12):122502.
[643] Coll M, Ye S, Rouco V, Palau A, Guzman R, Gazquez J, et al. Solution-derived $YBa_2Cu_3O_7$ nanocomposite films with a Ba_2YTaO_6 secondary phase for improved superconducting properties. Supercond Sci Technol 2012;26(1):015001.
[644] Puig T, Gutiérrez J, Pomar A, Llordés A, Gázquez J, Ricart S, et al. Vortex pinning in chemical solution nanostructured YBCO films. Supercond Sci Technol 2008;21(3):034008.
[645] Obradors X, Puig T, Ricart S, Coll M, Gazquez J, Palau A, et al. Growth, nanostructure and vortex pinning in superconducting $YBa_2Cu_3O_7$ thin films based on trifluoroacetate solutions. Supercond Sci Technol 2012;25(12):123001.

[646] Bartolomé E, Vallés F, Palau A, Rouco V, Pompeo N, Balakirev FF, et al. Intrinsic anisotropy versus effective pinning anisotropy in $YBa_2Cu_3O_7$ thin films and nanocomposites. Phys Rev B 2019;100:054502.

[647] Rouco V, Palau A, Guzman R, Gazquez J, Coll M, Obradors X, et al. Role of twin boundaries on vortex pinning of CSD YBCO nanocomposites. Supercond Sci Technol 2014;27(12):125009.

[648] Guzman R, Gazquez J, Rouco V, Palau A, Magen C, Varela M, et al. Strain-driven broken twin boundary coherence in $YBa_2Cu_3O_{7-\delta}$ nanocomposite thin films. Appl Phys Lett 2013;102(8):081906.

[649] Guzman R, Gazquez J, Mundet B, Coll M, Obradors X, Puig T. Probing localized strain in solution-derived $YBa_2Cu_3O_{7-\delta}$ nanocomposite thin films. Phys Rev Mater 2017;1:024801.

[650] Rouco V, Bartolomé E, Maiorov B, Palau A, Civale L, Obradors X, et al. Vortex creep in TFA–YBCO nanocomposite films. Supercond Sci Technol 2014;27(11):115008.

[651] Miura M, Yoshizumi M, Izumi T, Shiohara Y. Formation mechanism of $BaZrO_3$ nanoparticles in $Y_{1-x}Sm_xBa_2Cu_3O_y$-coated conductors derived from trifluoroacetate metal–organic deposition. Supercond Sci Technol 2009;23(1):014013.

[652] Miura M, Maiorov B, Baily SA, Haberkorn N, Willis JO, Marken K, et al. Mixed pinning landscape in nanoparticle-introduced $YGdBa_2Cu_3O_y$ films grown by metal organic deposition. Phys Rev B 2011;83:184519.

[653] Kimura K, Hironaga R, Nakamura T, Takahashi Y, Koizumi T, Hasegawa T, et al. Development of REBCO coated conductors by TFA-MOD method with high properties in magnetic fields. IEEE Trans Appl Supercond 2015;25(3):1–4.

[654] Cayado P, Keukeleere KD, Garzón A, Perez-Mirabet L, Meledin A, Roo JD, et al. Epitaxial $YBa_2Cu_3O_{7-x}$ nanocomposite thin films from colloidal solutions. Supercond Sci Technol 2015;28(12):124007.

[655] De Keukeleere K, Cayado P, Meledin A, Vallès F, De Roo J, Rijckaert H, et al. Superconducting $YBa_2Cu_3O_{7-\delta}$ nanocomposites using preformed ZrO_2 nanocrystals: Growth mechanisms and vortex pinning properties. Adv Electron Mater 2016;2(10):1600161.

[656] Rijckaert H, Cayado P, Nast R, Diez Sierra J, Erbe M, López Dominguez P, et al. Superconducting HfO_2-$YBa_2Cu_3O_{7-\delta}$ nanocomposite films deposited using ink-jet printing of colloidal solutions. Coatings 2020;10(1).

[657] Obradors X, Puig T, Li Z, Pop C, Mundet B, Chamorro N, et al. Epitaxial $YBa_2Cu_3O_{7-x}$ nanocomposite films and coated conductors from $BaMO_3$ (M=Zr, Hf) colloidal solutions. Supercond Sci Technol 2018;31(4):044001.

[658] Li Z, Coll M, Mundet B, Chamorro N, Vallès F, Palau A, et al. Control of nanostructure and pinning properties in solution deposited $YBa_2Cu_3O_{7-x}$ nanocomposites with preformed perovskite nanoparticles. Sci Rep 2019;9(1):5828.

[659] Blanca GRS, De Vero JC, Garcia WO, Sarmago RV. Enhanced flux pinning in IR PLD grown Y-doped Bi-2212 films. Phys C: Supercond 2013;484:74–6, Proceedings of the 24th International Symposium on Superconductivity (ISS2011).

[660] Boudjadja Y, Amira A, Mahamdioua N, Saoudel A, Menassel S, Varilci A, et al. Microstructural and magneto-transport properties of $Bi_{1.6}Pb_{0.4}Sr_2Ca_{1-x}Gd_xCu_2O_{8+\delta}$ superconducting ceramics. Phys B 2017;505:68–73.

[661] Ma R, Song W, Zhu X, Zhang L, Liu S, Fang J, et al. Enhanced flux pinning in (Bi,Pb)-2223/Ag tapes by slight Ni doping. Phys C: Supercond 2004;405(1):34–40.

[662] Pu M, Feng Y, Zhang P, Zhou L, Wang J, Sun Y, et al. Enhanced the flux pinning in Bi-2223/Ag by induced Cr-ion defects. Phys C: Supercond 2003;386:41–6, Proceedings of the topical conference of the International Cryogenic Materials Conference (ICMC 2002). Superconductors for Practical Applications.

[663] Amira A, Mosbah M, Molinié P, Leblanc A. Improvement of magnetic properties in Bi-2212 ceramics by fluorine doping. Solid State Sci 2005;7(1):53–7.

[664] Vinu S, Sarun P, Shabna R, Biju A, Syamaprasad U. Microstructure and transport properties of $Bi_{1.6}Pb_{0.5}Sr_{2-x}Lu_xCa_{1.1}Cu_{2.1}O_{8+\delta}$ superconductor. Mater Chem Phys 2010;119(1–2):135–9.

[665] Zhang J, Wang W, Wang T, Jiang L, Wang N, Sun D, et al. Nanoscale characterization of the doped $SrZrO_3$ nanoparticles distribution and its influence on the microstructure of $Bi_2Sr_2CaCu_2O_{8+\delta}$ film. J Alloys Compd 2021;858:157650.

[666] Kazin PE, Tretyakov YD, Lennikov VV, Jansen M. Formation of the $Bi_2Sr_2CaCu_2O_{8-\delta}$ superconductor with $Mg_{1-x}Cu_xO$ inclusions: the phases compatibility and the effect of the preparation route on the material microstructure and properties. J Mater Chem 2001;11:168–72.

[667] Ghattas A, Annabi M, Zouaoui M, Azzouz FB, Salem MB. Flux pinning by Al-based nano particles embedded in polycrystalline (Bi,Pb)-2223 superconductors. Phys C: Supercond Appl 2008;468(1):31–8.

[668] Hamid NA, Abd-Shukor R. Effects of TiO_2 addition on the superconducting properties of Bi-Sr-Ca-Cu-O system. J Mater Sci 2000;35:2325–9.

[669] Albiss B, Obaidat I, Gharaibeh M, Ghamlouche H, Obeidat S. Impact of addition of magnetic nanoparticles on vortex pinning and microstructure properties of Bi–Sr–Ca–Cu–O superconductor. Solid State Commun 2010;150(33):1542–7.

[670] Farah-Elia N, Ilhamsyah A, Abd-Shukor R. Ferrimagnetic Cr_2S_3 effects on $Bi_{1.6}Pb_{0.4}Sr_2CaCu_2O_8$ superconductor. J Mater Sci: Mater Electron Vol 2019;30:12031–5.

[671] Bagiah H, Halim S, Chen S, Lim K, Kechik MA. Effects of rare earth nanoparticles (M = Sm_2O_3, Ho_2O_3, Nd_2O_3) addition on the microstructure and superconducting transition of $Bi_{1.6}Pb_{0.4}Sr_2Ca_2Cu_3O_{10+\delta}$ ceramics. Sains Malays 2016;45(4):643–51.

[672] Abbas S, Basma H, Awad R, Matar M. Tailoring the physical properties of (Bi, Pb)-2212 superconductor by the addition of $Cd_{0.95}Mn_{0.05}O$ nanoparticles. J Low Temp Phys 2022;208:271–88.

[673] Abbas S, Basma H, Awad R, Hassan M. Structural and electrical investigations of novel CdFeO/(Bi,Pb)-2212 superconductor composite. Phase Transit 2022;95(8–9):651–66.

[674] Takahira S, Ichino Y, Yoshida Y. Fabrication of high J_c (Bi,Pb)2223 thin films by PLD and post-annealing process. Phys Procedia 2015;65:153–6, Proceedings of the 27th International Symposium on Superconductivity (ISS 2014) November 25–27, 2014, Tokyo, Japan.

[675] Naderi G, Schwartz J. On the roles of $Bi_2Sr_2CuO_x$ intergrowths in $Bi_2Sr_2CaCu_2O_x$/Ag round wires: c-axis transport and magnetic flux pinning. Appl Phys Lett 2014;104(15):152602.

[676] Zhao B, Song W, Wan X, Sun Y, Du J. The effect of nanometer Ca_2PbO_4 precipitates on flux pinning in Bi-2223/Ag tapes. Phys C: Supercond 2000;337(1):145–9.

[677] Yang P, Lieber CM. Nanorod-superconductor composites: A pathway to materials with high critical current densities. Science 1996;273(5283):1836–40.

[678] Labdi S, Raffy H, Laborde O, Monceau P. Angular dependence of critical currents in $Bi_2Sr_2CaCu_2O_8$ thin films predominant role of the transverse magnetic field component. Physica C 1992;197(3):274.

[679] Schmitt P, Schultz L, Saemann-Ischenko G. Electrical properties of $Bi_2Sr_2CaCu_2O_x$ thin films prepared in situ by pulsed laser deposition. Physica C 1990;168(5):475–8.

[680] Yamasaki H, Endo K. Nanostructural defects for effective flux pinning in high-quality $Bi_2Sr_2CaCu_2O_{8+x}$ epitaxial thin films with high critical current density. Supercond Sci Technol 2014;27(2):025014.

[681] Keppert S, Aichner B, Adhikari R, Faina B, Lang W, Pedarnig JD. Phase purity and surface morphology of high-J_c superconducting $Bi_2Sr_2Ca_1Cu_2O_{8+\delta}$ thin films. Appl Surf Sci 2023;636:157822.

[682] Hänisch J, Attenberger A, Holzapfel B, Schultz L. Electrical transport properties of $Bi_2Sr_2Ca_2Cu_3O_{10+\delta}$ thin film [001] tilt grain boundaries. Phys Rev B 2002;65:052507.

[683] Ghahfarokhi S, Hoseenzadeh N, Shoushtari M. The effect of CdO nanoparticles on the structure and magnetic properties of $Bi_{1.64}Pb_{0.36}Sr_2Ca_{2-x}Cd_xCu_3O_y$ superconductors. J Supercon. Nov Magn 2014;27:2217–23.

[684] Yahya N, Al-Gaashani R, Abd-Shukor R. Synthesis and characterization of PbO-CdO nanocomposite and its effect on (Bi,Pb)-2223 superconductor. Appl Phys A 2017;123:168.

[685] Guilmeau E, Andrzejewski B, Noudem J. The effect of MgO addition on the formation and the superconducting properties of the Bi2223 phase. Phys C: Supercond 2003;387(3):382–90.

[686] Zhao B, Wan X, Song W, Sun Y, Du J. Nano-MgO particle addition in silver-sheathed $(Bi,Pb)_2Sr_2Ca_2Cu_3O_x$ tapes. Phys C: Supercond 2000;337(1):138–44.

[687] Aftabi A, Mozaffari M. Fluctuation induced conductivity and pseudogap state studies of $Bi_{1.6}Pb_{0.4}Sr_2Ca_2Cu_3O_{10+\delta}$ superconductor added with ZnO nanoparticles. Sci Rep 2021;11:4341.

[688] Jia Z, Tang H, Yang Z, Xing Y, Wang Y, Qiao G. Effects of nano-ZrO_2 particles on the superconductivity of Pb-doped BSCCO. Phys C: Supercond 2000;337(1):130–2.

[689] Abbasi H, Taghipour J, Sedghi H. Superconducting and transport properties of (Bi–Pb)–Sr–Ca–Cu–O with Cr_2O_3 additions. J Alloys Compd 2010;494(1):305–8.

[690] Annabi M, M'chirgui A, Ben Azzouz F, Zouaoui M, Ben Salem M. Addition of nanometer Al_2O_3 during the final processing of (Bi,Pb)-2223 superconductors. Phys C: Supercond 2004;405(1):25–33.

[691] Guo Y, Tanaka Y, Kuroda T, Dou S, Yang Z. Addition of nanometer SiC in the silver-sheathed Bi2223 superconducting tapes. Phys C: Supercond 1999;311(1):65–74.

[692] Mua NT, Serrao CR, Shipra, Sundaresan A, Hien TD, Man NK. High critical current density in Ag-doped Bi-2212 thin films. Supercond Sci Technol 2008;21(10):105002.

[693] Basma H, Abbas S, Labban W, Awad R, Matar M. Investigation of the structural and electrical properties of CdO/(Bi,Pb)-2212 superconducting phase. Phys Scr 2022;97(6):065801.

[694] Bhattacharya RN, Spagnol P, Miao H, Marken K, Willis JO. Nanoparticle incorporated superconductor Bi-2212 tapes. Phys Status Solidi (A) 2004;201(13):2880–5.

[695] Ilyushechkin AY, Agranovskii IE, Altman IS, Zagainov VA, Choi M. Influence of magnesium oxide nanoparticles embedded in Bi-2212/Ag tapes on their superconducting properties. Tech Phys 2012;57:506–11.

[696] Ilyushechkin AY, Agranovski IE, Altman IS, Choi M. Effect of MgO nanoparticles embedded into Bi-2212/Ag tapes on the microstructure and superconducting properties. Mater Sci Eng: B 2010;167(1):60–4.

[697] Agranovski IE, Ilyushechkin AY, Altman IS, Bostrom TE, Choi M. Methods of introduction of MgO nanoparticles into Bi-2212/Ag tapes. Phys C: Supercond Appl 2006;434(1):115–20.

[698] Ni B, Asayama K, Kiyuna S. Relationship between MgO particles addition and critical current density in Bi-2212 thick film grown on oxidized Ni substrate. Phys C: Supercond 2002;372–376:1868–71.

[699] Trociewitz U, Sahm P, Koritala R, Brandao L, Bacaltchuk C, Schwartz J. The influence of BaO_2 additions on microstructure and superconducting properties of $Bi_2Sr_2CaCu_2O_{8+\delta}$. Phys C: Supercond 2002;366(2):80–92.

[700] Zhang B, Qi Y. Effect of Er/Y addition on the growth and superconductivity of Bi2212 films. RSC Adv 2023;13:17253–63.

[701] De Vero JC, Hwang I, Shin H, Santiago AC, Lee D, Chang J, et al. Growth and superconducting properties of $Bi_2Sr_2CaCu_2O_{8+\delta}$ thin films incorporated with iridate nanoparticles. Phys Status Solidi (A) 2014;211(8):1787–93.

[702] De Vero JC, Hwang I, Santiago ACL, Chang J, Kim J, Sarmago RV, et al. Growth of $Bi_2Sr_2CaCu_2O_{8+\delta}$ thin films with enhanced superconducting properties by incorporating $CaIrO_3$ nanoparticles. Appl Phys Lett 2014;104(17):172603.

[703] Kazin P, Jansen M, Tretyakov Y. Formation of sub-micron $SrZrO_3$ particles in $Bi_2Sr_2CaCu_2O_{8+x}$ superconductor. Phys C: Supercond 1994;235–240:493–4.

[704] Makarova M, Kazin P, Tretyakov Y, Jansen M, Reissner M, Steiner W. Zr, Hf, Mo and W-containing oxide phases as pinning additives in Bi-2212 superconductor. Phys C: Supercond 2005;419(1):61–9.

[705] Kazin P, Jansen M, Larrea A, de la Fuente G, Tretyakov Y. Flux pinning improvement in Bi-2212 silver sheathed tapes with submicron $SrZrO_3$ inclusions. Phys C: Supercond 1995;253(3):391–400.

[706] Buzea C, Yamashita T. Review of the superconducting properties of MgB_2. Supercond Sci Technol 2001;14(11):R115–46.

[707] Loudon JC, Yazdi S, Kasama T, Zhigadlo ND, Karpinski J. Measurement of the penetration depth and coherence length of MgB_2 in all directions using transmission electron microscopy. Phys Rev B 2015;91:054505.

[708] Larbalestier DC, Cooley LD, Rikel MO, Polyanskii AA, Jiang J, Patnaik S, et al. Strongly linked current flow in polycrystalline forms of the superconductor MgB_2. Nature 2001;410(6825):186–9.

[709] Groza JR, Zavaliangos A. Sintering activation by external electrical field. Mater Sci Eng: A 2000;287(2):171–7.

[710] Grasso S, Sakka Y, Maizza G. Electric current activated/assisted sintering (ECAS): a review of patents 1906–2008. Sci Technol Adv Mater 2009;10(5):053001.

[711] Anselmi-Tamburini U, Spinolo G, Maglia F, Tredici I, Holland TB, Mukherjee AK. Field assisted sintering mechanisms. In: Castro R, van Benthem K, editors. Sintering: mechanisms of convention nanodensification and field assisted processes. Berlin, Heidelberg: Springer Berlin Heidelberg; 2013, p. 159–93.

[712] Badica P, Crisan A, Aldica G, Endo K, Borodianska H, Togano K, et al. 'Beautiful' unconventional synthesis and processing technologies of superconductors and some other materials. Sci Technol Adv Mater 2011;12(1):013001.

[713] Shadab M, Xing Y, Noudem J, Miryala M. Enhanced superconducting properties in bulk MgB_2 through spark plasma sintering of ball-milled and sieved crystalline boron. J Mater Sci, Mater Electron 2024;35(26):1712.

[714] Gong C, Zhao Q, Lan F, Ping X, Zhang P, Liu Y, et al. Effect of Ni doping on microstructure and superconductivity of MgB_2 prepared by C-coated B powder. Phys C: Supercond Appl 2019;566:1353540.

[715] Yan G, Feng Y, Lu Y, Zhou L, Jing W, Wen H. Influences of heat treatment and doping on microstructure and superconducting properties of MgB_2 superconductor. Phys C: Supercond Appl 2006;445:466–70.

[716] Zhao Q, Liu Y, Han Y, Ma Z, Shi Q, Gao Z. Effect of heating rates on microstructure and superconducting properties of pure MgB_2. Phys C: Supercond 2009;469(14):857–61.

[717] Dou SX, Soltanian S, Horvat J, Wang XL, Zhou SH, Ionescu M, et al. Enhancement of the critical current density and flux pinning of MgB_2 superconductor by nanoparticle SiC doping. Appl Phys Lett 2002;81(18):3419–21.

[718] Badica P, Aldica G, Ionescu A, Burdusel M, Batalu D. The influence of different additives on MgB_2 superconductor obtained by ex situ spark plasma sintering: Pinning force aspects. In: Nishikawa H, Iwata N, Endo T, Takamura Y, Lee G-H, Mele P, editors. Correlated functional oxides. Springer International Publishing; 2017, p. Ch.4.

[719] Fietz WA, Webb WW. Hysteresis in superconducting alloys—Temperature and field dependence of dislocation pinning in niobium alloys. Phys Rev 1969;178:657–67.

[720] Badica P, Aldica G, Burdusel M, Grigoroscuta M, Ionescu AM, Sandu V, et al. Control of the critical current density through microstructural design by Ho_2O_3 and Te Co-addition into MgB_2 processed by ex situ spark plasma sintering. In: Mele P, Prassides K, Tarantini C, Palau A, Badica P, Jha A, Endo T, editors. Superconductivity: from materials science to practical applications. Springer Nature Switzerland AG; 2020, p. 303–24.

[721] Dou SX, Shcherbakova O, Yeoh WK, Kim JH, Soltanian S, Wang XL, et al. Mechanism of enhancement in electromagnetic properties of MgB_2 by nano SiC doping. Phys Rev Lett 2007;98:097002.

[722] Lee S, Masui T, Yamamoto A, Uchiyama H, Tajima S. Crystal growth of C-doped MgB_2 superconductors: accidental doping and inhomogeneity. Phys C: Supercond 2004;412–414:31–5.
[723] Ojha N, Malik VK, Singla R, Bernhard C, Varma GD. The effect of citric and oxalic acid doping on the superconducting properties of MgB_2. Supercond Sci Technol 2009;22(12):125014.
[724] Shahabuddin M, Ansari IA, Alzayed NS, Ziq KA, Salem AF. Effect of nano ZnO doping on the nature of pinning of MgB_2 superconductors. J Supercond Nov Magn 2013;26(5):1547–52.
[725] Grigoroscuta M, Aldica G, Burdusel M, Sandu V, Kuncser A, Pasuk I, et al. Towards high degree of *c*-axis orientation in MgB_2 bulks. J Magnes Alloy 2022;10:2173–84.
[726] Ma R, Ma Y, Song W, Zhu X, Liu S, Du J, et al. Imperfection of flux pinning classification based on the pinning center size. Phys C: Supercond 2004;411(1):77–82.
[727] Awaji S, Tsuchiya Y, Miura S, Ichino Y, Yoshida Y, Matsumoto K. *C*-axis correlated pinning mechanism in vortex liquid and solid phases for Sm123 film with well-aligned $BaHfO_3$ nanorods. Supercond Sci Technol 2017;30(11):114005.
[728] Rochester J, Ortino M, Xu X, Peng X, Sumption M. The roles of grain boundary refinement and nano-precipitates in flux pinning of APC Nb_3Sn. IEEE Trans Appl Supercond 2021;31(5):1–5.
[729] Crisan A, Dang V, Yearwood G, Mikheenko P, Huhtinen H, Paturi P. Investigation of the bulk pinning force in YBCO superconducting films with nano-engineered pinning centres. Phys C: Supercond Appl 2014;503:89–93.
[730] Eisterer M, Zehetmayer M, Weber HW. Current percolation and anisotropy in polycrystalline MgB_2. Phys Rev Lett 2003;90:247002.
[731] Eisterer M, Häßler W, Kováč P. Critical currents in weakly textured MgB_2: Nonlinear transport in anisotropic heterogeneous media. Phys Rev B 2009;80:174516.
[732] Eisterer M, Emhofer J, Sorta S, Zehetmayer M, Weber HW. Connectivity and critical currents in polycrystalline MgB_2. Supercond Sci Technol 2009;22(3):034016.
[733] Sandu V, Ionescu AM, Aldica G, Grigoroscuta MA, Burdusel M, Badica P. On the pinning force in high density MgB_2 samples. Sci Rep 2021;11(1):5951.
[734] Matera D, Bonura M, Giannini E, Senatore C. Electrical connectivity in MgB_2: The role of precursors and processing routes in controlling voids and detrimental secondary phases. IEEE Trans Appl Supercond 2017;27(4):1–6.
[735] Badica P, Aldica G, Burdusel M, Popa S, Negrea RF, Enculescu M, et al. Significant enhancement of the critical current density for cubic BN addition into ex situ spark plasma sintered MgB_2. Supercond Sci Technol 2014;27(9):095013.
[736] Sakoda M, Iida K, Naito M. Recent progress in thin-film growth of Fe-based superconductors: superior superconductivity achieved by thin films. Supercond Sci Technol 2018;31(9):093001.
[737] Hänisch J, Iida K, Hühne R, Tarantini C. Fe-based superconducting thin films—preparation and tuning of superconducting properties. Supercond Sci Technol 2019;32(9):093001.
[738] Ma Y. Development of high-performance iron-based superconducting wires and tapes. Phys C: Supercond Appl 2015;516:17–26.
[739] Meyer S. Introduction of quasi-multilayer pulsed laser deposition for enhanced superconducting properties of $Ba(Fe_{0.92}Co_{0.08})_2As_2$ thin films [Ph.D. thesis], Karlsruhe Institute of Technology; 2020.
[740] Horide T, Katagiri H, Ichinose A, Matsumoto K. Fabrication of Fe(Te,Se) films added with oxide or chalcogenide: Influence of added material on phase formation and superconducting properties. J Appl Phys 2022;131(10):103901.
[741] Tarantini C, Lee S, Zhang Y, Jiang J, Bark CW, Weiss JD, et al. Strong vortex pinning in Co-doped $BaFe_2As_2$ single crystal thin films. Appl Phys Lett 2010;96(14):142510.
[742] Zhang Y, Nelson CT, Lee S, Jiang J, Bark CW, Weiss JD, et al. Self-assembled oxide nanopillars in epitaxial $BaFe_2As_2$ thin films for vortex pinning. Appl Phys Lett 2011;98(4):042509.
[743] Tarantini C, Kametani F, Lee S, Jiang J, Weiss JD, Jaroszynski J, et al. Development of very high J_c in $Ba(Fe_{1-x}Co_x)_2As_2$ thin films grown on CaF_2. Sci Rep 2014;4:7305.
[744] Lee S, Tarantini C, Gao P, Jiang J, Weiss JD, Kametani F, et al. Artificially engineered superlattices of pnictide superconductors. Nat Mater 2013;12:392.
[745] Sato H, Hiramatsu H, Kamiya T, Hosono H. High critical-current density with less anisotropy in $BaFe_2(As,P)_2$ epitaxial thin films: Effect of intentionally grown c-axis vortex-pinning centers. Appl Phys Lett 2014;104(18):182603.
[746] Braccini V, Kawale S, Reich E, Bellingeri E, Pellegrino L, Sala A, et al. Highly effective and isotropic pinning in epitaxial Fe(Se,Te) thin films grown on CaF_2 substrates. Appl Phys Lett 2013;103(17):172601.
[747] Ishida S, Iyo A, Ogino H, Eisaki H, Takeshita N, Kawashima K, et al. Unique defect structure and advantageous vortex pinning properties in superconducting $CaKFe_4As_4$. NPJ Quantum Mater 2019;4:27.
[748] Miura M, Maiorov B, Kato T, Shimode T, Wada K, Adachi S, et al. Strongly enhanced flux pinning in one-step deposition of $BaFe_2(As_{0.66}P_{0.33})_2$ superconductor films with uniformly dispersed $BaZrO_3$ nanoparticles. Nat Commun 2013;4:2499.
[749] Miura M, Tsuchiya G, Harada T, Tanabe K, Kiuchi M, Matsushita T. Enhanced critical current density in $BaFe_2(As_{0.66}P_{0.33})_2$ nanocomposite superconducting films. Supercond Sci Technol 2019;32(6):064005.
[750] Lee J, Jiang J, Kametani F, Oh MJ, Weiss JD, Collantes Y, et al. High critical current density over 1 MA cm^{-2} at 13 T in $BaZrO_3$ incorporated $Ba(Fe,Co)_2As_2$ thin film. Supercond Sci Technol 2017;30(8):085006.
[751] Meyer S, Langer M, Grünewald L, Hänisch J, Gerthsen D, Holzapfel B. Pulsed laser deposition of quasi-multilayer superconducting $Ba(Fe_{0.92}Co_{0.08})_2As_2$-$BaHfO_3$ nanocomposite films. J Phys: Conf Ser 2020;1559(1):012052.
[752] Chen L, Tsai C-F, Zhu Y, Chen A, Bi Z, Lee J, et al. Enhanced flux pinning properties in superconducting $FeSe_{0.5}Te_{0.5}$ thin films with secondary phases. Supercond Sci Technol 2012;25(2):025020.
[753] Huang J, Chen L, Jian J, Khatkhatay F, Wang H. Nanostructured pinning centers in $FeSe_{0.1}Te_{0.9}$ thin films for enhanced superconducting properties. Supercond Sci Technol 2014;27(10):105006.
[754] Huang J, Chen L, Jian J, Tyler K, Li L, Wang H, et al. Magnetic $(CoFe_2O_4)_{0.1}(CeO_2)_{0.9}$ nanocomposite as effective pinning centers in $FeSe_{0.1}Te_{0.9}$ thin films. J Phys: Condens Matter 2015;28(2):025702.
[755] Oh M, Lee J, Seo S, Yoon S, Seo M, Park S, et al. Vortex pinning in artificially layered $Ba(Fe,Co)_2As_2$ film. Cryogenics 2018;92:1–4.
[756] Ozaki T, Wu L, Zhang C, Jaroszynski J, Si W, Zhou J, et al. A route for a strong increase of critical current in nanostrained iron-based superconductors. Nat Commun 2016;7(1):1–9.
[757] Seo S, Noh H, Li N, Jiang J, Tarantini C, Shi R, et al. Artificially engineered nanostrain in $FeSe_xTe_{1-x}$ superconductor thin films for supercurrent enhancement. NPG Asia Mater 2020;12:7.
[758] Sivakov A, Bondarenko S, Prokhvatilov A, Timofeev V, Pokhila A, Koverya V, et al. Microstructural and transport properties of superconducting $FeTe_{0.65}Se_{0.35}$ crystals. Supercond Sci Technol 2016;30(1):015018.
[759] Masi A, Alvani C, Armenio AA, Augieri A, Barba L, Campi G, et al. Fe(Se,Te) from melting routes: the influence of thermal processing on microstructure and superconducting properties. Supercond Sci Technol 2020;33(8):084007.
[760] Zhang Z, Qi Y, Wang L, Gao Z, Wang D, Zhang X, et al. Effects of heating conditions on the microstructure and superconducting properties of $Sr_{0.6}K_{0.4}Fe_2As_2$. Supercond Sci Technol 2010;23(6):065009.

[761] Shimada Y, Tokuta S, Yamanaka A, Yamamoto A, Konno TJ. Three-dimensional microstructure and critical current properties of ultrafine grain $Ba(Fe,Co)_2As_2$ bulk superconductors. J Alloys Compd 2022;923:166358.
[762] Tokuta S, Yamamoto A. Enhanced upper critical field in Co-doped Ba122 superconductors by lattice defect tuning. APL Mater 2019;7(11):111107.
[763] Ahn J-H, Oh S. Effect of hot-consolidation method on the superconducting properties of B- and C-doped $FeSe_{0.5}Te_{0.5}$. Curr Appl Phys 2013;13(6):1096–100.
[764] Puneet P, Podila R, He J, Rao AM, Howard A, Cornell N, et al. Synthesis and superconductivity in spark plasma sintered pristine and graphene-doped $FeSe_{0.5}Te_{0.5}$. Nanotechnol Rev 2015;4(5):411–7.
[765] Iebole M, Braccini V, Bernini C, Malagoli A, Manca N, Martinelli A, et al. Fe(Se,Te) thin films deposited through pulsed laser ablation from spark plasma sintered targets. Materials 2024;17(11).
[766] Zaikina JV, Kwong MY, Baccam B, Kauzlarich SM. Superconductor-in-an-hour: Spark plasma synthesis of Co- and Ni-doped $BaFe_2As_2$. Chem Mater 2018;30(24):8883–90.
[767] Yamamoto A, Tokuta S, Ishii A, Yamanaka A, Shimada Y, Ainslie MD. Superstrength permanent magnets with iron-based superconductors by data- and researcher-driven process design. NPG Asia Mater 2024;16:29.
[768] Hirabayashi Y, Iga H, Ogawa H, Tokuta S, Shimada Y, Yamamoto A. Deep learning for three-dimensional segmentation of electron microscopy images of complex ceramic materials. NPJ Comput Mater 2024;10:46.
[769] Guo Z, Muraoka K, Gao H, Shimada Y, Harada T, Tokuta S, et al. Planar defects and strain distributions in polycrystalline $BaFe_2As_2$ superconductors synthesized by mechanochemical methods. Acta Mater 2024;266:119648.
[770] Strickland NM. Qualifying high-temperature superconductors for fusion reactors. Supercond Sci Technol 2021;34(11):110502.
[771] Parizh M. Viewpoint on the manuscript by Zachary S Hartwig et al 'VIPER: an industrially scalable high-current high-temperature superconductor cable' 2020 Supercond. Sci. Technol. 33 11lt01. Supercond Sci Technol 2021;35(1):010501.
[772] Torsello D, Gambino D, Gozzelino L, Trotta A, Laviano F. Expected radiation environment and damage for YBCO tapes in compact fusion reactors. Supercond Sci Technol 2022;36(1):014003.
[773] Civale L. Vortex pinning and creep in high-temperature superconductors with columnar defects. Supercond Sci Technol 1997;10(7A):A11–28.
[774] Kirk M, Yan Y. Structure and properties of irradiation defects in $YBa_2Cu_3O_{7-x}$. Micron 1999;30(5):507–26.
[775] Lang W, Pedarnig JD. Ion irradiation of high-temperature superconductors and its application for nanopatterning. In: Nanoscience and engineering in superconductivity. Berlin, Heidelberg: Springer Berlin Heidelberg; 2010, p. 81–104.
[776] Eisterer M. Radiation effects on iron-based superconductors. Supercond Sci Technol 2017;31(1):013001.
[777] Torsello D, Gerbaldo R, Gozzelino L, Laviano F, Takahashi A, Park A, et al. Twofold role of columnar defects in iron based superconductors. Supercond Sci Technol 2020;33(9):094012.
[778] Mishra V, Boyd GR, Graser S, Maier T, Hirschfeld PJ, Scalapino DJ. Lifting of nodes by disorder in extended-*s*-state superconductors: Application to ferropnictides. Phys Rev B 2009;79:094512.
[779] Ghigo G, Torsello D, Ummarino GA, Gozzelino L, Tanatar MA, Prozorov R, et al. Disorder-driven transition from $s_{\pm}$ to s_{++} superconducting order parameter in proton irradiated $Ba(Fe_{1-x}Rh_x)_2As_2$ single crystals. Phys Rev Lett 2018;121:107001.
[780] Torsello D, Ummarino G, Bekaert J, Gozzelino L, Gerbaldo R, Tanatar M, et al. Tuning the Intrinsic anisotropy with disorder in the $CaKFe_4As_4$ superconductor. Phys Rev Appl 2020;13:064046.
[781] Tamegai T, Taen T, Yagyuda H, Tsuchiya Y, Mohan S, Taniguchi T, et al. Effects of particle irradiations on vortex states in iron-based superconductors. Supercond Sci Technol 2012;25(8):084008.
[782] Fischer DX, Prokopec R, Emhofer J, Eisterer M. The effect of fast neutron irradiation on the superconducting properties of REBCO coated conductors with and without artificial pinning centers. Supercond Sci Technol 2018;31(4):044006.
[783] Torsello D, Gozzelino L, Gerbaldo R, Tamegai T, Ghigo G. Scaling laws for ion irradiation effects in iron-based superconductors. Sci Rep 2021;11(1):1–10.
[784] Giapintzakis J, Lee W, Rice J, Ginsberg D, Robertson I, Wheeler R, et al. Production and identification of flux-pinning defects by electron irradiation in $YBa_2Cu_3O_{7-x}$ single crystals. Phys Rev B 1992;45(18):10677.
[785] Konobeyev A, Fischer U, Korovin Y, Simakov S. Evaluation of effective threshold displacement energies and other data required for the calculation of advanced atomic displacement cross-sections. Nucl Energy Technol 2017;3(3):169–75.
[786] Torsello D, Mino L, Bonino V, Agostino A, Operti L, Borfecchia E, et al. Monte Carlo analysis of the oxygen knock-on effects induced by synchrotron x-ray radiation in the $Bi_2Sr_2CaCu_2O_{8+\delta}$ superconductor. Phys Rev Mater 2018;2:014801.
[787] Frischherz M, Kirk M, Farmer J, Greenwood L, Weber H. Defect cascades produced by neutron irradiation in $YBa_2Cu_3O_{7-\delta}$. Phys C: Supercond 1994;232(3):309–27.
[788] Weber HW. Radiation effects on superconducting fusion magnet components. Int J Mod Phys E 2011;20(06):1325–78.
[789] Linden Y, Iliffe W, He G, Danaie M, Fischer D, Eisterer M, et al. Analysing neutron radiation damage in $YBa_2Cu_3O_{7-x}$ high-temperature superconductor tapes. J Microsc 2022;286(1):3–12.
[790] Eisterer M, Zehetmayer M, Tönies S, Weber HW, Kambara M, Babu NH, et al. Neutron irradiation of MgB_2 bulk superconductors. Supercond Sci Technol 2002;15(2):L9.
[791] Tarantini C, Aebersold H, Braccini V, Celentano G, Ferdeghini C, Ferrando V, et al. Effects of neutron irradiation on polycrystalline $Mg^{11}B_2$. Phys Rev B—Condens Matter Mater Phys 2006;73(13):134518.
[792] Emhofer J, Eisterer M, Weber HW. Stress dependence of the critical currents in neutron irradiated (RE)BCO coated conductors. Supercond Sci Technol 2013;26(3):035009.
[793] Ozaki T, Wu L, Gu G, Li Q. Ion irradiation of iron chalcogenide superconducting films. Supercond Sci Technol 2020;33(9):094008.
[794] Zhang Y, Rupich M, Solovyov V, Li Q, Goyal A. Dynamic behavior of reversible oxygen migration in irradiated-annealed high temperature superconducting wires. Sci Rep 2020;10(1):1–8.
[795] Suvorova EI, Degtyarenko PN, Karateev IA, Ovcharov AV, Vasiliev AL, Skuratov VA, et al. Energy dependent structure of Xe ion tracks in YBCO and the effect on the superconductive properties in magnetic fields. J Appl Phys 2019;126(14):145106.
[796] Sueyoshi T. Modification of critical current density anisotropy in high-T_c superconductors by using heavy-ion irradiations. Quantum Beam Sci 2021;5(2):16.
[797] Strickland NM, Wimbush SC, Soman AA, Kluth P, Notthoff C, Knibbe R, et al. Isotropic and anisotropic flux pinning induced by heavy-ion irradiation. IEEE Trans Appl Supercond 2022;32(4):1–5.
[798] Shinde S, Ogale S, Higgins J, Choudhary R, Kulkarni V, Venkatesan T, et al. Modification of critical current density of MgB_2 films irradiated with 200 MeV Ag ions. Appl Phys Lett 2004;84(13):2352–4.
[799] Kaushik S, Kumar R, Mishra P, Giencke J, Kim D, Eom C, et al. Modification of intergrain connectivity, upper critical field anisotropy and critical current density in ion irradiated MgB_2 films. Phys C: Supercond Appl 2006;442(1):73–8.
[800] Safar H, Cho J, Fleshler S, Maley M, Willis J, Coulter J, et al. Enhancement of transport critical current densities at 75 K in $(Bi,Pb)_2Sr_2Ca_2Cu_3O_y$/Ag tapes by means of fission tracks from irradiation by 0.8 GeV protons. Appl Phys Lett 1995;67(1):130–2.
[801] Coulter J, Willis J, Maley M, Ullmann J. Improved critical currents in a Bi-2223/Ag coil using splayed columnar defects. Phys C: Supercond 2004;412–414:1079–84.
[802] Knaster J, Moeslang A, Muroga T. Materials research for fusion. Nat Phys 2016;12(5):424–34.

[803] Bonino V, Torsello D, Prestipino C, Mino L, Truccato M. Time and space resolved modelling of the heating induced by synchrotron X-ray nanobeams. J Synchrotron Radiat 2020;27(6):1662–73.
[804] Powis I, Baer T, Ng C. High resolution laser photoionization and photoelectron studies. In: Wiley series in ion chemistry and physics, Chichester: John Wiley & Sons; 1995.
[805] Reinert F, Hüfner S. Photoemission spectroscopy—from early days to recent applications. New J Phys 2005;7:97.
[806] Tietz LA, Barry Carter C, Lathrop DK, Russek SE, Buhrman RA, Michael JR. Crystallography of $YBa_2Cu_3O_{6+x}$ thin film-substrate interfaces. J Mater Res 1989;4(5):1072–81.
[807] Karmanenko S. Influence of growth rate on the structural orientation of YBCO superconducting films. Supercond Sci Technol 1999;12(1):36–44.
[808] J. Birgeneau R, Stock C, M. Tranquada J, Yamada K. Magnetic neutron scattering in hole-doped cuprate superconductors. J Phys Soc Japan 2006;75(11):111003.
[809] Tanabe K, Kubo S, Hosseini Teherani F, Asano H, Suzuki M. Effects of photoinduced hole doping on normal-state and superconducting transport in oxygen-deficient $YBa_2Cu_3O_y$. Phys Rev Lett 1994;72:1537–40.
[810] Iio M, Yoshida M, Nakamoto T, Ogitsu T, Sugano M, Suzuki K, et al. Investigation of irradiation effect on REBCO coated conductors for future radiation-resistant magnet applications. IEEE Trans Appl Supercond 2022;32(6):1–5.
[811] Leyva A, Mora M, Martin G, Martinez A. Irradiation effect of Co-60 gamma rays in YBCO thick films. Supercond Sci Technol 1995;8(11):816–21.
[812] Enokihara A, Kohiki S, Setsune K, Wasa K, Higashi Y, Fukushima S, et al. X-ray irradiation effects on $ErBa_2Cu_3O_{7-x}$ superconducting thin films. Phys C: Supercond 1989;161(3):431–4.
[813] Bian W, Zhao G, Nishii J. The effect of heating temperature in ultraviolet irradiation process on properties of $YBa_2Cu_3O_{7-x}$ superconducting films processed from photosensitive solution. IEEE Trans Appl Supercond 2020;30(1):1–5.
[814] Giapintzakis J, Ginsberg DM, Kirk MA, Ockers S. Testing models of the symmetry of the superconducting pairing state by low-temperature electron irradiation of an untwinned single crystal of $YBa_2Cu_3O_{7-\delta}$. Phys Rev B 1994;50:15967–73.
[815] Antonova LK, Belov A, Voronov V, Didyk AY, Demikhov E, Ivanov L, et al. Dependences of HTS tape critical parameters on fluences under irradiation with heavy ions and high energy electrons. J Surf Investig X-Ray, Synchrotron Neutron Tech 2011;5(3):484–91.
[816] Chudy M, Fuger R, Eisterer M, Weber HW. Characterization of commercial YBCO coated conductors after neutron irradiation. IEEE Trans Appl Supercond 2011;21(3):3162–5.
[817] Fuger R, Eisterer M, Weber HW. YBCO coated conductors for fusion magnets. IEEE Trans Appl Supercond 2009;19(3):1532–5.
[818] Eisterer M, Fuger R, Chudy M, Hengstberger F, Weber HW. Neutron irradiation of coated conductors. Supercond Sci Technol 2010;23(1):014009.
[819] Jirsa M, Rameš M, Ďuran I, Melíšek T, Kováč P, Viererbl L. Electric currents in REBaCuO superconducting tapes. Supercond Sci Technol 2017;30(4):045010.
[820] Prokopec R, Fischer DX, Weber HW, Eisterer M. Suitability of coated conductors for fusion magnets in view of their radiation response. Supercond Sci Technol 2014;28(1):014005.
[821] Unterrainer R, Fischer DX, Lorenz A, Eisterer M. Recovering the performance of irradiated high-temperature superconductors for use in fusion magnets. Supercond Sci Technol 2022;35(4):04LT01.
[822] Unterrainer R, Gambino D, Semper F, Bodenseher A, Torsello D, Laviano F, et al. Responsibility of small defects for the low radiation tolerance of coated conductors. Supercond Sci Technol 2024;37(10):105008.
[823] Eisterer M, Bodenseher A, Unterrainer R. Universal degradation of high-temperature superconductors due to impurity scattering: predicting the performance loss in fusion magnets. 2024, arXiv preprint arXiv:2409.01376.
[824] Tönies S, Weber H, Guo Y, Dou S, Sawh R, Weinstein R. On the current transport limitations in Bi-based high temperature superconducting tapes. Appl Phys Lett 2001;78(24):3851–3.
[825] Tönies S, Weber H, Milliken D, Guo Y, Dou S, Gandini A, Sawh R, Ren Y, Weinstein R. Influence of neutron irradiation on the superconducting properties of BiSCCO-tapes containing different amounts of uranium. Phys C: Supercond 2000;341:1427–30.
[826] Wilke R, Bud'ko SL, Canfield P, Farmer J, Hannahs S. Systematic study of the superconducting and normal-state properties of neutron-irradiated MgB_2. Phys Rev B—Condens Matter Mater Phys 2006;73(13):134512.
[827] Putti M, Braccini V, Ferdeghini C, Gatti F, Grasso G, Manfrinetti P, et al. Neutron irradiation of $Mg^{11}B_2$: From the enhancement to the suppression of superconducting properties. Appl Phys Lett 2005;86(11).
[828] Eisterer M. Influence of disorder on H_{c2}-anisotropy and flux pinning in MgB_2. Phys Status Solidi (C) 2005;2(5):1606–14.
[829] Pallecchi I, Putti M. Properties of irradiated MgB_2, bulk and wires. In: MgB_2 superconducting wires: basics and applications. World Scientific; 2016, p. 455–83.
[830] Ozaki T, Jaroszynski J, Li Q. Two-fold reduction of J_c anisotropy in $FeSe_{0.5}Te_{0.5}$ films using low-energy proton irradiation. IEEE Trans Appl Supercond 2019;29(5):1–3.
[831] Leonard KJ, Aytug T, Gapud AA, III FAL, Greenwood NT, Zhang Y, et al. Irradiation response of next generation high temperature superconductors for fusion energy applications. Fusion Sci Technol 2014;66(1):57–62.
[832] Rupich MW, Sathyamurthy S, Fleshler S, Li Q, Solovyov V, Ozaki T, et al. Engineered pinning landscapes for enhanced 2G coil wire. IEEE Trans Appl Supercond 2016;26(3):1–4.
[833] Ozaki T, Wu L, Zhang C, Si W, Jie Q, Li Q. Enhanced critical current in superconducting $FeSe_{0.5}Te_{0.5}$ films at all magnetic field orientations by scalable gold ion irradiation. Supercond Sci Technol 2018;31(2):024002.
[834] Leroux M, Kihlstrom KJ, Holleis S, Rupich MW, Sathyamurthy S, Fleshler S, et al. Rapid doubling of the critical current of $YBa_2Cu_3O_{7-\delta}$ coated conductors for viable high-speed industrial processing. Appl Phys Lett 2015;107(19):192601.
[835] Jia Y, LeRoux M, Miller DJ, Wen JG, Kwok WK, Welp U. Doubling the critical current density of high temperature superconducting coated conductors through proton irradiation. Appl Phys Lett 2013;103(12):122601.
[836] Haberkorn N, Kim J, Suárez S, Lee J-H, Moon SH. Influence of random point defects introduced by proton irradiation on the flux creep rates and magnetic field dependence of the critical current density J_c of co-evaporated $GdBa_2Cu_3O_{7-\delta}$ coated conductors. Supercond Sci Technol 2015;28(12):125007.
[837] Rudnev I, Abin D, Pokrovskii S, Anishchenko I, Starikovskii A, Osipov M, Kulevoy T, Fedin P, Pryanishnikov K, Batulin R, et al. Influence of ion irradiation on critical characteristics of second-generation HTSC tapes. IEEE Trans Appl Supercond 2022;32(4):1–5.
[838] Sorbom BN. The effect of irradiation temperature on REBCO J_c degradation and implications for fusion magnets [Ph.D. thesis], Massachusetts Institute of Technology; 2017.
[839] Hardy V, Provost J, Groult D, Simon C, Hervieu M, Raveau B. Columnar defects induced by high energy heavy ions in HTSC. Their effect on irreversibility line and pinning properties. J Alloys Compd 1993;195:395–402.
[840] Isobe G, Kiuchi M, Otabe E, Matsushita T, Okayasu S, Prusseit W. Effect of heavy ion irradiation on critical current property in DyBCO coated conductors. Phys C: Supercond 2008;468(15–20):1656–60.
[841] Soman AA, Wimbush SC, Rupich MW, Notthoff C, Kluth P, Knibbe R, et al. The role of stacking faults in the enhancement of the ab plane peak in silver ion-irradiated commercial MOD REBCO wires. IEEE Trans Appl Supercond 2022.
[842] Sueyoshi T, Semboshi S, Ozaki T, Sakane H, Nishizaki T, Ishikawa N. Morphology of columnar defects dependent on irradiation direction in High-T_c superconductors. IEEE Trans Appl Supercond 2022;32(6):1–4.
[843] Sueyoshi T, Kotaki T, Furuki Y, Fujiyoshi T, Semboshi S, Ozaki T, et al. Strong flux pinning by columnar defects with directionally dependent morphologies in GdBCO-coated conductors irradiated with 80 MeV Xe ions. Japan J Appl Phys 2020;59(2):023001.

[844] Fujikura-Group. Fujikura superconductor technologies. 2022, Technical information available at https://www.fujikura.com/solutions/superconductingwire/.
[845] Iliffe WR, Peng N, Brittles GD, Bateman R, Webb RP, Grovenor CRM, et al. In-situ measurements of the effect of radiation damage on the superconducting properties of coated conductors. Supercond Sci Technol 2021.
[846] Liu L, Liu J, Zhang S, Zeng J, Zhai P, Hu P, et al. Radiation effect of swift heavy ions on current-carrying capability of commercial YBCO coated conductors. Appl Phys A 2020;126(6):1–6.
[847] Gu Y, Cai C, Liu Z, Liu J, Liu L, Huang R. Effect of Ta irradiation on microstructure and current carrying properties of YBCO coated conductors with element doping. J Appl Phys 2021;130(8):085304.
[848] Mezzetti E, Gerbaldo R, Ghigo G, Gozzelino L, Gherardi L. Confinement of fluxons by surface columnar defects in $Bi_{1.8}Pb_{0.33}Sr_{1.87}Ca_2Cu_3O_y$ tapes. Phys Rev B 1999;59(5):3890.
[849] Gerbaldo R, Botta D, Chiodoni A, Ghigo G, Gozzelino L, Laviano F, et al. Pseudo-periodic nanostructuring of Ag-clad BSCCO-2223 multifilamentary tapes as a tool to tune in-field superconducting performance. IEEE Trans Appl Supercond 2003;13(2):3000–3.
[850] Budhani R, Willis J, Suenaga M, Maley M, Coulter J, Safar H, et al. Studies of flux pinning by proton-induced fission tracks in multifilamentary tapes of $(Bi,Pb)_2Sr_2Ca_2Cu_3O_{10}$/Ag superconductors. J Appl Phys 1997;82(6):3014–8.
[851] Krusin-Elbaum L, Thompson J, Wheeler R, Marwick A, Li C, Patel S, et al. Enhancement of persistent currents in $Bi_2Sr_2CaCu_2O_8$ tapes with splayed columnar defects induced with 0.8 GeV protons. Appl Phys Lett 1994;64(24):3331–3.
[852] Sylva G, Bellingeri E, Ferdeghini C, Martinelli A, Pallecchi I, Pellegrino L, et al. Effects of high-energy proton irradiation on the superconducting properties of Fe(Se,Te) thin films. Supercond Sci Technol 2018;31(5):054001.
[853] Torsello D, Fracasso M, Gerbaldo R, Ghigo G, Laviano F, Napolitano A, et al. Proton irradiation effects on the superconducting properties of Fe(Se,Te) thin films. IEEE Trans Appl Supercond 2022;32(4):1–5.
[854] Nazir M, Xu Z, Peng N, Akhtar N, Papakonstantinou P, Webb R, et al. Enhancement of critical current density in helium ion irradiated $Ba(Fe,Co)_2As_2$ thin films. Supercond Sci Technol 2020;33(7):075012.
[855] Oliva AB, Aprili P, Bellesia B, Rebollo EB, Boutboul T, de Sousa PC. Toward completion and delivery of the first EU ITER magnets. IEEE Trans Appl Supercond 2020;30(4):1–13.
[856] Bayer CM. Characterization of high temperature superconductor cables for magnet toroidal field coils of the Demo fusion power plant, vol. 18. KIT Scientific Publishing; 2017.
[857] Greenwald M. Status of the SPARC physics basis. J Plasma Phys 2020;86(5):861860501.
[858] Kuang A, Cao N, Creely A, Dennett C, Hecla J, LaBombard B, et al. Conceptual design study for heat exhaust management in the ARC fusion pilot plant. Fusion Eng Des 2018;137:221–42.
[859] Zhai Y, Larbalestier D, Duckworth R, Hartwig Z, Prestemon S, Forest C. R&D needs for a U.S. fusion magnet base program. IEEE Trans Appl Supercond 2024;34(5):1–5.
[860] Iliffe W, Chislett-McDonald S, Harden F, Adams K, Tufnail J, Grovenor C, et al. STEP's plan for understanding REBCO Coated Conductors in the fusion environment. IEEE Trans Plasma Sci 2024;1–6.
[861] Korshunov MM, Togushova YN, Dolgov OV. Impurities in multiband superconductors. Phys-Usp 2016;59(12):1211.
[862] Torsello D, Gerbaldo R, Gozzelino L, Tanatar MA, Prozorov R, Canfield PC, et al. Electrodynamic response of $Ba(Fe_{1-x}Rh_x)_2As_2$ across the s± to s_{++} order parameter transition. Eur Phys J Spec Top 2019;228(3):719–23.
[863] Radtke RJ, Levin K, Schüttler H-B, Norman MR. Predictions for impurity-induced T_c suppression in the high-temperature superconductors. Phys Rev B 1993;48:653–6.
[864] Hartwig ZS, Vieira RF, Sorbom BN, Badcock RA, Bajko M, Beck WK, et al. VIPER: an industrially scalable high-current high-temperature superconductor cable. Supercond Sci Technol 2020;33(11):11LT01.
[865] Zinkle S, Snead L. Designing radiation resistance in materials for fusion energy. Annu Rev Mater Res 2014;44(1):241–67.
[866] Tinguely R, Rosenthal A, Simpson R, Ballinger S, Creely A, Frank S, et al. Neutron diagnostics for the physics of a high-field, compact, $Q \geq 1$ tokamak. Fusion Eng Des 2019;143:212–25.
[867] Ericsson G, Conroy S, Gatu Johnson M, Andersson Sundén E, Cecconello M, Eriksson Ja. Neutron spectroscopy as a fuel ion ratio diagnostic: Lessons from JET and prospects for ITER. Rev Sci Instrum 2010;81(10):10D324.
[868] Donne A, Costley A. Key issues in diagnostics for burning plasma experiments. IEEE Trans Plasma Sci 2004;32(1):177–86.
[869] Källne J, Gorini G, Ballabio L. Feasibility of neutron spectrometry diagnostic for the fuel ion density in DT tokamak plasmas. Rev Sci Instrum 1997;68(1):581–4.
[870] Goorley T, James M, Booth T, Brown F, Bull J, Cox LJ, et al. Initial MCNP6 Release Overview. Nucl Technol 2012;180(3):298–315.
[871] Sato T, Niita K, Matsuda N, Hashimoto S, Iwamoto Y, Noda S, et al. Particle and heavy ion transport code system, PHITS, version 2.52. J Nucl Sci Technol 2013;50(9):913–23.
[872] Allison J, Amako K, Apostolakis J, Arce P, Asai M, Aso T, et al. Recent developments in GEANT4. Nucl Instruments Methods Phys Res Sect A: Accel Spectrometers, Detect Assoc Equip 2016;835:186–225.
[873] Jaboulay J-C, Cayla P-Y, Fausser C, Damian F, Lee Y-K, Puma AL, et al. TRIPOLI-4® Monte Carlo code ITER A-lite neutronic model validation. Fusion Eng Des 2014;89(9):2174–8.
[874] Böhlen T, Cerutti F, Chin M, Fassò A, Ferrari A, Ortega P, et al. The FLUKA code: Developments and challenges for high energy and medical applications. Nucl Data Sheets 2014;120:211–4.
[875] Ledda F, Pettinari D, Ferrero G, Hartwig Z, Laviano F, Meschini S, et al. 3D neutronic analysis on compact fusion reactors: PHITS-OpenMC cross-comparison. Fusion Eng Des 2024;202:114323.
[876] Ledda F, Torsello D, Pettinari D, Sparacio S, Hartwig Z, Zucchetti M, et al. 3D neutronic and secondary particles analysis on $YBa_2Cu_3O_{7-\delta}$ tapes for compact fusion reactors. IEEE Trans Appl Supercond 2024;34(3):1–5.
[877] Sparacio S, Viarengo S, Ledda F, Torsello D, Riva N, Hartwig ZS, et al. Analysis framework for nuclear heating effects on HTS-based conductors in fusion power plants. IEEE Trans Appl Supercond 2024;34(3):1–8.
[878] Pinto V, Celentano G, De Angelis M, Laviano F, Masi A, Pietropaolo A, et al. Effect of 14.1 MeV fusion neutron irradiation on YBCO thin films and commercial REBCO tapes. IEEE Trans Appl Supercond 2024;34(3):1–4.
[879] Torsello D, Casalegno V, Divitini G, Ghigo G, Gerbaldo R, Fracasso M, et al. Triple ion beam irradiation of glass-ceramic materials for nuclear fusion technology. J Nucl Mater 2022;153783.
[880] Gapud A, Greenwood N, Alexander J, Khan A, Leonard K, Aytug T, et al. Irradiation response of commercial, high-T_c superconducting tapes: Electromagnetic transport properties. J Nucl Mater 2015;462:108–13.
[881] Civale L. Comparative analysis of particle irradiation and second phases additions on the critical current densities of $YBa_2Cu_3O_7$ single crystals, thin films, and coated conductors: implications for fusion reactors magnets. Supercond Sci Technol 2025;38:043003.
[882] Eley S, Glatz A, Willa R. Challenges and transformative opportunities in superconductor vortex physics. J Appl Phys 2021;130(5):050901.
[883] Cayado P, Rosas Ja, Murta-Pina Ja, Ruiz HS. An open and collaborative database of properties of materials for high-temperature superconducting-based devices. IEEE Transactions on Applied Superconductivity 2025;35(6):1–6.

Harold S. Ruiz (ORCID:0000-0002-6100-1918) is the Head of the Green Energy and Transport (GrEaT) research group and the Electrical Engineering Division at the University of Leicester in the UK. He leads the research topic of applied superconductivity both at the University of Leicester and at the UK National Space Park Leicester. Harold got his diploma in Physics in 2004, holds a M.Sc. in Condensed Matter Physics and Superconductivity from the National University of Colombia (2007), a M.Sc. on Physical Technologies (2008), and a Cum Laude Ph.D. and European Doctorate in Applied Superconductivity from the University of Zaragoza in Spain (2012). Before joining the University of Leicester in 2015, he used to work for the Center for Advanced Photonics and Electronics Systems at the University of Cambridge (UK), the Center for Advanced Power Systems at Florida State University (USA), and the Materials Science Institute of Aragón ICMA-CSIC (Spain). He has co-authored more than 10 funded research projects accounting for circa 3.5M (USD), and leads the largest of the four specialized workgroups within the European COST Action CA19108, Hi-Scale, which encompass about 140 senior researchers focused on the advancement of applied superconductivity, from materials to devices.

Jens Hänisch (ORCID:0000-0003-2757-236X) is leading the research topic Superconducting Materials at the Institute for Technical Physics, Karlsruhe Institute of Technology as senior scientist. He studied physics at TU Dresden and University of Sheffield. After his Ph.D. at TU Dresden in 2005, he did a post-doc at the Superconductivity Technology Center at Los Alamos National Laboratory for 3 years and worked at IFW Dresden for several years. His research has been focused on structure–property relations of cuprate and Fe-based superconducting films, especially concerning their electro-magnetic transport properties.

Massimiliano Polichetti (ORCID:0000-0002-4534-3301) is Associate Professor at the Department of Physics, and leads the laboratory for magnetic measurements "LAMBDA" ('Laboratory for Analysis of Materials Behavior in Dc and Ac fields') at the University of Salerno. He got his Ph.D. in Physics in 1997 on the study of the ac and dc magnetic properties of superconducting materials, focusing on the analysis of the vortex dynamics and pinning properties. He made research activity at the University of Salerno, with a "Visiting Fellowship" at the Imperial College London (England), at the University of Leiden (The Netherlands) and at the Slovak Academy of Sciences of Bratislava (Slovakia). Since 2001 he has been teaching courses at students in Physics, in Chemistry and in Biology. He has been member of the Salerno University Scientific Board, of the Quality System Committee, and of the "Dottorato" (Ph.D.) Teaching Board. He is associated to the Consiglio Nazionale delle Ricerche (CNR) and has been the Italian responsible of two International Projects for Scientific Cooperation between CNR and the Bulgarian Academy of Sciences (2013–2015 and 2019–2021/22). He has research and professional experience in Condensed Matter Physics, ac and dc magnetic properties of superconductors, magnetic materials and nanoparticles, automated data acquisition systems, high field magnets, cryogenic techniques, design, realization and test of equipment for measurements of electrical and magnetic properties of materials.

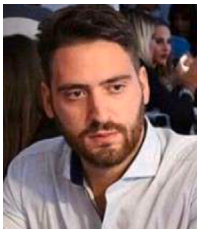

Armando Galluzzi (ORCID:0000-0002-1372-357X) is currently a postdoctoral researcher at the Department of Physics of the University of Salerno. He received the Ph.D. in 2018 from the Vanvitelli University for his studies on the vortex dynamics and pinning characteristics of FeSe iron-based superconductors having different doping. His experimental research is focused on the DC and AC magnetic field characterization of superconducting materials (cuprates, iron-based superconductors) in order to study both fundamental and applicative properties. Among his main investigated topics there are the vortex dynamics, the interaction between the vortices and the pinning landscape, and the non-monotonous behavior of the critical current density as a function of field and temperature.

Laura Gozzelino (ORCID:0000-0002-9204-0792) is an Associate Professor at the Department of Applied Science and Technology of the Politecnico di Torino. Her research activity has been mainly focused on the study of the electromagnetic properties of superconducting materials (cuprates, MgB_2, iron-based superconductors), aimed at both fundamental and applicative aspects. Among the main investigated topics there is the study of the influence of intrinsic and extrinsic (e.g. ion-irradiation induced) defects on the superconductor phase diagram and vortex dynamics.

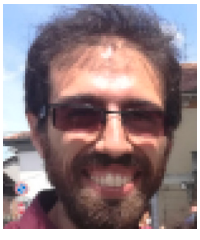

Daniele Torsello (ORCID:0000-0001-9551-1716) is currently a Research Fellow at the Department of Applied Science and Technology of the Politecnico di Torino. His research is focused on the characterization of the high frequency electromagnetic properties of novel superconductors and their response to structural disorder. He analyzes both computationally and experimentally radiation damage in superconductors, both for fundamental investigations and for fusion applications.

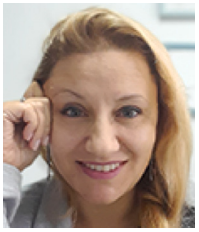

Sanja Milošević Govedarović (ORCID:0000-0002-4705-1177) is Doctor of physical chemistry, Senior Research Associate at the Department of Physics in Vinča Institute of Nuclear Sciences - National Institute of the Republic of Serbia, University of Belgrade. As a participant of Centre of Excellence for Hydrogen and Renewable Energy - CONVINCE, she is dedicated to promote renewable energy sources and alternative technologies. Her main interests are solid-state synthesis of powders and thin films, methods of structural, material characterizations, and methods of material modification. Thermal modification, mechanical milling, ion-irradiation are the most common methods in her work and the most often used in order to meet demands and needs. She currently serves as management committee member for Serbia in the COST action CA19108: High-Temperature SuperConductivity for AcceLerating the Energy Transition (2020–2024).

Jasmina Grbović Novaković (ORCID:0000-0002-8481-6407) is Full Research Professor at the University of Belgrade and head of the Centre of Excellence for Hydrogen and Renewable Energy of the Vinča Institute of Nuclear Sciences in Serbia. She has a Ph.D in physical chemistry and has acted as a member of the steering committees of the international COST Actions MP1103 and CA15102. From 2010 to 2020, she was the President of the Serbian Microscopy Society. She is one of the founders of the Hydrogen Economy Initiative Serbia, a member of the Commission for Acquiring Degrees, and a reviewer of the National Body for Accreditation and Quality Assurance in Higher Education. She is the winner of the award of the International Association for Hydrogen Energy for outstanding contribution to the development of hydrogen energy in this region (Outstanding service award for 2009). She has co-authored over 200 works published in journals and conference proceedings. Her fields of expertise are mechanochemical synthesis, ion beam modification of materials, development of energy-related materials, and sensors. She is also associate editor of the journal Gas Science and Engineering.

Oleksandr Dobrovolskiy (ORCID:0000-0002-7895-8265) is Professor and Head of Cryogenic Quantum Electronics Division at the Institute for Electrical Measurement Science and Fundamental Electrical Engineering of the Technische Universität Braunschweig in Germany. He received his Ph.D. degree from the B. Verkin ILTPE (Kharkiv, Ukraine, 2009) and Habilitation in Physics from the Goethe University (Frankfurt am Main, Germany, 2016) where he was a postdoc and Principal Investigator from 2009 to 2019. From 2019 to 2024 Oleksandr was leading the Superconductivity and Spintronics laboratory at the Faculty of Physics of the University of Vienna and has been representing Germany and Austria in various European networking programs. His research interests encompass superconductivity and fluxonics, magnetism and spintronics, 3D nanostructures and sensors, topological and hybrid systems, as well as quantum electronic devices.

Wolfgang Lang (ORCID:0000-0001-8722-2674) is Professor (ao.) at the Faculty of Physics of the University of Vienna in Austria. He received his Ph.D. in 1985 and his habilitation in 1996 from the University of Vienna. He has held research fellowships at the Ludwig Boltzmann Institute of Solid State Physics in Vienna and the Princeton University, USA, as well as guest professorships at the University of Rochester, USA, and at the Johannes-Kepler-University of Linz, Austria. Wolfgang represented Austria in various European networking programs and was the Vice Dean for Finance and Infrastructure at the University of Vienna's Faculty of Physics. His previous and current scientific interests span a wide range of materials, from graphite intercalation compounds, fullerenes and carbon nanotubes, colossal magnetoresistance perovskites, unconventional solar cell materials to superconductors emphasizing copper-oxides.

Gaia Grimaldi (ORCID:0000-0001-5438-8379) has completed her Ph.D. in 2001 at Salerno University, made in collaboration with ENEA, at the National Superconductivity Lab in the Research Center in Frascati (Rome), and as visiting fellowship at Technical University of Munich (Germany). Since 2003, Researcher at National Institute of Matter Physics, then at National Council of Research CNR in the SuPerconducting and other INnovative materials and device Institute. From 2015 she is scientific responsible of the MAterial Science and TEchnology Research Lab in Salerno, where experimental studies are performed in extremely high magnetic fields and very low temperatures as a function of the direction of the applied magnetic field on superconducting materials useful for large-scale applications and/or photon detection. Research developed mainly on vortex dynamics in HTS, LTS, IBS superconductors by critical vortex velocity measurements and non-equilibrium phenomena in the interaction between vortices and material defects: magnetic field-temperature phase diagram, order–disorder transitions induced by relatively high bias current, pinning influence on vortex dynamics even at high speed, material and pinning anisotropy.

Adrian Crisan (ORCID:0000-0002-0662-0177) is currently Senior Scientist Grade 1 - Professor, at the National Institute for Materials Physics Magurele-Bucharest, Romania, and Associate Professor at Faculty of Physics Doctoral School, University of Bucharest. He graduated in 1985 University of Bucharest, Faculty of Physics, as Engineering Physicist - Master of Science. In 1994 he was awarded a Ph.D. from Institute of Atomic Physics, Bucharest, and in 2013 he obtained a Higher Doctorate Degree, Doctor of Science, from University of Birmingham. He has a research experience of over 35 years in Condensed Matter and Materials Physics, Superconductivity, and Nanotechnology, in universities and research institutions from UK, Italy, Japan and Romania. As winner of the prestigious Marie Curie Excellence Grant at University of Birmingham, of about 1.6M Euro, he led the research on self-assembled nanotechnology of pinning centers in YBCO film. He is a former fellow of NATO/Royal Society, Science and Technology Agency of Japan, Japanese Society for the Promotion of Science. As Visiting Professor he was awarded both short-time and long time JSPS Invitational Fellowships. Within the EU Framework Operational Program Competitiveness he was Director of a 1.8 M Euro research project on rare-earth- and boron-based advanced functional materials for various applications, including superconductivity. He has major contributions in studies of vortex matter, dynamics and pinning, being one of the pioneers of artificial pinning in high-Tc superconductors.

Petre Badica (ORCID:0000-0003-3038-2110) is a Senior Scientist Grade 1 - Professor, at the National Institute for Materials Physics Magurele-Bucharest, Romania. He graduated in 1992 from University 'Politehnica' of Bucharest, Romania and was awarded in 1996 a Ph.D. from National Technical University of Ukraine 'Igor Sikorsky Kiev Polytechnic Institute'. He is a former JSPS-STA, NIMS, NEDO, MANA, Alexander von Humboldt fellow and Visiting Prof. of Nanyang Technological University, Singapore and Tohoku University, Japan. His contributions are on synthesis/processing by conventional and unconventional methods, advanced characterization, and applied physics of selected materials including superconductors.

Alina Marinela Ionescu (ORCID:0000-0001-7357-4249) is Senior Scientist Grade 3 at the National Institute for Materials Physics Magurele-Bucharest, Romania. She was awarded a Ph.D. in 2018. She is working on magnetic properties of various superconducting materials, like YBCO films with nano-engineered pinning centers, magnesium diboride Nb-Ti, and cuprates and pnictides single crystals. She was a postdoctoral fellow at Max Planck Institute for Intelligent Systems, Stuttgart, Germany.

Pablo Cayado (ORCID:0000-0003-3703-6122) Pablo Cayado is a Lecturer at University of Oviedo, Spain, since January 2025. Before, he was Research Associate at the Department of Quantum Matter Physics (DQMP) at University of Geneva in Switzerland for 4 years and, previously, he worked another 4 years at the Institute of Technical Physics at Karlsruhe Institute of Technology in Germany. He studied physics at the University of Oviedo and graduated in 2011. Afterwards, he moved to the Material Science Institute of Barcelona (ICMAB) where he completed his master's degree in Nanotechnology and Materials Science (2012) and PhD in Materials Science (2016) working on the preparation and characterization of REBCO nanocomposite films by chemical solution deposition and the oxygen diffusion in these films. His current research activities are focused on electrical and mechanical properties of coated conductors for the development of REBCO superconducting joints. He is also working on using chemical solution deposition for REBCO films with new pinning scenarios (mixing of different REBCO compounds and new nanoparticles) and on the optimization of the oxygenation process in such films.

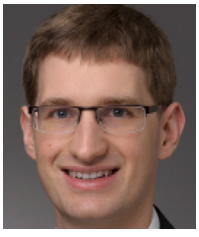

Roland Willa (ORCID:0000-0003-1537-0824) is professor and research group leader at the University of Applied Sciences, HES-SO Valais/Wallis in Switzerland. He studied physics at ETH Zurich. After his Ph.D. in 2016, he was awarded a postdoctoral fellowship from the Swiss National Science Foundation to pursue his research career with a postdoc at the Argonne National Laboratory. In 2018, he moved to Germany for a second postdoctoral stay at the Karlsruhe Institute for Technology, partially funded through a Young Researcher Grant from the Heidelberger Academy of Sciences. His research revolves around low-temperature quantum matter with a particular focus on vortices in superconductors and vestigial orders in magnetic systems and iron-based/topological superconductors.

Bernardo Barbiellini (ORCID:0000-0002-3309-1362) is a full professor of Physics at the Lappeenranta-Lahti University of Technology (LUT University). He conducts fundamental research at the electronic, atomic and molecular levels to understand matter and energy. His work extends to using this fundamental knowledge to develop cutting-edge materials to support new sustainable technologies. A key aspect of his research is the numerical study of the Kohn–Sham equations within Density Functional Theory. These equations play a crucial role in the calculation of electronic structures and facilitate the study of quantum mechanical properties in magnetic, superconducting and battery materials probed with advanced spectroscopy techniques.

Serena Eley (ORCID:0000-0002-2928-5316) is an Assistant Professor in the Department of Electrical & Computer Engineering at the University of Washington in Seattle, WA. She earned her B.S. in physics at the California Institute of Technology then conducted research at the International Superconductivity Technology Center in Tokyo, Japan as a Henry Luce Scholar before earning her Ph.D. in physics at the University of Illinois Urbana-Champaign. Her dissertation work, for which she received the John Bardeen Award, explored proximity effects and vortex dynamics in nanostructured superconductor—normal-metal arrays, revealing behavior that deviates from conventional proximity effect theories. After graduate school, she worked on vortex dynamics in superconductors as a postdoctoral researcher at Los Alamos National Laboratory. Currently, Eley's research group focuses on understanding vortex–defect interactions in superconductors, skyrmion-defect interactions in magnetic materials, and mitigating materials related issues that limit superconducting quantum circuit operation. Eley won a National Science Foundation CAREER award, a Cottrell Scholars award from the Research Corporation for Science Advancement, and the American Institute of Physics Joseph A. Johnson Award.

Antonio Badía Majós (ORCID:0000-0002-8753-23978) received his Ph.D. degree in Physics from the University of Zaragoza. He is now a Full Professor in the Condensed Matter Physics Department of the University of Zaragoza and also a member of Institute of Nanoscience and Materials of Aragón (INMA). His research has focused on superconducting materials, mainly contributing to a number of phenomenological theories such as the Critical State Model. To date, he has authored over 70 scientific papers in this field, and recently a monographic book entitled 'Macroscopic Superconducting Phenomena'. He works actively to promote superconductivity through educational materials and outreach activities.